The cosmic origins of carbon and the evolution of dust, gas and the CNO elements in galaxies

David J. Stock

Thesis submitted for the degree of

Doctor of Philosophy

Department of Physics & Astrophysics

University College London

April 25, 2011

I, David J. Stock confirm that the work presented in this thesis is my own. Where information has been derived from other sources, I confirm that this has been indicated in the thesis.

Abstract

Carbon, along with nitrogen and oxygen, is produced by stars of differing mass and metallicity throughout the evolutionary history of galaxies. The production of oxygen and nitrogen is believed to be dominated by stars of high and low mass respectively, while the origin of carbon is less settled, as it can be produced by both low and high mass stars. An observational approach to determining whether low or high mass stars dominate carbon production is desirable, via studies of the nebulae that such stars produce during their advanced evolutionary stages. However, ionized carbon does not have forbidden emission lines in the optical range, making optical carbon abundance measurements reliant on the use of carbon recombination lines or neutral carbon forbidden lines. Carbonaceous dust is inferred to exist in many nebulae, though the amount of carbon in such dust can be difficult to determine.

This thesis presents observations and numerical modelling results aimed at tracing the origins of carbon in galaxies. The contribution of individual stars is probed, focusing first on nebulae around massive Wolf-Rayet (WR) stars, particularly those with C-rich WC stars. The properties of the population of Galactic and LMC circumstellar nebulae around WR stars are examined, followed by a spectroscopic investigation of abundances in nebulae around both WN and WC stars. Carbon production rates by low and intermediate mass stars are inferred from published carbon abundance measurements for planetary nebulae.

The second approach used to trace the origin and evolution of carbon is through numerical modelling of the chemical histories of galaxies. Using various formulations for the inputs of C, N and O by low and high mass stars, models are constructed which trace the overall abundances of these elements over the history of a galaxy, from their birth to the present day. By tuning the input data for stellar elemental yields to best match observed abundance patterns, the mass and metallicity ranges which are responsible for creating carbon can potentially be diagnosed. Finally, these models are adapted to investigate the evolution of the dust content of galaxies, including galaxies at high redshifts.

Contents

List of Figures

List of Tables

Acronyms

AGB Asymptotic Giant Branch.

BBN Big Bang Nucleosynthesis.

CCD Charge Coupled Device.

CCSN(e) Core Collapse Supernova(e).

CEL Collisionally Excited Line.

CNO Carbon, Nitrogen, Oxygen.

EFOSC2 ESO Faint Object Spectrograph & Camera.

ESO European Southern Observatory.

FWHM Full Width Half Maximum.

GCE Galactic Chemical Evolution.

HBB Hot Bottom Burning.

ICM Inter-Cluster Medium.

IMF Initial Mass Function.

IRA Instantaneous Recycling Approximation.

ISM Interstellar Medium.

LBV Luminous Blue Variable.

LIMs Low- Intermediate-Mass star.

LMC Large Magellanic Cloud.

LSS Long Slit Spectroscopy.

MW Milky Way.

NEAT Nebular Empirical Analysis Tool.

NTT New Technology Telescope.

PAH Polycyclic Aromatic Hydrocarbon.

PDR Photo-Dominated Region.

PN(e) Planetary Nebula(e).

PP Proton-Proton.

RSG Red Supergiant.

S-AGB Super Asymptotic Giant Branch.

SED Spectral Energy Distribution.

SFE Star Formation Efficiency.

SFH Star Formation History.

SFR Star Formation Rate.

SHS Southern Hα Survey.

SN(e) Supernova(e).

SNR Supernova Remnant.

UVES Ultra-Violet Eschelle Spectrograph.

WC Carbon Rich Wolf-Rayet.

WN Nitrogen Rich Wolf-Rayet.

WR Wolf-Rayet.

Chapter 1

Introduction

> "Life exists in the universe only because the carbon atom possesses certain exceptional properties."
> — James Jeans

It is said that life as we know it is carbon-based, that is, all life on earth is based on the chemistry of the element carbon. Which types of stars produce this carbon, and other elements necessary for life, like oxygen and nitrogen? Specifically, which kinds of stars are the dominant contributors to the carbon in present-day galaxies, and has there been any evolution in this dominance?

Recent years have seen claims that low mass stars are responsible for carbon production (Chiappini et al., 2003), that massive stars are largely responsible (Henry et al., 2000) and that maybe both are significant (Cescutti et al., 2009). This debate is in sharp contrast to the other elements mentioned which have well known production sites — oxygen is usually created in massive stars while nitrogen is created in low mass stars.

The problem with stellar carbon production that we are investigating is essentially a degeneracy. Low mass stars are known to produce carbon — which will be discussed at some length later — but over very long timescales. Massive stars are also predicted to make carbon, usually this would imply short timescales as massive stars have short lifetimes. However carbon production by massive stars is strongly dependent on the non-hydrogen/helium mass fraction, the metallicity. Galactic metallicity is built up by generations of stars over long periods of time — meaning that massive stars may only produce carbon at later periods in the history of the galaxy, the same time at which the low mass stars are producing carbon.

Investigating this question can lead us down two distinct avenues, firstly we can probe the circumstellar environs of stars which we suspect to be producing carbon for evidence of such production, as will be discussed later. Secondly, we can simulate the chemical enrichment histories of galaxies using different stellar recycling models.

1.1 Evolution of Galactic Gas and Dust

To state that there is evolution in the abundances of the chemical elements in the universe is no longer controversial. The question has moved on to become, "how did the universe and individual galaxies arrive at their present set of chemical abundances?", which is an altogether more complex issue. Possessing a complete answer to that question would imply that all the relevant astrophysics, from the big bang to the present day, was understood.

It is possible to attempt an answer on a simpler basis, though, by modelling the chemical evolution of individual galaxies. Such a model is normally termed a "Galactic Chemical Evolution" (GCE) model. These models include parameterisations of all of the quantities and galactic properties which are necessary to simulate the history of a galaxy from its origin as a cloud of gas, through the formation of the first stars, and generations thereafter. It is important to bear in mind that such simulations are a sketch of the true evolution and that much of the sophistication of reality is removed from these models.

Such modelling has its problems too, as the histories of galaxies, in terms of mergers and star formation, are still very much under debate. Indeed, whether galaxies form via mergers or through some kind of infall episode is far from settled; GCE models suggest that the stochastic merger histories that are in vogue in cosmological N-body simulations do not produce chemical evolutionary histories in line with what is observed.

The main input to a GCE model is a prescription for stellar recycling, that is, a description of how stars return processed material to the interstellar medium (ISM). This is usually expressed as a grid of elemental mass yields for stars of varying initial mass and metallicity. These mass yields are a quantification of stellar recycling and will be discussed later. By experimenting with using different combinations of yields for the same galaxy model, we can ascertain which combination best matches the abundance data we possess, where both the model and the abundance data are functions of time. It is then possible to calculate which types of stars dominate the creation of different elements, during which periods in the history of our galaxy model.

The precise mathematical basis of a general GCE model will be presented in Chapter 4. A sketch of what a GCE model does at each timestep is as follows:

1. Calculate current star formation rate (SFR) based on present conditions

2. Incorporate the nucleosynthetic contribution of all stars which would have died during this timestep into the current metallicity and galactic gas mass

3. Calculate, based on the metallicity and star formation history of the galaxy, how many

stars would come to the ends of their lives in this timestep and their masses

4. Calculate the nucleosynthetic contributions of this population based on a detailed knowledge of stellar recycling

5. Subtract the mass of stars formed during this timestep from the galactic gas mass

6. Add inflowing gas and subtract outflowing gas to the galactic gas mass and update the total galaxy mass

1.1.1 Primordial Nucleosynthesis

The initial abundances used in almost all models are those that arise from Big Bang Nucleosynthesis (BBN), which we shall use as a starting point for the first generations of stars. This initial set of abundances are usually referred to as primordial abundances.

In the mid 1960's the discovery of the Cosmic Microwave Background (Penzias & Wilson, 1965), as predicted by the hot Big Bang models of Gamow and collaborators (e.g., Alpher & Herman 1948) gave credence to the Big Bang model as a whole and sparked interest in the nucleosynthesis that must have occurred immediately after the Big Bang.

The result that is of paramount importance to this work was published several years beforehand: Alpher et al. (1948) gave predictions of the ratio of hydrogen and helium produced by the Big Bang. The process by which this ratio is established is determined by basic thermodynamics, and, while the full treatment is not necessary here, an illustrative sketch following the arguments of Hayashi (1950); Hayashi & Nishida (1956) runs as follows: at the high temperatures and densities prevalent immediately after the Big Bang, the neutron and proton species would be in thermal equilibrium. Deuterium formation was suppressed as its binding energy was lower than that associated with the ambient temperature. As the temperature gradually lowered below the binding energy, deuterium started to form, leading to helium formation. Eventually the temperature fell below that required for nuclear reactions and the then current abundances were "frozen in" as nuclear reactions ceased.

This initial work did not include the processes necessary to make heavier elements – these were considered in later papers (e.g., Peebles 1966a,b). The Big Bang nucleosynthesis model is now regarded as a major success of cosmology; it accurately predicts the abundances of the light elements created during the Big Bang. In particular the abundances of deuterium and lithium-7 which are predicted match those observed in unevolved objects. This is important, as there are no known stellar nucleosynthetic processes which are net producers of deuterium and lithium-7, and these isotopes are destroyed by star formation. Therefore the lithium and

deuterium abundances are good indicators of the level of primordial nucleosynthetic processing and the subsequent level of processing by stellar recycling.

However the main result of interest here is the mass fraction of hydrogen to helium. The heavier elements created by BBN (e.g ^{7}Li) are useful as diagnostics in some cases, and may help catalyse the collapse of clouds to form the first stars, but take little part in the chemical evolution to follow. In almost all models it is usual to set the initial mass ratio within the primordial gas to X=0.75, Y=0.25 and Z=0 (Wagoner et al., 1967), where X and Y represent the hydrogen and helium mass fractions respectively and Z is the mass fraction of all heavier elements.

We can use this approximation for two reasons: first, the initial metallicity is very low compared to that which will be achieved later (typically by as much as five orders of magnitude) and exists in the form of elements that will be destroyed to make heavier elements anyway; secondly, and more importantly, our prescriptions for stellar recycling have no dependence on these elements, as they are instantly destroyed in stars.

All models that will be used assume the primordial gas composition described above ($X_0 = 0.75, Y_0 = 0.25, Z_0 = 0$). It has been argued that in some cases this is not representative of gas accreted at later times; specifically, galaxies in clusters may be accreting Inter-Cluster Medium (ICM) gas which could have been enriched by galactic winds from other cluster galaxies (Metzler & Evrard, 1994). This situation is not commonly invoked in GCE models as the Milky Way does not exist in such a system, making such a model difficult to constrain with observations.

1.1.2 Galaxy-Model Ingredients

If we combine our knowledge of stellar recycling with some other vital ingredients we can form a very simple picture of how galaxies evolve or, at least, how their chemical compositions evolve. The other ingredients are parameterisations of our ideas about how galaxies and stars live and die, combined with basic parameters like the mass of the galaxy ($M_{\rm GAL}$). The two most basic influences are the Initial Mass Function (IMF, usually denoted $\phi(m)$) and Star Formation Rate (usually denoted $\psi(t)$). For more complex models we can include more accurate pictures of galaxy formation and stellar lifetimes.

1.1.2.1 The Initial Mass Function

The initial mass function describes the relative frequency of the birth of stars in different mass ranges. It was derived initially by counting stars in the local volume (Salpeter, 1955). This method, although fraught with difficulty due to lack of precise knowledge of the distances to

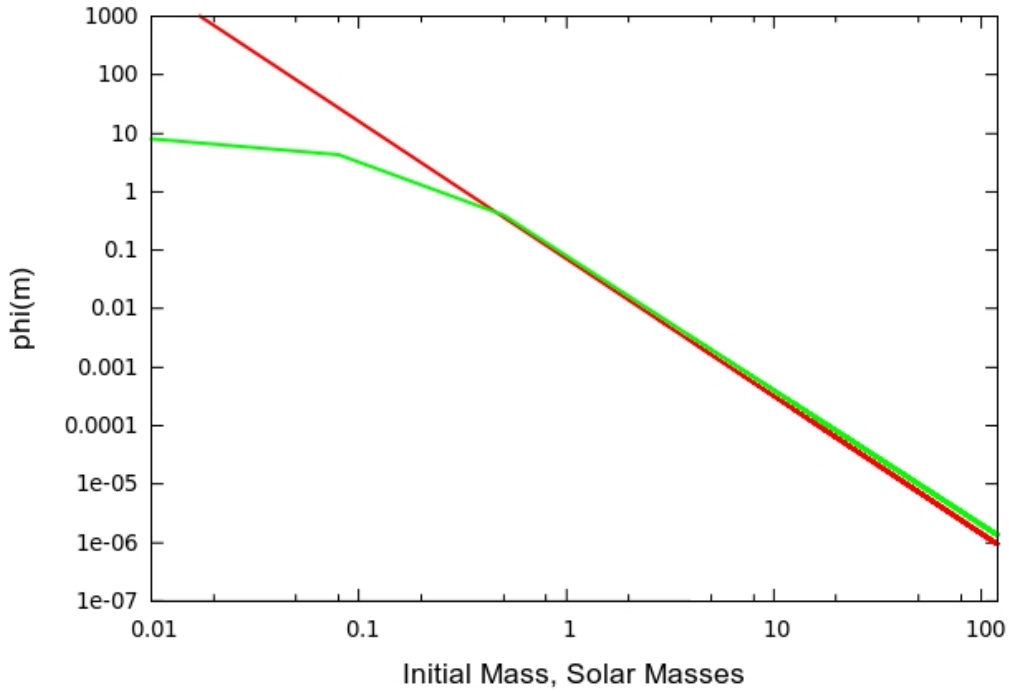

Figure 1.1: Comparison of Salpeter (red) and multi-slope Kroupa (green) IMF prescriptions in log space.

stars, produced a remarkably resilient result: initial stellar masses are distributed as a power law of the form ${}^{dN}/_{dlogM} = \phi(M) \propto M^{-\gamma}$. Salpeter derived $\gamma = 2.35$, a value that has proven robust over the past half century, albeit with slight issues at very low mass ranges.

Other prescriptions for the IMF have been postulated, all of which involve adding some characteristic scale mass to the distribution in order to solve an over-prediction of low-mass stars by the Salpeter IMF. These either take the form of having a two-(or more) slope power law (e.g., Scalo (1986); Kroupa (2001a,b)), typically breaking at around a solar mass, or adding some more complex function describing the behaviour of low mass stars (e.g., Chabrier 2003b). The differences in shapes between Kroupa and Salpeter IMFs are shown in Figure 1.1.

A common question of the last decade has been whether the IMF is the same at all times and throughout space; i.e., is the IMF the same in high-redshift galaxies under very different star-formation conditions? It is still controversial to state that in the very earliest generations of star formation the IMF would be different. If the conditions are dramatically different, as they would have been for the first generations of stars (so-called Population III, which had no metal content to facilitate cooling and hence collapse), then we might expect a different IMF. However this is a very difficult effect to constrain with observations.

Detections of a variable IMF have been claimed in other contexts, including the bulge of

our own galaxy (Maness et al., 2007; Löckmann et al., 2010), ultra-compact dwarf galaxies (Dabringhausen et al., 2010), star-forming globules (Getman et al., 2007), Extremely Metal-Poor (EMP) stars in our galaxy (Komiya et al., 2008), young super star clusters in M82 (Smith & Gallagher, 2001), and many others (Elmegreen, 2009). However most of these studies do not conclude that the average IMF deviates from the standard prescriptions by a substantial margin, merely that the IMF *can* be different in different situations. Averaged over entire galaxies the standard IMF formulations appear still to be the best option.

The debate is far from settled, but we will adopt what has been described as "Bernard's First Law": Thou shalt not change the stellar initial mass function. We do this because changes in the IMF can allow us to match any data, in practice mimicking the effects we are trying to investigate, and rendering the process futile.

1.1.2.2 The Star Formation Rate

The second major parameterisation is the Star Formation Rate, (SFR); in principle the SFR may be a function of the gas density, turbulence, galaxy mass, and other factors. In practice, we can use an observationally derived relationship to recover the SFR for a given set of conditions. Such a relationship was first derived by Schmidt (1959), and has subsequently been called the Schmidt law. The initial parameterisation was that the SFR of a patch of galaxy varied in proportion to the surface gas density of that patch of galaxy to some exponent, which was initially thought to be two.

This relationship has been re-examined using more recently gathered data (e.g., Kennicutt 1998). Several proxies are used as neither the surface gas density nor the star formation rate can be measured directly. For the surface gas density, molecular gas tracers are usually used (e.g., ^{12}CO), as relations exist to transform their densities into surface gas densities (e.g. Arimoto et al. 1996). Many different measurements can be made and used as a proxy for the SFR – Kennicutt (1998) used Hα and IR observations. Kennicutt also suggests that the exponent is close to two; however, other authors have explored varying exponents, and no conclusive agreement has been reached other than that the SFR exponent lies somewhere between one and three.

The product of the SFR and IMF are known as the "Birthrate Function" (Matteucci, 2003), as these quantities are degenerate and usually used together as a product. This entanglement is what makes it difficult to detect changes in the IMF - any change could easily be described by a difference in the SFR.

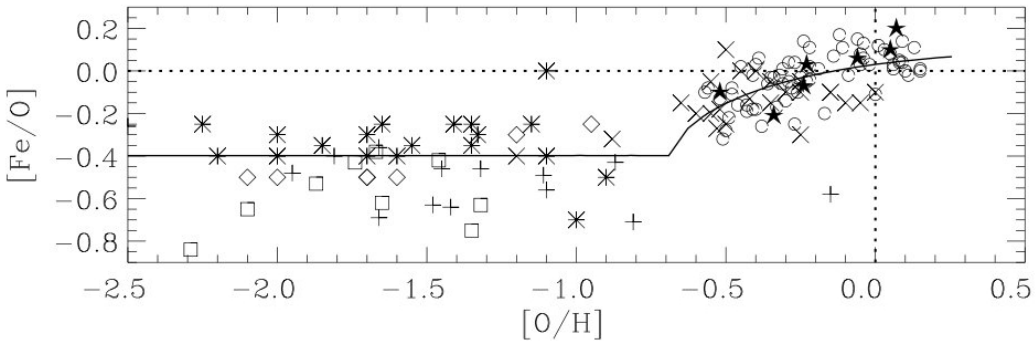

Figure 1.2: Result of a chemical evolution model including delayed recycling by low mass stars (Pagel & Tautvaisiene, 1995). The upturn in Fe abundance at late times is the result of SN Ia.

1.1.2.3 Stellar Lifetimes

Stellar lifetimes are of paramount importance for GCE. It will be shown later that different stellar masses will characteristically produce different sets of elements; therefore the way in which stellar lifetimes vary with mass will control the timescales on which these characteristic elements are released.

A good example of the importance of including stellar lifetimes as opposed to assuming either a constant lifetime (not a function of mass) or zero lifetime, is the case of the [O/Fe] trend in the Galaxy. Oxygen and iron, as we will see later, are produced by high and low-mass stars (via Type II and Type Ia Supernovae respectively). An upturn in [Fe/O] is observed at late times (high [O/H][1]) in the [Fe/O] versus [O/H] plot (see Figure 1.2) which cannot be explained satisfactorily by models which do not allow for finite stellar lifetimes. Conversely this trend arises as a natural consequence of the longer lifetimes that are associated with the low-mass stars that go on to produce Fe.

In general, massive stars have much shorter lives than low-mass stars. This is caused by the higher temperatures and pressures at the cores of massive stars, which increases the rate of nuclear burning and hence reduces the time over which the nuclear fuel is used up.

A review of stellar lifetime parameterisations is provided by Romano et al. (2004). They compared the lifetimes published by Tinsley (1980); Tosi (1982); Maeder & Meynet (1989); Padovani & Matteucci (1993) and Kodama (1997) along with lifetimes derived from the evolutionary tracks published by the Geneva & Padova groups (Schaller et al., 1992; Alongi et al., 1993; Bressan et al., 1993; Bertelli et al., 1994; Portinari et al., 1998). There is not a great amount of variation in these stellar-lifetime prescriptions, and what variation there is is concen-

[1] Bracketed abundance ratios denote the logarithmic ratio of any pair of abundances with respect to the same ratio in the Sun.

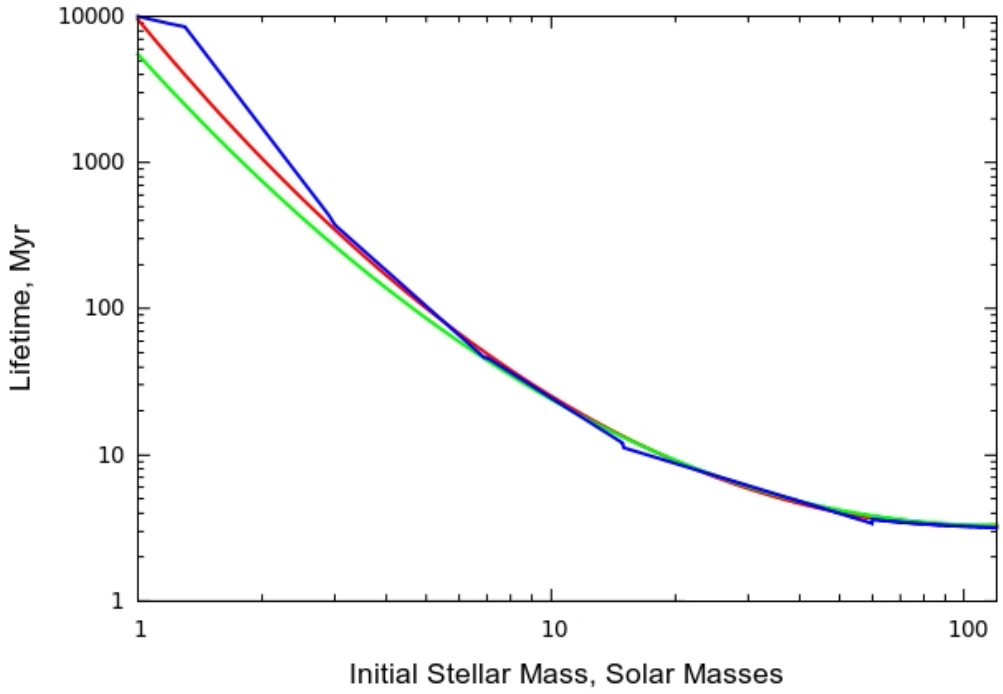

Figure 1.3: Plot of Lifetimes from Raiteri et al. (1996) at Z=0.02 (red), Raiteri et al. (1996) at Z=0.00002 (green), and the metallicity independent values of Maeder & Meynet (1989) (blue).

trated at the lowest and highest masses. In Figure 1.3 we show the lifetimes derived by Raiteri et al. (1996) and Maeder & Meynet (1989). The Raiteri et al. (1996) lifetimes are parameterisations for the Padova group models mentioned earlier. The Raiteri et al. (1996) parameterisation will be further discussed in Chapter 5 where the metallicity dependence of stellar lifetimes may be of importance.

1.1.2.4 Stellar Yield Prescriptions

The factor that we refer to as "Stellar Yields" is simply either the total mass, or the freshly synthesized mass of a set of elements emitted by the star upon its death. Published yield sets vary drastically, depending on the authors' scientific aims. Some cover only stellar models at solar metallicity and some cover a range of metallicities for a very limited mass range. In general no two cover quite the same volume in (M_i, Z_i, N; where N is the range of elements included) however they are usually split along mass lines due to the differences in simulating low-mass and high-mass stars. Additionally high-mass yields are further split into those covering pre-Supernova (SN) mass loss and those covering the products of SNe (e.g. Woosley & Weaver (1995) cover only CCSNe while Dray et al. (2003) include stellar winds and SNe).

Relatively few yield sets exist for massive pre-SNe stars. The most comprehensive are those of Maeder (1992); Dray et al. (2003); Dray & Tout (2003); Meynet & Maeder (2002) and

Hirschi et al. (2005) which cover pre-SNe mass-loss phases for a variety of metallicities and masses along with the SNe yields. Woosley & Weaver (1995) give the most widely used set of SN yields in the range $13M_{\odot} < M < 40M_{\odot}$. The prescription of Nomoto et al. (1997) is commonly used for stars outwith the Woosley & Weaver (1995) range, particularly at the high end, as the Nomoto et al. (1997) set includes stars up to $70M_{\odot}$.

For low-mass stars several yield prescriptions exist which are suitable for GCE models. The van den Hoek & Groenewegen (1997) (hereafter HG97) prescriptions have been used in most recent GCE models (e.g. Calura et al. (2009)). The HG97 yields are based on the Geneva stellar model grids (e.g. Schaller et al. 1992). Other groups have published chemical yields based on other models, (e.g. Marigo 2001) based on the Padova stellar models (Girardi et al., 2000). However the HG97 yields have proved very durable and as such are the baseline to which we compare other yields.

1.1.2.5 Galaxy Formation

Earlier it was mentioned that there are disputes regarding the general picture of galaxy formation. It is clear though, that galaxies do not form with their mass completely assembled. Cosmological models of galaxy formation tend to involve either continuous infall of mass onto a central galaxy, normally following some theoretical prescription (e.g. Larson 1976), or multiple-merger scenarios which arise in large N-body numerical simulations. The work of Murali et al. (2002) and Maller et al. (2006) suggests that there may be a compromise, whereby certain types of galaxies grow by accretion (massive ellipticals) while others are indeed dominated by mergers.

It has been found that double-infall scenarios produce the best fit to observational abundance data (Chiappini et al., 1997) for the Milky Way. In general, it seems that we require multiple infall episodes to create the observed abundance patterns in disk galaxies (Chiappini et al., 1997). Ellipticals are simpler in that they are believed to have formed very quickly with a massive starburst (Calura et al., 2009) (as we will explore further in Chapter 5); this initial starburst predicates a single infall prescription.

1.1.2.6 Outflow Prescriptions

The main driver of galactic outflows is core-collapse (massive star) supernova events, i.e., Type Ibc and Type II SNe (Gibson, 1997). These SNe release vast amounts of kinetic energy into the ISM, so much so that they can drive both their own ejecta and swept-up ISM entirely out of galaxies, should enough SNe happen near-simultaneously. This kind of situation is common in “starburst” galaxies. This name reflects the reason for the outflow: a burst of star formation will inevitably be followed by a burst of core collapse SNe (CCSNe) several million years later.

Figure 1.4: The starburst galaxy M82. The red and blue in this image correspond to *Spitzer* and *Chandra* observations, in the infrared and X-rays respectively. The observed outflows are the result of a period of intense star formation triggering supernovae.

Such a galaxy is shown in Figure 1.4.

This process is not always as violent as that shown in Figure 1.4. While many galaxies will go through a starburst phase at some point in their evolution, it is more common for SNe to drive smaller outflows. In this case it is also less likely that the outflow will be efficient, as much of the matter will accrete back onto the disk. This situation is called a "galactic fountain" (e.g. Melioli et al. 2009).

In GCE models the effects of starbursts are usually included by including a factor which removes gas from the system, assuming it to be well mixed (i.e. the gas removed reflects current ISM abundances). This is usually parameterized by:

$$\frac{dG}{dt} = -A \times \psi(t) M_{\odot} yr^{-1} \tag{1.1}$$

where G represents the total mass in the system, t represents time, $\psi(t)$ is the star formation rate in $M_{\odot} yr^{-1}$ and A is an efficiency constant. This is clearly a crude approximation to

the actual rate of mass ejection as there it contains no dependence on galaxy mass.

In general, the star-formation rate would have to cross some threshhold value representing the balance between the energy introduced to the ISM by SNe and the potential well in which the gas resides. However this kind of complication is rarely introduced in general GCE models as it is not required to match observations, while introducing an additional free parameter to the model.

1.1.3 Simple Galaxy Models

The simplest form of galaxy model is, in principle, a closed "box" full of primordial gas allowed to evolve and form stars in a manner described by the birthrate function. This type of model has a long history; a very early version was used by van den Bergh (1962), and more thoroughly formulated and explored by Talbot & Arnett (1971). This simplistic model can explain a number of phenomena, e.g., the build up of heavy elements to the levels observed today, and some relationships between specific abundances. Early implementations of these simple models tended to use parameterisations of stellar recycling as an input, as opposed to modern models which use grids of stellar yields.

The closed box model also contains two further tacit assumptions: instantaneous recycling and instantaneous mixing. The Instantaneous Recycling Approximation (IRA) states that all stars die and release their nucleosynthetic products at the instant they are born.

It is interesting to explore why this approximation was adopted. Simply put, the IRA allows the problem of chemical evolution to be solved without the aid of computers. With one approximation the whole business of modelling the build-up of elements in a galaxy can be solved without the aid of machines, so before the era of plentiful computing power, the IRA was a powerful tool.

It should be noted that the approximation of instantaneous mixing is not usually thought to be too problematic, as the effects of supernovae and stellar winds are thought to mix the ISM on roughly the same timescales as the timesteps that will be adopted by our models. These assumptions both break down at some level. However instantaneous recycling is particularly egregious in the context of modelling entire galaxies.

If we are to abandon the IRA, we need a prescription for stellar lifetimes as a function of initial stellar mass and metallicity. In practice such prescriptions are usually interwoven into the stellar evolution tracks which are used to provide recycling descriptions.

1.1.4 Generalised Galactic Chemical Evolution models

1.1.4.1 Incorporating Dust

A model of dust evolution in galaxies works along the same lines as one for elements in the ISM, except that it is, in general, simpler because fewer dust species are to be included. This simplicity is, in one respect an illusion. It is difficult to include the vast variety of dust species as yields for the various species from different astronomical sources are not known. In fact, the yields of all dust, regardless of species, is not known to even an order of magnitude.

There is another complication when considering galactic dust models: dust destruction and modification. Unlike GCE models where we can assume heavy elements are not destroyed in the ISM, dust destruction in the ISM is a significant effect. The blast waves from supernovae drive shocks through the ISM, destroying dust particles via sputtering and grain-grain collisions. Ironically, these supernova shocks may also be responsible for creating dust, although the amount is still under debate. The type of dust can also be modified by a variety of processes like by accretion or the formation of ice mantles.

1.1.4.2 Multi-Zone models

Thus far we have described "one-zone" models. It is common to use "multi-zone" models to attempt to explain certain data, typically metallicity gradients in the disks of galaxies. In this case a multi-zone model would consist of concentric rings forming the different zones. Normally these models do not include flows between the different zones; however, this is starting to be explored as certain metallicity trends cannot be explained without radial flows (Jungwiert et al., 2004). We will not use multi-zone models as relevant data to constrain them is not available.

1.1.5 Constraining Data

The output of our general GCE model consists of a time series of abundances, and "structural" information such as the current SFR etc. From this we can plot metallicity trends in the model and compare them to observed data regarding astronomical objects which are presumed to be representative of the state of galactic abundances at different times and metallicities.

The most common type of object that provides constraints on the models are stars in our own Galaxy. The envelopes of F & G dwarfs and B stars are assumed to not have been processed, and therefore represent galactic metallicities at the moment of their births.

Secondly we shall consider HII regions in the Milky Way and other spiral galaxies. In some ways these are the most convenient objects to study and certainly offer the most accurate measurements, owing to the ease of deriving abundances from nebular emission spectra (as opposed to stellar absorption spectra).

Lastly, we shall include samples of "Damped Lyman α systems" (DLAs) which are postulated to be the most distant objects for which we have ever measured metallicities. These objects are relatively young galaxies at very high redshift, representing the earliest constraint for our models.

Metallicities in these objects are derived via spectral lines observed either in emission or absorption. For example, stellar metallicities are derived from absorption lines - which are generated by the cooler, outer layers of the star. Derived stellar metallicities are therefore dependent on not just the metal content of the star, but also the properties of the star. The most important of these are its mass or radius, as these combine to give the surface gravity of a star and play a role, along with the metallicity, in generating the observed line shape.

The situation for ionized nebulae is simpler as the emission processes are less subject to external alteration. However the metallicities derived can be affected by a different issue. Metallicities are derived relative to the most abundant element, hydrogen, however in ionized nebulae the observed hydrogen (and helium) lines are formed in a very different way (recombination) than the bright heavy element lines (collisional excitation) from which metallicities are derived. This means that while we can derive the helium abundance to great accuracy because both the helium and hydrogen lines are emitted in the same way, the same cannot be said of any other elements. This problem has been the focus of some debate in recent years as it has been found that recombination lines from heavier elements (which are very faint compared to their collisionally excited counterparts) tend to yield lower abundances than those from collisional excitation. This phenomena is known as the "abundance discrepancy".

1.2 Stellar Recycling

The first question posed in the preamble concerns fundamental aspects of stellar evolution for which our understanding is still incomplete: mass loss and nucleosynthesis. Together these topics are often referred to as *stellar recycling*: the processes by which the matter in stars is nucleosynthetically processed and expelled into the ISM.

This thesis approaches stellar recycling from two opposite directions. From the point of view of GCE modelling, stellar recycling is one of the main components of the theoretical underpinning. In Chapters 2 and 3, we describe the visible effects of recycling by certain types of massive star. In this section we shall discuss the theory of stellar recycling, which all stellar yield computations are based on, before going on to discuss topics peculiar to the study of nebulae around Wolf-Rayet stars.

The nucleosynthetic processes in stars of all masses are well known and were mainly

derived by Bethe (1939) and by Burbidge et al. (1957). The work of this early period was driven by debate as to whether the relative abundances of elements in the universe were constant or evolved with time. The suggestion that stellar cores might be subject to temperatures and pressures conducive to nuclear fusion was still a controversial issue. The competing idea was that all elements were formed by nucleosynthesis during the Big Bang and had evolved little since.

Our understanding of mass loss, especially by massive stars ($M > 10M_{\odot}$), is still incomplete to the extent that we do not know the process driving the episodic mass-loss mechanisms (e.g. for luminous blue variables; LBVs) thought to dominate for massive stars. Not all stars undergo such processes, though, and the stellar-wind-driven mass loss that all stars experience during their lives is understood much better (for a recent review, see Puls et al. (2009)). However, in recent years debate has raged as to whether wind driven mass-loss is smooth or clumpy – the answer to which may influence the mass loss rates and the stellar yield prescriptions described later.

Stars may be broadly split into groups along the lines of their eventual fates. High-mass stars are those which end their lives as core-collapse supernovae (CCSNe), while isolated low- and intermediate- mass stars suffer a less violent fate, eventually expelling their outer layers to form planetary nebulae (PNe). The evolution of binary low-mass stars may result in type Ia supernovae (SNe Ia) and, in general, chemical-evolution models cannot match the evolution of Fe without them. However in order to include them, many extra free parameters describing the evolution of binary systems must be introduced.

To quantify the nucleosynthetic contribution made by stars of different masses and metallicities, much theoretical work has been done to construct sets of *yields*. A yield is defined in various ways, as was briefly mentioned in the previous section, most commonly it is the amount of an element created within a star. However it is sometimes expressed as the total amount of a certain element expelled by a star. These yields are normally calculated using models of stellar nucleosynthesis in combination with some parameterisation of the mass loss rate over the star's lifetime. A synthetic HertzsprungRussell diagram for such a set of stellar models is shown in Figure 1.5 (Schaller et al., 1992).

For a full and detailed view of stellar evolution see the monograph by Prialnik (2000), or the relevant sections in the monographs by Matteucci (2003) or Pagel (1997).

1.2.1 Nucleosynthesis in Stars

Stars are powered by the fusion reactions taking place towards their cores; the photons that make them shine are but a by-product of the nucleosynthesis. Stars of almost[2]all masses share some

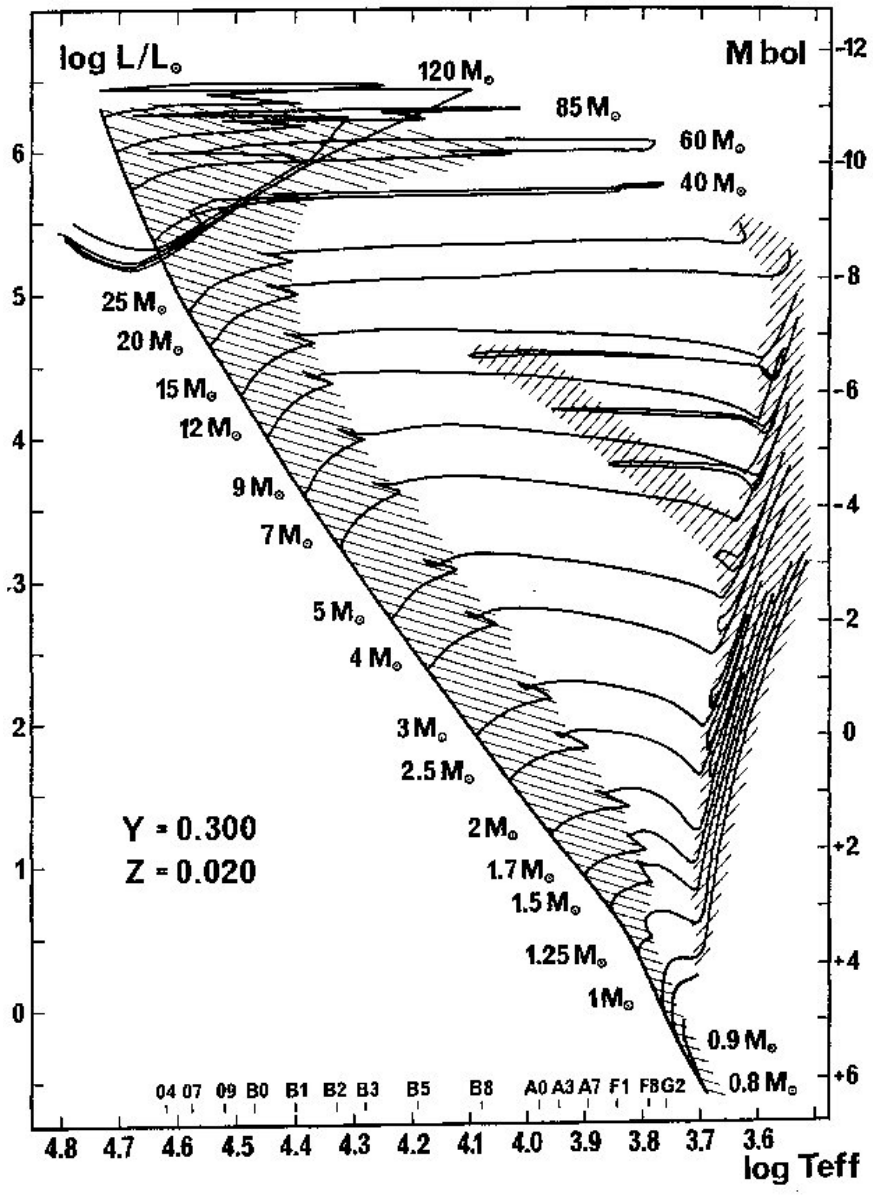

Figure 1.5: Theoretical HertzsprungRussell diagram for the synthetic stellar evolution models of Schaller et al. (1992).

common nuclear reaction paths which produce heavy elements from the constituent hydrogen and helium that dominates all stellar compositions at their births. In this section the reaction paths which lead to the creation of the CNO elements will be discussed, although initially the processes which create helium from hydrogen will be presented. These reactions were first shown in this form by Bethe (1939).

The most important reaction is the proton-proton (PP) chain, as it can proceed in the absence of elements heavier than helium and without which there would be no significant amounts of elements heavier than helium. The PP chain provides a path for four hydrogen atoms to produce a single ^{4}He atom via deuterium and ^{3}He. It was thought at first that this reaction could not take place, as the deuterium (D) produced is unstable, but if the deuterium reacts with another hydrogen atom before decaying then ^{3}He can be formed. The ^{3}He can then react with another ^{3}He to form stable ^{4}He.

Main PP chain:

$$\begin{aligned} &1: && {}^1H + {}^1H \rightarrow D + e^+ + \nu_e \\ &2: && D + {}^1H \rightarrow {}^3He + \gamma \\ &3: && {}^3He + {}^3He \rightarrow {}^4He + {}^1H + {}^1H \end{aligned} \tag{1.2}$$

There are multiple branches of the PP chain, the first allows ^{3}He to react with existing ^{4}He atoms which then form beryllium and consequently decays into two ^{4}He nuclei. The second branch of the PP chain proceeds from the beryllium produced by the first branch and creates boron which again, decays into two helium nuclei.

Ultimately, the energy released by this process is the rest mass energy difference between the reactants 4(^{1}H) and the product (^{4}He):

$$Q_{pp} = 4M(^1H) - M(^4He) = 26.7 \text{ MeV}$$

With an energy production rate of:

$$\epsilon_{pp} = 0.45\rho X^2 \left(\frac{T/_{10^6}}{15} \right)^{3.95} \text{ erg g}^{-1} \text{ sec}^{-1} \tag{1.3}$$

Where X is the hydrogen mass fraction, ρ is the density and T is the temperature.

If the star already contains some carbon, nitrogen, or oxygen, then the CNO cycle may be the most efficient way of transmuting hydrogen atoms into helium, should the core temperature

[2]Excluding very low mass stars.

be high enough. In this reaction the CNO nuclei function as catalysts, allowing the reaction to proceed more efficiently than in the PP-chain. While the initial CNO number density is conserved, the reactions do not proceed at the same rates, so the relative abundances of CN and O are not preserved. The fourth reaction below is the slowest and hence the abundance of ^{14}N can come to represent 90%+ of the initial CNO abundance.

The CNO cycle:

$$
\begin{aligned}
&1: && {}^{12}C + {}^{1}H \rightarrow {}^{13}N + \gamma \\
&2: && {}^{13}N \rightarrow {}^{13}C + e^{+} + \nu_e \\
&3: && {}^{13}C + {}^{1}H \rightarrow {}^{14}N + \gamma \\
&4: && {}^{14}N + {}^{1}H \rightarrow {}^{15}O + \gamma \\
&5: && {}^{15}O \rightarrow {}^{15}N + e^{+} + \nu_e \\
&6: && {}^{15}N + {}^{1}H \rightarrow {}^{12}C + {}^{4}He
\end{aligned}
\tag{1.4}
$$

The CNO cycle has one branch which results in the production of ^{14}N and ^{4}He and thus rejoins the regular cycle at reaction 4.

CNO cycle branch 1:

$$
\begin{aligned}
&6a: && {}^{15}N + {}^{1}H \rightarrow {}^{16}O + \gamma \\
&7a: && {}^{16}O + {}^{1}H \rightarrow {}^{17}F + \gamma \\
&8a: && {}^{17}F \rightarrow {}^{17}O + e^{+} + \nu_e \\
&9a: && {}^{17}O + {}^{1}H \rightarrow {}^{14}N + {}^{4}He
\end{aligned}
\tag{1.5}
$$

With a net energy release of:

$$
\epsilon_{CNO} = 2.16 \times 10^{4} \rho X Z_{CNO} \left(\frac{T/10^{6}}{25} \right)^{16.7} \text{ erg g}^{-1} \text{ sec}^{-1} \tag{1.6}
$$

Where X is the hydrogen mass fraction, Z_{CNO} is the abundance by mass of carbon, nitrogen and oxygen, ρ is the density and T is the temperature. ϵ_{CNO} is a function of Z_{CNO} rather than the individual CNO metallicities because ϵ_{CNO} is the average energy output at the equilibrium CNO abundances which the CNO cycle creates. The CNO cycle is much more sensitive to temperature than the PP chain and it comes to dominate when the temperature exceeds 10^{7} K. The dominance of the PP chain or CNO cycle is therefore determined by the quantity:

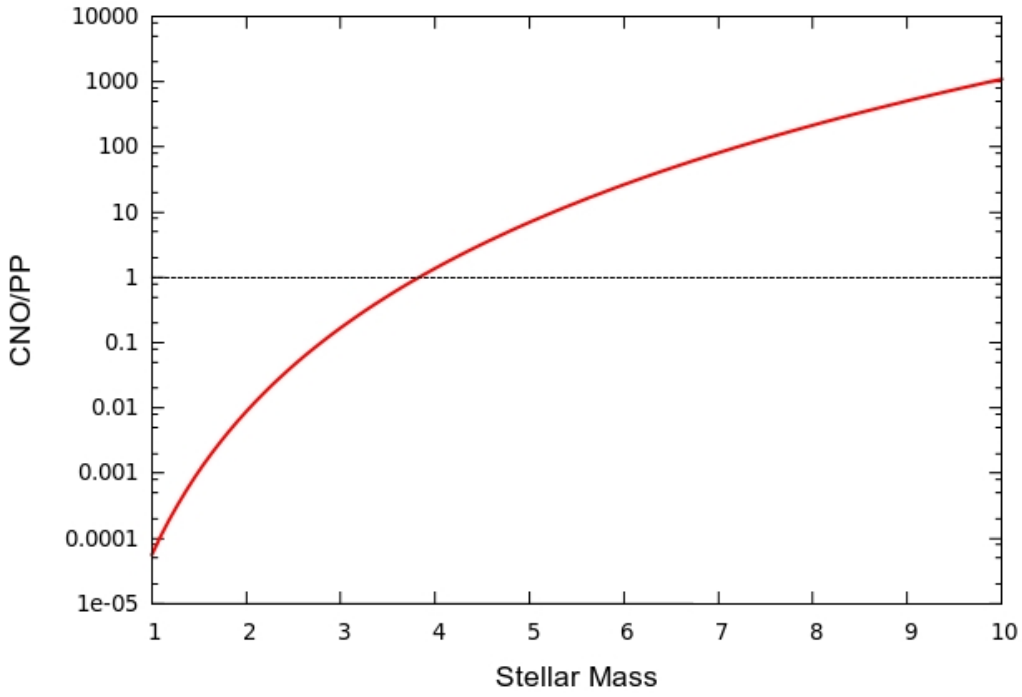

Figure 1.6: The relative importance of the CNO cycle compared to the PP chain as a function of stellar mass.

$$\frac{\epsilon_{CNO}}{\epsilon_{PP}} \propto \frac{\left(\frac{T/_{10^6}}{25}\right)^{16.7}}{\left(\frac{T/_{10^6}}{15}\right)^{3.95}} \tag{1.7}$$

If we combine this with:

$$T_{core} \propto M^{4/7} \tag{1.8}$$

(see Prialnik, 2000, chap 7) we can determine the stellar mass at which the CNO cycle will come to dominate core helium production by calibrating Equation 1.8 using the core solar temperature of 15×10^6 K. The resulting relationship is shown in Figure 1.6.

The reactions described so far convert hydrogen into helium and thereby raise the helium abundance to the point where it, too, can react and form heavier elements. The most common reaction which proceeds this way is called the triple-α process, (^{4}He nuclei are also known as α particles). The triple α process can be represented as:

$$\begin{aligned} &^4He +^4 He \rightleftharpoons^8 Be \\ &^8Be +^4 He \rightarrow^{12} C^* \rightarrow^{12} C + \gamma + \gamma \end{aligned} \tag{1.9}$$

Initially this reaction was thought to be highly improbable due to the relative unlikeliness of three body collisions which were thought to be neccessary to convert three helium nuclei one carbon nucleus. However this reaction is possible because the first reaction supports a low equilibrium abundance of unstable ^{8}Be which, if the temperature and density are sufficient, can then react further instead of decaying. It is important to note that due to a resonance the ^{12}C is produced in an excited state which increases the rate of this reaction (Hoyle, 1954).

The ^{12}C resonance was discovered as a result of the anthropic principle. Hoyle reasoned thus: carbon is abundant in the universe; the only way of creating carbon is via nuclear reactions in stars; but the triple α process (without the resonance) does not proceed quickly enough to create the observed abundance of carbon. Thus there must be a resonance of carbon at the appropriate energy such that more carbon can be produced. The resonance was predicted in 1952 and subsequently discovered the following year by Dunbar et al. (1953).

The energy released by the triple α process is:

$$\epsilon_{3\alpha} = 4.4 \times 10^{-8} \rho^2 Y^3 \left(\frac{T}{10^8}\right)^{40} \text{ erg g}^{-1} \text{ sec}^{-1} \tag{1.10}$$

This reaction mainly takes place in massive stars simply because the energy produced per unit mass of material is proportional to T^{40} and more massive stars have hotter cores (Equation 1.8). This is the main avenue for the creation of carbon in the universe.

Following the triple-α process, α captures produce elements whose compositions are an integer number of α captures. These are known collectively as the *α-process elements* and are produced in the following way:

$$^{12}C +^{4} He \rightarrow^{16} O + \gamma \tag{1.11}$$

$$^{16}O +^{4} He \rightarrow^{20} Ne + \gamma \tag{1.12}$$

$$^{20}Ne +^{4} He \rightarrow^{24} Mg + \gamma \tag{1.13}$$

$$^{24}Mg +^{4} He \rightarrow^{28} Si + \gamma \tag{1.14}$$

With a release of energy accompanying each reaction.

1.2.2 Massive Star recycling

Before considering the nucleosynthetic and mass-loss properties of massive stars it is important to review their general structure, as this has a pivotal role in determining the eventual yields. Massive stars, as might be expected, have much higher pressures and temperatures in their cores, leading to faster nuclear burning and correspondingly shorter lifetimes.

On the initial collapse of the star, a helium core forms from pp and CNO reactions until there is a high enough abundance of helium to begin triple-α reactions. From this point the star forms a characteristic onion-skin structure with the envelope at the surface, followed by a layer of hydrogen burning then progressively heavier elements in shells: helium, carbon, etc.

There are two very different methods for massive stars to inject mass into the ISM. The main event is the Core Collapse Supernova (CCSN) which occurs at the end of their lives. However, during the earlier stages of their lives, another effect can dominate: stellar winds. This distinction is important as, in principle, different sets of elements are expelled from the star during the different phases.

It has long been known that throughout the lives of massive stars, mass is lost via radiatively driven stellar winds. This idea was first suggested and developed in the late 1920s and 1930s by Milne (1926); Beals (1929); Chandrasekhar (1934). During the early stages, the mass lost is from the top of the envelope, i.e., not nucleosynthetically enriched material. Eventually the stellar winds will carry away enriched material, either because all of the unenriched material has already been expelled, or because mixing has driven enriched material to the surface, where it can be driven off. Usually these winds are described as "line driven", which means that the continuum emission from the star has become strong enough that the radiative force of photons on ions in the upper atmosphere can impart momentum to the material. On its own this would not be enough to drive much matter as the ionic absorption lines are very narrow. However, as the material accelerates, the ions redshift from the point of view of the continuum radiation, effectively broadening the absorption lines and magnifying the effect[3].

The evolutionary paths and fates of massive stars depend on their initial masses and metallicities. Crowther (2007) has sketched evolutionary paths as a function of initial mass (at solar metallicity) where WN and WC represent nitrogen and oxygen rich Wolf-Rayet stars respectively:

$\mathrm{M} > 75\ \mathrm{M}_{\odot}$ $\qquad O \rightarrow WN(H-Rich) \rightarrow LBV \rightarrow WN(H-poor) \rightarrow WC \rightarrow SNIc$

$40\ \mathrm{M}_{\odot} > \mathrm{M} > 75\ \mathrm{M}_{\odot}$ $\qquad O \rightarrow LBV \rightarrow WN(H-poor) \rightarrow WC \rightarrow SNIc$

$25\ \mathrm{M}_{\odot} > \mathrm{M} > 40\ \mathrm{M}_{\odot}$ $\qquad O \rightarrow LBV/RSG \rightarrow WN(H-poor) \rightarrow SNIb.$

[3]The monograph by Lamers & Cassinelli (1999) provides a thorough description on stellar wind theory.

Given that a WR star typically has a mass of 10–25 $M_{\odot}$ (Crowther, 2007), in each of these scenarios the star must lose a considerable amount of mass. Multiplying a typical line-driven-wind mass-loss rate by the lifetime of the star gives a mass much lower than that which must have been lost (initial mass - remnant mass), but the mechanism to account for the rest of the mass-loss is presently unknown. We can infer some properties of the process, though, using other data. Some WR and LBV stars are observed to have nebulae (see 1.2.5) whose masses are such that they must represent short, furious bursts of mass loss (Smith et al., 1988). It has been suggested that these bursts accompany the changes between RSG, LBV and WR phases in the evolutionary schematics above (e.g. Humphreys (1991)).

The SNe II / Ibc (CCSNe) which mark the deaths of massive stars are among the most energetic stellar events in the universe. As we saw earlier (Section 1.1.2.6), they are powerful enough to drive the ISMs from galaxies. In chemical-evolution terms though, CCSNe are the dominant producers of oxygen and contribute somewhat to the nitrogen budget. They also create elements past the iron peak, via the rapid neutron capture process (r-process). The supernovae themselves are triggered by the collapse of the core of a massive star, hence their categorisation as CCSNe. As the collapse proceeds, the core heats up and produces gamma rays, which decompose many of the iron nuclei. At some point during the collapse, protons and electrons recombine into neutrons, these will eventually make up the stellar remnant (a neutron star) if the remnant is not sufficiently massive to form a black hole. At some point during the collapse, the neutron core reaches nuclear density and can collapse no further. The matter outside the core which is still collapsing "bounces" and forms an outward propagating shock. The neutrinos which are created during this process then impart a small fraction of their kinetic energy into the envelope of the star, adding to the energy of the outward propagating shock. In the shocked ejecta gas which was formerly the envelope of the now collapsed star, temperatures and densities can be achieved which are suitable for dust formation (e.g. Sugerman et al. (2006)).

1.2.3 Low- & Intermediate-mass star (LIMs) recycling

Recycling in lower mass stars is a slightly simpler affair. All isolated low mass stars evolve in a drawn-out way, removing their outer layers and, in general, becoming Planetary Nebulae (PNe). For such stars mass loss via winds is the dominant, indeed the only, mass loss process.

Within the LIMs mass range, there are substantial differences between the degree of nucleosythetic enhancements that are found. In general, this dependence exists because of the interplay of several effects. Firstly, the temperature dependence of the CNO cycle, as discussed earlier, can significantly alter the abundances of carbon, nitrogen and oxygen. Secondly, LIMs

undergo several stages of evolution where material is "dredged up" from the stellar interior (where nuclear fusion has created new elements) to the surface, where it may be ejected. And thirdly, the process known as "hot bottom burning" which can re-process the material which is dredged up from the stellar interior. Each of these effects has a characteristic mass dependence, the interplay of the three defining the eventual stellar yields. A comprehensive review of these topics is given by Iben & Renzini (1983).

Stars at the high end of the LIMs range, (i.e. $M_i > \sim 4\ M_\odot$), will suffer the most from CNO cycling at the early stages of their evolution. The initial carbon abundance will have been almost completely transformed into nitrogen, which is then brought to the surface in the second dredge up episode. This can double the surface nitrogen abundance at this stage. Subsequently the star will begin to thermally pulsate, with the energy provided by the triple-α process. The last few thermal pulses can coincide with descent of the convective atmosphere into the triple-α fusion zones, this initiates the third and final dredge up. At this stage more nucleosynthetically enhanced material is brought to the stellar surface, however this time it represents the ashes of the triple-α process, i.e. carbon, rather than the previous dredge up which brought CNO-cycled elements to the surface. This can create a significant carbon abundance in the stellar envelope, which can then be processed by hot bottom burning (HBB) if the temperature at the base of the envelope is sufficient. HBB can transform the carbon abundance which has been dredged up (^{12}C) into first ^{13}C and subsequently ^{14}N via neutron captures. This envelope, which has been enriched in nitrogen by two processes, will later be ejected as a Type I (nitrogen rich) PNe.

Stars with initial masses large enough to ignite helium burning ($M_i < \sim$ 1–2 $M_\odot$) but less than the mass required to ignite HBB ($M_i > \sim 4.5\ M_\odot$; Boothroyd et al. 1995), undergo similar processes as their more massive brethren. There are two important differences though, initially the CNO cycling will not be complete for stars in this mass range, so strong nitrogen enrichments would not be expected. After the third dredge up, stars in this mass range do not undergo HBB and as such their surface carbon abundances remain high, usually this type of star is called a "carbon star". The PNe created by stars in this mass range are characteristically carbon rich and these PNe make up roughly half of all observed PNe Kingsburgh & Barlow (1994).

Stars with masses less than that required to ignite core helium burning but greater than that required to ignite hydrogen ($M_i > \sim 0.5\ M_\odot$), become main sequence stars with very long lifetimes (see Section 1.1.2.3). When they do leave the main sequence, they will become red giant stars (RGB) with a hydrogen burning shell around a degenerate helium core. Eventually these stars will undergo a "helium flash", where the core conditions are conducive to the triple-α pro-

cess without any restraints, and subsequently become a C-O white dwarf and PNe. The helium flash can be responsible for expelling some newly created carbon into the stellar envelope (e.g. Michaud et al. (2007)).

1.2.4 Dust Formation

The very property of carbon that makes it the basis of life on earth also makes it troublesome to observe astronomically. The electronic structure of carbon is such that it has four electrons available to form bonds with other atoms. On earth this makes it vital in creating all the compounds for life but for astronomy is a challenge as carbon tends to form not only simple molecules (such as carbon monoxide), but also larger compounds (such as Polycyclic Aromatic Hydrocarbons (PAHs)) and still larger species collectively called dust[4].

Astronomical dust is fairly easy to detect as it absorbs UV / optical stellar radiation and re-emits this energy in the infrared. The chemical composition of the dust can be loosely inferred based on its emission. There are believed to be two general components: carbon dust (amorphous carbon) and silicates which have characteristic absorption features at around 10 and 20 μm.

Our knowledge of the sites and types of dust emission has blossomed in recent years with the proliferation of infra-red observing facilities. This led to the detection of highly redshifted (young) galaxies with anomalously high dust content (Bertoldi et al., 2003; Beelen et al., 2006)– much higher than expected given their metallicity and what we know about stellar recycling.

It is believed that all stars produce dust, regardless of mass or metallicity. However they produce the dust in drastically different ways. Massive stars can contribute dust formed in the ejecta of supernovae (Sugerman et al., 2006) or in the winds of LBV stars (Gomez et al., 2010). The masses of dust that are formed by massive stars, both before and after their SN, is currently undergoing intense debate. This stems from the idea that certain high redshift, dusty, quasars are young enough that low mass stars could not have contributed to the observed dust mass, yet SNe and SNRs do not display high enough dust yields to account for the observed dust masses if it is assumed that all pre-SN dust is subsequently destroyed by SN.

Low-mass stars can produce dust in their envelopes and outflows. In the previous section we discussed the enrichment of the envelopes of LIMs stars — this enriched material can go on to form dust in the cooler temperatures of the outer envelope and stellar winds (Salpeter, 1977).

The natures and contributions of the various sources of dust are in the universe will be

[4]Dust, in this context, is a shorthand referring to all the solid-phase matter in particle sizes from a few atoms to a fraction of a millimeter. The vast majority of this matter is in grains far smaller than those normally associated with terrestrial (household) “Dust”.

explored in Chapter 5.

1.2.5 Wolf-Rayet Nebulae

It has been suggested that carbon rich WR stars (WC stars) are responsible for injecting large amounts of carbon into the ISM. The WR phase of stellar evolution has long been known as the prime period of pre-supernova massive star mass loss. Investigations into this phase are hampered by the small number statistics inherent with massive stars ($\sim$400 resolved examples of Wolf-Rayet stars are known, the bulk of which are in our galaxy).

1.2.5.1 Surveys of WR Nebulae

Despite their low numbers, the natures of WR stars are well understood. They are the stripped cores of stars which formed with masses greater than 20 $M_{\odot}$ (e.g. Crowther (2007) and reference therein). Successive periods of mass loss (either bursts, e.g. the LBV phases or continuous, e.g. O star winds) have led to the outer layers being expelled. The effects of these objects on their immediate neighbourhoods is profound. Firstly, the very intense UV radiation ionises its surroundings; secondly, the interaction between the strong winds and the surrounding ISM, and later with the ejecta previously expelled from the star, can produce spectacular nebulae. This process represents the initial stages of massive-star recycling as chemically enriched material is returned to the ISM. That such circumstellar matter was the result of stellar processes was suggested by Johnson & Hogg (1965); previously any nebular ring structures had been interpreted as a planetary nebula or a supernova remnant.

Chu (1981) was the first to devise a classification system based on nebular morphologies. Nebulae were described as being created by Winds (W), Ejecta (E) or Radiation (R). This scheme was used for the southern Galactic survey WR stars of Marston et al. (1994a,b) and Marston (1997) but not for the corresponding northern survey of (Miller & Chu, 1993) which merely described the probability of a "ring" nebula being present. A survey of the environs of all Magellanic Cloud WR nebulae (Dopita et al., 1994) also ignored the Chu categorisation system and commented only on the presence of a ring or whether the star was in a superbubble.

Chu's initial survey did not utilise any spectroscopic abundances to assist with categorisation, as these were not available at the time, hence the derived morphological criteria for ejecta nebulae were very strict. This was shown by subsequent spectroscopy (Esteban et al., 1990, 1991, 1992) which identified the presence of ejecta in nebulae that Chu's scheme would have excluded, such as NGC 3199 and NGC 6888, which appear to be complex structures combining a swept-up ISM component and a bow shock but also contain processed material. This strictness was addressed in later work by Chu (1991), which added the W/E classification for these

Figure 1.7: False colour image of the Wolf-Rayet Nebula NGC 6888. The star WR 136 is near the center. The red nebulosity is Hα emission, while the blue is [O III] emission. Image courtesy IPHAS collaboration.

cases where the nebulosity appears to be generated by winds but are likely to contain ejecta.

Abundances can be derived for WR nebulae from spectroscopy. Samples of WR nebulae have been observed previously, most thoroughly in the early nineties by Esteban et al. (1990, 1991, 1992); Esteban & Vilchez (1992) and Esteban et al. (1993). This series of papers observed a sample of ~ 10 nebulae with the same instruments in the northern and southern hemispheres. They found a range of metallicities in their sample, some suggestive of the presence of ejecta and others with more ISM-like patterns. These results are summarised at the beginning of Chapter 2.

1.3 This Thesis

The overall aim of this thesis is to investigate relative importance of different sites of carbon and dust production in the universe. This question shall be tackled from two distinct directions. Initially, the nucleosynthetic products of massive stars in the WC phase will be investigated. Chapter 2 regards the search for WC type stars with circumstellar nebulae that are likely to be the product of stellar outflows. A new WR nebulae around a WC/WN transition is found and several likely candidates in the LMC documented.

Chapter 3 will document spectroscopic observations of nebulae around WC stars drawn

from the survey of Chapter 2. The observations were designed to allow access to the far-red [C I] carbon lines, should they be of sufficient intensity, from which carbon abundances could be derived along with other nebular abundances.

The second method of investigating carbon production, explored in Chapter 4, is to construct GCE models, along with a thorough exploration of carbon yields in the literature. The results of the GCE models are compared with galactic abundance data to attempt to constrain the origin of carbon in the Milky Way. It will be shown that various different yield combinations can adequately explain the observed galactic trends.

The penultimate chapter (Chapter 5) documents the reconfiguration of the GCE model into a model for the dust build-up in galaxies, focusing on the mysterious high redshift dusty galaxies. Observational dust yields are reviewed for both massive and low mass stars and these are used in our dust evolution model to test the hypothesis that we can explain the observed dust masses around high redshift quasars without resorting to theoretical stellar dust yields.

Conclusions are presented in Chapter 6, along with ideas for future work on this topic.

Chapter 2

Nebulae Around Resolved Wolf-Rayet Stars

> "Reality is that which, when you stop believing in it, doesn't go away."
>
> — Philip K. Dick

2.1 Introduction

Since the suggestion that some Wolf-Rayet stars could be creating nebulae via mass loss (Johnson & Hogg, 1965), efforts to detect more examples have been ongoing. The first attempt to morphologically categorise nebulae presumed to have been created by the influence of WR stars was performed by Chu (1981), who devised three broad categories for possible nebulae: W, R & E.

W type nebulae are those which are assumed to be "Wind-Blown Bubbles". These objects were inferred to have been created when material ejected from the star interacted with the surrounding ISM. R type nebulae were postulated to be those in which the strong radiation field from the host star excites the surrounding ISM. These are only visible when the surrounding ISM is of sufficient density to produce detectable emission.

Our interest lies with the E type nebulae, which were defined to be those which were likely to contain processed ejecta from the progenitor star. These were suggested by Chu to have been formed by a violent mass loss episode recently in the star's history, which may not have been isotropic or homogeneous. The nebulosity can therefore be very clumped and irregular. The lifetime of E type nebulae should be much lower than for the other two types, since as the ejected mass expands as it moves away from the star, its surface brightness should diminish very quickly. It should be noted that actual Wolf-Rayet nebulae can (and do) display any combination of the above traits. Chu (1991) modified the scheme to refine the definition of E type nebulae, splitting the category into Stellar Ejecta nebulae and Bubble/Ejecta (W/E) nebulae. The former covered pure E type nebulae as defined above, the latter introduced to cover the case of ejecta shells having merged with the swept up shell.

The Chu (1981, 1991) criteria were used for the southern galactic plane surveys of Marston et al. (1994a,b) and Marston (1997) but not for the northern survey of Miller & Chu (1993) which described the probability of a "ring" nebula being present. The survey of the environs of all Magellanic Cloud WR nebulae by Dopita et al. (1994) also ignored the Chu categorisation system and commented only on the presence of a ring or whether the star was in a superbubble.

In this work we shall consider only morphological information in our classifications of new nebulae and will not delve into the physical details of their formation and evolution. Theory and models of the formation of nebulae around massive stars were presented by Chu (1991, 2003).

Recent publicly available Hα surveys (Drew et al., 2005; Parker et al., 2005) allow re-inspection of the environs of all known WR stars with a view to identifying new E type nebulosities which can provide constraints on the nucleosynthetic effects of WR stars.

2.2 Morphologies of Spectroscopically confirmed WR Ejecta nebulae

The W, R and E categories of Chu (1981) and Chu (1991) were tested over the following decades as spectroscopic data for the different subtypes of WR nebulae began to appear.

For the two nebulae which Chu (1981) regarded as E type (M 1-67 and RCW 58) the nebulosities were found to be enriched relative to the ISM in nitrogen and helium but depleted in oxygen (Kwitter, 1984; Esteban et al., 1991). The anonymous nebula surrounding WR 16 was also shown to be comprised of material with a very similar abundance pattern to those of M1-67 and RCW 58 (Marston et al., 1999). The detection of processed material in these nebulae was a major success for the categorisation scheme, as this showed that it is possible to infer likely patterns in the chemical composition of a WR nebula by studying its morphology.

However, material displaying the same patterns of enrichment was also detected in NGC 6888 - a nebula Chu had initially classified as W type (Esteban & Vilchez, 1992; Moore et al., 2000). This showed clearly that the lines between the initial Chu classes can be blurred, indeed NGC 6888 - see Figure 2.1, top right - appears to be a mixture of different kinds of nebulosity. The edge looks like a wind-blown shell, whilst there is evidence of flocculent nebulosity in the central regions, suggesting ejected material. NGC 6888 was later re-classified as a W/E nebulae by Chu (1991).

Garnett et al. (1993) noted that the nebulosity around BAT99-16 in the LMC displays the same abundance pattern as RCW 58, M 1-67, WR 16 & NGC 6888.

The results of Esteban et al. (1990) & Esteban et al. (1991) also suggested another class of WR nebula, those containing helium overabundances without any enrichment in heavier el-

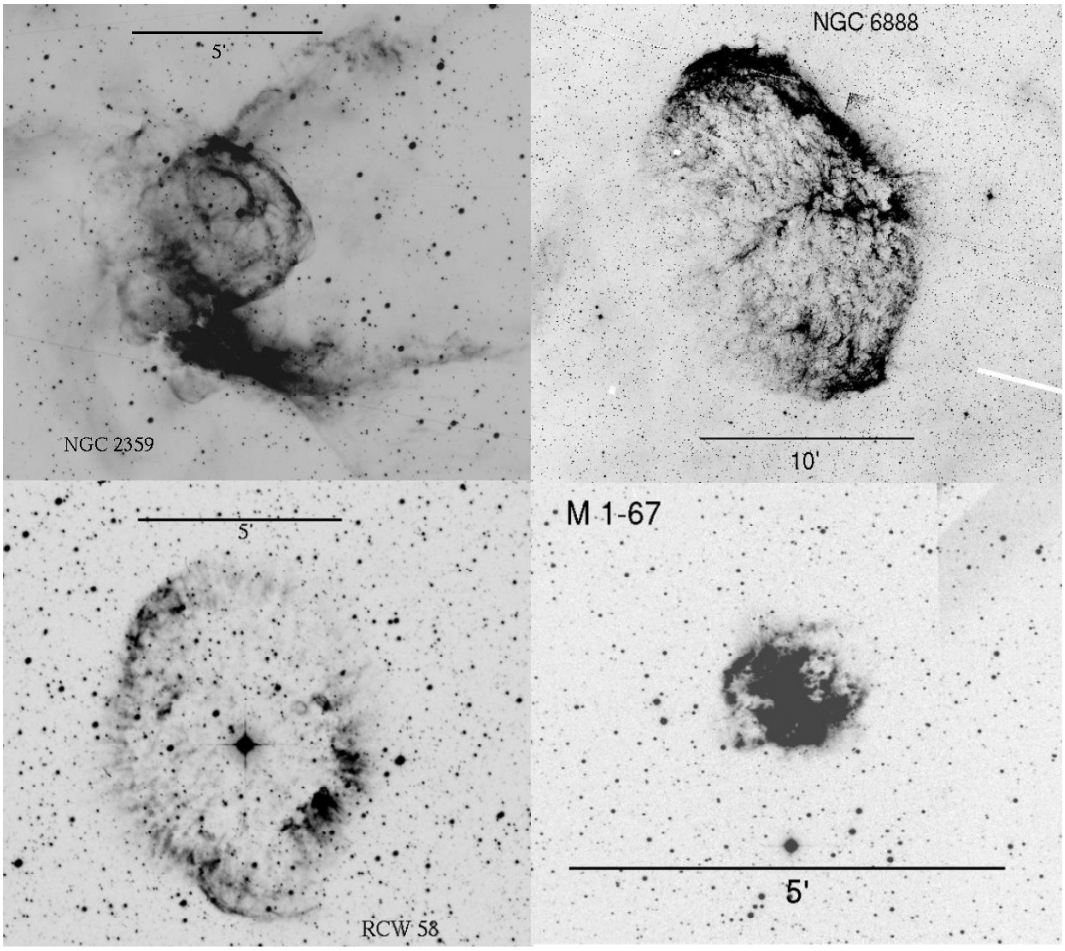

Figure 2.1: Morphologies of WR Ejecta nebulae spectroscopically confirmed to have a chemically processed component. Clockwise from top left: SHS imagery of NGC 2359 (WR 7,WN4); IPHAS montage of NGC 6888 (WR 136, WN6h), kindly supplied by Nick Wright, IfA Harvard; IPHAS image of M1-67 (WR 124, WN8h); SHS imagery of RCW 58 (WR 40, WN8h). North is up and east to the left in all images.

Table 2.1: Nebulae Spectroscopically Confirmed to contain Nucleosynthetic products

WR[a]	Spectral Type[b]	Nebular Name	Classification[c]	Reference	Enrichment	Reference
6	WN4	S308	W	Chu (1991)	N and He enriched	Esteban et al. (1992)
7	WN4	NGC 2359	W	Chu (1991)	enriched He knots	Esteban et al. (1990)
16	WN8h	Anon	W/E	Marston (1997)	enriched N throughout	Marston et al. (1999)
40	WN8h	RCW 58	W/E	Chu (1991)	N and He enriched	Kwitter (1984)
75	WN6	RCW 104	W/E	Chu (1991)	N enrichment	Esteban et al. (1992)
102	WO2	G 2.4+1.4	W	Chu (1991)	enriched He	Esteban et al. (1991)
124	WN8h	M 1-67	E	Chu (1991)	N overabundance	Esteban et al. (1991)
136	WN6h	NGC 6888	W/E	Chu (1991)	Strong N, He enrichment	Esteban & Vilchez (1992), Moore et al. (2000)

a: Catalogue numbers from van der Hucht (2001).

b: Spectral types from van der Hucht (2001). *c*: Using the Chu (1991) scheme

ements. Two nebulae, NGC 2359 (Esteban et al., 1990) and G 2.4+1.4 (Esteban et al., 1991), which present this abundance pattern display striking similarities, but appear to have been created in different ways. G 2.4+1.4 was initially classed as a supernova remnant (Dopita et al., 1990), but Chu (1991) categorised it as W type. G 2.4+1.4 was later found to have a mass of 4200 $M_{\odot}$ (Gosachinskij & Lozinskaya, 2002) which implies that the nebulosity is primarily swept up, agreeing with the Chu (1991) categorisation. NGC 2359 is a very clear example of a wind-blown bubble. The ionized mass of NGC 2359 has been estimated to be of around $70M_{\odot}$ and the mass of the whole complex over $1000M_{\odot}$ (Cappa et al., 1999), which clearly precludes a pure ejecta origin. However, both nebulae display helium enrichment - showing again that the lines between Chu's classes can be blurred.

The above spectroscopic results lead to the conclusion that the morphological criteria for ejecta nebulae presented by Chu (1981) may be too stringent, a problem addressed by the introduction of the Bubble/Ejecta (W/E) class (Chu, 1991). Wind-blown bubbles can also contain ejecta in their filamentary nebulosities (e.g. NGC 6888).

The above spectroscopic information suggests the following, revised criteria: ejecta nebula candidates must have either a highly flocculent structure, as in Chu's scheme or, alternatively, possess flocculent structure within their wind-blown shells, similar to that shown by NGC 2359, NGC 6888 & NGC 3199.

Radiatively excited nebulae, (R type) are more difficult to classify under this scheme as they tend to possess highly irregular morphologies which are dependent not on stellar outflows but on the density distribution of material in the local ISM.

2.3 Expected Wolf-Rayet Nebular Size Scales

The angular scales over which Wolf-Rayet Nebulae have previously been detected span several orders of magnitude, with the smallest being of the order of arcseconds in diameter (BAT99-2, LMC, Dopita et al. (1994)) and the largest were claimed to have an angular radius of a degree or more e.g. θ Muscae (Guillermo Gimenez de Castro & Niemela, 1998). However the nebulosity surrounding θ Muscae has been shown not to be related to the star (Stupar et al., 2010a).

An upper limit on the angular radius of a nebula composed of ejecta from the WR or immediate pre-WR phase is given by: $\theta = \frac{\tau_{WR} \times V_{exp}}{D}$ where V_{exp} is the expansion velocity of the nebula, D is the distance to the nebula and τ_{WR} is the time spent in the WR phase $\sim 3 \times 10^5$ years (Crowther, 2007). We have chosen this upper bound as a representative figure for the largest wind blown nebulae, as it is suspected that ejecta can expand much faster in the evacuated volume within a wind-blown bubble, allowing ejecta nebulae to possibly take on

much larger sizes. V_{exp} is a typical expansion velocity of a WR nebula: $\sim 25 - 50$ km/s (Chu et al., 1982; Chu, 1983) we assume this figure is typical for expanding shells around galactic WR stars.

For a WR star at 1 kpc this predicts a maximum angular diameter of ~ 45 arcmin. We can also estimate the distance threshhold below which 30 arcmin extractions from the SHS could be insufficient to encompass a WR nebula. Rearranging for distance and using $\theta = 0.5^{\circ}$, this yields a distance of ~ 1.5 kpc.

2.4 SHS Hα imagery

The AAO/UKST Southern Hα Survey (SHS) took place during the early 2000's and covered the entire southern galactic plane (Parker et al., 2005). The survey was one of the last examples of the use of photographic imaging in astronomy and demonstrates neatly the advantages and disadvantages of this approach. The survey was performed using the 1.2m UK Schmidt Telescope (UKST) at the Anglo-Australian Observatory (AAO), on 5 degree square photographic plates using three hour exposures. Each plate was subsequently transported to the Royal Observatory Edinburgh (ROE) and digitised using the SuperCOSMOS plate scanning machine at a resolution of 0.67 arcseconds/pixel. The data were then montaged and made publicly available via the internet.

The advantages of photographic plates are twofold, firstly a large amount of data can be captured on each 25 square degree exposure, with comparatively little effort needed to extract images. Secondly the photographic emulsion was tuned such that the exposures were sensitive to very faint structure. The obvious disadvantage to utilising these data is the difficulty of flux calibration, since photographic emulsion is not a linear detector and intensity calibration can be very troublesome.

The SHS also covered the Magellanic Clouds and while these data were digitised by the SuperCOSMOS project they were never made publicly available. They were kindly made available to us by the Wide-Field Astronomy Unit (WFAU) at the ROE-IfA (Royal Observatory Edinburgh - Institute for Astronomy) .

The SuperCOSMOS interface to the SHS imagery allows extractions of up to 900 square arcminutes, in order to inspect WR nebulae larger than this the "Montage" package, produced by NASA's IPAC (Infrared Processing and Analysis Center), was utilized to combine SHS extractions.

Northen galactic plane WR stars were examined using IPHAS survey data (Drew et al., 2005). However as no disagreement was found between IPHAS imagery and the survey of

Miller & Chu (1993) no further discussion will be presented.

2.5 Results & Comparisons with previous work

2.5.1 Results

Each southern star in the Sixth catalogue of Galactic Wolf-Rayet Stars (van der Hucht, 2001) and its annex (van der Hucht, 2006) was inspected visually using SHS imaging data as described above. The results are summarised in Table 2.3. Each WR star in the LMC catalogue of Breysacher et al. (1999) (hereafter BAT99) was also visually inspected and resolvable nebulae categorised in the same way. SMC WR stars were also investigated but none appeared to possess resolvable ejecta nebulae. In addition, the positions of several WR ring nebulae that were discovered by Wachter et al. (2010) at mid-infrared wavelengths were inspected - yielding one candidate ejecta nebula.

For the LMC it is difficult to identify WR nebulae whose absolute sizes are as small as some Galactic WR nebulae such as M1-67, since their angular sizes would have been smaller than the overexposed PSF of the host star in SHS imagery. Conversely, if we place the largest LMC WR nebula: Anon (HD 32402) at 1 kpc, it would have an angular size of 1.5° which would not have been discernable to our survey. However very few (< 10) WR stars are closer than 1 kpc. This effect means that we cannot see details on the same scales as their galactic counterparts; we can only determine likely candidates for further study.

2.5.2 Comparison with previous work

A comparison of our results with those presented by Chu (1991) and by Marston (1997) is presented in Table 2.2.

The survey of Marston (1997) listed 22 southern Galactic WR ejecta nebulae, as opposed to the 10 that we find in the SHS imagery of the same region. There are several reasons for this disparity. We omitted WR stars that were in clusters or were heavily embedded within H II regions, this accounts for 8 of the Marston (1997) sample which are classified as having an E component (WR 6, 11, 18, 38, 42, 68, 85 and 98) which will not be discussed in section 2.5.3.

Secondly imagery used by Marston (1997) was obtained using the Curtis Schmidt 0.6m telescope at the Cerro Tololo Inter-American Observatory (CTIO) in Chile, with a resolution of 1.94 arcseconds per pixel compared to the SHS resolution of 0.66 arcseconds per pixel. A direct comparison of SHS and Marston (1997) images of the clear nebulosity around WR 16 is shown in Figure 2.2.

Table 2.2: WR Nebular Classifications

Cat. No.	Spectral Type[a]	Chu (1991)[b]	Marston (1997)[b]	This Work
WR 6	WN5	W	E	E
WR 7	WN4	W	W/E	W/E
WR 8	WN7/WC4			E
WR 11	WC8+0		E	
WR 16	WN8h		W/E	W/E
WR 18	WN4	W	W/E	W/E?
WR 30	WC6+O		W/E	
WR 31	WN4+O		E	
WR 38	WC4		E?	
WR 40	WN8h	W/E	W/E	W/E
WR 42	WC7+O		E	
WR 42d	WN4		W/E	
WR 52	WC5	R	E/R	
WR 54	WN4		E/R	
WR 57	WC7		E?	
WR 60	WC8		E?	
WR 68	WC7		W/E	
WR 71	WN6+?		E	E
WR 75	WN6	W/E	W	W/E
WR 85	WN6	R	W/E	
WR 91	WN7		W/E	R/E?
WR 94	WN6		E	
WR 98	WC7/WN6		W/E	
WR 101	WC8		W/E	
WR 102	WO2	W	W	R/E
WR 116	WN8h			E
WR 124	WN8h	E		E
WR 131	WN7	R		
WR 134	WN6	W		
WR 136	WN6h	W/E		W/E

a: from van der Hucht (2001), except WR 8 from Crowther et al. (1995)

b: uses the categories of Chu (1991)

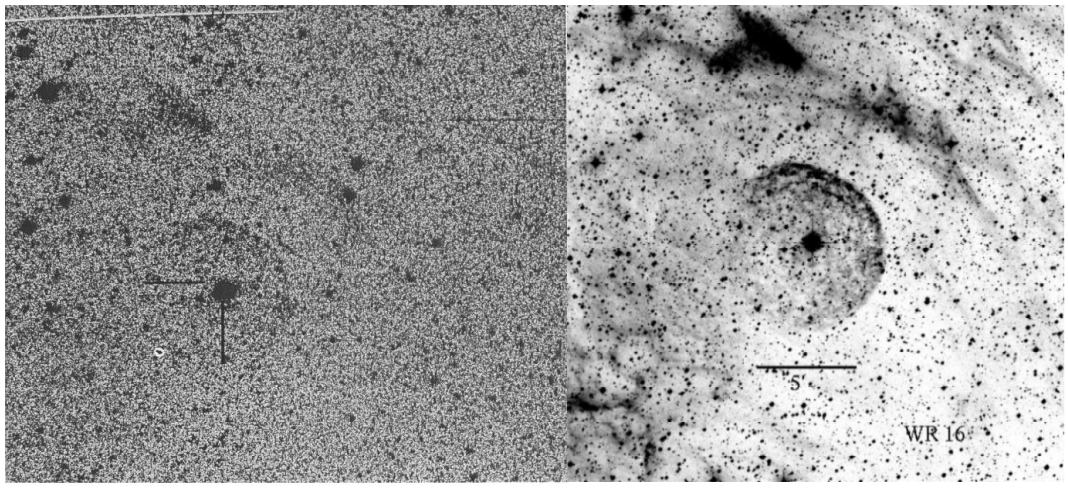

Figure 2.2: WR 16 (WN8h) The image from Marston (1997) is shown on the left, the image from the SHS is shown on the right. The main orb of nebulosity around WR16 can be clearly seen in the SHS image while it is less prominent in the left hand image. In the SHS image a second and possibly a third concentric ring section can also be discerned. In these images north is up and east is to the left.

2.5.3 Notes on Individual Objects

WR 8 - HD 62910

In the SHS imagery of the region around WR 8 (Figure 2.3) one can clearly discern nebulosity that appears to be associated with the star. It is aligned along radial "spokes" with an especially prominent example to the south-west. These spokes define a circular structure approximately 5 arcminutes in diameter, internal to which there are several prominent clumps of nebulosity.

The spectral type of the host star is listed by van der Hucht (2001) as WN7/WC4. Its spectrum places WR 8 neatly between those of WN and WC stars (Crowther et al., 1995). This was initially interpreted as a sign of binarity - a system comprising both WC and WN stars - however Crowther et al. (1995) showed that the wind properties were the same for both the N and C components - implying a single star origin.

The presence of an ejecta nebula around such an unusual host star - a star possibly seen during the transition from the WN to the WC phase - is especially interesting since the composition of the nebula could be helpful towards understanding the evolutionary state of the star.

WR 30 - HD 94305

WR 30 was listed as posessing a ring nebula by Marston (1997). The SHS imagery shows some filamentary structures around the star, some of which take the form of arcs roughly centred on the star, shown in 2.4. The structure shown appears to be related to the star however there

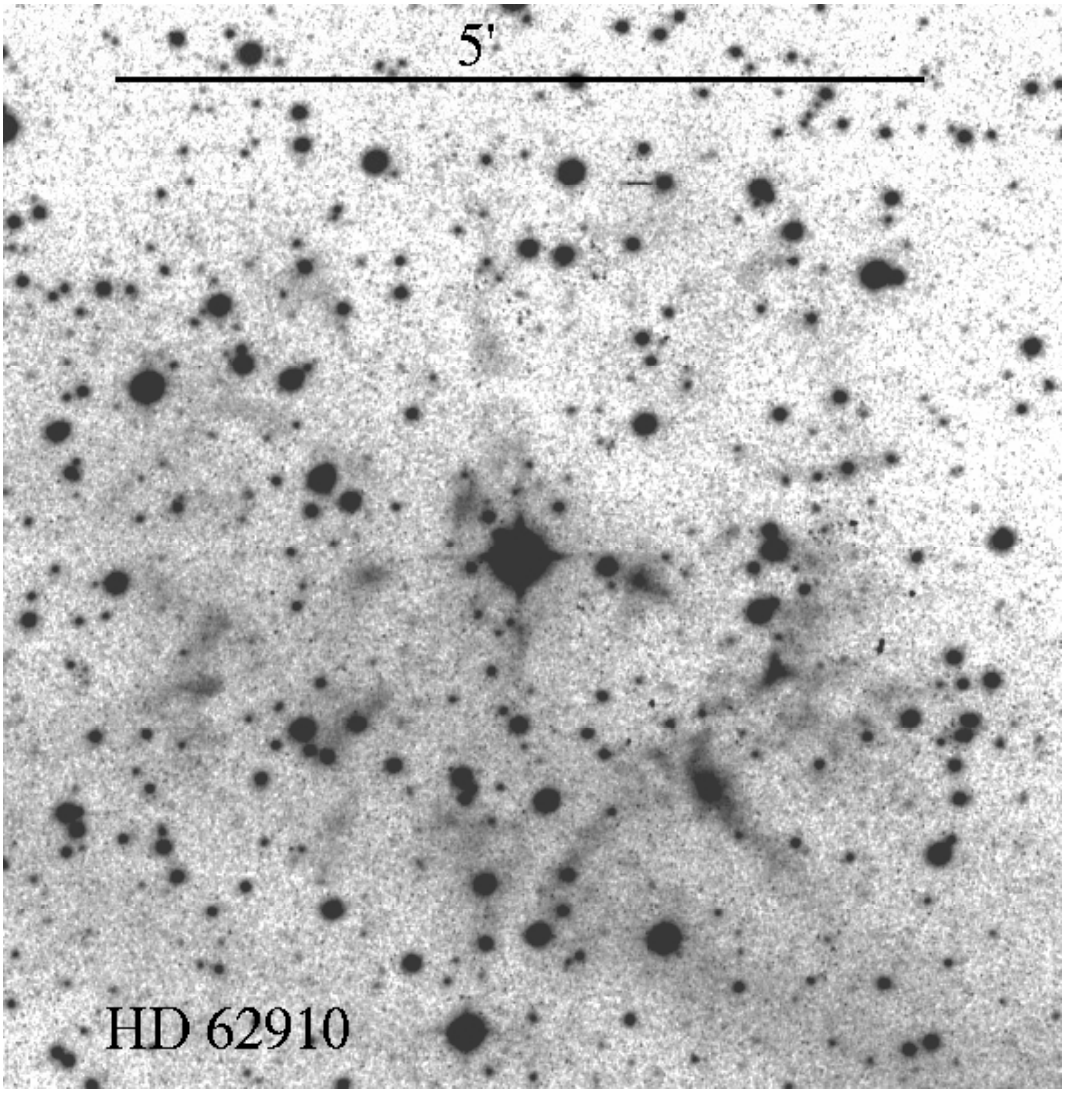

Figure 2.3: The SHS Hα image of the field around HD 62910 (WR 8, WCE+) shows newly revealed nebulosity. North is up, east is to the left.

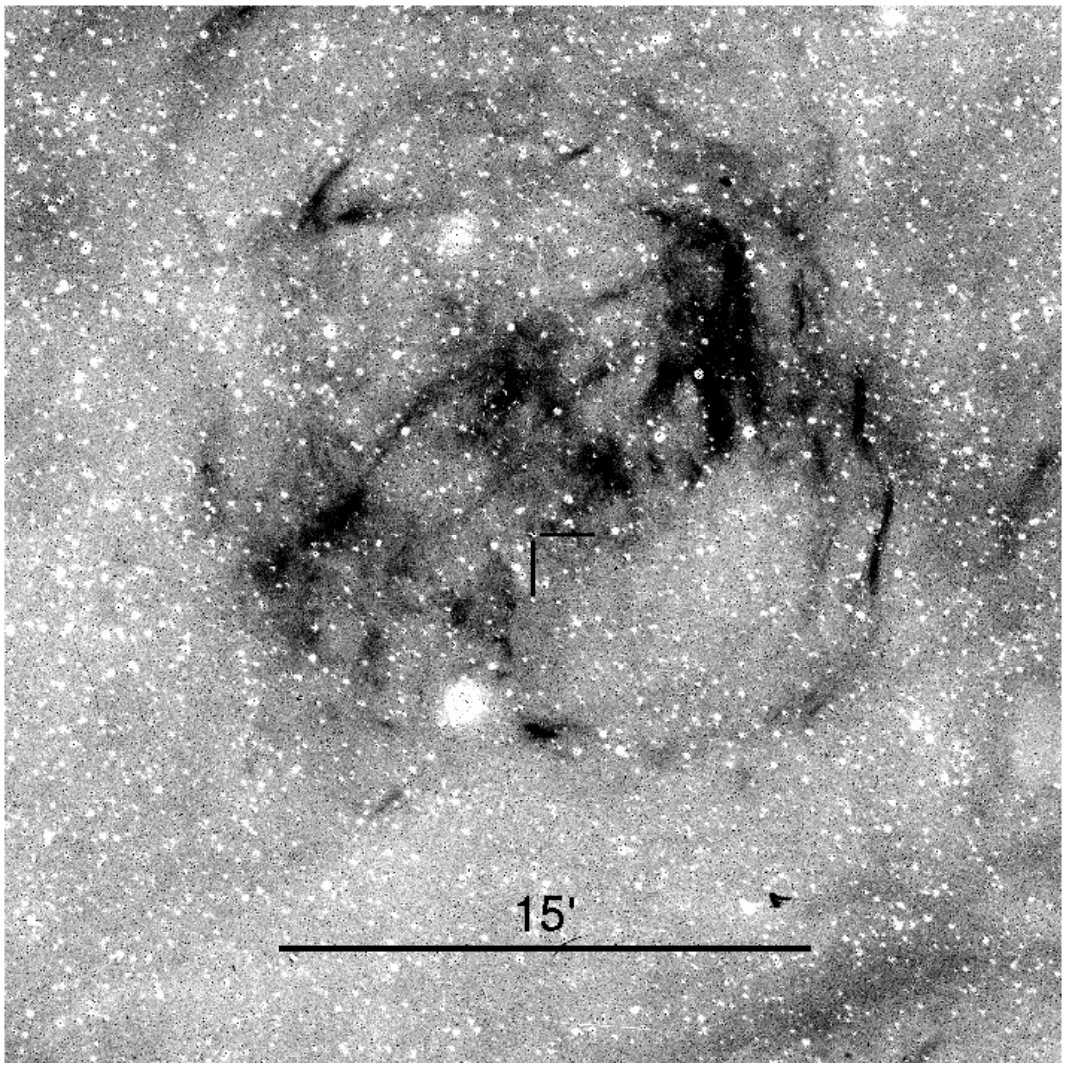

Figure 2.4: SHS image subtraction (Hα - Short Red) of the field around WR 30 (WC6+O). The filamentary structures were listed as a ring nebula of W/E type by Marston (1997). North is up and east is to the left.

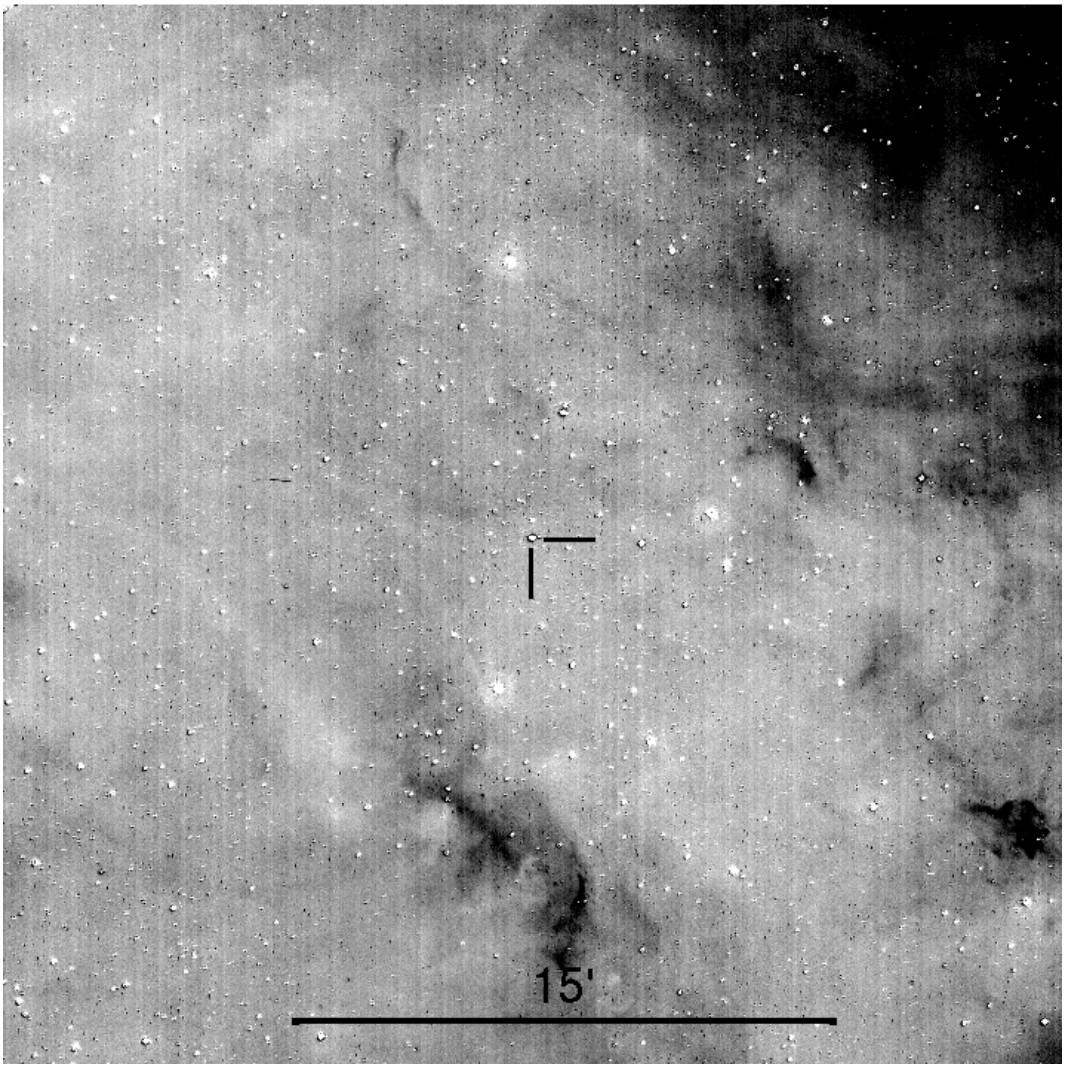

Figure 2.5: SHS image subtraction (Hα - Short Red) of the field around WR 31 (WN4+O7). The very faint, indistinct arc of emission to the west was suggested to be part of a ring by Marston et al. (1994b) and Marston (1997). North is up, east is to the left.

is no morphological evidence in the form of flocculence within the arcs to indicate that this nebulosity contains ejecta.

WR 31 - HD 94546

The nebula around this object, shown in Figure 2.5, was classified by Marston et al. (1994b) as an R type ring nebula, with a diameter of 6.7 arcminutes and was later upgraded to ejecta (E) type by Marston (1997). One can perhaps see faint traces of what appears to be an arc to the east of the star, but this is inconclusive and there is no other evidence for structure on the scales indicated by Marston or that this could be an E type WR nebula.

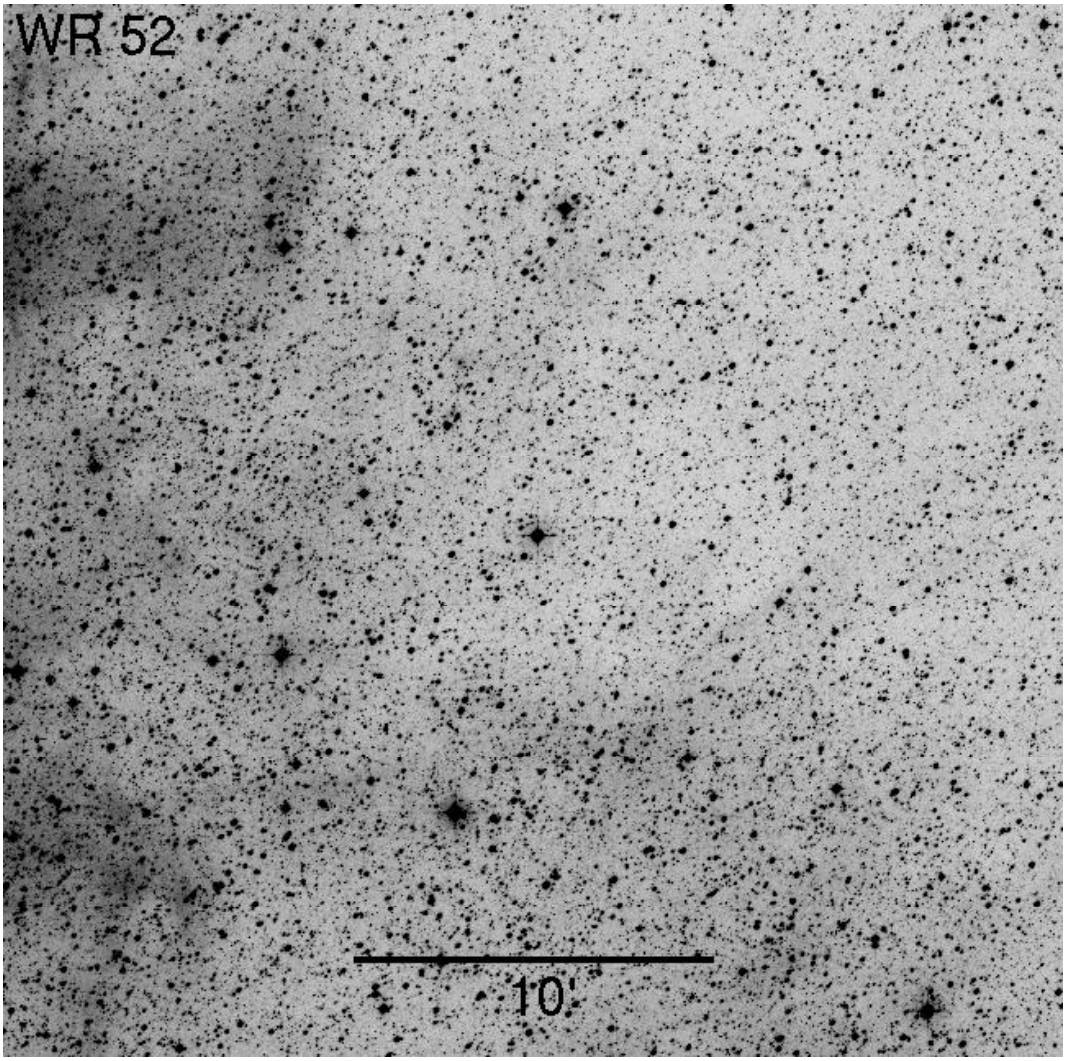

Figure 2.6: SHS image of the region around WR 52 (WC5). The faint diffuse emission has been suggested to be part of a ring, however this is not supported by the SHS imagery. North is up, east is to the left.

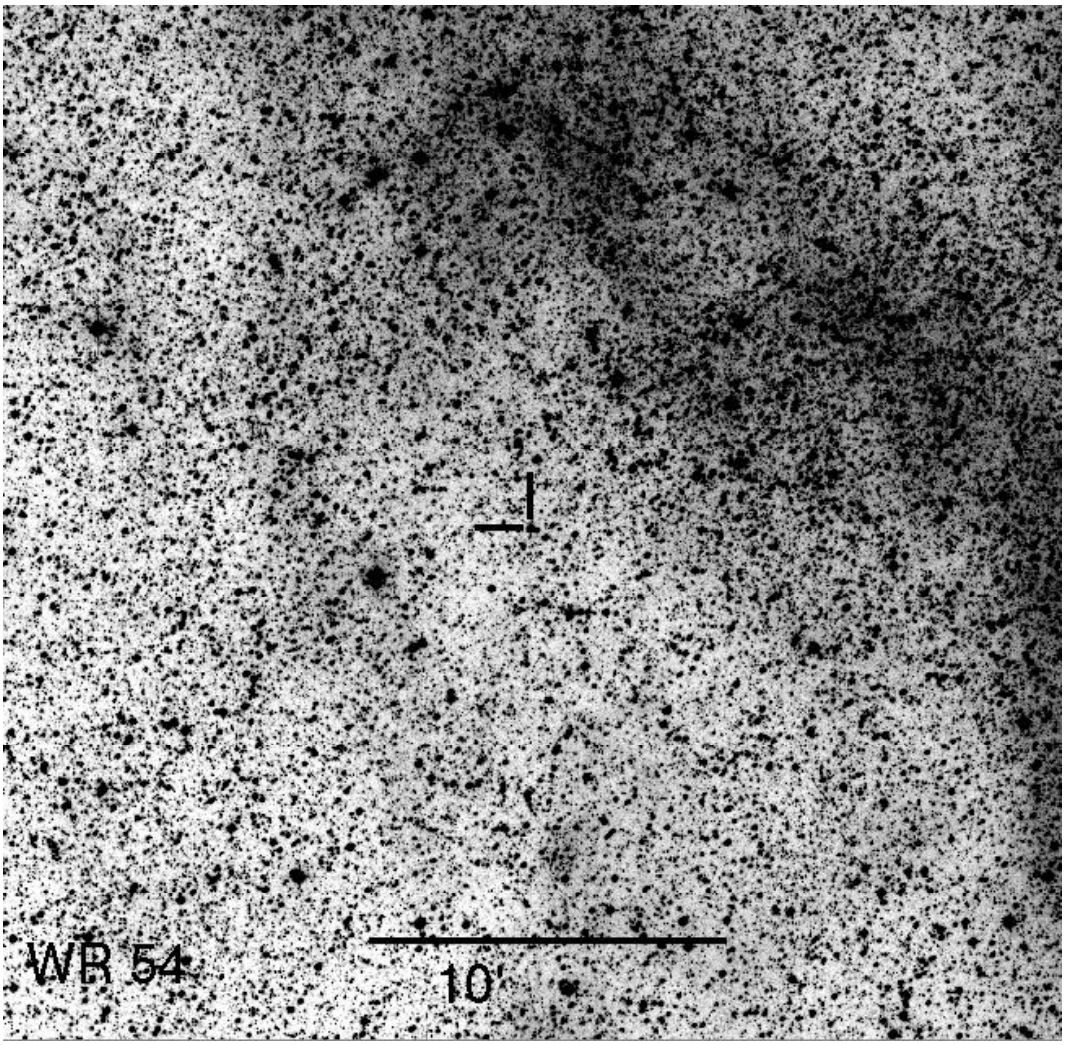

Figure 2.7: SHS image of the region around WR 54 (WN4). The filamentary nebulosity surrounding the star has been proposed to possibly be part of a ring. North is up, east is to the left.

WR 52 - HD 115473

The nebulosity around this object, shown in Figure 2.6, was identified by Marston et al. (1994a) as a possible ring nebula with radius 60 arcminutes. Later it was classified as an R type nebula by Marston (1997) because of diffuse [O III] emission. The region which Marston identified as being one half of a ring is shown in the SHS imagery but does not appear to exhibit any ring-like structures. Although WR 52 appears to be embedded in diffuse Hα emission, there appears to be no evidence for an ejecta nebula.

WR 54

This object, shown in Figure 2.7, was noted as a possible faint ring nebula of radius 20 arcminutes by Marston et al. (1994a). Subsequently this object was classified as an E/R type by

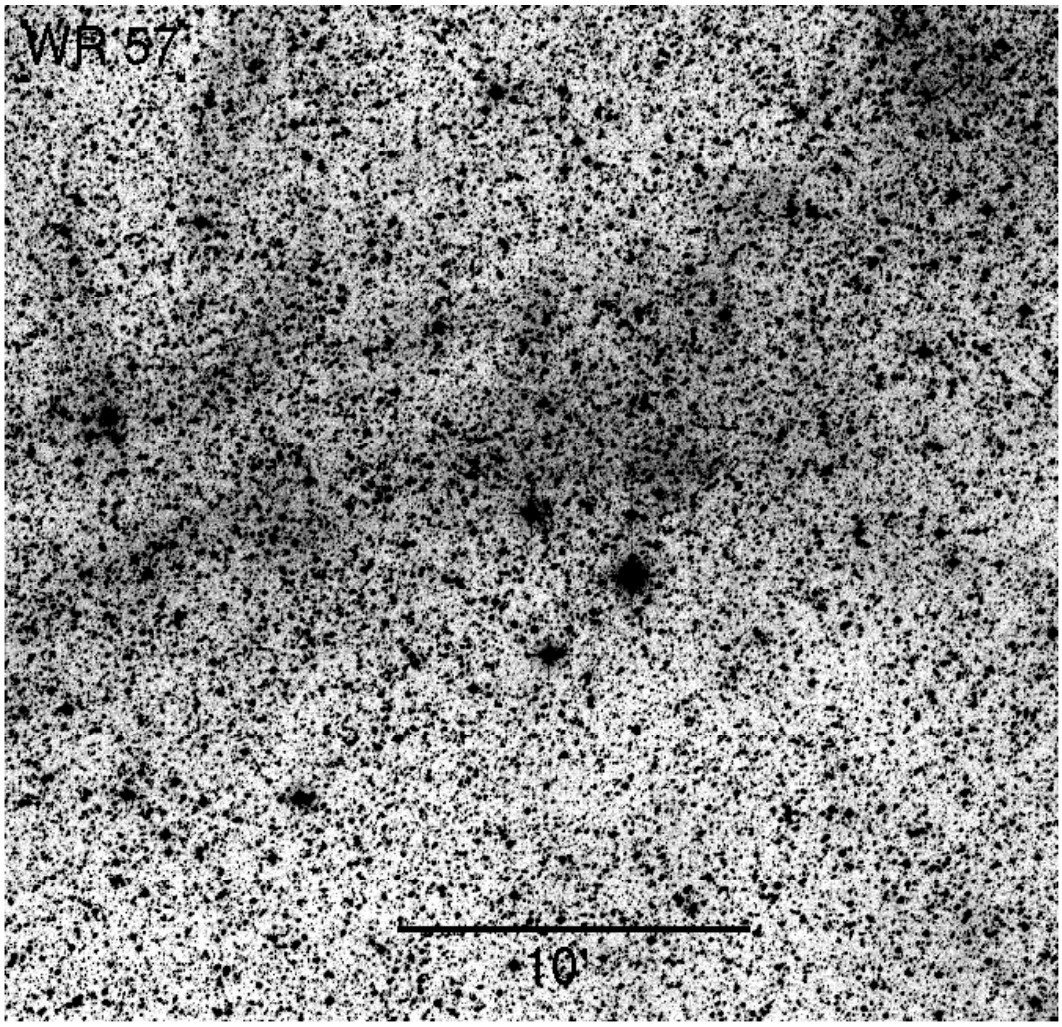

Figure 2.8: SHS image of the region around WR 57 (WC7). The filament running east-west in this image was suggested by Marston (1997) to be a possible ring section. North is up, east is to the left.

Marston (1997). In the SHS image we can see an apparent arc of nebulosity to the NW but this appears to be filamentary and of dubious relation to the star.

WR 57

WR 57 was suggested to have a possible ejecta nebula of radius 8 arcminutes by Marston (1997). The SHS image, Figure 2.8, shows a filament running E-W across the image, with no obvious evidence of a connection with WR 57.

WR 60

WR 60 was claimed to have a "90% complete" ring nebula with a radius of 9 arcminutes by Marston et al. (1994b) and later tentatively ascribed E type status by Marston (1997). The SHS image, shown in Figure 2.9, confirms the detection of a possible ring section to the NE of WR

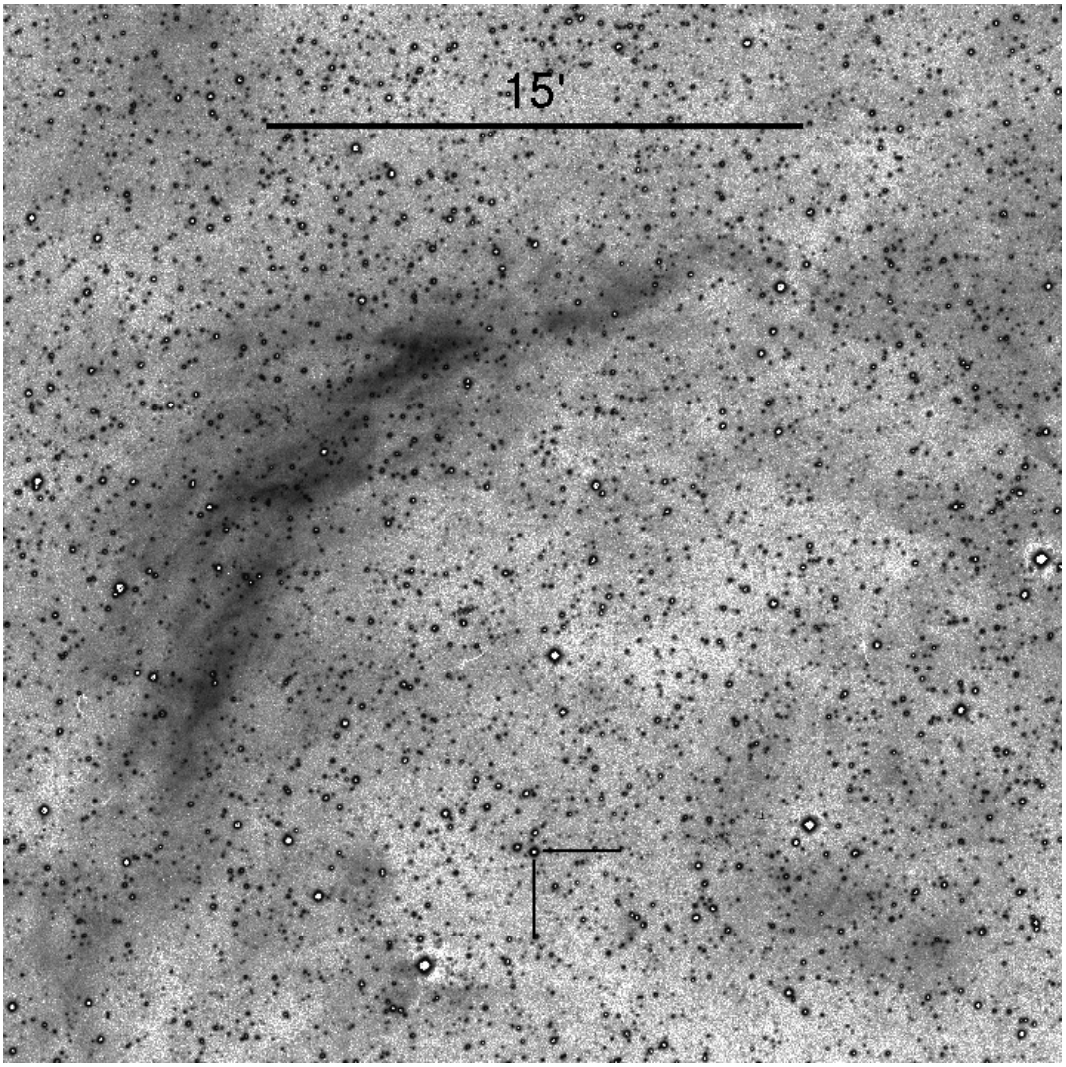

Figure 2.9: SHS image subtraction (Hα - Short Red) of the field around WR 60 (WC8). This provides confirmation of the ring section previously detected by Marston et al. (1994b). North is up, east is to the left.

60. However there is no evidence of the star being further encircled beyond this, suggesting that this nebulosity is merely a diffuse filament.

Stupar et al. (2010b) show that the arc of nebulosity possesses spectral features similar to those associated with supernova remnants (SNRs) and propose a new designation for this nebula as an SNR - G310.5 + 0.8.

WR 71

The SHS image, shown in Figure 2.10, confirms the tenuous nebula around WR 71 first noted by Marston et al. (1994b) and later classified as an E type nebula by Marston (1997). It appears similar to RCW 58 and anon (WR 8), in that it has highly clumped nebulosity to the south, although much fainter than either of the above. The SHS subtracted (Hα-R) image (Figure 2.10) also shows some arcs to the west while improving on the detail of the flocculent structure to the south. The progenitor is a runaway star and as such is significantly out of the plane ($z = 1190$ pc) suggesting that this object may have unique kinematics due to the low ISM density at this z distance. For further discussion of this object see Section 2.6.3.

WR 91

For the region around WR 91, shown in Figure 2.11, the nebulosity was classified as W/E by Marston (1997). The structure, however, is not centred on WR 91 in the manner that would be expected of a nebulosity created by a stellar wind. Instead the associated diffuse nebulosity appears to be radiatively excited.

WR 94

The nebulosity around WR 94, shown in Figure 2.12, appears to be radiatively excited by the star. It displays no signs of clumpiness or flocculence and hence we are unable to confirm this as an ejecta nebula of radius 11 arcminutes as suggested by Marston (1997).

WR 101

The strangely shaped nebula near WR 101, shown in Figure 2.13, was detected and classified as a W/E type nebula by Marston et al. (1994b). Upon inspection of the SHS imagery it is clear that there is a main clump to the south east of the star that is reminiscent of other ejecta type nebulae, however it is unusual in that it appears to be so highly asymmetric, resembling the northern clump in the Bubble Nebula (NGC 7635) around the Of-type star BD+602522. The arcs of nebulosity to the north and east are possibly associated with the star. Cappa et al. (2002) showed that the ionized mass of the nebulosity is of the order $200 M_{\odot}$ for a distance of 3.2 kpc, too high to be pure ejecta. Thus this is likely a swept up ISM nebula with at best some processed component.

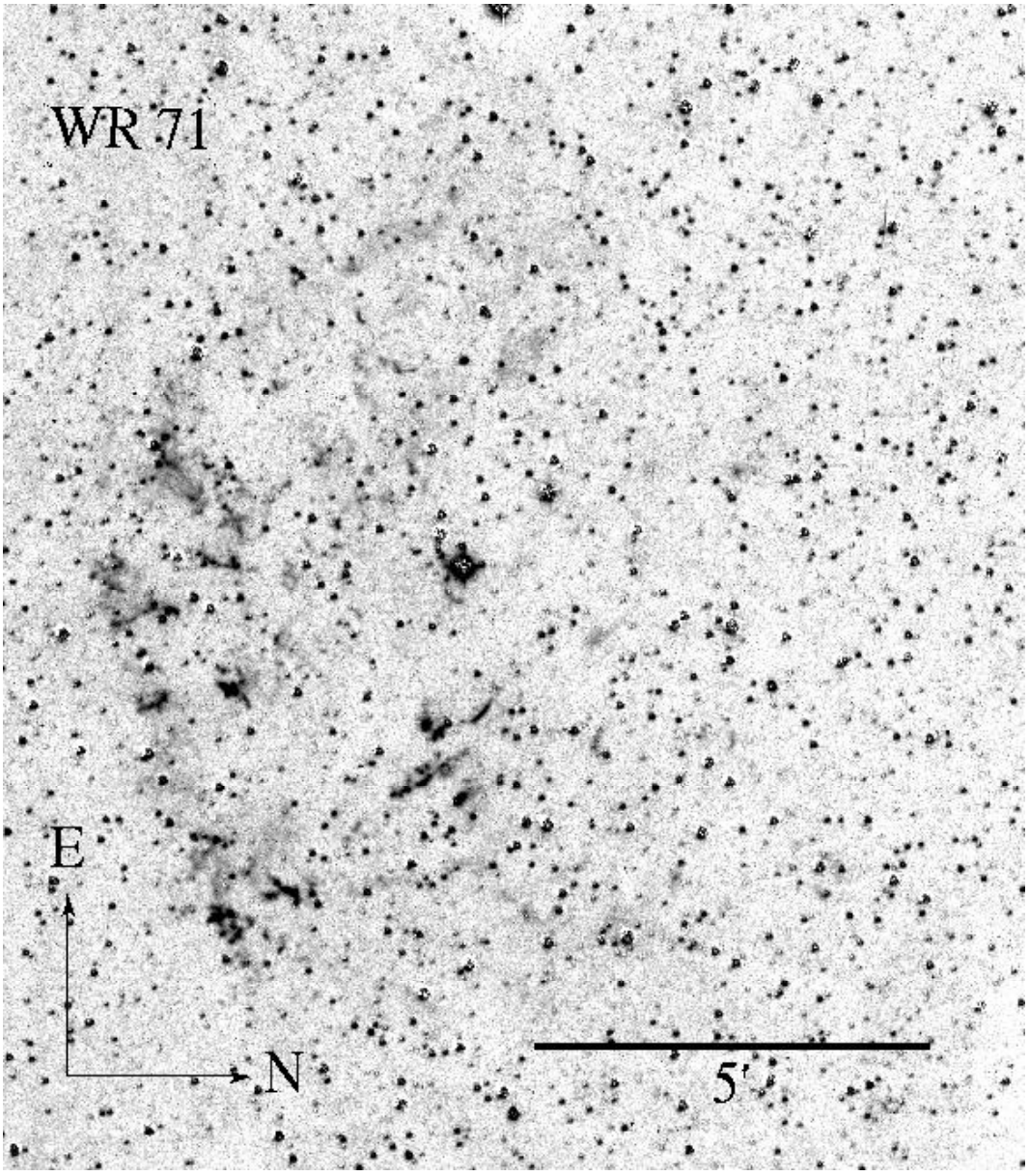

Figure 2.10: SHS image of the field around WR 71 (WN6) (Hα-red subtraction). The tenuous flocculent nebulosity to the south strongly suggests stellar ejecta, as noted by Marston et al. (1994b).

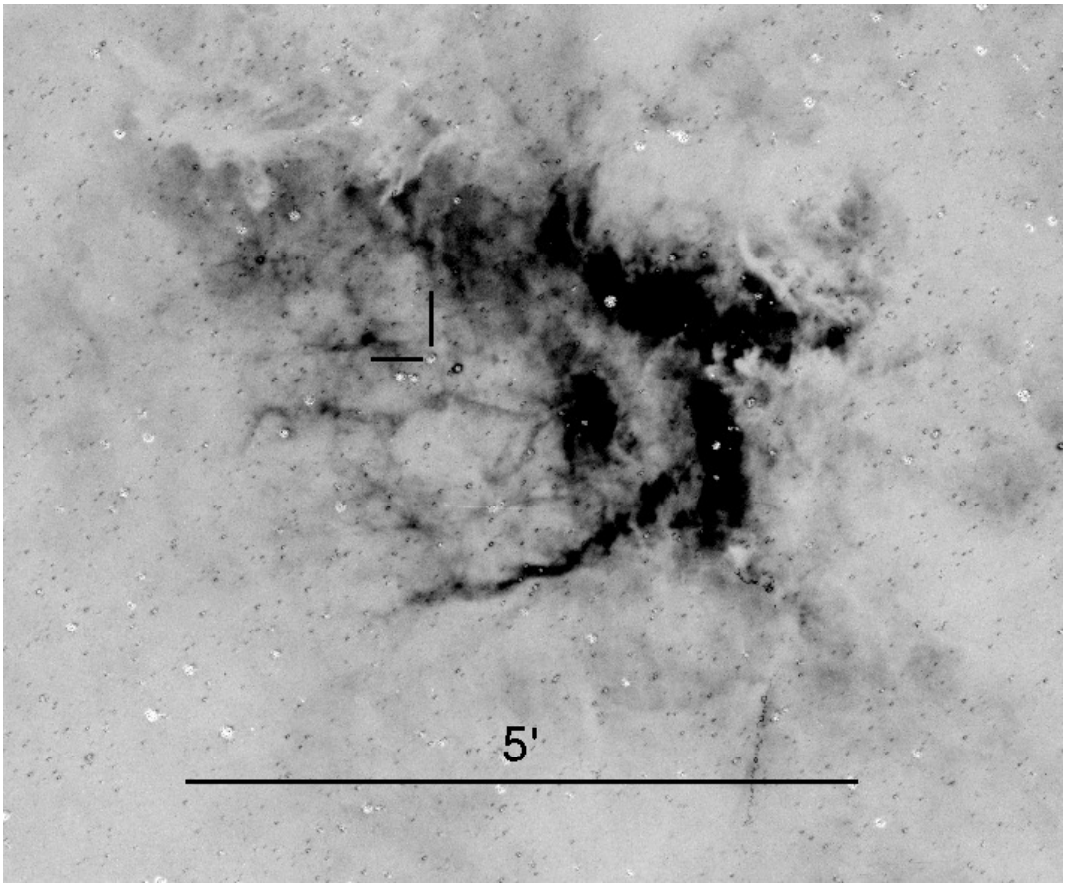

Figure 2.11: SHS image subtraction (Hα - Short Red) of the field around WR 91 (WN7). North is up, east is to the left.

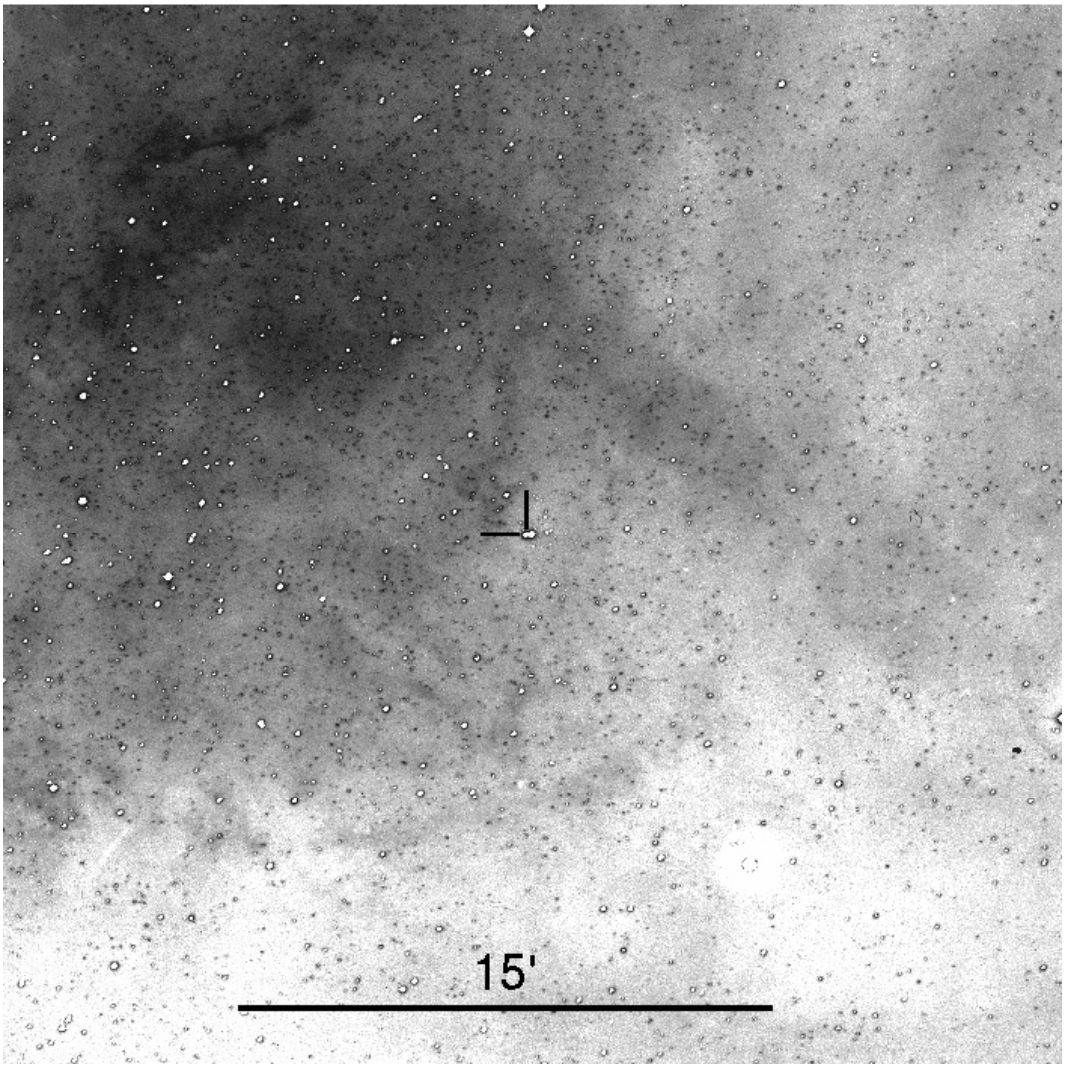

Figure 2.12: SHS image subtraction (Hα - Short Red) of the field around WR 94 (WN6). North is up, east is to the left.

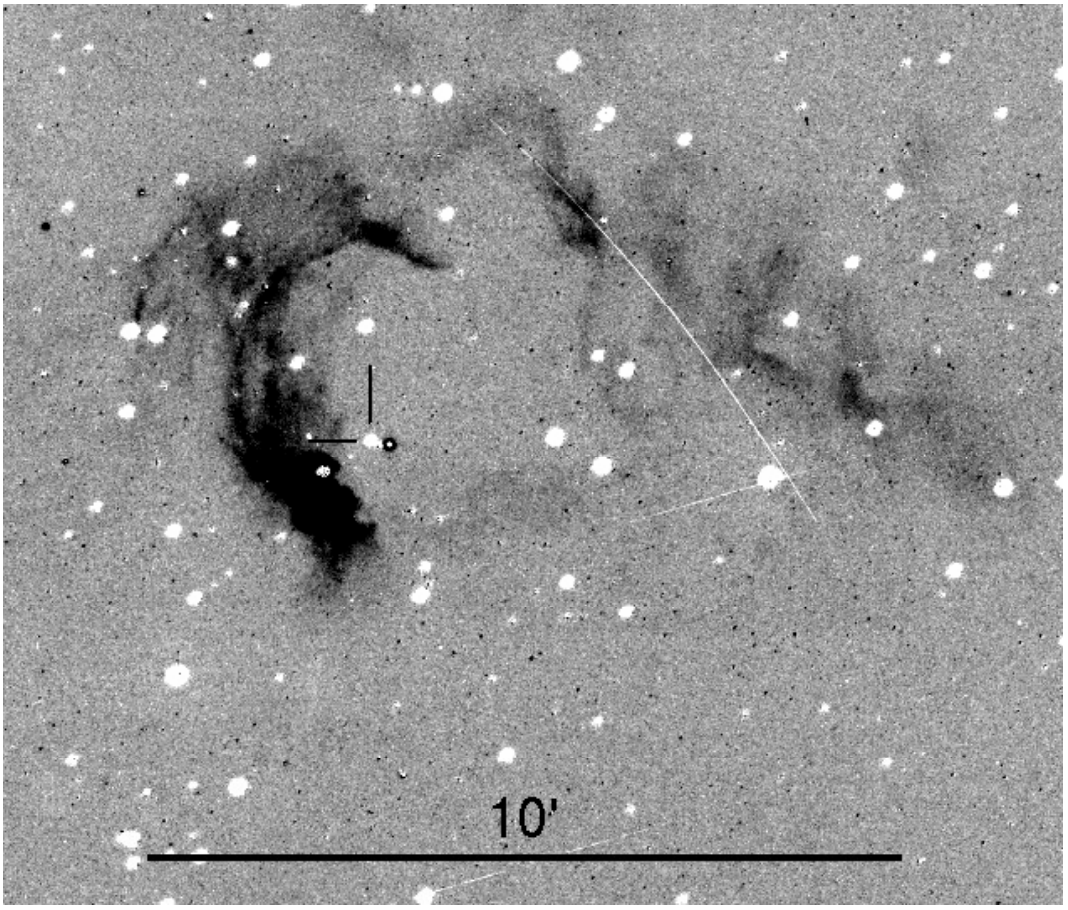

Figure 2.13: SHS image subtraction (Hα - Short Red) for the field around WR 101 (WC8). North is up, east is to the left.

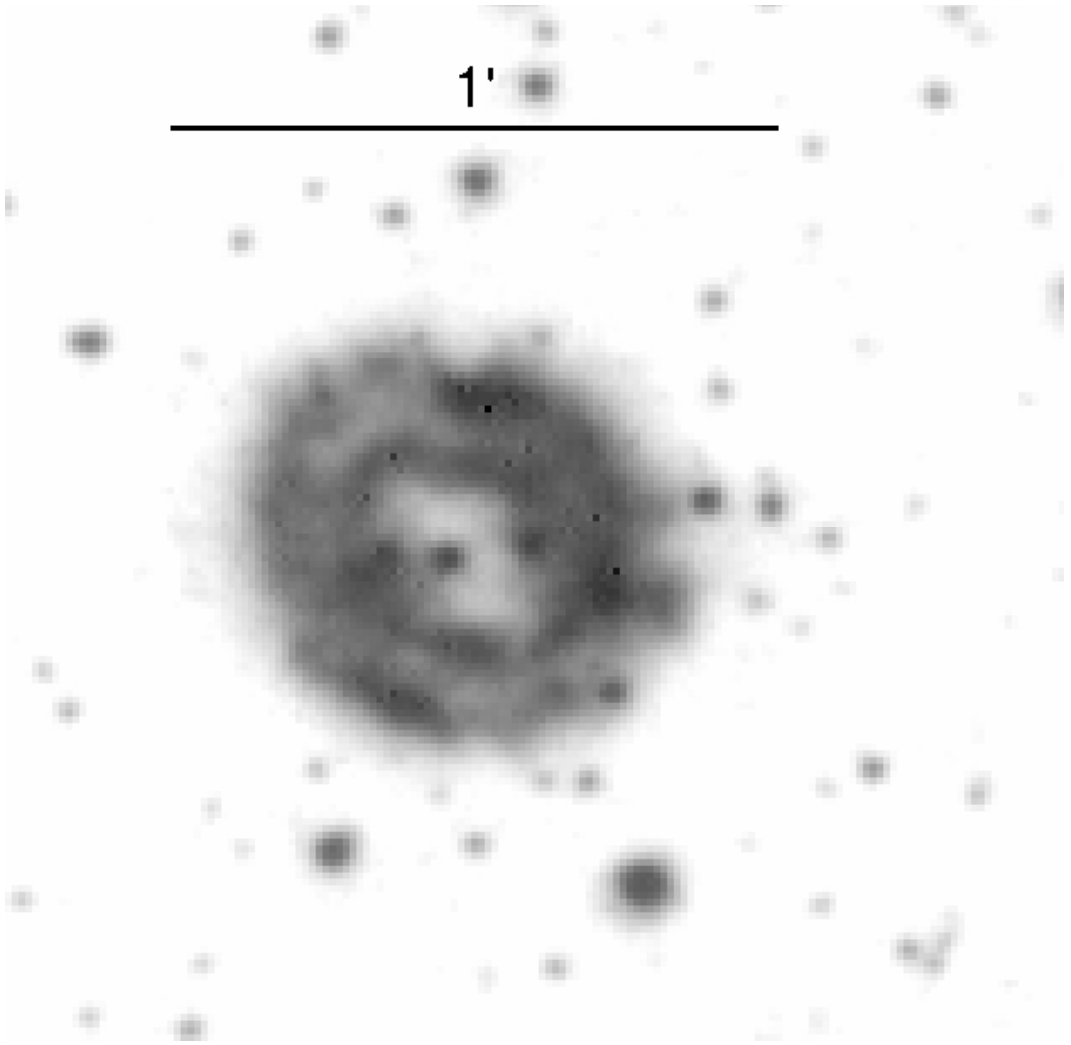

Figure 2.14: SHS image for the field around A48 (WN6). North is up, east is to the left.

A48: Wachter et al. (2010) - 50

This object, shown in Figure 2.14, was discovered by Abell (1966) appears to have two very distinct complete rings. The possible implications of nebular detections with multiple rings are discussed in Section 2.6.1. The Wachter et al. (2010) ring seen at 8 and 24 μm is coincident with the optical ring which appears in the R band as well as Hα.

The SHS image lacks the resolution to determine whether the rings have any flocculent structure and as such it is difficult to classify this nebulosity beyond the default classification of W type. The Spitzer 8μm image of A48 presented by Wachter et al. (2010) appear to have higher resolution and show more structure in the inner ring. This implies that the inner ring is likely to be composed of ejected stellar material, if this is the case then the classification will be W/E.

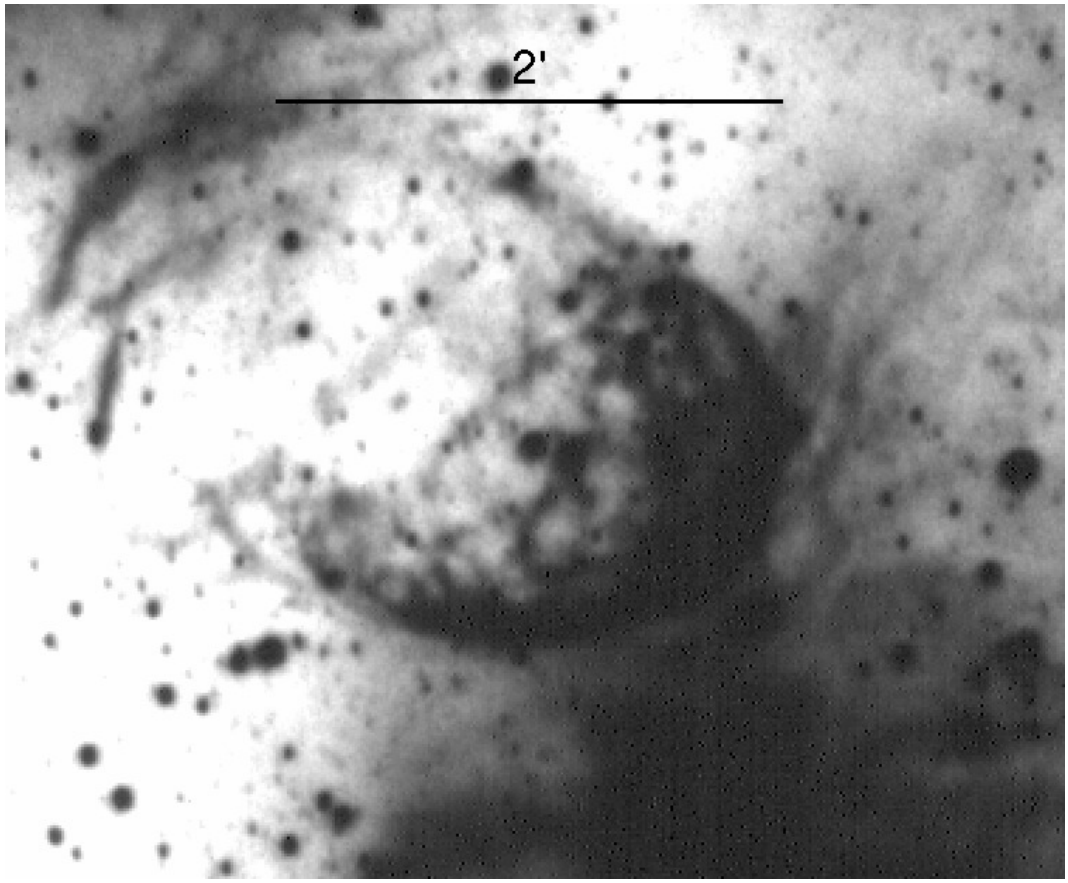

Figure 2.15: SHS image for the field around the LMC star HD 32402 (WC4). North is up, east is to the left.

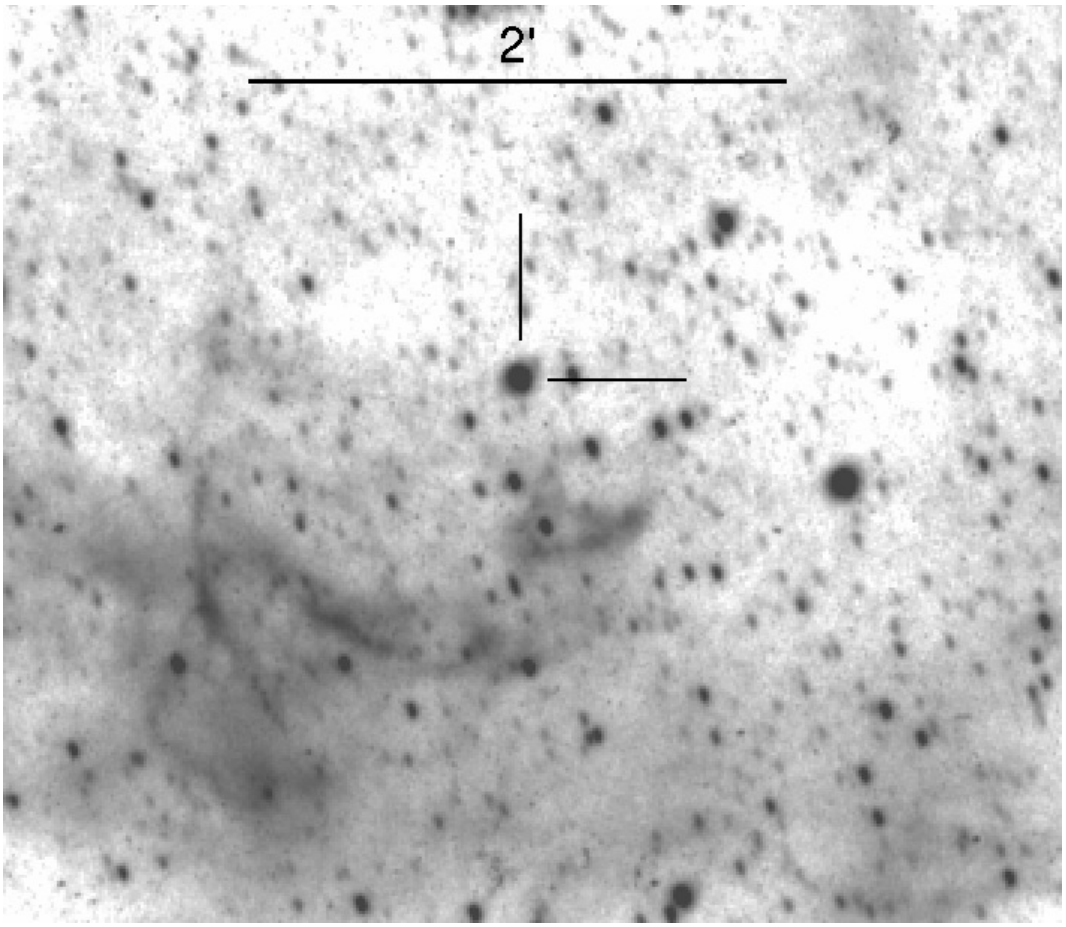

Figure 2.16: SHS image for the field around the LMC star HD 268847 (WN4b). North is up, east is to the left.

BAT99-11 - HD 32402

The nebulosity around BAT99-11 (Figure 2.15) appears ovoid in the same manner as NGC 6888, a bright shock with clear internal structure. If a bona-fide WR nebula it is the largest with the main bubble having a radius of almost 13 pc and distinct arcs at still greater distances. In the SHS imagery it is impossible to make out the internal structure beyond several filaments confined to the interior of the main shock.

We classify this object as a W/E type nebula based on the internal structure and obvious crescent ring section created by wind interactions.

BAT99-15 - HD 268847

BAT99-15, shown in Figure 2.16, has two clear nebulous arcs to the south. These arcs reside in a region of diffuse Hα emission suggesting that they are the interaction between stellar wind and this diffuse material. Given the faintness of this object however it is impossible to clearly rule in or out any E type contribution to this W type nebulosity.

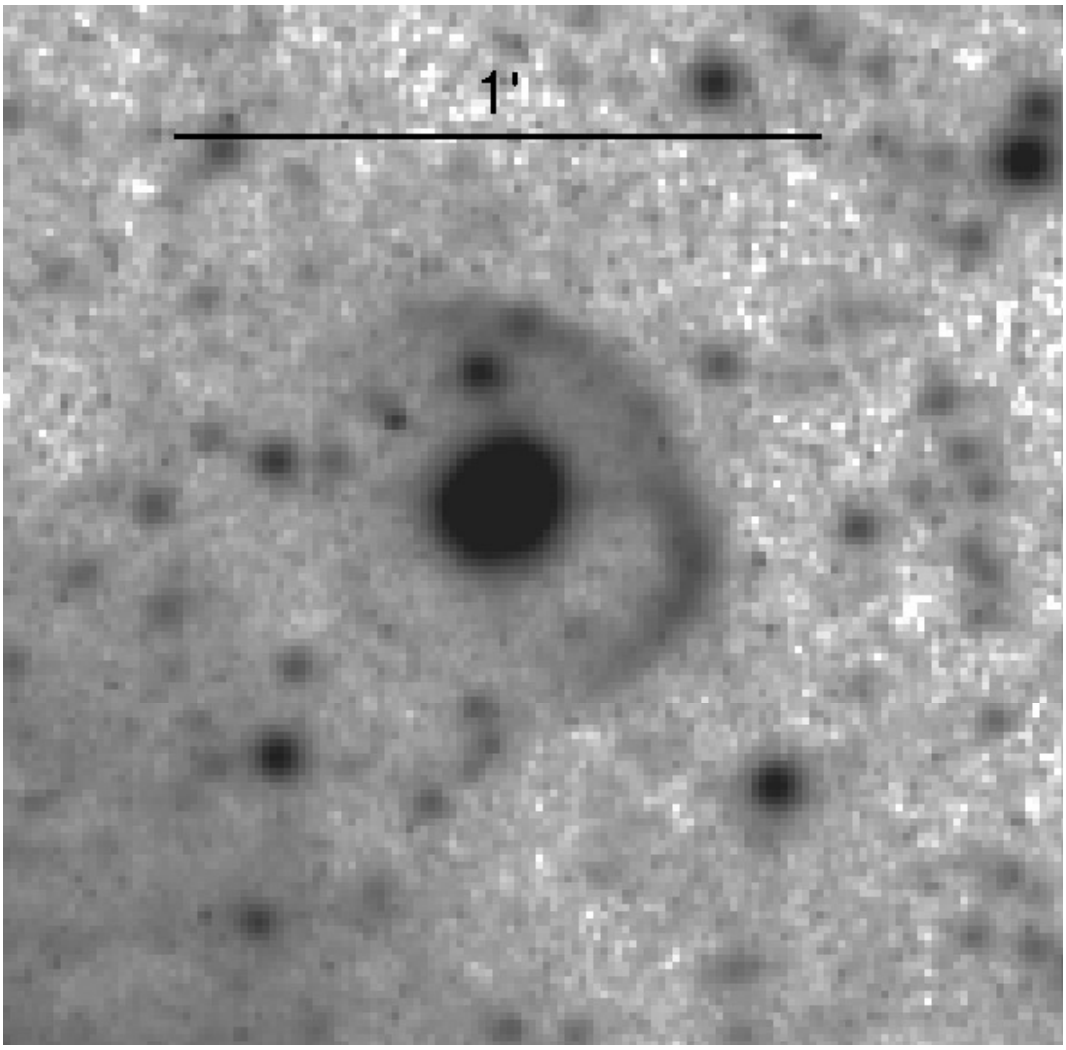

Figure 2.17: SHS image for the field around the LMC star HD 33133 (WN8h). North is up, east is to the left.

BAT99-16 - HD 33133

The crescent nebulosity to the north and west of BAT99-16 (Figure 2.17) is deceptively small, the arc of radius 3.8 pc is actually larger than for NGC 6888 which has a radius of 3.0 pc. As with BAT99-15 we cannot see any internal structure, so it is impossible to ascertain whether the classification should be W or W/E.

BAT99-65

The oval ring nebula around BAT99-65 (Figure 2.18) suggests a W type origin. Again, we cannot reliably ascribe any further classification to this object.

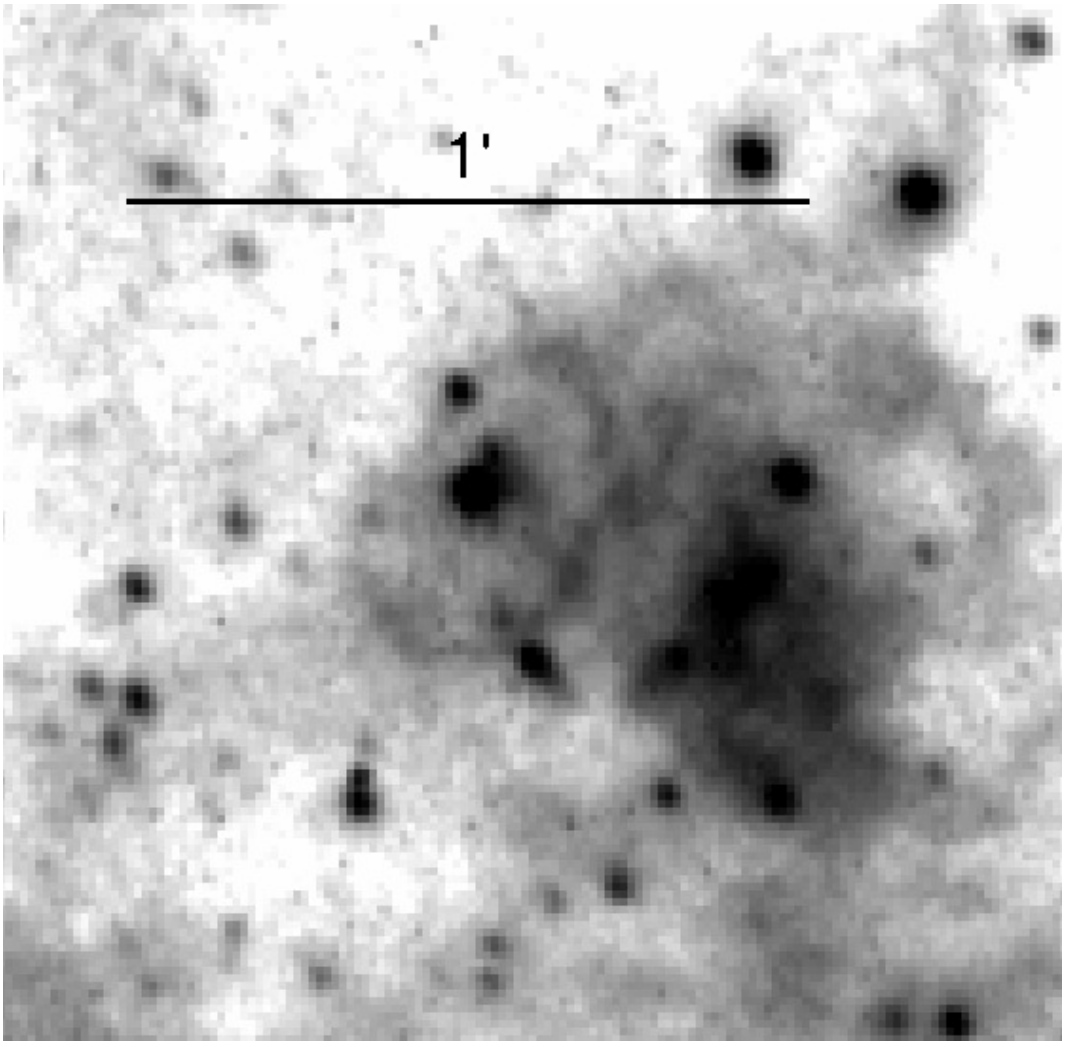

Figure 2.18: SHS image for the LMC field around BAT99-65 (WN4). North is up, east is to the left.

2.6 Discussion

In Table 2.3 we summarise the properties of each nebula detected in the MW and LMC surveys along with the implied physical extent. The fractions of WR nebulae in the MW or LMC with either WN or WC central stars are presented in Table 2.4 along with the fractions for the complete WR population.

2.6.1 Multiple Rings?

Several WR stars have been suggested to have multiple rings, e.g. two by Marston (1995), however WR 16 represents the clearest example of a multiple ringed object as both concentric rings are clearly visible in Hα (Figure 2.2). The inner ring is undisputably created by stellar outflows, as has been confirmed spectroscopically (Marston et al., 1999) - the outer ring though could be swept up material. If the outer ring contains some component, however small, of processed material, the relative compositions and kinematics of the structures could provide useful constraints on the evolution of the star.

The recent discovery of a new double ring structure surrounding a WR star (Wachter et al. (2010) - 50) presents another opportunity to study multiple epochs of a star's history. The SHS imagery does not reveal enough detail to reveal whether the inner ring is likely to be ejected material. However, as mentioned in Section 2.5.3, there is some evidence of knots in the inner ring in the 8 μm image presented by Wachter et al. (2010).

2.6.2 Central Star Properties

The most prominent WR ejecta nebulae are associated with WNh stars, namely: WR 16, 40, 124 and 136. These nebulae have all been confirmed to contain nucleosynthetic products. WNh stars still have some hydrogen left in their atmospheres, i.e. the loss of the H dominated envelope is not complete (Crowther, 2007). The fact that there are bright, N and/or He enriched nebulae around such objects is consistent with the material formerly having made up part of their envelopes. That the shells of matter around these stars are broadly circular indicates that the beginning of the WR phase for these objects may have been dominated by an extreme mass loss event which created the nebulae.

In section 2.5.3 we commented on the unusual spectral type of WR 8, (WN7/WC4); (Crowther et al., 1995). This transition star's nebulosity is strongly reminiscent of RCW 58 - a confirmed ejecta nebula. Assuming that it is an ejecta nebula, the nebula around WR 8 may provide an opportunity to spectroscopically probe matter ejected prior to or during this transition phase.

Table 2.3: Wolf-Rayet stars with Ejecta Nebulae

Nebular Name	Stellar Catalogue Number[a]	Name	Spectral Type[a]	Angular Radius (arcmin)	Distance[b] (kpc)	Radius (pc)	$\|z\|$[a] (pc)
Milky Way							
NGC 2359	WR 7	HD 56925	WN4	2.2	3.7	2.3	8
Anon	WR 8	HD 62910	WN7/WC4	1.9	3.5	1.9	230
Anon	WR 16	HD 86161	WN8h	3.7	2.4	2.5	110
NGC 3199	WR 18	HD 89358	WN4	4.8	2.2	3.1	37
RCW 58	WR 40	HD 96548	WN8h	3.3	2.3	2.2	190
Anon	WR 68	Anon	WC7	6.6	3.3	6.3	110
Anon	WR 71	HD 143414	WN6+?	4.5	9.0	12	1200
RCW 104	WR 75	HD 147419	WN6	9.3	2.2	5.9	56
Anon	WR 91	Anon	WN7	3.7	7.2	7.7	130
G 2.4+1.4	WR 102	Anon	WO2	3.1	5.6	5.0	140
Anon	WR 116	Anon	WN8h	3.3	2.5	2.4	14
M 1-67	WR 124	Merrill's Star	WN8h	0.7	3.4	0.70	190
NGC 6888	WR 136	HD 192163	WN6h	8.2	1.3	3.0	53
A48[c]			WN6	0.3			
LMC Candidates							
Anon	BAT99-11	HD 32402	WC4	0.88	50	12.8	
Anon	BAT99-15	HD 268847	WN4b	0.66	50	9.6	
Anon	BAT99-16	HD 33133	WN8h	0.26	50	3.8	
Anon	BAT99-65	Anon	WN4	0.23	50	3.4	

a: from van der Hucht (2001) (Galactic), Breysacher et al. (1999) (LMC)

b: Galactic distances from van der Hucht (2001), LMC distance Macri et al. (2006)

c: Wachter et al. (2010) - 50

Table 2.4: Results of Survey

	WN	WC	(WN/WC & WO)	WR
Milky Way[a]				
WR stars with Ejecta nebula	10	1	2	13
Total WR stars	127	87	13	227
Ratio	0.08	0.01	0.15	0.06
LMC[b]				
WR stars with candidate Ejecta nebulae	3	1	0	4
Total WR stars	108	24	2	134
Ratio	0.03	0.04	0.00	0.03

a: Not including WR stars discovered by Wachter et al. (2010) as they were found by examining central stars of detected IR ring nebulae.

b: Counting all O3If*/WN6-A stars as isolated WN type.

Table 2.5: WR Nebulae with Binary Central Stars

	Isolated WR	Binary WR	All WR
Milky Way[a]			
Ejecta Nebulae	12	1	13
All WR Stars	141	86	227
Ratio	0.09	0.01	0.06
LMC[b]			
Candidate Ejecta Nebulae	4	0	4
All WR Stars	102	32	134
Ratio	0.04	0.00	0.03

a: Not including WR stars discovered by Wachter et al. (2010).

b: Counting all O3If*/WN6-A stars as isolated WN type.

2.6.3 Binarity

From Table 2.3 a curious fact emerges: only two out of the nineteen WR Ejecta nebula central stars listed here are binaries. In Table 2.5 we summarise the binary fractions for the WR populations in the MW and LMC along with the fraction that we have identified as ejecta nebulae for each case. The binarity classifications of van der Hucht (2001) and Breysacher et al. (1999) were adopted for the Galactic and LMC populations respectively. It is striking that the fraction of binary WR stars having ejecta nebulae is so low.

If the fraction of WR stars with ejecta nebulae was the same for binaries as single WR stars we would expect $\sim 10\%$ of WR binary stars to possess ejecta nebulae - which translates to around 8–9 expected in the MW compared to 1 observed (WR 71). In the LMC there are no binary WR stars with ejecta type nebula, whereas we might expect $\sim$ 1–2 LMC binary WR stars to possess ejecta nebulae.

It has long been speculated that there are two methods of creating WR stars, mass transfer between binary partners and mass loss of an isolated star (e.g. Smith & Payne-Gaposhkin 1968). A possible reason for the relative absence of ejecta nebulae around binary WR stars is that mass transfer onto a companion inhibits the mechanism that produces an ejecta nebulae around single WR stars.

The nebulosity surrounding WR 71 (see Figure 2.10) is an exception to the previous discussion. The progenitor star is of spectral type WN6+? (van der Hucht, 2001). Isserstedt et al. (1983) suggested that the binary partner is a low mass evolved stellar remnant, either a neutron star or a black hole and that the supernova which created the collapsed object likely occured when the system was in the disk of the MW. The loss of mass which occured then left the binary companion (which we now see as WR 71) travelling along whichever velocity vector it possessed at the moment of the supernova. The large elevation of WR 71 above the Galactic plane ($z = -1185$ pc) suggests that a significant component of this velocity was in the z direction. The nebulosity is physically much larger than counterparts in the plane because the density of the ISM at this elevation is much lower, implying that all the circumstellar material is ejecta, as there is so little ISM to be swept up.

It is odd, considering the previously noted anticorrelation of ejecta nebulae and binary WR systems, that such a clear ejecta nebulae should surround such a star. However the explanation may lie in the very low mass of the unseen binary companion ($\sim 3M_{\odot}$ - Isserstedt et al. 1983), since normally WR binary companions are O stars of $\sim 30M_{\odot}$ (van der Hucht (2001) - Tables 18-19). A low mass binary companion may not influence the later creation of an ejecta nebula to the same degree as a less evolved high mass companion. This echoes the work of Nichols &

Fesen (1994), who discussed different scenarios for massive binary star evolution. If the WR 71 nebulosity originated in this way, then the material that comprises the nebula would be expected to have the same enrichment pattern as other WR nebulae. If, on the other hand, the nebulosity is the product of more complex binary interaction and mass transfer then its composition would be more difficult to predict.

This suggests that over the history of a binary system with two close stars of high initial mass the more massive partner will not create an ejecta nebula - all the mass will be accreted by the partner - while the initially lower mass star can create an ejecta nebula as its mass loss is not as influenced by its low mass post-SN companion.

2.7 Conclusions

The morphological classification scheme of Chu (1981, 1991) has been discussed and compared with spectroscopically derived abundances of WR nebulae and a modified set of criteria for ejecta nebulae around WR stars derived.

Using SHS Hα survey data we have examined the environs of each WR star in the Milky Way and Magellanic Clouds for evidence of the presence of nebulae that could be composed of stellar ejecta. This has yielded one new strong candidate (WR 8), confirmed the morphology of another (WR 71) and shown several previously claimed examples to be unlikely candidates.

A prevalence of WNh subtypes amongst ejecta nebulae central stars was found. In addition an anti-correlation between WR binarity and the occurence of an associated nebulosity was also found. It is speculated that this may be because binary interactions and mass transfer may inhibit the formation of an ejecta nebula. This hypothesis is discussed in light of the status of WR 71 - a binary runaway star with an ejecta nebula.

Chapter 3

Spectroscopic Observations of Seven Wolf-Rayet Nebulae

"Errors using inadequate data are much less than those using no data at all."

— Charles Babbage

3.1 Introduction

Massive stars are known to be prodigious recyclers of the ISM, for example a 60 $M_{\odot}$ star is thought to end its life as a > 5 $M_{\odot}$ black hole, implying that that the star will expel ~ 55 $M_{\odot}$ of material (91% of its initial mass) into the ISM during its lifetime. This mass loss, either as a smooth wind or a violent episode, can create circumstellar nebulae. We can help to quantify massive star recycling, in terms of its nucleosynthetic effects, by spectroscopically investigating the nebulae they create. In this Chapter the methods and results of such a study will be presented, with the aim of discovering whether a selection of nebulae around massive stars contain any abundance enhancements indicative of stellar nucleosynthesis.

In the previous chapter we surveyed and classified nebulae around WR stars, discovering a new nebula around a WN/WC type star and identifying an LMC WC star that would be appropriate for this project. These nebulae, along with a "control group" of other WR nebulae were identified and observed with ESO's 3.6m NTT/EFOSC2 (ESO faint object spectrograph and camera) (Buzzoni et al., 1984; Snodgrass et al., 2008) in long slit spectroscopy mode with grisms covering regions from 3100-10000Å that included a variety of standard nebular diagnostics. Complementary service mode observations of NGC 3199 around WR 18 were performed concurrently using ESO's UVES instrument mounted on UT2 of the Very Large Telescope (VLT) (Dekker et al., 2000).

Observations of WR nebulae have been performed several times in the past, usually focusing on the brightest galactic examples e.g. Kwitter (1984); Esteban et al. (1990, 1991, 1992);

Esteban & Vilchez (1992); Marston et al. (1999). As summarised in Chapter 2, the nebular abundances found tend to fall into three groups: no enrichments (typically W type nebulae); helium enrichment (some W/E type nebulae) and full blown He and N enrichments which are taken to be evidence for stellar ejecta. None of the previous studies have attempted to detect the far-red carbon lines, and therefore no neutral carbon abundances exist for these nebulae. Furthermore, no ionized carbon abundances have ever been measured for these nebulae.

Massive stars have been mooted as possible sites of significant carbon formation (Henry et al., 2000). Wolf-Rayet stars in their WC phase appear to be a plausible manifestation of this idea, as they possess very carbon rich atmospheres and high mass loss rates. This assertion has proven difficult to quantify given the challenge of observing gaseous carbon in nebulae around evolved stars. The Collisionally Excited Lines (CELs) of carbon are elusive, lying in relatively inconvenient parts of the electromagnetic spectrum: e.g. the [C II] fine structure line in the far IR (158μm), various lines in the UV (e.g. C III] 1909Å) and [C I] lines in the far red (8700-9900Å). Observations of the far-IR and UV lines rely upon satellite missions like Herschel and the HST (Hubble Space Telescope). In contrast, the [C I] lines can be accessed from the ground, should they have sufficient intensity.

The far-red carbon triplet ([C I] 8727, 9824, 9850Å) is routinely observed in certain astrophysical contexts, particularly from planetary nebulae and H II regions. Liu et al. (1995) first sucessfully identified the triplet in PN spectra, detecting all three in observations of IC 4406 and NGC 2240. The triplet is also common in the photodissociated regions (PDRs) surrounding H II regions, e.g. Munch & Hippelein (1982) for NGC 2024, Burton et al. (1992) for NGC 2023. However it was subsequently shown that in PDRs the lines must arise from recombination rather than collisional excitation (Escalante et al., 1991) which is also the case for some PNe (Danziger & Goad, 1973; Jewitt et al., 1983) but not for the PNe observed by Liu et al. (1995).

From the data obtained we derive nebular physical conditions using standard nebular density and temperature indicators and then use these to derive elemental abundances from the CELs. We then compare these quantities with previously published nebular physical conditions and abundances for these nebulae and with those predicted by stellar evolution models. For the nebulae which are previously unobserved, we determine whether there is any stellar ejecta content within the nebular material.

Table 3.1: Target Parameters

Nebula	Central Star	Spectral Type[a]	v mag.[a]	A_v^a	E(B-V)[a]	α	δ
Galactic							
Anon	WR 8	WN7/WC4	10.48	2.64	0.85	07 44 58.2	-31 54 29.6
Anon	WR 16	WN8h	8.44	2.05	0.66	09 54 52.9	-57 43 38.3
NGC 3199	WR 18	WN4	11.11	2.92	0.94	10 17 02.3	-57 54 46.9
RCW 58	WR 40	WN8h	7.85	1.56	0.50	11 06 17.2	-65 30 35.2
LMC							
Anon	BAT99-2	WN1	16.22	< 0.5		04 49 36.1	-69 20 54.5
Anon	BAT99-11	WC4	13.95	< 0.5		04 57 24.1	-68 23 57.3
Anon	BAT99-38	WC4+O	11.50	< 0.5		05 26 03.9	-67 29 57.0

a: from van der Hucht (2001) (galactic), Breysacher et al. (1999) (LMC)

3.2 Target Selection

The LMC WC star BAT99-11 and the Milky Way WN/WC star WR 8 are carbon rich (WC type) WR stars with ejecta-type circumstellar nebulae. One of the aims of our observing program was to attempt to detect the far-red carbon triplet ([C I] 8727, 9824, 9850Å) in the nebulae surrounding both stars, as such these two objects were given a higher fraction of the observing time than the other nebulae. Four other nebulae, each around a nitrogen rich (WN type) WR star, were chosen as a representative sample against which comparisons could be drawn; both with the nebulae with WC central stars and nebulae analysed by previous authors. The parameters of each of the chosen targets are summarised in Table 3.1.

Four of the targets (WR 16, NGC 3199, RCW58 and BAT99-2) have been the subject of previous spectroscopic analyses, as briefly discussed in the previous chapter. In general helium and nitrogen overabundances are found, however in each case the origin of the ejecta is still subject to debate in that it is possible that the nebular material could have been ejected during the red supergiant (RSG) or luminous blue variable (LBV) phases through which massive stars pass prior to becoming a WR star.

3.2.1 Previous Spectroscopic Observations

RCW 58 was the subject of several spectroscopic investigations in the years following its identification as a potential WR ejecta nebula by Chu (1981). Kwitter (1984) presented the first long slit spectra of the nebulosity, which was found to be highly enriched in helium and nitrogen at an assumed temperature of 7500K. Subsequently the dynamical structure of the nebula was revealed by Smith et al. (1988) to be a combination of a quickly expanding shell interspersed with higher density clumps. It was speculated that the higher density material was the product of pre-WR stellar evolution and did not represent ejecta from the WR phase.

The anonymous circumstellar nebula surrounding WR 16 has been observed by Marston et al. (1999) with surprising results. The nebular spectrum is devoid of several expected lines e.g. [O III] 4959, 5007Å; [S II] 6717, 6731Å. Marston et al. (1999) suggested that this was due to high densities ($n_e > 10^4$ cm^{-3}) suppressing these lines. They noted that the [S II] 6717, 6731Å lines reappear in the outer regions of the nebula, which was assumed to indicate a much lower density of a tenth of the value which they assumed for the inner nebula.

NGC 3199 has been the subject of several spectral analyses, albeit none with comparable resolution to our VLT/UVES dataset. Esteban et al. (1992) found abundances generally in accordance with Galactic HII regions.

The circumstellar nebula around BAT99-2 was first observed spectroscopically by Garnett & Chu (1994) and subsequently by Nazé et al. (2003) (although the star was referred to in both cases as Brey-2). Both found that the nebula was highly ionized - displaying He II and Ar IV lines which is not normally observed in WR nebulae. BAT99-2 is a WN2 type star (Foellmi et al., 2003), amongst the hottest WR stars, with a surface temperature above 90,000K (Crowther, 2007), which produces very intense UV radiation and hence ionizes its surroundings to a greater degree than the nebulae around other, cooler, WR stars. No significant abundance enhancements were detected in the nebula by Nazé et al. (2003).

3.3 Observations

3.3.1 NTT/EFOSC2

Most of the observations were performed in visitor mode over five days in December 2009 using the EFOSC2 instrument mounted on the 3.6m ESO New Technology Telescope (NTT) at La Silla Observatory, Chile. Two grisms were used in long slit spectroscopy mode providing a wavelength coverage from 3095-5085Å and 6015-10320Å. The EFOSC2 slit length was 4.1 arcmin which, due to the fact that almost all of our targets had smaller angular sizes than this, enabled us to use the off-target portions of the slit for sky-subtraction. In all science observa-

tions the slit width was set to 1 arcsecond, while for standard stars the widest slit (5 arcseconds) was used.

Grisms 14 (hereafter Blue) and 16 (hereafter Red) respectively have resolutions (FWHM) of 8Å and 14Å respectively. This allowed us to use 2*2 binning throughout our observations without losing any information as the line profiles were still adequately sampled in this binning mode. This translated to 1030 pixels in both the dispersion and spatial axes.

A log of the nebular observations is presented in Table 3.2. Included in Table 3.2 is the offset of each observation from the parallactic angle as this is thought to be at least partially responsible for reddening problems which emerged later. A corresponding log of our observations of the central stars of our target nebulae is presented in Table 3.3. It did not prove possible to observe two of the LMC WR central stars as they were too faint. A summary of the total integration times in both blue and red grisms is shown in Table 3.4.

Multiple spectroscopic standard stars were observed each night, notably LTT 1788, HR718, and LTT 3864. Observing templates for these stars existed in the EFOSC2 database and were used each night so as to acquire the appropriate signal to noise level for each object to allow later flux calibration.

3.3.2 VLT/UVES

Service mode VLT/UVES observations of NGC 3199 were peformed almost concurrently with the NTT/EFOSC2 observations (see Table 3.2). These were designed to assist with the main science goal while also potentially detecting heavy element recombination lines. The data cover the wavelength region from 3000-10400Å with only small gaps between 5700-5800Å and 8500-8650Å[1]. The UVES dataset had a resolving power of $\frac{\lambda}{\delta\lambda} = 40000$ with a 0.6 arcsecond slit. Its high resolution allowed us to forego the sky subtraction process, as night-sky emission lines appear at the instrumental resolution as opposed to the nebular lines for which we could measure their true widths.

The slit length of up to 30 arcseconds of the UVES instrument is much shorter than that of the EFOSC2 instrument as it is an echelle spectrograph and thus disperses in both planes of the CCD as opposed to long slit spectroscopy using a simple grism where the dispersion is only along one axis (as illustrated in Figure 3.10).

Due to the service mode nature of our observations several calibration steps were unnecessary (or performed on our behalf by ESO). The characteristics of the UVES instrument are very well known, and as such standard flux calibration functions exist for each potential spectral range. Hence we did not need to observe standard stars in the same manner as with EFOSC2.

[1]The red arm of the UVES instrument uses two CCDs with a small gap between them.

Table 3.2: Journal of Nebular Observations

Nebula	Central Star	Date	Instrument	Grism	$\Delta\lambda$ (Å)	Exposure Time (s)	No. Exposures	$\delta\Theta^a$ (°)	Reddening Issues
Anon	WR 8	2009 Dec. 19/20	EFOSC2	14	3095-5085	1800	2	26	×
Anon	WR 8	2009 Dec. 19/20	EFOSC2	16	6015-10320	1800	4	45	×
Anon	WR 8	2009 Dec. 20/21	EFOSC2	14	3095-5085	1200	4	50	×
Anon	WR 8	2009 Dec. 20/21	EFOSC2	16	6015-10320	1500	6	30	×
Anon	WR 16	2009 Dec. 21/22	EFOSC2	14	3095-5085	1800	3	10	×
Anon	WR 16	2009 Dec. 21/22	EFOSC2	16	6015-10320	1800	3	45	×
NGC3199	WR 18	2009 Dec. 28/29	UVES	DIC1	3030-3880 & 4760-6840	1490	4		
NGC3199	WR 18	2009 Dec. 28/29	UVES	DIC2	3730-4990 & 6600-10600	1490	2		
NGC3199	WR 18	2010 Jan. 1/2	UVES	DIC2	3730-4990 & 6600-10600	1490	2		
RCW 58	WR 40	2009 Dec. 18/19	EFOSC2	14	3095-5085	600	4	39	
RCW 58	WR 40	2009 Dec. 18/19	EFOSC2	16	6015-10320	600	5	22	
RCW 58	WR 40	2009 Dec. 19/20	EFOSC2	14	3095-5085	600	5	23	
RCW 58	WR 40	2009 Dec. 19/20	EFOSC2	16	6015-10320	600	5	39	
Anon	BAT99-2	2009 Dec. 22/23	EFOSC2	14	3095-5085	1200	3	15	
Anon	BAT99-2	2009 Dec. 22/23	EFOSC2	16	6015-10320	1200	3	35	
Anon	BAT99-2	2009 Dec. 21/22	EFOSC2	14	3095-5085	1200	3	57	
Anon	BAT99-2	2009 Dec. 21/22	EFOSC2	16	6015-10320	1200	3	77	
Anon	BAT99-11	2009 Dec. 18/19	EFOSC2	14	3095-5085	1500	4	10	×
Anon	BAT99-11	2009 Dec. 18/19	EFOSC2	16	6015-10320	1500	8	78	×
Anon	BAT99-11	2009 Dec. 22/23	EFOSC2	14	3095-5085	1800	3	84	×
Anon	BAT99-11	2009 Dec. 22/23	EFOSC2	16	6015-10320	1800	6	55	×
Anon	BAT99-38	2009 Dec. 19/20	EFOSC2	14	3095-5085	900	3	75	
Anon	BAT99-38	2009 Dec. 19/20	EFOSC2	16	6015-10320	900	3	60	

^{a}: Average difference between Parallactic angle and Slit angle

Table 3.3: Journal of Stellar Observations

Star	Date	Grism	$\Delta\lambda$ (Å)	Exposure Time (s)
BAT99-11	2009 Dec 22/23	14	3095-5085	300
BAT99-11	2009 Dec 22/23	16	6015-10320	300
WR 8	2009 Dec 22/23	14	3095-5085	10
WR 8	2009 Dec 22/23	16	6015-10320	10
WR 16	2009 Dec 22/23	14	3095-5085	4
WR 16	2009 Dec 22/23	16	6015-10320	3
WR 40	2009 Dec 22/23	14	3095-5085	2
WR 40	2009 Dec 22/23	16	6015-10320	2

Table 3.4: Total integration times by target

Nebula	Central Star	Total Red (hours)	Total Blue (hours)
Anon	WR 8	4.5	2.33
Anon	WR 16	1.5	1.5
NGC3199	WR 18	1.6	1.6
RCW 58	WR 40	1.5	1.66
Anon	BAT99-2	2	2
Anon	BAT99-11	6.33	3.16
Anon	BAT99-38	0.75	0.75

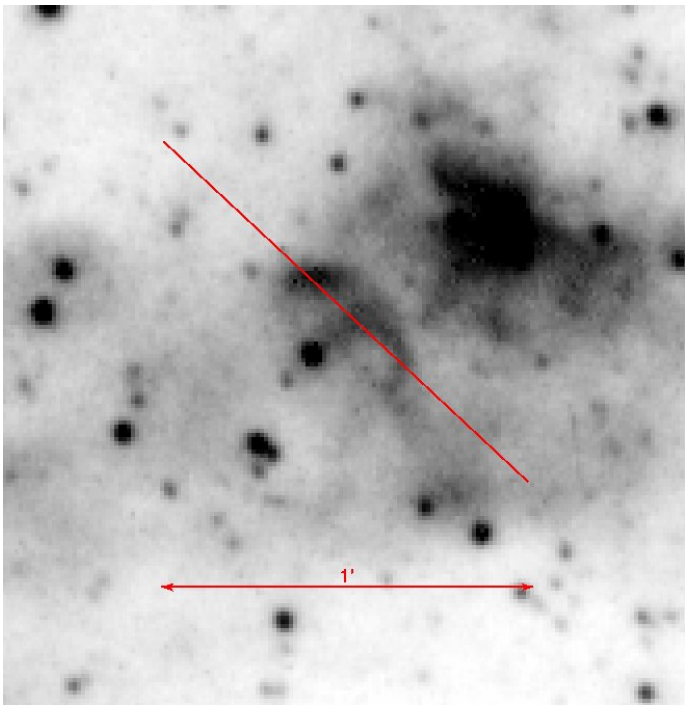

Figure 3.1: Location of slit for the nebula around BAT99-2. Entire slit length (5') is not shown.

3.3.3 Individual Objects

BAT99-2

The slit position adopted for the LMC WR nebula around BAT99-2 is shown in Figure 3.1. This position was adopted as it placed the greatest extent of the arc shaped nebulosity under the EFOSC2 slit. The slit position we adopted roughly matches the position described as "arc" by Nazé et al. (2003).

BAT99-11

The slit position adopted for the nebula around BAT99-11 in the LMC is shown in Figure 3.2. The nebulosity around BAT99-11 is physically much larger than that normally associated with WR ejecta nebulae, so the slit position was chosen to intersect the inner portions of the nebula as this may be more recently expelled material.

BAT99-38

The slit position adopted for the nebulosity near BAT99-38 is shown in Figure 3.3. It was discovered later that BAT99-38 was not the star which appears at the center of the arc, but embedded in the arc itself. This was due to an error in the WCS system of the digitised SHS survey plates which were used to identify WR nebulae in the LMC (see previous chapter). The slit position shown unexpectedly included BAT99-38 spectra along with the nebulosity. The slit was subseqently moved slightly such that BAT99-38 was no longer included in the slit.

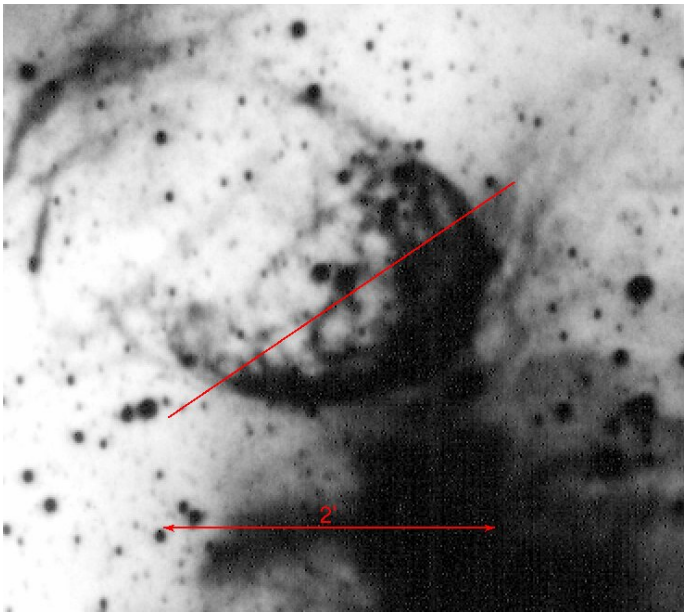

Figure 3.2: Location of slit for the nebula around BAT99-11. Entire slit length (5') is not shown.

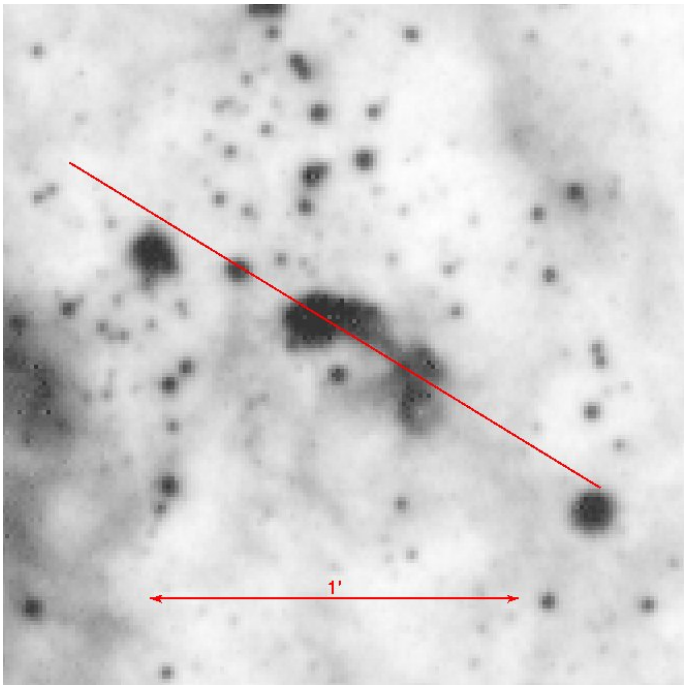

Figure 3.3: Location of slit for the nebula around BAT99-38. Entire slit length (5') is not shown.

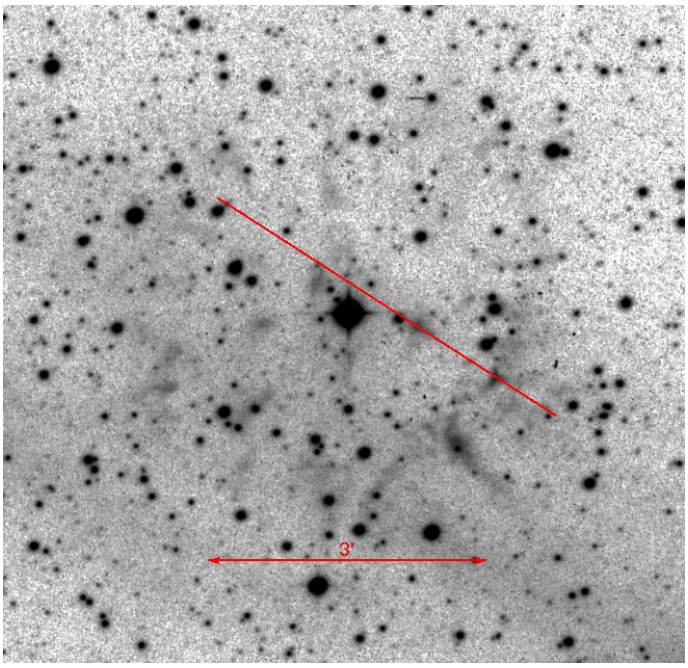

Figure 3.4: Location of slit for the nebula around WR 8. Entire slit length (5') is not shown.

This fact called into question our preliminary morphological identification of this nebula as a possible ejecta nebula.

WR 8

As with BAT99-11, it is unclear whether the knots which appear interior to the outer ring of nebulosity are in the same sphere as the visible ring, or are really spatially closer to WR 8. The slit position was chosen to encompass the two brightest Hα emitting knots which did not coincide with stars. The slit position adopted is shown in Figure 3.4.

WR 16

The adopted slit position for WR 16 is shown in Figure 3.5. Due to the large size of this nebula the slit shown in Figure 3.5 is appoximately the true length of the EFOSC2 slit ($\sim$ 5'). The slit position was chosen such that it encompassed some of the brighter Hα knots seen in the SHS imagery, along with enough off-nebula sky to perform a reasonable sky subtraction.

NGC 3199 (WR 18)

The slit position adopted for NGC3199 is shown in Figure 3.6. Given the shorter (30") UVES slit the brightest knot visible in the short red SHS exposure was chosen. For this object the Hα SHS image is saturated and so not useful in terms of selecting the brightest parts of the nebulosity. While NGC 3199 is very much brighter in Hα than our other targets, it was still important to select the brightest possible section of nebulosity such that the likelihood of detecting weak lines was maximised.

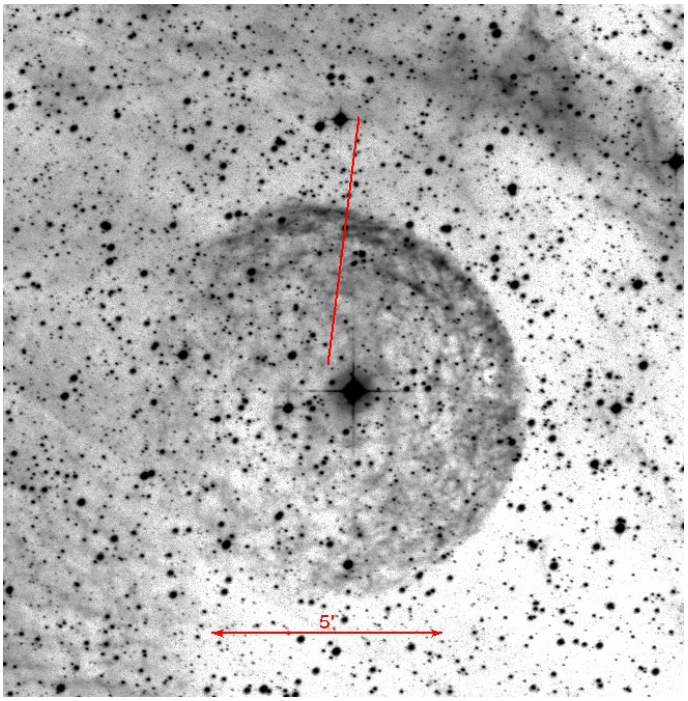

Figure 3.5: Location of slit for the nebula around WR 16.

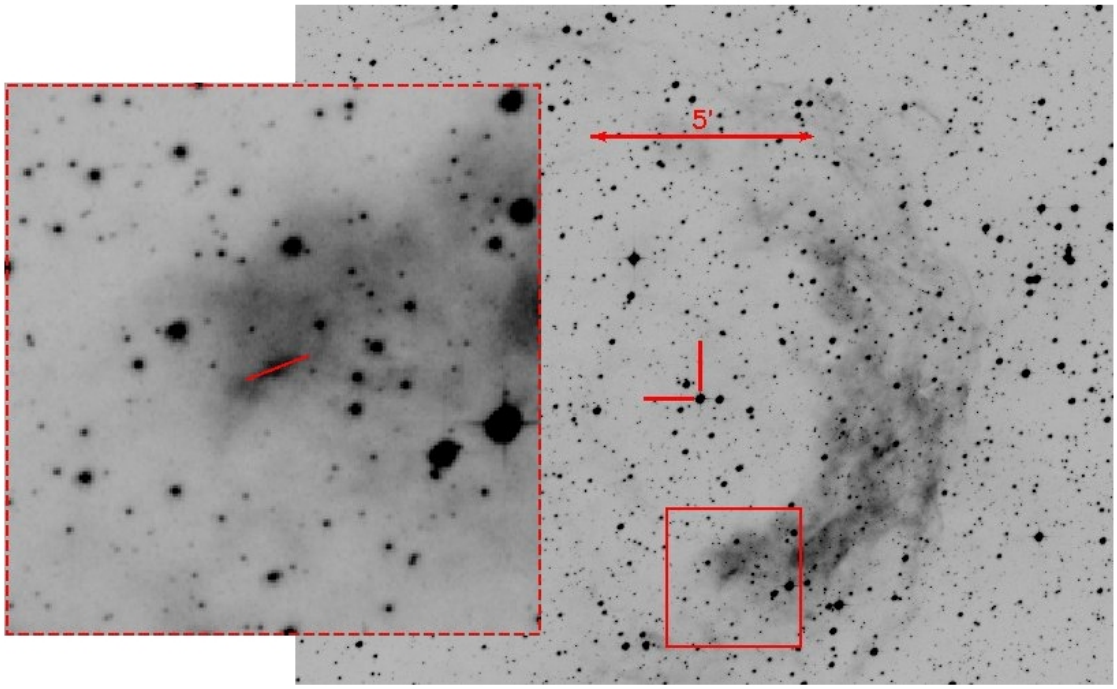

Figure 3.6: SHS short red image of NGC3199 (location of WR 18 indicated with dashes), $\sim$ 15 arcsecond VLT/UVES slit is shown in the expanded section.

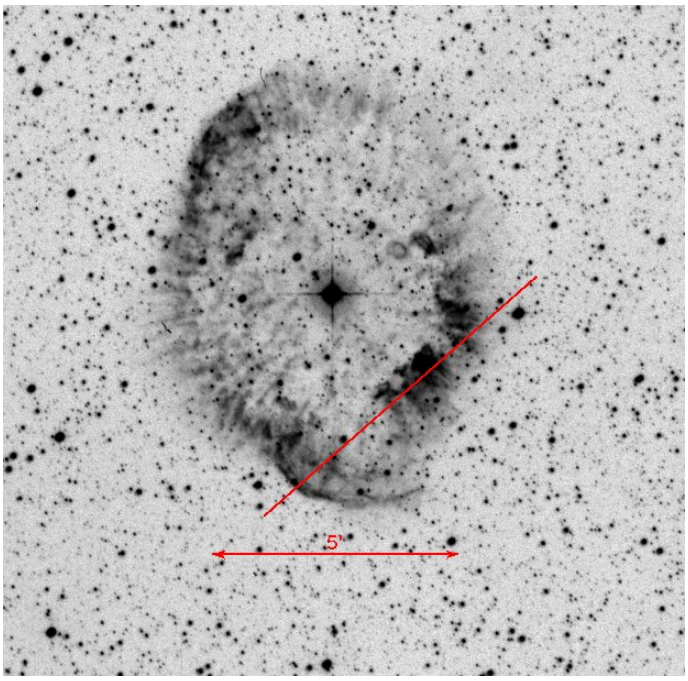

Figure 3.7: Location of slit for RCW 58 (WR 40).

RCW 58 (WR 40)

The slit position used for observations of RCW 58 is shown in Figure 3.7. This slit position was adopted to maximise the amount of bright nebulosity on the western side of RCW 58 in the slit.

3.3.4 Calibration Frames For EFOSC2

3.3.4.1 Bias

Modern astronomical CCD (Charge Coupled Device) chips include many features to ensure the accuracy of the data they produce. First amongst these is the presence of a bias level on the chip. In practice this means that each CCD pixel begins each frame with a certain initial value which should be identical from pixel to pixel, this ensures that each pixel has a positive value (i.e. some signal) regardless of the length of the exposure.

Despite having been designed to be uniform, manufacturing tolerances mean that each CCD pixel will be slightly different in terms of gain and initial bias level. To remove the bias from our science exposures we simply observe the bias level on the CCD several times by taking zero length exposures, take the median of these frames (called the master bias frame) and subtract this from all of our observations. At the beginning and end of each observing night we took a series of ten bias frames using the same binning settings as our science frames (2 by 2).

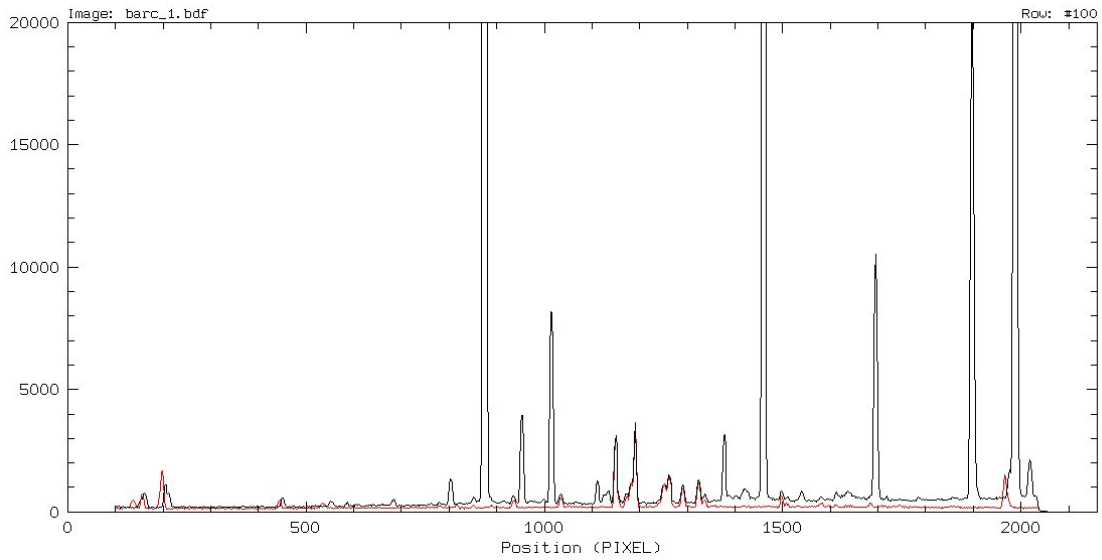

Figure 3.8: 1D He-Ar arc blue spectra extracted from the archived arc frames (black) and from the arc frames from our run (red). Note the absent strong lines in our spectra.

3.3.4.2 Arcs

To calibrate the wavelength scale of our data a known spectrum is necessary to compare with our astronomical observations. The EFOSC2 instrument provides a Helium-Argon lamp for this purpose. As recommended by the manuals supplied by ESO, we used 30s exposures for grism 14 and 3 second exposures for grism 16. These frames were taken before and after observations during each observing night.

Unfortunately during our run the He lamp in the EFOSC2 instrument did not function correctly, leading to underexposed or absent He lines in our arc frames. In grism 16 this is not a problem, owing to the large number of Ar lines in that spectral region. Grism 14 presented a larger problem as there were very few Ar lines in this region (Figure 3.8), and those that are there are close together and in the centre of the frame - a recipe for extremely poor wavelength calibrations.

In order to fix this problem it was necessary to use an arc frame from a later observing session to calibrate our data. The same grism was used by an observing program (084.B-0711) several weeks after our data were taken and the instrument was not removed from the telescope in this time. The arc frames which were taken as part of the subsequent observing program were retrieved from the ESO archive[2]. The resulting wavelength solution was used for all blue frames.

The red calibration proved stable over the five days of our run. It was therefore possible

[2]http://archive.eso.org/

to derive a single calibration from all the red arc frames, which was then used to derive the wavelength solution used for all red frames.

3.3.4.3 Flat Fields

In long slit spectroscopy (LSS) different types of flat fields serve two distinct purposes. The first type of flat field, known as a "dome flat" is a spectroscopic image of a uniformly illuminated surface. This provides a two dimensional spectrum of the fringing effects in the telescope optics combined with the spectrum of the illuminating lamp. By averaging the spectrum in the spatial direction and smoothing, the lamp spectrum can be obtained. Upon dividing the original image by this lamp spectrum all that remains is the fringing pattern which we wish to eliminate in our science observations.

The second type of flat field that will be used is created by taking an image of an illuminated screen within the EFOSC2 instrument, these are known as "internal flats". These perform the same function as dome flats and are treated in the same way but with one important difference, they can be taken with the telescope in any position. This allows for the removal of fringing effects due to flexure of the CCD chip at different angles.

The final type of flat field, a "sky flat", serves a different purpose, it allows corrections for variations in the spatial direction, that is, along the slit. To make this correction we take images of the sky through the slit during civil twilight (immediately following sunset and preceding sunrise). We then average these frames along the spectral direction, smoothing as necessary. After division by the spectral average the resulting frame provides a measure of the relative illumination of the slit - allowing corrections to be made. This kind of correction is vital for extended objects as there will typically be significant variation in throughput along the slit.

A known flaw of the EFOSC2 instrument CCD detectors is their introduction of significant fringing in the far red region ($>$8000Å). Almost all of this fringing is removed by the dome flat fields, but a these flat fields can prove insufficient to remove all fringing effects in some cases, thought to be caused by flexure of the CCD chip when oriented at different angles. To compensate for this, internal flat fields, using the quartz-halogen lamp, were observed for each target immediately following the red exposures.

3.3.4.4 Standard Stars

The standard stars LTT 1788 and LTT 3864 were observed at the beginning and end of each night to allow flux calibration of that night's observations. Standard observing blocks were available in the ESO database facilitating this process for each grism setting. Standard stars were observed with the widest available slit (5") to ensure that all of the stellar flux was included.

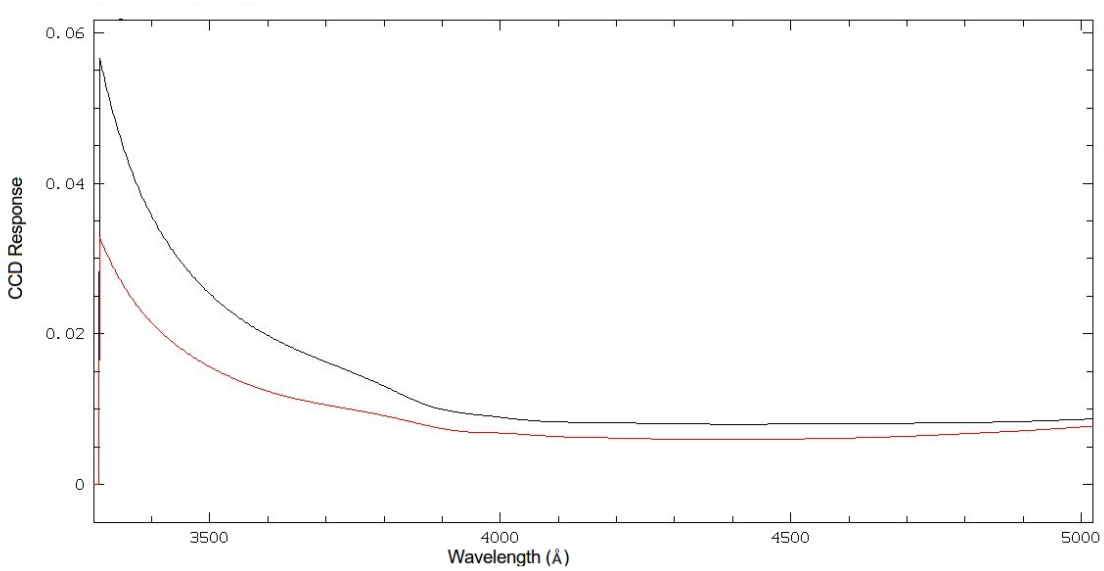

Figure 3.9: Response functions calculated at the beginning and end of the second observing night using the blue grism. The red line is the response function derived using LTT 1788 at the beginning of the second night, the black line is the LTT3864 response function derived at the end of the night.

An absolute flux calibration was not necessary to achieve our science goals, and would have proved impossible anyway as none of the nights we were allocated were photometric. Instead the goal was to achieve the correct relative flux calibration, so that the detected lines have the correct relative intensities. The nebular information is contained in the relative, as well as the absolute strengths of the lines.

The spectrophotometric response curves derived for the beginning and end of each night did not reliably cross-calibrate as the conditions changed throughout each night as shown in Figure 3.9. Despite that, the shape of each star's curve was constant from night to night in both the blue and red spectral regions. The choice of spectrophotometric response curves is discussed below.

3.4 Data Reduction

3.4.1 EFOSC2

At the beginning and end of each night a series of calibration frames were acquired, including bias, arc and flat field frames. The reduction of the data was performed using ESO-MIDAS and gaussian line measurements were performed using Dipso/ELF. A typical result of the data reduction process, a 2D spectral image showing nebular lines, is shown in Figure 3.10

Sky subtraction was performed using the ESO-MIDAS routine "SKYFIT/LONG", which,

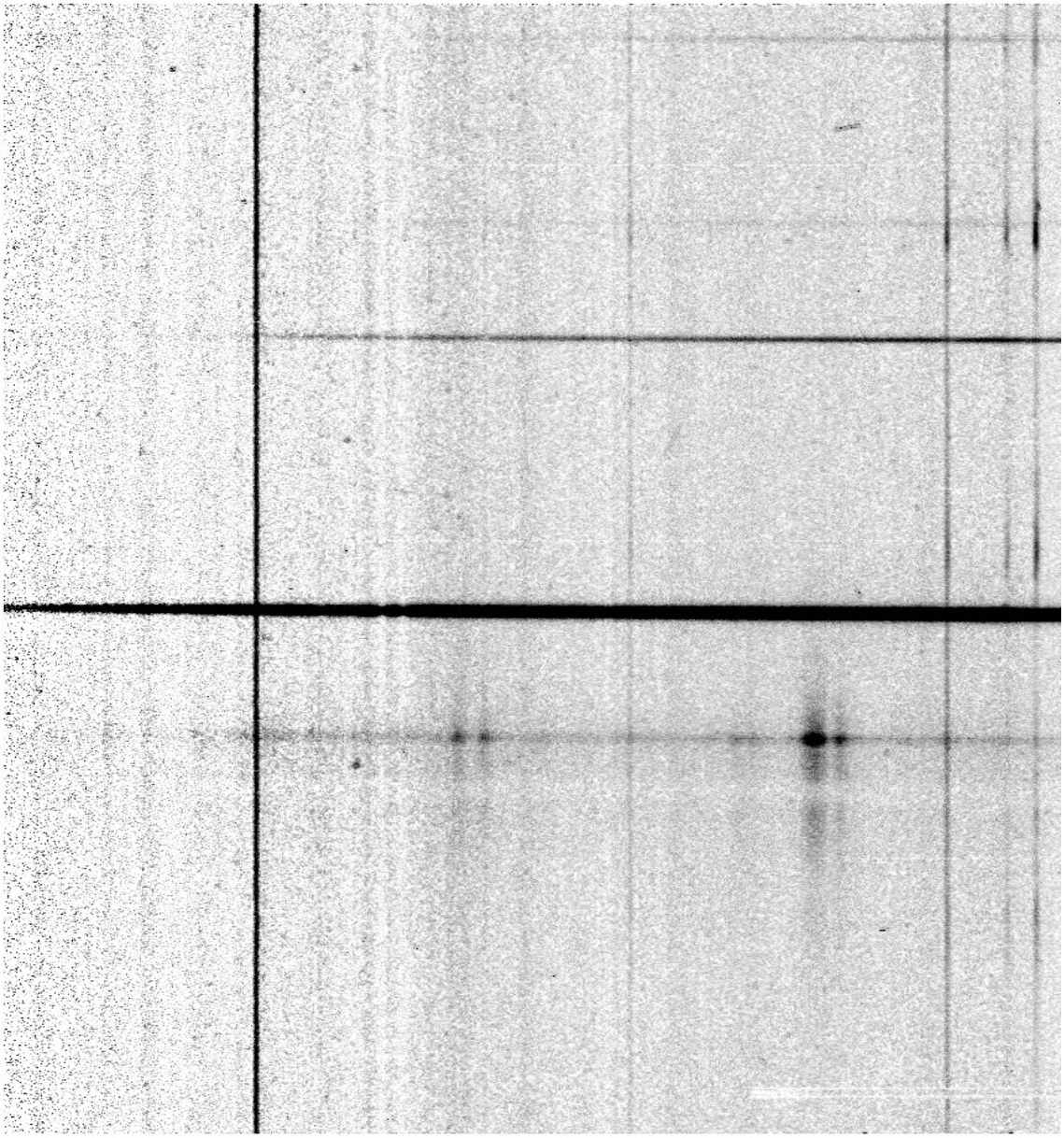

Figure 3.10: 2D Spectra of the nebulosity around WR 8 in the 3000-5050Å wavelength region (Grism #14). The nebular lines at the top are from the nebulosity shown in Figure 3.4. The apparent nebulosity in the lower portion of this spectrum is the scattered light of the WR central star.

given two sky windows either side of the object spectrum, calculates a 2D frame of the night sky lines by interpolating across between the windows. This can then be subtracted from the data frame to leave just the object spectrum in the resulting frame. The 7000-9000Å region is particularly blighted by night sky lines, as shown in the composite Figure 3.11, which displays a non-sky subtracted frame, an interpolated sky frame and the sky-subtracted image. Post sky-subtraction, some evidence of fringing appears which we were not able to remove using any combination of internal flats or dome flats. This residual fringing is not thought to be a problem as there were very few lines being measured in the 7000-9000Å spectral region.

For each 2D co-added sky-subtracted nebular spectrum, every row of pixels which was thought to contain an uncontaminated nebular spectrum was co-added to produce 1D spectra. Subsequently each line was measured using Dipso/ELF.

The dereddening was derived using the Balmer series ratios to calculate c(Hβ) - the logarithmic extinction at Hβ - derived using pairs of Balmer lines (one of which was always Hβ). The relationships between the ratios of the H I Balmer series recombination lines is set by atomic physics (e.g. Hummer & Storey (1987)) such that deviations from these relationships can be used to quantify the degree by which the light has been reddened by interstellar dust and gas. The derived reddening values (Table 3.5) were consistent with literature values derived by previous authors in the cases of WR 16 (Marston et al., 1999), WR 40 (Kwitter, 1984) and BAT99-2 (Nazé et al., 2003). They were also checked against the galactic extinction maps of Schlegel et al. (1998). In every case the galactic WR nebulae had derived E(B-V) values lower than the Schlegel et al maximum value (indicating that they are, in fact, resident in the Galaxy - a useful sanity check). However for the LMC nebulae the Schlegel dust maps indicated E(B-V) values which were too high by at least a factor of five, possibly because the Schelgel et al values included the entire LMC dust columns. For LMC nebula we resorted to the Burstein & Heiles (1982) E(B-V) maps which were found to agree much better with our data.

In some cases the dereddening process highlighted a lack of a reliable flux calibration between the blue and red spectra. For the nebulae around WR 16 and BAT99-11, this manifested itself as very different c(Hβ)'s when comparing Hα in the red spectra to Hβ in the blue, compared with those derived from just the blue spectra (using Hδ and Hγ). For the nebula around WR 8, the converse situation applied in that a very low c(Hβ) was found between the blue lines and a high c(Hβ) was found for Hα. This is likely to be caused by changing conditions throughout our allocated nights making the flux calibrations derived for the beginning and end of each night inappropriate for the middle of each night. This was minimised by using the nearest (in time) flux calibration to each observation.

Figure 3.11: *left:* 2D spectra of the region around WR 8 for the red spectral region (6000-10000Å Grism #16); *centre:* ESO-MIDAS "SKYFIT/LONG" generated 2D sky spectrum for the frame shown; *right:* Sky subtracted spectra of the region around WR 8.

A futher complication was intoduced via the choice to deviate from the parallactic angle in order to maximise the amount of nebulosity falling under the slit. In cases where the nebulae were large and of fairly constant surface brightness, this did not cause a problem. However, the nebulae with discordant blue/red reddening values were those where the slit passed through several small clumps, e.g. WR 8 (See Figure 3.4). In these cases the effects of atmospheric dispersion combined with the small angular scales of the clumps of nebulosity may be the cause of the reddening issues. The offsets from the parallactic angle for each object are listed in Table 3.2.

By adopting a different reddening solution for the red spectra we effectively de-redden and flux calibrate Hα and the adjacent lines ([N II], [S II], He I 6678Å) but lose flux calibration for lines far from Hα ([S III] 9069, 9531Å for example). For the nebulae which required this technique (around WR 8, WR 16 and BAT99-11), this would render their [S III] diagnostic temperatures unreliable.

Due to the relatively low resolution in both the blue and red spectra, blended lines are a problem in these data. Most seriously, the standard density diagnostic line pairs [S II] 6717, 6731Å and [O II] 3727. 3729Å were blended to some degree. The [O II] doublet is completely unresolved: its measured FWHM is very close to instrumental. The [S II] doublet is marginally resolved in that there are clearly two components. This situation is far from ideal as this leaves the [S II] doublet as the only density diagnostic, and with a larger uncertainty on the [S II] doublet ratio due to its semi-blended nature. The profile of the [S II] doublet in the nebulosity surrounding BAT99-38 is shown in Figure 3.12 along with a Dipso/ELF line fit.

The line blend between [Ne III] 3967Å and H5 3970Å was only an issue from the point of view of calculating the neon abundance. However the [Ne III] 3868Å line is isolated in this dataset and could be easily used for that purpose. The blended higher order hydrogen/helium lines (e.g. H8, 3889Å and He I 3888.6Å) were not problematic as we do not have sufficient S/N to use the lines as diagnostics.

It was also found that the observed intensity ratio of the [O III] lines of 5007Å to 4959Å was incorrect. This intensity ratio is fixed and by can be derived from atomic transition probabilities (e.g. Storey & Zeippen 2000) and has a value of 2.98, whereas we observed it to be nearer 2.0 in all cases. This is attributed to the 5007Å line falling very close (3–4 pixels) to the edge of the detector, and the flux calibration being unreliable there. It was therefore assumed that the 4959Å line was correctly flux calibrated and it was used on its own at the [O III] temperature diagnostic stage. The cause of this problem has not been ascertained as it is present in all of the EFOSC observations despite the smoothness of the derived response functions at the

Table 3.5: Reddening

Nebula	Central Star	c(Hβ)$_{blue}$	c(Hβ)$^{a}_{red}$	Implied E(B-V)^{b}	Stellar E(B-V)^{c}	Maximum Galactic E(B-V)^{d}	Lit. E(B-V)	Ref.
Galactic								
Anon	WR 8	0.04	1.73	0.02	0.85	1.23		
Anon	WR 16	0.99	2.43	0.68	0.66	2.97	0.44	Marston et al. (1999)
NGC 3199	WR 18	1.18		0.81	0.94		0.79	Kwitter (1984)
							1.10	Esteban et al. (1992)
RCW 58	WR 40	1.07		0.74	0.50	0.79	0.77	Kwitter (1984)
LMC								
Anon	BAT99-2	0.42		0.29		0.09	0.20	Nazé et al. (2003)
Anon	BAT99-11	0.16	0.62	0.11		0.06		
Anon	BAT99-38	0.06		0.04		0.05		

a: In some cases different c(Hβ) were adopted for blue/red settings, see text.

b: Calculated using relations from Howarth (1983)

c: van der Hucht (2001) galactic; unknown LMC

d: Schlegel et al. (1998) Galactic; Burstein & Heiles (1982) LMC

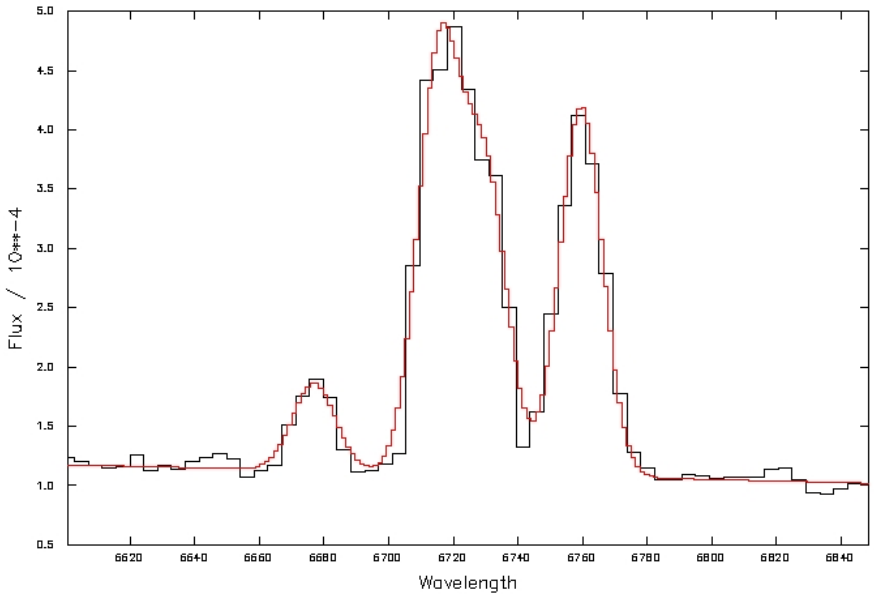

Figure 3.12: The blended [S II] 6717, 6731Å doublet in BAT99-38 along with a Dipso/ELF line fit (red). The lines to the left and right are HeI 6678Å and the second order contaminant [O II] 3727, 3729Å.

red edge of the detector.

A further complication to finding the correct intensities of the lines was the contamination of the red spectra by second order lines. The first order red spectral region (6000Å - 10000Å) is overlapped by the second order blue spectral region (3000Å - 5000Å), essentially the same wavelength coverage as the blue (Grism #14), except these lines are not correctly flux calibrated in the red spectra. Order blocking filters were available, but since they also removed the lines which we must use to derive nebular diagnostics and abundances from the 6000-7000Å region, they were not used.

This effect is most clear if we compare the spectrum of WR 40, in which the [O III] 4959, 5007 Å lines are missing, with the spectrum of BAT99-11 which has strong [O III] lines (See Figure 3.13). In the spectrum of BAT99-11 [O III] 4959, 5007 Å appear at 9550 Å and 9650 Å respectively. This causes a slight problem as the 9550 Å feature is blended with [S III] 9532 Å, which will be used as a temperature diagnostic. The deblended [S III] 9532 Å line strength falls below that expected given its intrinsic relationship with [S III] 9069 Å (i.e. I(9532 Å)/I(9069 Å) < 2.48[3]) which indicates that not only is the [S III] 9532 Å blended, it is also tellurically absorbed, as discussed by Liu et al. (1995).

These second order lines are present throughout the red spectral region, starting with [O

[3]Derived using atomic data published by Mendoza & Zeippen (1982a) and Mendoza (1983)

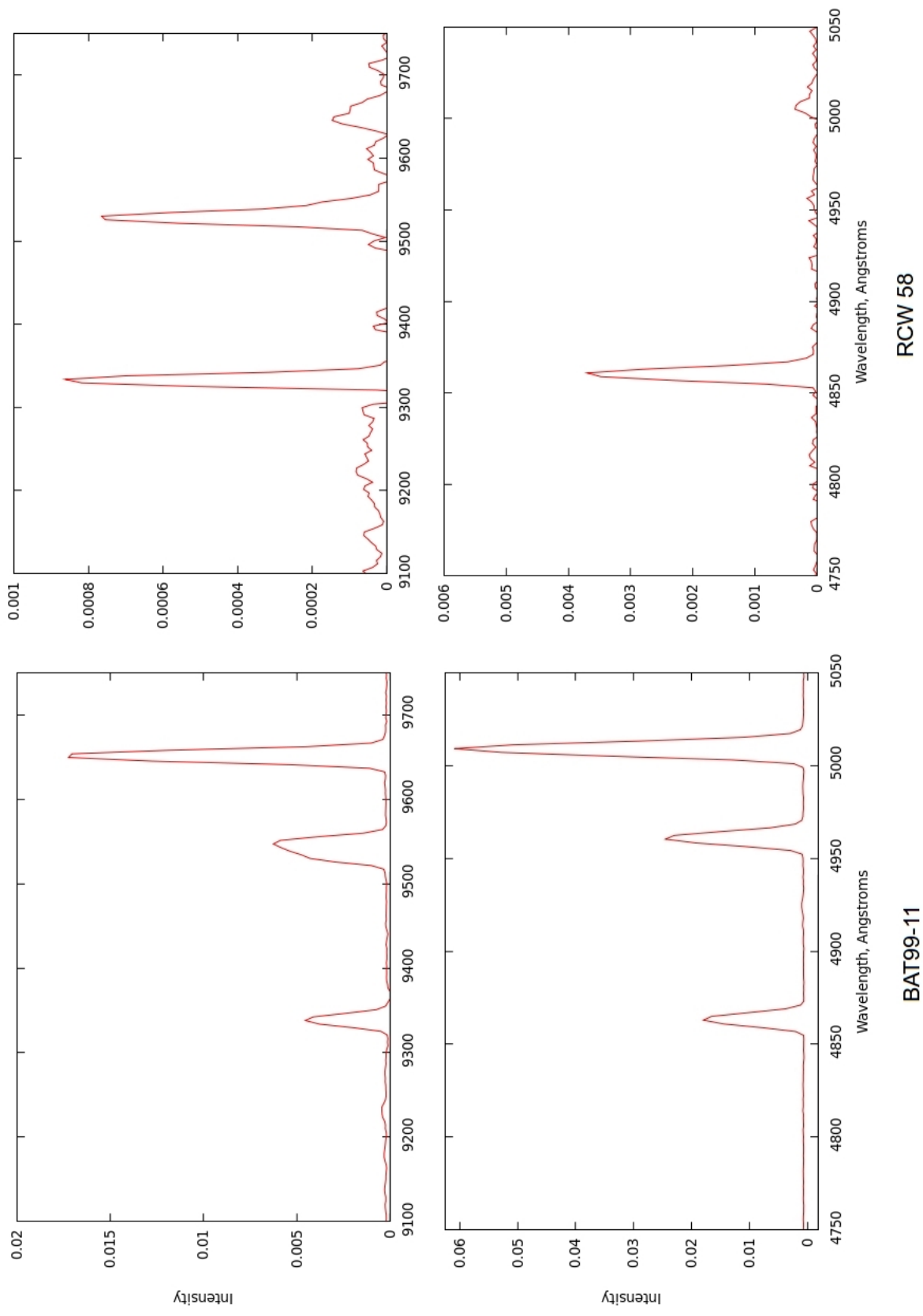

Figure 3.13: Intrusion of strong second order lines into the far-red region of the spectra of the nebula around BAT99-11 and RCW 58. The [O III] 4959 and 5007Å lines, along with Hβ, appear in both the blue and far-red spectral regions of the BAT99-11 nebular spectra, while only Hβ intrudes into the far-red RCW 58 spectra due to the faintness of the [O III] lines. [S III] 9532 Å appears prominently in the RCW 58 spectra while in the BAT99-11 nebular spectra it is blended with 2nd order [O III] 4959Å.

II] 3727 Å+3729 Å which appears slightly redward of the [S II] doublet at ∼6755Å, although at much reduced strength due to the lower efficiency of the CCD at this wavelength (∼3728Å). The second order lines do not occur at precisely twice their rest wavelengths, the second order 5007Å line occuring at 9650Å. We attribute this offset to the refractive index of the material used to make the grism, as the observed ratio of the wavelengths of second order lines to first order lines is itself a function of wavelength.

3.4.2 The UVES Spectra

As briefly mentioned in Section 3.3.2, the UVES instrument is very popular and as such has a variety of standard calibrations available. For service mode observations ESO provides the raw spectra along with reduced spectra and appropriate calibration files produced using their standard calibrations and the publicly available pipeline.

The reduced observations provided by ESO are intended for point source objects, however, and included a sky-subtraction step which was inappropriate for our observations. By default the UVES reduction pipeline assumes that two strips along the edges of the slit are free of the science target spectrum and treats them as sky pixels. The pipeline then averages between these sky pixels and subtracts this from the overall reduced spectrum. The nebulosity of NGC 3199 is very much larger than the $\sim$ 30" slit and as such no region of the slit represented a "sky" spectrum. The reduced spectra provided to us by ESO had strange line profiles due to this subtraction and were very much fainter than expected. The pipeline was therefore re-run with the sky subtraction phase excluded for all the UVES observations.

Cosmic ray subtraction was performed for the UVES observations by median combination of our four science frames for each setting. This then produced a final science frame for each setting. The flux calibration was checked by comparing line fluxes in the overlap regions between detectors, which were found to agree to slightly better than 10%.

The EFOSC2 problem of line blends was, of course, absent from the UVES observations and lines which are usually blended in lower resolution spectra are well resolved, e.g. [O II] 7319, 7320, 7330, 7331Å. In fact the higher resolution of the UVES instrument made the velocity structure of the nebula evident in the bright lines. The best resolution of this velocity structure is seen in the far red [S III] lines, due to their high atomic weight minimising thermal broadening effects (Figure 3.14). It was found that the best fit to this structure utilised four components, two of which comprised the majority of the emission while a further two are distinctly seen redward of the main emission.

The lines generated by lower mass ions are subject to a greater degree of thermal broadening, widening the redshifted components to the point where they are indistinguishable. As

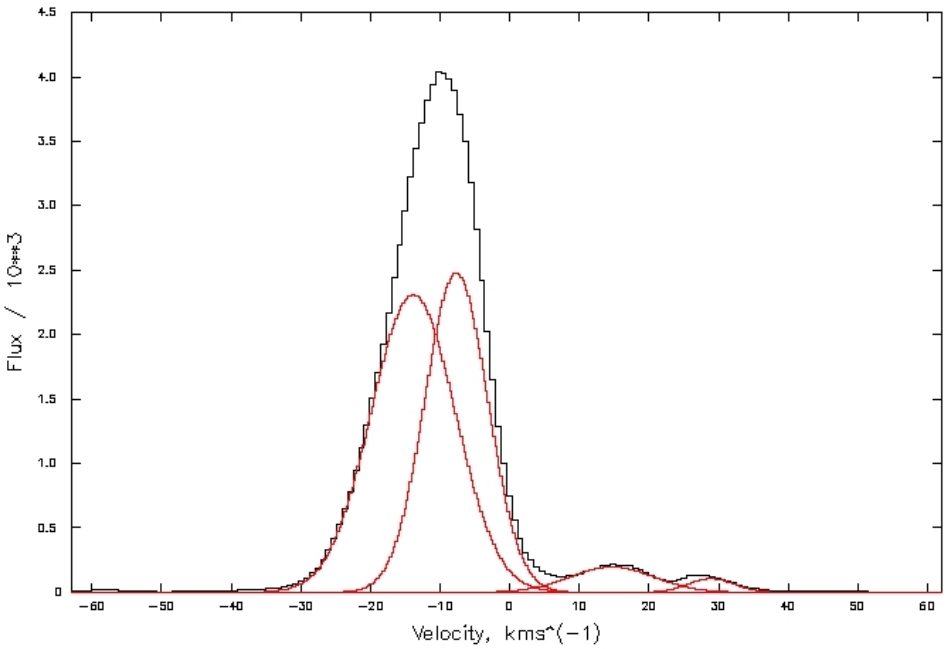

Figure 3.14: Velocity profile of [S III] 9531Å, observed profile in black, four component Dipso/Elf fit in red.

such it proved difficult to derive a separate reddening solution for the second component. In fact it proved difficult to fit the line profiles with a consistent number of velocity components. The adopted solution was to fit the brighter component with one gaussian, if it produced an accurate fit (the strongest lines: Hα, [N II], [O III] etc) and to use an extra component where it was required and subsequently to sum the components in the bright section.

Reddening was derived for the UVES NGC 3199 data in exactly the same way as described for the EFOSC2 dataset earlier. However there were no calibration errors apparent in the derivation, the derived c(Hβ) was constant regardless of the line combination chosen. The c(Hβ) that we derived, listed in Table 3.5 with those of the other nebulae, largely agreed with previous derivations by Kwitter (1984) and Esteban et al. (1992). The minor differences in reddening are likely due to the fact that each study has observed a different section of a large nebula.

3.5 Results

Observed and dereddened relative line intensity lists for each nebula can be found in Tables 3.6 – 3.12.

The [C I] 8727, 9824, 9850Å triplet was not detected in our NTT/EFOSC2 observations. However, in the VLT/UVES observations of NGC 3199 we did detect the [C I] triplet, giving

Table 3.6: EFOSC2 Line Detections - BAT99-2

Line	Ion	Observed	±	Dereddened	±
3727.0	[O II]	58.53	0.72	75.00	0.92
3868.7	[Ne III]	53.11	0.69	66.36	0.86
4101.7	Hδ	24.49	1.43	29.19	1.71
4340.5	Hγ	42.11	1.43	47.60	1.61
4363.2	[O III]	12.85	1.42	14.45	1.60
4471.5	He I	1.77	0.32	1.94	0.35
4685.7	He II	72.52	0.68	75.61	0.71
4711.4	[Ar IV]	13.21	0.63	13.69	0.65
4740.2	[Ar IV]	8.64	0.62	8.89	0.63
4861.3	Hβ	100.00	0.82	100.00	0.82
4958.9	[O III]	212.87	1.48	208.00	1.45
5006.8	[O III]	592.93	1.73	572.82	1.67
6312.1	[S III]	2.62	0.33	1.99	0.25
6562.8	Hα	394.99	1.64	289.88	1.20
6583.5	[N II]	6.55	1.42	4.79	1.04
6716.4	[S II]	18.95	1.66	13.62	1.19
6730.8	[S II]	11.29	1.67	8.10	1.20
7005.4	[Ar V]	3.43	1.30	2.37	0.90
7135.8	[Ar III]	11.16	1.39	7.61	0.95
9068.6	[S III]	16.10	0.77	9.14	0.43
9530.6	[S III]	22.26	1.33	12.25	0.73
4861.3	Hβ	1.359×10^{-18} erg cm^{-2} s^{-1} Å^{-1}			

Table 3.7: EFOSC2 Line Detections - BAT99-11

Line	Ion	Observed	±	Dereddened	±
3727.0	[O II]	260.95	0.97	286.59	1.06
3868.7	[Ne III]	4.21	0.80	4.58	0.87
4101.7	Hδ	23.23	0.80	24.82	0.85
4340.5	Hγ	46.15	0.79	48.33	0.83
4363.2	[O III]	2.76	0.79	2.88	0.82
4471.5	He I	4.73	0.78	4.90	0.81
4861.3	Hβ	100.00	0.81	100.00	0.81
4958.9	[O III]	140.47	0.83	139.25	0.82
5006.8	[O III]	352.67	0.96	348.10	0.95
6312.1	[S III]	3.06	1.38	2.04	0.92
6562.8	Hα	449.79	3.05	284.95	1.93
6583.5	[N II]	20.82	2.51	13.13	1.58
6678.2	He I	6.29	2.51	3.89	1.55
6716.4	[S II]	18.36	3.15	11.28	1.93
6730.8	[S II]	12.93	3.12	7.92	1.91
7135.8	[Ar III]	19.45	2.51	11.05	1.42
9068.6	[S III]	29.56	0.71	12.84	0.31
9530.6	[S III]	49.91	0.88	20.69	0.36
4861.3	Hβ	1.460×10^{-17} erg cm^{-2} s^{-1} Å^{-1}			

Table 3.8: EFOSC2 Line Detections - BAT99-38

Line	Ion	Observed	±	Dereddened	±
3727.0	[O II]	168.10	8.94	174.01	9.26
3868.7	[Ne III]	9.58	6.91	9.89	7.13
4101.7	Hδ	24.51	0.70	25.12	0.72
4340.5	Hγ	43.66	0.69	44.41	0.71
4471.5	He I	3.82	0.70	3.87	0.70
4861.3	Hβ	100.00	1.13	100.00	1.13
4958.9	[O III]	76.92	0.74	76.67	0.74
5006.8	[O III]	178.59	0.85	177.73	0.85
6312.1	[S III]	0.71	0.27	0.69	0.26
6562.8	Hα	290.15	2.07	277.89	1.98
6583.5	[N II]	13.80	1.69	13.22	1.62
6678.2	He I	3.44	1.71	3.29	1.63
6716.4	[S II]	15.83	2.12	15.11	2.03
6730.8	[S II]	11.66	2.12	11.13	2.02
7135.8	[Ar III]	9.72	1.67	9.21	1.58
9068.6	[S III]	10.98	0.77	10.15	0.71
9530.6	[S III]	5.03	1.15	4.62	1.06
4861.3	Hβ	3.536×10^{-18} erg cm^{-2} s^{-1} Å^{-1}			

Table 3.9: EFOSC2 Line Detections - WR 8

Line	Ion	Observed	±	Dereddened	±
3727.0	[O II]	60.72	6.98	62.05	7.13
4101.7	Hδ	23.93	4.04	24.30	4.11
4340.5	Hγ	48.52	4.03	49.05	4.07
4861.3	Hβ	100.00	4.20	100.00	4.20
4958.9	[O III]	109.15	4.27	108.93	4.26
5006.8	[O III]	226.13	4.84	225.45	4.82
6548.1	[N II]	108.59	7.83	30.40	2.19
6562.8	Hα	1026.07	9.40	284.87	2.61
6583.5	[N II]	438.50	4.91	120.32	1.34
6678.2	He I	43.01	4.69	11.19	1.22
6716.4	[S II]	16.99	6.30	4.32	1.60
6730.8	[S II]	11.27	6.13	2.84	1.55
7135.8	[Ar III]	47.69	4.63	9.76	0.94
9068.6	[S III]	65.30	6.31	6.28	0.60
9530.6	[S III]	84.69	9.40	7.14	0.79
4861.3	Hβ	2.992×10^{-19} erg cm^{-2} s^{-1} Å^{-1}			

Table 3.10: EFOSC2 Line Detections - WR 16

Line	Ion	Observed	±	Dereddened	±
4101.7	Hδ	22.63	2.12	34.28	3.22
4340.5	Hγ	28.86	2.12	38.56	2.84
4861.3	Hβ	100.00	2.52	100.00	2.52
4958.9	[O III]	7.17	2.18	6.79	2.06
5006.8	[O III]	7.67	2.12	7.07	1.95
6548.1	[N II]	288.38	14.40	48.57	2.42
6562.8	Hα	1711.12	16.04	284.82	2.67
6583.5	[N II]	1140.75	12.77	186.78	2.09
6678.2	He I	55.69	12.10	8.46	1.84
7135.8	[Ar III]	43.66	10.92	4.74	1.18
4861.3	Hβ	2.473×10^{-19} erg cm^{-2} s^{-1} Å^{-1}			

Table 3.11: UVES Line Detections - NGC 3199

Line	Ion	Observed	±	Dereddened	±
3726.0	[O II]	87.62	0.43	175.51	0.86
3728.8	[O II]	107.42	0.52	214.88	1.05
3868.7	[Ne III]	36.24	0.22	67.62	0.41
3967.5	[Ne III]	11.16	0.19	19.72	0.34
4101.7	Hδ	15.11	0.22	24.70	0.36
4340.5	Hγ	32.91	0.25	46.38	0.35
4363.2	[O III]	2.45	0.08	3.41	0.11
4471.5	He I	3.37	0.13	4.37	0.17
4861.3	Hβ	100.00	0.24	100.00	0.24
4958.9	[O III]	218.60	0.81	204.88	0.76
5006.8	[O III]	680.69	2.26	618.02	2.05
5517.7	[Cl III]	1.85	0.14	1.22	0.09
5537.6	[Cl III]	1.40	0.08	0.91	0.05
5577.3	[O I]	0.25*	0.22	0.16	0.14
5875.7	He I	21.93	0.14	12.27	0.08
6300.3	[O I]	17.17	0.39	8.01	0.18
6312.1	[S III]	5.92	0.07	2.75	0.03
6363.8	[O I]	5.78	0.14	2.62	0.06
6548.1	[N II]	91.97	0.40	38.90	0.17
6562.8	Hα	675.20	1.33	283.96	0.56
6583.5	[N II]	287.83	1.16	120.09	0.48
6678.2	He I	8.79	0.11	3.54	0.04
6716.4	[S II]	118.35	0.88	46.96	0.35
6730.8	[S II]	96.39	0.65	38.04	0.26
7135.8	[Ar III]	61.93	0.37	21.19	0.12
7318.9	[O II]	11.40	0.09	3.67	0.02
7320.0	[O II]	11.40	0.09	3.67	0.02
7329.7	[O II]	6.15	0.08	1.97	0.02
7330.7	[O II]	6.15	0.08	1.97	0.02
8727.1	[C I]	1.11	0.06	0.24	0.01
9068.6	[S III]	480.20	5.56	98.72	1.14
9530.6	[S III]	1416.72	14.39	266.44	2.70
9824.1	[C I]	3.44	0.20	0.61	0.03
9850.2	[C I]	8.94	0.13	1.59	0.02
4861.3	Hβ	3.536×10^{-14} erg cm^{-2} s^{-1} Å^{-1}			

* upper limit

Table 3.12: EFOSC2 Line Detections - RCW 58 (WR 40)

Line	Ion	Observed	±	Dereddened	±
3727.0	[O II]	22.43	6.32	42.23	11.91
4101.7	Hδ	17.36	0.86	27.17	1.35
4340.5	Hγ	35.20	0.87	48.12	1.19
4471.5	He I	6.00	0.85	7.60	1.08
4861.3	Hβ	100.00	1.03	100.00	1.03
5006.8	[O III]	8.82	0.86	8.08	0.79
6548.1	[N II]	144.02	5.77	65.73	2.63
6562.8	Hα	631.23	6.23	286.59	2.83
6583.5	[N II]	543.30	5.04	244.89	2.27
6678.2	He I	17.91	4.67	7.81	2.03
6716.4	[S II]	13.82	5.51	5.95	2.37
6730.8	[S II]	9.92	5.47	4.25	2.34
7135.8	[Ar III]	13.58	4.75	5.11	1.78
9068.6	[S III]	19.45	1.71	4.60	0.40
9530.6	[S III]	41.63	2.56	9.07	0.55
4861.3	Hβ	3.048×10^{-18} erg cm^{-2} s^{-1} Å^{-1}			

an example of what their expected intensity might be. The ratio of the dereddened intensities of [C I] 9850Å to [S III] 9531Å in NGC 3199 is 0.006. If we apply this ratio to the NTT/EFOSC2 observations we find expected line fluxes of less than half the faintest detected line. We conclude from this that the [C I] triplet is not strong enough in any of the NTT/EFOSC2 observed sample to be detected with the NTT/EFOSC2 in the configuration which we utilised, or indeed with any of the available grisms for EFOSC2.

The detection of [C I] 8727, 9824, 9850Å in NGC 3199 is largely due to the high resolution of the UVES instrument. The enhanced resolution did not yield the detection of any recombination lines (other than those of hydrogen and helium). The brightest recombination line (C II 4267Å) was not detected despite experimenting with spectral binning of the high resolution observations to attempt to increase the S/N. The relatively high reddening of NGC 3199 (E(B-V) = 0.81), does not help.

3.6 Analysis

3.6.1 Plasma Diagnostics

In total, four different density diagnostic line doublets were employed during the analysis. The [S II] doublet was present in most cases, however the [O II], [Ar IV] and [Cl III] doublets were

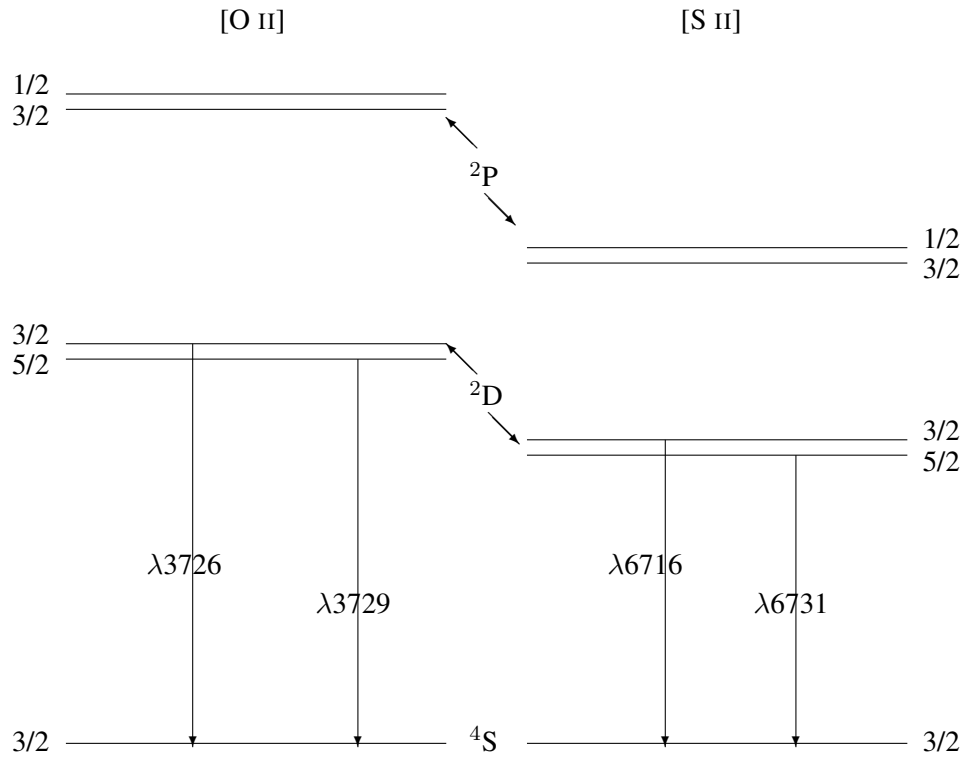

Figure 3.15: Energy-level diagrams for the $2p^3$ ground configuration of [O II] and the $3p^3$ ground configuration of [S II]

also used when the instrumental resolution and nebular ionisation permitted.

An energy level diagram for [O II] and [S II] is shown in Figure 3.15. These two ions share structural properties which allows their use as density diagnostics. A sketch of the density sensitive properties of these ions runs as follows[4]: In the limit of very low electron density, the ratio between the two excited lines of [O II] or [S II] (^{2}D 3/2, 5/2) is given simply by the ratio of their emission coefficients as each collisional excitiation is followed by the emission of a photon. In the high density regime however, the lines will be in the ratio of their statistical weights as the effects of collisional excitiation and de-excitation dominate - such that the relative populations reflect the Boltzmann populations ratio. The transition between these two regimes allows the use of such lines to quantify the importance of collisional de-excitation and hence the density. The [O II] and [S II] doublets are usually employed for this purpose as the lines are very close in energy, which suppresses the temperature sensitivity of the intensity ratio.

All but one of the nebulae (WR 16) displayed the [S II] doublet at 6716 Å,6731 Å, which allowed calculation of their electron densities. Possible reasons for the absence of these lines

[4]see Osterbrock & Ferland (2006, Chapter 5) for a complete description and mathematical derivation of the density sensitive properties.

in the nebula around WR 16 are discussed in Section 3.7. In each case where the [S II] doublet was detected, its ratio indicated electron densities near the low density limit ($1 < n_e <\sim 300$ cm^{-3}). In cases where the [S II] doublet ratio indicated a density less than 50 cm^{-3}, a density of 50 cm^{-3} was adopted. As discussed in Section 3.4, the NTT/EFOSC detections of the [S II] doublet are blended. This results in a high uncertainty on both the line measurements and subsequently the ratio of the two lines. In contrast the ratio of the [S II] lines detected in NGC 3199 with UVES carries a much lower uncertainty as both lines were well resolved.

The higher excitation nebulosity around BAT99-2 displayed the [Ar IV] 4711Å, 4740Å doublet. It yielded a density consistent with the [S II] density, i.e. the low density limit.

The increased resolution and wavelength coverage of the UVES instrument allowed the use of the other two line pairs mentioned, [O II] and [Cl III]. The densities yielded were consistent with each other and with the [S II] density (see Table 3.14). The [O II] density in particular agrees very well with the [S II] density and carries a low uncertainty. The [Cl III] lines are comparatively weak, so the ratio ${}^{\delta I(\lambda)}/_{I(\lambda)}$ is much higher. This results in a less well constrained diagnostic, albeit one that peaks in roughly the same place as the [O II] and [S II] densities.

Since the derived electron densities were all below the critical densities of the abundance diagnostic lines, the uncertainties associated with the electron densities will have no effect on the abundance uncertainties we will derive.

In general, the electron temperature diagnostics are more important to the final abundance determinations due to the emissivity of collisionally excited lines being dependent on a Boltzmann factor of $e^{-\frac{E}{kT_e}}$ where E is the excitation energy above the ground state of the upper level of the transition. With this in mind then, it was of importance to exploit all the available temperature diagnostics. The NTT/EFOSC observations were designed to access the [O III] 5007, 4959, 4363 Å triplet in the blue and the [S III] 9532, 9069, 6312 Å triplet in the red. These diagnostics are strongly dependent upon the very weak, temperature sensitive, [O III] 4363 Å and [S III] 6312 Å lines. These lines were detected in some cases, typically where high temperatures might be expected (BAT99-2 for example). The [S III] 6312 Å line detections, in particular, should be treated as upper limits as they were typically blended with [O I] 6300.

The VLT/UVES observations yielded a richer set of temperature diagnostics. In addition to those outlined, which should be regarded as the *primary* temperature diagnostics that we can derive from the detected lines, temperature diagnostics involving [O I], [O II] and [C I] were also detected. The UVES instrument, in the dichroic configuration we utilized, has an unfortunate wavelength coverage gap between the red and blue arms of the spectrograph in the region of [N II] 5755 Å which precluded the use of the [N II] 6584, 6548, 5755 Å triplet as a

Table 3.13: Nebular Diagnostics - NTT/EFOSC Observations

Nebula	[S II] $\frac{6716Å}{6731Å}$	n_e([S II]) cm^{-3}	[Ar IV] $\frac{4711Å}{4740Å}$	n_e([Ar IV]) cm^{-3}	[S III] $\frac{9069Å+9531Å}{6312Å}$ [1]	T_e([S III]) K	[O III] $\frac{5007Å+4959Å}{4363Å}$ [2]	T_e([O III]) K
Galactic								
WR 8		1[a]						
WR 16								
RCW 58		22						
LMC								
BAT99-2	1.66 ± 0.29	1[a]	0.65 ± 0.06	1[a]	15 ± 3	20000[b]	56 ± 10	16300 ± 1000
BAT99-11	1.41 ± 0.43	1^{+440}_{-0}			17^{+16}_{-4}	20000[b]	150^{+90}_{-20}	10400 ± 1000
BAT99-38	1.35 ± 0.31	78^{+380}_{-77}			41^{+32}_{-8}	11200 ± 2200		

[1]: [S III] 9531Å was tellurically absorbed, its intensity was calculated using the ratio I(9531Å)/I(9069Å) = 2.48

[2]: [O III] 5007Å was observed but poorly calibrated, its intensity was calculated using the ratio I(5007Å)/I(4959Å) = 2.98

[a]: Low density limit.

[b]: High temperature limit.

temperature diagnostic.

The [O I] triplet diagnostic (5577Å, 6300Å and 6363Å) is only available as an upper limit since the temperature sensitive component ([O I] 5577Å) was not detected from the nebula.

The [O II] temperature diagnostic (7319Å + 7320Å + 7330Å + 7331Å versus 3726Å + 3729Å) was calculated but was ultimately disregarded for two reasons. Firstly, the uncertainty on the diagnostic ratio is rather high due to the weakness of the [O II] lines at around 7325Å; secondly, this ratio has proven vulnerable to several further systematic uncertainties due to the large wavelength separation between the lines and the possibility of a significant recombination line contribution to the 7320+7330 Å lines (e.g. Liu et al. 2000).

The [C I] triplet ratio derived for NGC 3199 (8.9$\pm$0.5) implies that the [C I] lines are predominantly generated by recombination rather than by collisional excitation. Figure 2 of Liu et al. (1995), reproduced here as Figure 3.16, shows the sensitivity to electron temperature and density of collisionally excited [C I] 9850Å + 9824Å/ 8727Å(dotted lines). For Case B recombination (indicated by ratios of 8-9) the temperature dependence is very weak (solid lines) (Escalante & Victor, 1990). It should be noted though that the 9824Å and 9850Å lines are emitted in a fixed ratio (2.96), we observe these lines to have a ratio of 2.6 – suggesting that the uncertainty on the [C I] triplet ratio is higher than that quoted. From Figure 3.16 we can see that at T=12,000K the difference between the ratios expected of Case B recombination and collisional excitation (using the lowest density track) is of the order 5-10. Using the quoted line ratio we can find the [C I] triplet ratio using either 9850Åor 9824Å, the maximum ratio occuring when we use only the 9824Å line – this gives a ratio of around 10.

When the [C I] triplet is observed as recombination lines it is usually though to be emanating from a photo-dissociation region (PDR) surrounding the ionized regions. Escalante et al. (1991) showed that these lines can emanate from PDRs next to high density molecular material, which has been detected in the vicinity of NGC 3199 (Marston, 2001).

For each nebula, diagnostic uncertainties were computed via a novel Monte-Carlo technique. The "NEAT" (Nebular Empirical Analysis Tool) software, developed at UCL, allows an exploration of the parameter space defined by the uncertainties associated with nebular line measurements. A full description of this code and its capabilities will be forthcoming (Wesson et al., 2011, in prep). Briefly, NEAT reads in a list of measured spectral lines (their wavelengths, relative intensities and uncertainties), and generates a "possible" line list by randomly[5] offsetting the line intensities using the quoted uncertainties as limits. It then performs a full

[5]The random numbers in this case are drawn from a gaussian distribution with mean zero and standard deviation one.

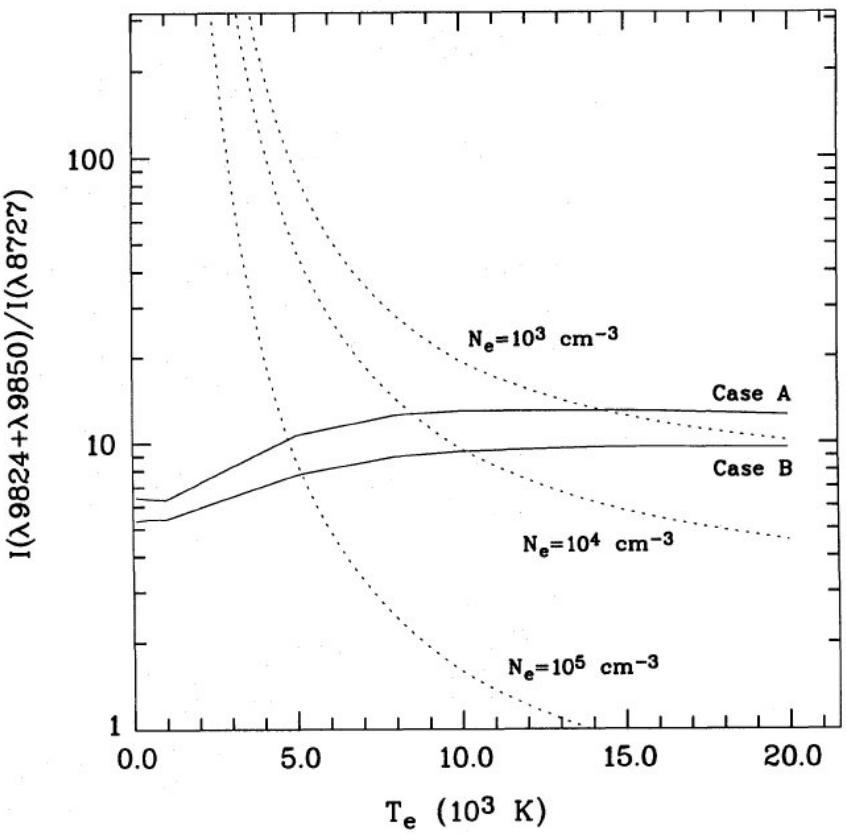

Figure 3.16: The temperature sensitivity of the [C I] 9850Å+ 9824Å/ 8727Å ratio, in cases where the lines are generated from recombination, (solid lines labelled for Case A & B recombination respectively, Escalante & Victor 1990) and for cases where the lines are collisionally excited (dotted lines plotted for various electron densities). Reproduced from Liu et al. (1995).

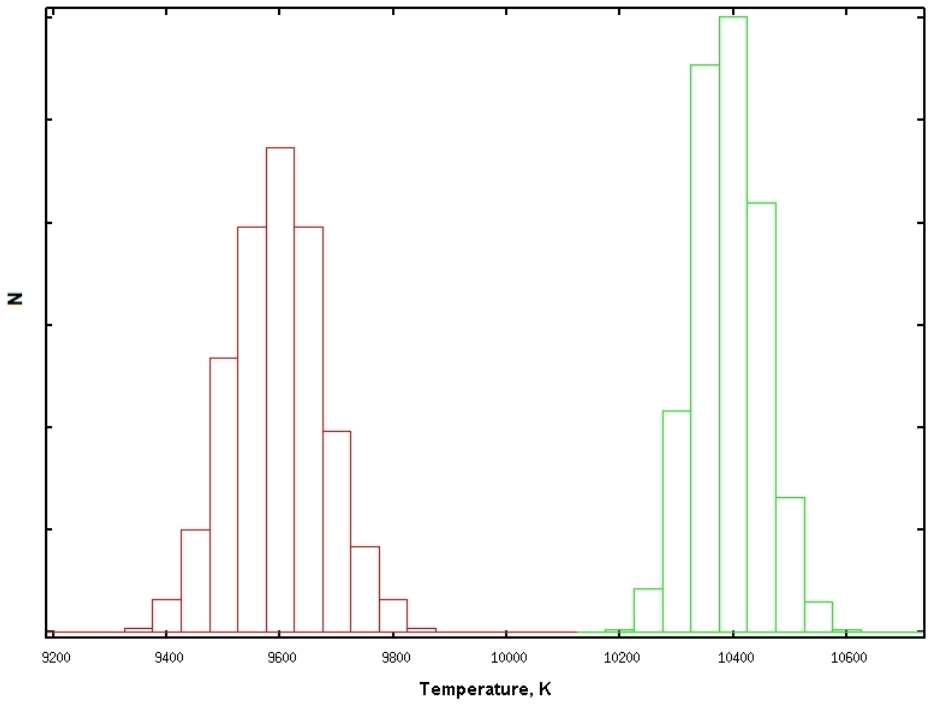

Figure 3.17: NEAT uncertainty distributions generated for [O III] (red) and [O II] (green) temperature diagnostics for NGC 3199 after 10,000 iterations. The Y axis in this plot represents the number of iterations which fell into each bin, for a temperature in the appropriate range.

empirical analysis on this "possible" line list, calculating all diagnostic ratios and plasma parameters, along with a full abundance analysis using a three-zone ionization model by default. It will repeat this process as many times as the user requires, building up a picture of the uncertainties associated with each diagnostic, abundance, etc as the number of data points increases. We then bin these values to obtain an uncertainty distribution. An example of the distributions generated by NEAT using ten thousand iterations is shown in Figure 3.17. NEAT was used to generate all of the values and uncertainties in Table 3.14, along with the abundance derivations described later.

3.6.1.1 Line Broadening Temperatures

The observed width of a spectral line depends upon several factors, primarily the nebular temperature, turbulence and expansion along with the instrumental line profile. Thus if we can measure the widths of several lines from ions of different atomic weight to sufficient accuracy, it is possible to derive the temperature of the line-emitting plasma. Historically this process has usually been performed using only a single pair of lines, [N II] 6584Å and Hα, due to both their proximity and strengths (e.g. Dopita 1972). The velocity profiles of [N II] 6584Å and Hα in our UVES observations are shown in Figure 3.18. Given the resolution of the VLT/UVES ob-

Table 3.14: NGC 3199 Nebular Diagnostics

Ion	Diagnostic	Ratio	Electron Density or Temperature
[S II]	$\frac{6716Å}{6731Å}$	1.23 ± 0.01	220 ± 20 cm^{-3}
[O II]	$\frac{3729Å}{3726Å}$	1.22 ± 0.01	230 ± 20 cm^{-3}
[Cl III]	$\frac{5717Å}{5737Å}$	$0.744^{+0.069}_{-0.058}$	500 ± 330 cm^{-3}
[S III]	$\frac{9069Å+9531Å}{6312Å}$	133 ± 2	7650 ± 50 K
[O III]	$\frac{5007Å+4959Å}{4363Å}$	241 ± 7	9600 ± 100 K
[O II]	$\frac{7319Å+7320Å+7330Å+7331Å}{3726Å+3729Å}$	34.5 ± 0.50	12200 ± 100 K
[O I]	$\frac{6300Å+6364Å}{5577Å}$	$51.5\ ^{+70}_{-20}$	12250* K
[S II]	$\frac{4076Å+4068Å}{6717Å+6731Å}$	13.90 ± 0.50	9000 ± 1000 K
[C I]	$\frac{9850Å+9824Å}{8727Å}$	8.90 ± 0.50	

* upper limit

servations it is possible to accurately determine the widths of a large number of strong emission lines (including the traditional pair) and to derive temperatures from more than one pair.

The major obstacle which must be overcome to perform this process is a detailed description of the intrinsic line shapes. For collisionally excited lines this is relatively simple: most have negligible intrinsic fine structure broadening and all broadening in excess of the instrumental broadening must be a combination of thermal and turbulent broadening. The situation is rather different for recombination lines, which are often comprised of several very closely spaced fine-structure components. The first work done to describe the fine structure components of the Hα line in this context found that the "natural" profile of the line could have a significant effect on the derived electron temperature (Dyson & Meaburn, 1971). In our analysis we shall use the fine structure correction term provided by Clegg et al. (1999) [Equation 9] for Hα, which follows the same form as those derived from earlier formulations while introducing a correction factor δ which combines with the Hα FWHM in quadrature :

$$T_e = \frac{FWHM(H\alpha)^2 - \delta^2 - FWHM([\text{N II}])^2}{8kln2[\frac{1}{m_H} - \frac{1}{m_N}]} \tag{3.1}$$

where T_e is the electron temperature, FWHM(Hα) and FWHM(N II) are the FWHMs of Hα and [N II], m_H and m_N are the atomic weights of hydrogen and nitrogen respectively and k is the Boltzmann constant. An explicit equation for calculating δ is not quoted, but a table of values suitable for interpolation was included by Clegg et al. (1999).

We can generalise Equation 3.1 to apply it to other species, replacing $FWHM([\text{N II}])$

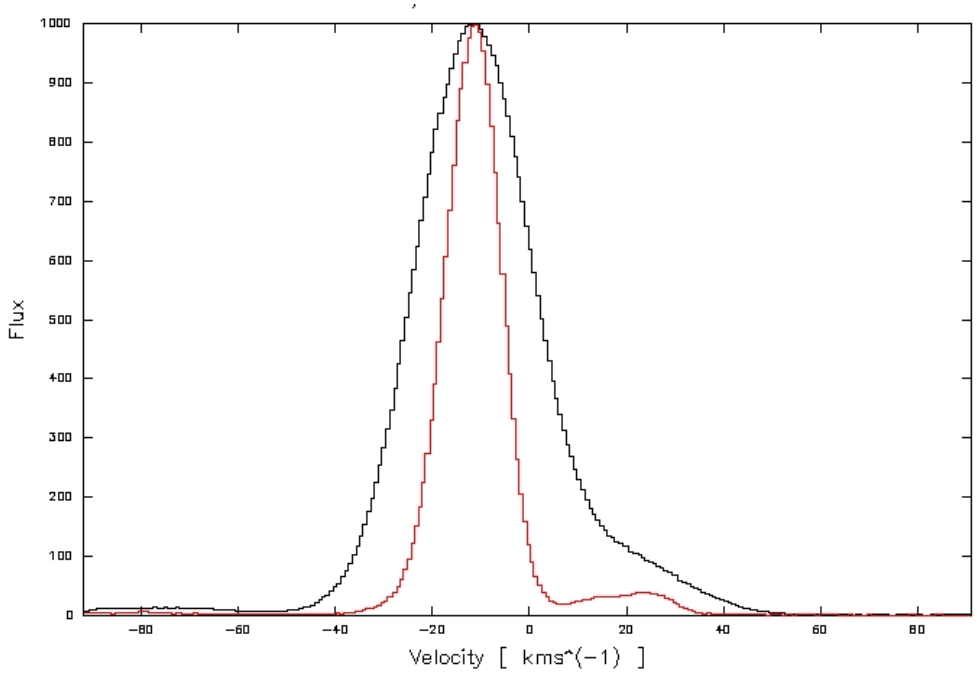

Figure 3.18: Observed velocity profiles of Hα (black) and [N II] 6584Å (red) in NGC 3199. The Hα line is broadened by fine structure components along with the thermal and turbulent broadening that also affect [N II]. (Flux coordinate has been normalised to allow better comparison.)

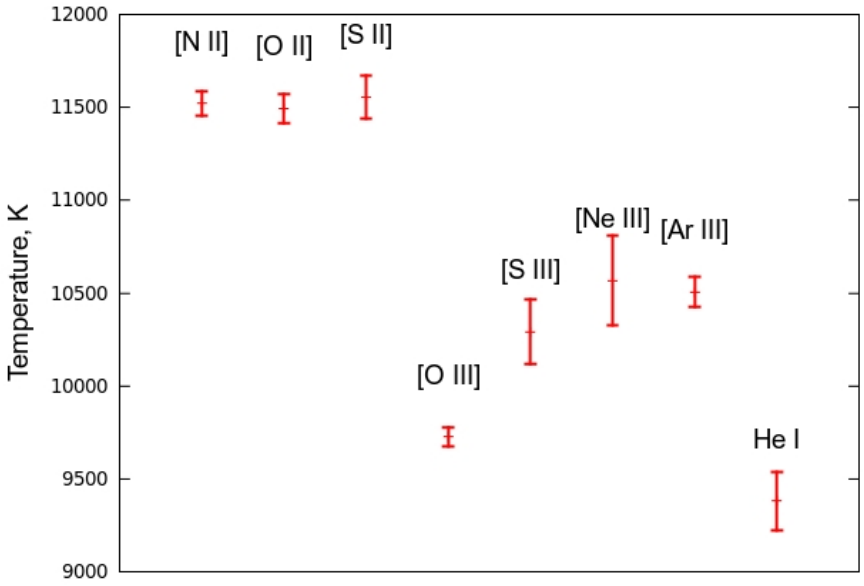

Figure 3.19: Temperatures derived by comparing line widths of CELs with the Hα line width.

and m_N with values appropriate for the line and species we wish to use (e.g. Equation 3.2).

$$T_e = \frac{FWHM(H\alpha)^2 - \delta^2 - FWHM([\mathrm{X}])^2}{8kln2[\frac{1}{m_H} - \frac{1}{m_X}]} \tag{3.2}$$

The results of using this method for the strongest collisionally excited lines with Hα appear in Table 3.15 and are presented graphically in Figure 3.19. Singlet He I lines can be included as they have no fine structure components. The only singlet He I line found with sufficient strength to measure its width accurately was He I 6678.2 Å. In cases where an electron temperature has also been calculated from strong line methods we can compare the two temperatures (Figure 3.21).

In Figure 3.20, we show the line broadening temperature versus the ionization potential for each species. We see the same general trend that is evident from Figure 3.19 in that the species with higher ionisation potentials generally have lower temperatures by at least 1000K. This trend can be attributed to an effect known as "radiation hardening" (see Tielens, 2005, Section 7.3.2). The ionization cross section of HI is proportional to ν^{-3}, meaning that the lowest energy photons are absorbed by the inner regions of the nebula. Hence as radius increases the average energy of the escaping photons also increases while the number of photons decreases. When the hardened radiation field encounters the outer regions of the nebula the extra energy is deposited as kinetic energy – increasing the nebular temperature.

Table 3.15: Temperature determinations from line broadening

Species	Line (Å)	FWHM (km s^{-1})	T_e	$\pm$
HI	6562.80	27.113 $\pm$ 0.045	–	–
[N II]	6548.10	13.411 $\pm$ 0.055	11580	72
[N II]	6583.50	13.505 $\pm$ 0.050	11520	66
[O II]	3726.03	13.250 $\pm$ 0.062	11570	81
[O II]	3728.82	13.373 $\pm$ 0.062	11490	80
[S II]	6716.44	12.629 $\pm$ 0.087	11560	120
[S II]	6730.82	12.597 $\pm$ 0.080	11570	110
[O III]	4958.91	15.975 $\pm$ 0.054	9730	52
[O III]	5006.84	15.840 $\pm$ 0.047	9820	47
[S III]	9068.90	14.250 $\pm$ 0.142	10570	151
[S III]	9531.00	14.695 $\pm$ 0.175	10290	175
[Ne III]	3869.06	15.036 $\pm$ 0.086	10260	86
[Ne III]	3967.79	14.578 $\pm$ 0.234	10570	241
[Ar III]	7135.90	14.267 $\pm$ 0.075	10510	82
He I	6678.15	18.739 $\pm$ 0.219	9380	157

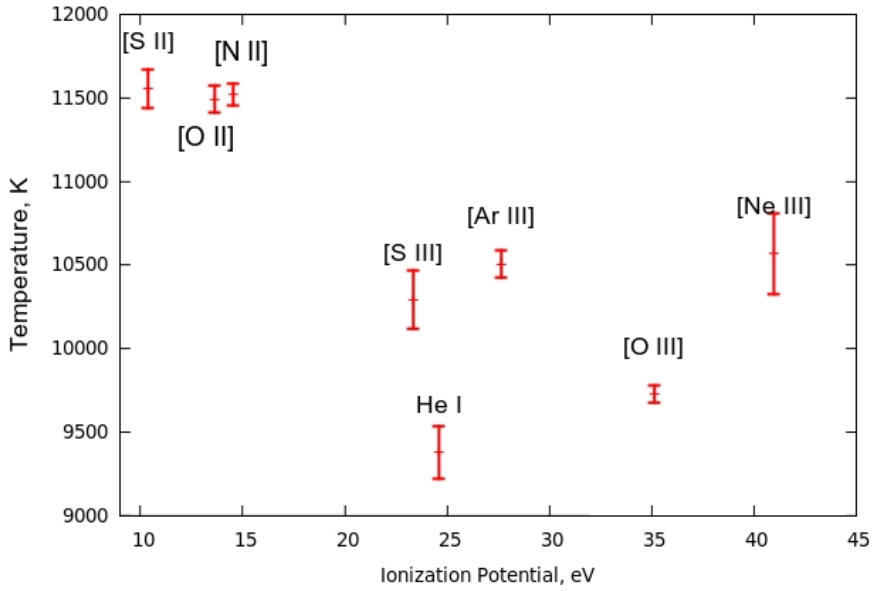

Figure 3.20: Line broadening temperatures for various ions relative to Hα, versus the ionization potential to obtain the parent ion.

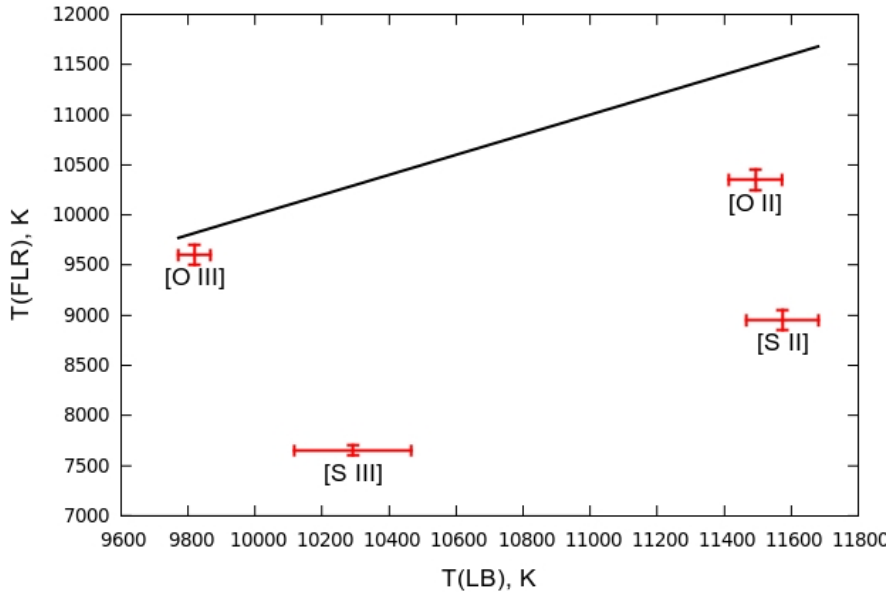

Figure 3.21: Comparison of line broadening temperatures T(LB) (x axis) with forbidden line ratio temperatures T(FLR) (y axis). The black solid line corresponds to T(LB) = T(FLR).

3.6.2 Nebular Abundances

The NEAT code, mentioned earlier, uses the same statistical equilibrium methods as the earlier EQUIB code (also developed at UCL) to derive abundances for CELs. That is, we solve the equation:

$$\frac{N(ion)}{N(H^+)} \times A = \frac{I(line)}{I(H\beta)} \tag{3.3}$$

Where A is related to the emissivities of the two ions, with the following basic relationship:

$$A \propto \frac{\epsilon(line)}{\epsilon(H\beta)} \propto \frac{n(ion)n_e e^{-\frac{E}{kT_e}}}{N(H^+)n_e T_e^{-0.9}} \tag{3.4}$$

The A value for the specific ion at given n_e and T_e is calculated and then used to provide $\frac{N(ion)}{N(H^+)}$, the linear abundance of the specific ion as indicated by the particular line chosen. NEAT derives uncertainties on the abundance determinations in the same manner as described for the temperature and density diagnostics. The provenance of the atomic data used is shown in Table 3.16.

In the simplest cases, only one of each type of diagnostic was available per nebula e.g. BAT99-38, where T([S III]) and n_e([S II]) were available. This led to a very simple abundance determination where the same temperature and density was used for every ion. This was the situation for each of the LMC WR nebulae.

For NGC 3199, multiple density and temperature diagnostics were calculated. Each density diagnostic was found to place the nebula in the diagnostic's low density limit. The forbidden

Table 3.16: Sources of Atomic data

Ion	Reference
C^0	Pequignot & Aldrovandi (1976), Johnson et al. (1987), Nussbaumer & Rusca (1979)
Cl^{++}	Mendoza & Zeippen (1982b), Butler & Zeippen (1989),
O^+	Berrington & Burke (1981), Berrington (1988), Baluja & Zeippen (1988)
O^{++}	Pradhan (1976), Zeippen (1982)
S^{++}	Mendoza & Zeippen (1982a), Mendoza (1983)
All others	Landi et al. (2006)

line ratio temperature diagnostics indicated that a multi-zone ionisation model may be appropriate, in that lower ionisation species (e.g. [O II] and [S II]) gave higher temperatures than those from moderate ionisation species (e.g. [O III] and [S III]). This trend was corroborated by the line broadening temperature measurements (see Figure 3.20). Ultimately it was decided to use a two zone model where we used the average of the [O II] and [S II] forbidden line ratio temperatures for the low ionisation species, the [S III] temperature for [S III], and the [O III] temperature for all other ions.

The results of the abundance calculations for the LMC WR nebulae and NGC 3199 are listed for individual ions in Table 3.17 and total abundances are listed in Table 3.18 with ICFs (Ionisation Correction Factors) from Kingsburgh & Barlow (1994).

The remaining nebulae in our NTT/EFOSC2 Galactic sample have no observed temperature diagnostic. As discussed earlier in this Section, the abundances from CELs are proportional to a factor of $e^{-\frac{E}{kT_e}}$ and as such are very sensitive to the adopted electron temperature.

Previous authors have adopted temperatures for some of these objects based on matching the oxygen abundance to those of H II regions in the same galaxy. However I do not think this approach is appropriate in this situation, as the oxygen abundance could easily be depleted relative to the galactic H II regions due to CNO cycling by the massive star prior to it becoming a WR star. A sensible solution might be to assume a nebular temperature that yields Galactic H II region neon abundances, as neon should not have been astrated by stellar processing. Unfortunately the higher reddening in the galactic plane meant that we had no detections of [Ne III] 3868, 3967Å for RCW 58 or the nebulae around WR 8 and WR 16, and hence no neon abundance for these objects.

However we can infer that the abundance pattern in these nebulae is not the same as in H II regions, or indeed in the other WR nebulae in our sample, by simple inspection of the line lists. WR 16 and RCW 58 in particular display [N II] lines comparable in intensity to Hα, indicating likely nitrogen enhancement.

In the absence of a temperature diagnostic for these nebulae, we employed a different approach to finding one important diagnostic - log(N/O). We know, from our observations and from previous authors, that WR nebulae are likely to possess electron temperatures in the range 8000-12000K.

The EQUIB code, as mentioned previously, can be used to generate the appropriate line emissivities ϵ across this range. We can then plot log(N^+/O^+) as a function of electron temperature T_e as:

$$log\frac{N^+}{O^+}(T_e) = \frac{\text{I([N II] 6548Å)}/\epsilon_{\text{[N II] 6548Å}}(T_e)}{\text{I([O II] 3727 + 3729Å)}/(\epsilon_{\text{[O II] 3727Å}}(T_e) + \epsilon_{\text{[O II] 3729Å}}(T_e))} \tag{3.5}$$

Where I(line) is the line intensity relative to Hβ = 100 and $\epsilon(T_e)$ is the lime emissivity at temperature T_e. This $^{N+}/_{O+}$ relationship is shown in Figure 3.22 for RCW 58 and the nebula around WR 8. As expected, the ratio is not a strong function of temperature and therefore provides a reasonable constraint upon the value of $log\frac{N^+}{O^+}$ and hence the degree of enrichment within each nebula.

As mentioned in this Section, we used the icf scheme of (Kingsburgh & Barlow, 1994) which specifies identical icfs for N^+ and O^+. This means that the N^+/O^+ ratio that we calculate should be the same as the overall N/O ratio. The range of N/O ratios derived for RCW 58 and for the nebula around WR 8 will be discussed in Section 3.7.

3.7 Discussion of Individual Objects

BAT99-2

The EFOSC2 optical spectrum of the nebula around BAT99-2 (WN2) is in good agreement with that presented by Nazé et al. (2003). The nebula is highly ionized which manifests itself as the presence of [Ar IV] lines along with HeII 4686 Å, which was only detected in BAT99-2.

The nebula around BAT99-2 does not display any significant overabundances relative to LMC H II regions (see Table 3.18). There is a hint of an N/O overabundance but the uncertainties are consistent with normal H II region values. In general the abundances we derive agree with those derived by Nazé et al. (2003) and we agree with their conclusion that BAT99-2 does not contain any abundance enhancements.

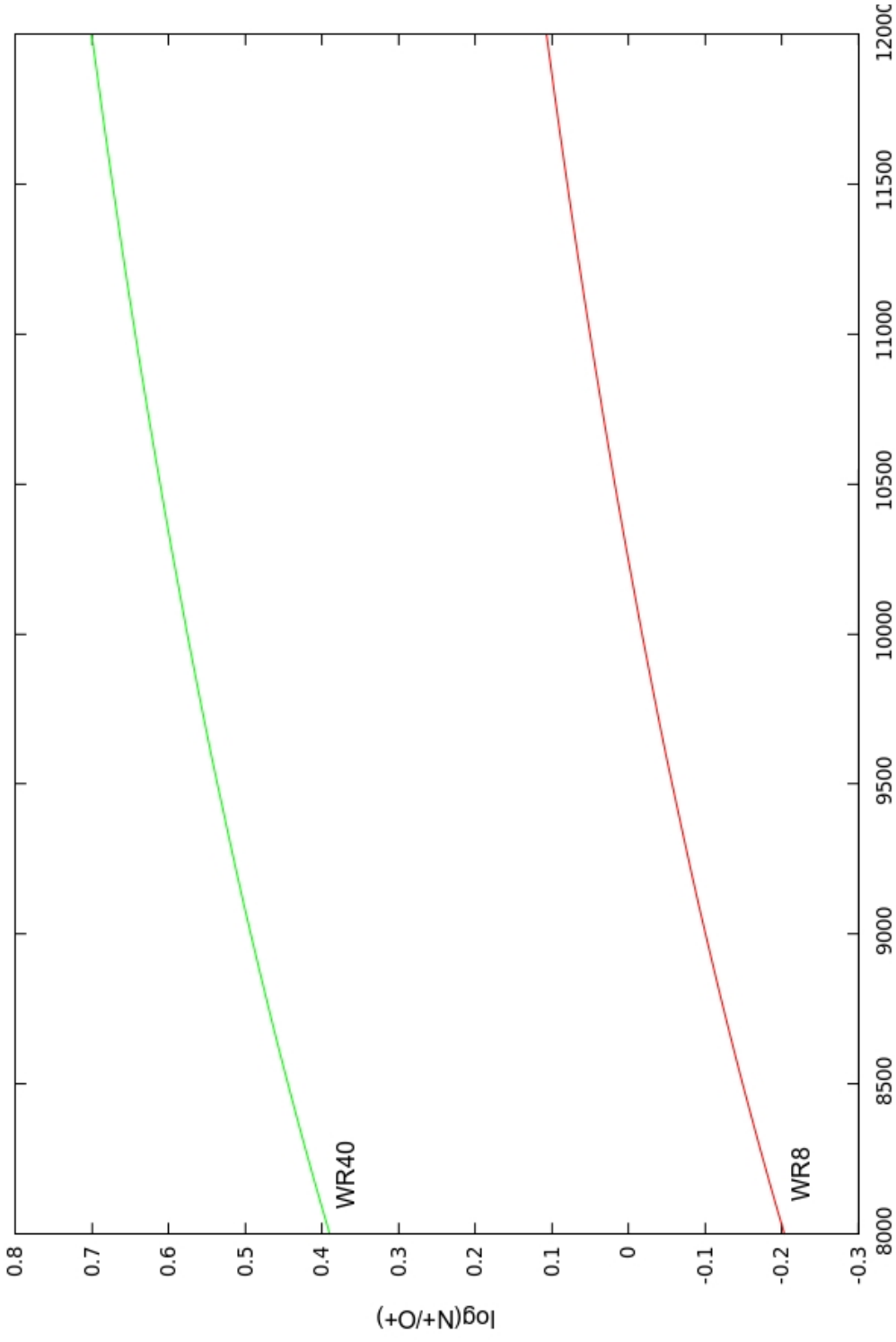

Figure 3.22: Range of possible $\log \frac{N^+}{O^+}$ values over the range 8000-12000K for the nebulae around WR 8 and WR 40 (RCW 58).

Table 3.17: Ionic Abundances

	BAT99-2	BAT99-11	BAT99-38	NGC 3199
He^{+} / H^{+}	0.041 ± 0.008	0.103 ± 0.015	$0.082 \pm +0.014$	0.088 ± 0.01
He^{++} / H^{+}	0.066 ± 0.002			
O^{0} / H^{+} ($\times 10^{5}$)				1.86 ± 0.09
O^{+} / H^{+} ($\times 10^{4}$)	0.05 ± 0.01	$0.50^{+0.01}_{-0.05}$	$0.27^{+0.53}_{-0.09}$	1.73 ± 0.08
O^{++} / H^{+} ($\times 10^{4}$)	0.53 ± 0.01	$1.16^{+0.55}_{-0.22}$	$0.40^{+0.53}_{-0.11}$	2.89 ± 0.08
N^{+} / H^{+} ($\times 10^{5}$)	0.03 ± 0.01	0.02 ± 0.01	$0.12^{+0.12}_{-0.03}$	2.18 ± 0.06
C^{0} / H^{+} ($\times 10^{7}$)				6.05 ± 0.20
Ne^{++} / H^{+} ($\times 10^{5}$)	1.31 ± 0.02	$0.36^{+0.26}_{-0.09}$	$0.33^{+1.10}_{-0.19}$	10.1 ± 1.0
S^{+} / H^{+} ($\times 10^{6}$)	0.19 ± 0.03	$0.39^{+0.15}_{-0.08}$	$0.39^{+0.32}_{-0.10}$	2.10 ± 0.06
S^{++} / H^{+} ($\times 10^{6}$)	0.51 ± 0.06	$1.41^{+0.37}_{-0.15}$	$0.91^{+0.56}_{-0.20}$	15.6 ± 0.50
Ar^{++} / H^{+} ($\times 10^{6}$)	0.26 ± 0.05	$0.80^{+0.34}_{-0.12}$	$0.50^{+0.46}_{-0.12}$	2.37 ± 0.05
Ar^{3+} / H^{+} ($\times 10^{6}$)	0.82 ± 0.14			
Ar^{4+} / H^{+} ($\times 10^{6}$)	0.17 ± 0.07			

Table 3.18: Total Abundances

	BAT99-2	BAT99-11	BAT99-38	LMC HII Region[a]	NGC 3199	Milky Way HII region[a]
12 + log He / H	$11.03^{+0.03}_{-0.04}$	$11.02^{+0.08}_{-0.12}$	$10.91^{+0.11}_{-0.14}$	10.98	10.95 ± 0.01	10.98
O ICF[b]	$1.90^{+0.17}_{-0.13}$	1	1		1	1
12 + log O / H	$8.05^{+0.09}_{-0.07}$	$8.33^{+0.20}_{-0.12}$	$7.93^{+0.41}_{-0.21}$	8.41	8.66 ± 0.02	8.55
12 + log O^0/H^+					7.28 ± 0.02	
N ICF[b]	$1.79^{+0.26}_{-0.07}$	$2.36^{+0.11}_{-0.18}$	$2.25^{+0.21}_{-0.27}$	2.31	2.67 ± 0.02	3.87
12 + log N / H	$6.81^{+0.13}_{-0.12}$	$6.68^{+0.12}_{-0.09}$	$6.57^{+0.23}_{-0.13}$	6.92	7.77 ± 0.01	7.49
log N / O	$-1.21^{+0.09}_{-0.13}$	$-1.67^{+0.08}_{-0.12}$	$-1.40^{+0.13}_{-0.20}$	-1.49	-0.90 ± 0.01	-0.91
12 + log C^0/H^+					5.79 ± 0.02	
Ne ICF[b]	$2.06^{+0.19}_{-0.13}$	$1.73^{+0.11}_{-0.05}$	$1.72^{+0.19}_{-0.07}$	1.76	1.60 ± 0.01	1.39
12 + log Ne / H	$7.45^{+0.09}_{-0.07}$	$6.87^{+0.24}_{-0.17}$	$7.04^{+0.55}_{-0.42}$	7.62	8.23 ± 0.02	7.99
S ICF[b]	$1.99^{+0.10}_{-0.06}$	$1.07^{+0.01}_{-0.02}$	1.07 ± 0.02		1.10 ± 0.01	1.19
12 + log S / H	$6.14^{+0.06}_{-0.04}$	$6.31^{+0.10}_{-0.07}$	$6.16^{+0.23}_{-0.11}$	6.70	7.29 ± 0.01	7.00
Ar ICF[b]	1	1.87	1.87	1.79	1.87	1.35
12 + log Ar / H	$6.08^{+0.07}_{-0.05}$	$6.21^{+0.14}_{-0.09}$	$6.07^{+0.23}_{-0.16}$	6.30	6.65 ± 0.01	6.31

a: Tsamis et al. (2003) (LMC N11B), (M 17)

b: Using the Ionisation Correction Factor scheme of Kingsburgh & Barlow (1994)

BAT99-11

The nebula encircling BAT99-11 (WC4) displays a lower degree of ionization which is more typical of WR nebulae despite having a relatively high excitation (WC4) central star. The [Ne III] and [Ar IV] lines seen in the nebula around BAT99-2 are not observed. Instead we see pronounced higher order Balmer series lines along with several HeI lines, most prominently HeI 4471Å.

The nebular abundances display no signs of stellar processing (see Table 3.18). Since BAT99-11 is a WC4 star it had been anticipated that the nebula might contain an ejecta component. Based on our analysis, the nebula around BAT99-11 is a wind-blown shell.

BAT99-38

The spectrum of the nebula surrounding BAT99-38 (WC4+O) is very similar to that of the nebula around BAT99-11, albeit roughly a factor of five fainter in surface brightness. Many HeI lines are present, including 7065Å, 6678Å, 4471Å and several higher order Balmer lines are present blue-wards of 4000Å.

The nebula near BAT99-38 displays no abundance enhancements (see Table 3.18). Based on our results, it is dubious whether the nebula near BAT99-38 is actually related to BAT99-38 at all.

WR 8

The nebulosity surrounding WR 8 (WC7/WN4) presents clear evidence of nitrogen enrichment in the form of strong [N II] 6548, 6584Å emission lines relative to Hα. There is also some evidence of WR features scattered into the slit, a wide bump at around 4650Å corresponds to a known WR emission feature.

From Figure 3.22 we can see that the range of log(N/O) indicated, -0.2 $<$ log(N/O) $<$ 0.1, is well above the N/O ratio found for the M17 Galactic H II region (-0.91). Even the lower bound, -0.2, is a factor of five above the Galactic ISM value, indicating a high degree of nitrogen overabundance compared to oxygen. This supports the conclusion of Chapter 2 that this nebula has a significant stellar ejecta component.

WR 16

The nebulosity around WR 16 (WN8) displays a sparse, but interesting spectrum. It was noted earlier that previous observations (Marston et al., 1999) had not detected the [S II] doublet, a result repeated in our spectrum. The spectrum also contains the strongest [N II] lines in our sample along with no trace of [O III], [O II] or [O I] lines, making an N/O determination impossible. This kind of composition is precisely what one might expect from stellar outflows

of a WN type WR star. There is a strong sign of helium overabundance though, with HeI 6678Å present and stronger than in all but the nebula around WR 8. Given the non-detection of the [O II] doublet at 3727Å we cannot employ our 'bootstrapping" approach to calculating an approximate log(N/O) value for the nebulosity, except to say that it must be strongly nitrogen enriched (log(N/O) > 0) since if we assume a conservative upper limit for the [O II] 3727Å intensity, for example $\frac{[OII]3727Å}{H\beta} \sim 1$, then we find log(N/O) > 1.95.

Marston et al. (1999) claimed that the lack of [S II] and [O III] lines in the spectrum of the WR 16 nebula was evidence of extremely high nebular density (> 10000 cm^{-3}). The critical densities of [S II] and [O III] do indeed lies in this range, however we attribute the weakness of these lines to the low effective temperature of the WN8 central star.

NGC 3199 (WR 18)

NGC 3199 displays very similar abundances to Galactic H II regions (see Table 3.18). We conclude that the nebulosity is mainly a swept-up ISM shell. Previous observations of this nebula have derived an expansion velocity of around 15 km s^{-1} (Chu, 1982; Marston, 2001). This value is suspiciously similar to the velocity-space positions of the main nebular emission components (see Figure 3.14). The low intensity of the red-shifted component suggests that it is unlikely to have the same intrinsic luminosity as the blue-shifted component as the mass of dust required to produce the required (A(Hα) $>$ 4mags) extinction is unphysical. However by inspection of Figure 3.6 it is obvious that NGC 3199 is not spherically symmetric, its shape suggesting a swept up origin, in which case the relative intensities and velocities of the emission components most likely represent variations in the local ISM density.

Following Liu et al. (1995)[Section 4.1], the dominant excitation mechanism for the observed [C I] triplet in NGC 3199 appears to be recombination of C^+ in a PDR, as was discussed in Section 3.6.1. It is surprising then that the [C I] lines have the same width as the collisionally excited [O I] and [O II] lines from the ionized nebula as shown in Figure 3.23. Line broadening temperatures can be derived for the [C I] lines via the measured line FWHMs relative to Hα in the same manner as before. This yields a value of 12900 $\pm$ 800K from [C I] 9850Å, the strongest [C I] line, which is in the same range as the temperature derived using the same method for [O I], [O II] and [S II].

This temperature consistency is surprising as PDR recombination lines should originate from much lower temperature regions (< 1000K). It is important to note that the observed line widths are at least a factor of five wider than the instrumental value, so there is no systematic reason for these lines to have the same width. This may be evidence that the [C I] ratio we derived is incorrect and that these lines are being emitted by collisional excitiation in the outer

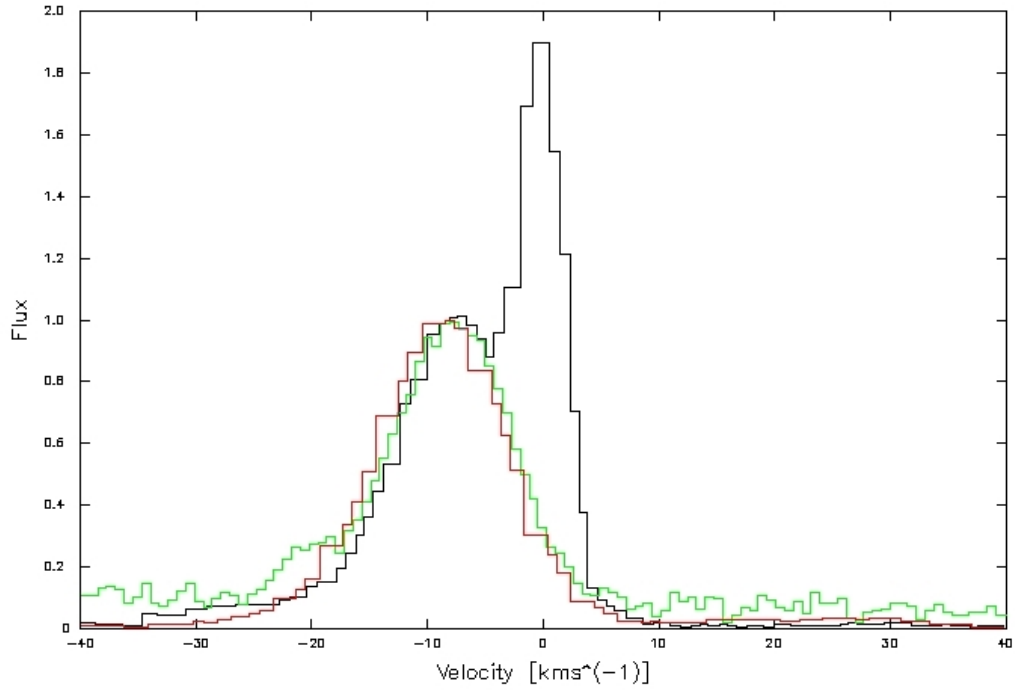

Figure 3.23: Comparison of the velocity profiles of [O I] 6300Å (black), [C I] 9850Å (green) and [O II] 3726Å (red) in the UVES spectrum of NGC 3199. The narrow component of the [O I] 6300Å line arises from night sky emission.

regions of the ionized nebula.

RCW 58 (WR 40)

RCW 58 displays typical a spectrum with much in common with the other Galactic WR nebulae in our sample. Strong [N II] features are combined with weak [O III] lines and a clear He I spectrum.

From Figure 3.22 it is clear that RCW 58 has a very high measured log(N/O) lying in the range $0.39 < \log(\mathrm{N/O}) < 0.70$. The lower limit on this value (assuming a factor of two uncertainty) is still very high. This implies that the material posesses a CNO-cycle processed stellar ejecta component.

This finding agrees with previous results, however the analysis of Rosa & Mathis (1990) relied upon the method of tuning the electron temperature until the "correct" oxygen abundance was achieved (in this case the Galactic ISM oxygen abundance). This methodology may be inappropriate for nebulae which are believed to contain processed material as the true oxygen abundance is likely to differ from the ISM oxygen abundance. Rosa & Mathis (1990) found log(N/O)=-0.3 for RCW 58, however the authors did not include lists of line detections, or finding charts indicating which part of RCW 58 they observed so it is impossible to draw further comparisons.

3.8 Conclusions

A secondary goal of this project was to determine whether [C I] abundances could be derived for nebulae around carbon rich WR stars. Technical limitations have precluded us from finding [C I] around the WC nebulae which we targetted. However it has been shown that the [C I] triplet could be detected from NGC 3199, albeit as likely PDR recombination lines, in a relatively modest amount of time with a suitably high resolution instrument.

We did not detect any heavy element recombination lines in the UVES spectra of NGC 3199. Since these lie mainly in the blue this is likely due to the high reddening towards targets in the Galactic plane. A similar set of UVES observations of a suitable nebula in the LMC could yield both the [C I] triplet and the C II 4267Å recombination line, which would allow quantification of the abundance discrepancy in WR nebulae.

The lack of appropriate temperature diagnostics for several nebulae made calculating abundances for them impossible. The non-detections of the [O III] 4363Å line in galactic WR nebulae is likely due to several effects: low resolution, high reddening and low O^{2+} abundances. However, we did not have spectral coverage of the 5700Å region which would have allowed us to measure [N II] 5755Å. The UVES instrument can reach these regions using different dichroic

settings, however we felt at the proposal stage that the chosen setting would maximise spectral coverage. Given the very high intensities of the observed [N II] 6584, 6548Å lines, the [N II] temperature diagnostic would seem an ideal candidate for future spectroscopic observations of these nebulae with UVES.

We found evidence of significant nitrogen abundance enhancements in the nebula around WR 8, the newly discovered nebula (see Chapter 2) which we morphologically categorised as an ejecta type nebula. The Galactic nebulae, with the exception of NGC 3199, were found to have significantly enhanced N/O ratios compared to the M17 Galactic H II region value. The nebulosity around WR 16 is the most enriched (log(N/O) $\sim$ +2), followed by RCW 58 (log(N/O) $\sim$ +0.5), both of which have WN8h exciting stars. The nebula around WR 8 (WN7/WC4) is also significantly enriched in nitrogen (log(N/O) $\sim$ 0), but not to the degree derived for the nebulae with WN8 central stars.

The nitrogen abundances derived for the LMC nebulae were all consistent with LMC H II region values (log(N/O) = -1.49). The nebula around BAT99-2 would seem to be the best candidate for displaying an abundance enhancement, however it is certainly not as pronounced as for the Galactic nebulae.

Chapter 4

The Chemical Evolution of Carbon and Oxygen

> "On two occasions I have been asked, -'Pray, Mr. Babbage, if you put into the machine wrong figures, will the right answers come out?' ... I am not able rightly to apprehend the kind of confusion of ideas that could provoke such a question."
> — Charles Babbage

4.1 Introduction

The origins of the nitrogen and oxygen present in the universe are well established. The dominant source of oxygen is the core collapse SNe (see, for example, Woosley & Weaver 1995) – from massive stars which form shells of the α elements over their lifetimes which are then expelled as SN ejecta. For nitrogen, however, the dominant source is thought to be via CNO cycling in intermediate-mass stars where the production can be both primary (independent of the initial abundances) and secondary (some of the intial metallicity is transformed into nitrogen) (Renzini & Voli, 1981; Vila Costas & Edmunds, 1993). As a consequence, this Chapter will focus mainly on the origins of carbon.

The key goal of this Chapter is to investigate the likely production sites of the carbon that is at large in the universe. In Figure 4.1 observations are plotted in log(C/O) versus 12 + log(O/H) of various astrophysical objects thought to display representative abundances of some epoch in the history of the Milky Way. The rise in the C/O ratio at late times (high 12+log(O/H)), can be explained in two distinct ways. Firstly, it could be produced by low mass stars (1–8 $M_{\odot}$) of all metallicities, as one might guess given the long lifetimes of such stars and the timescale needed for this enrichment. Conversely, it could be produced by massive stars ($M > 10\ M_{\odot}$) with strongly metallicity dependent carbon yields. This degeneracy in the stellar recycling history of galaxies has been the cause of some debate in the last decade.

Two general camps have emerged which are split along the following lines. The first group (e.g. Chiappini et al. 2003), support the proposition that carbon is mainly produced by low mass stars. The second group dispute this, instead invoking massive stars as carbon producers (e.g. Henry et al. 2000, Akerman et al. 2004). More recently, suggestions have been made that the influence of massive and low/intermediate mass stars might be roughly equal, at least in the galactic disk (Carigi et al., 2005; Cescutti et al., 2009). The prediction of carbon production equality between low/intermediate mass stars and massive stars is not a new one though, as it was first mooted by Iben & Truran (1978).

While this question has been vigorously examined in recent years, it originates from an era in which the concept of chemical evolution was still novel. The idea that certain phases of stellar evolution contribute carbon to the ISM originated with Burbidge et al. (1957). That carbon may be preferentially contributed by massive stars however, was first suggested by Arnett & Schramm (1973). The theme was continued into the first yield prescriptions (e.g. Talbot & Arnett 1974), which featured carbon production only by massive stars.

The possible contributions from lower mass stars were not recognised until the late seventies/early eighties[1]. Around this time it was realised that the thermally pulsing AGB phase could dredge up freshly produced carbon from the interior of AGB stars (e.g. Dearborn et al. 1978). That this carbon may be recycled into the ISM is implied by the presence of carbon rich planetary nebulae and carbon rich AGB stars with high mass loss rates (Tinsley, 1978).

Massive stars contribute to stellar recycling in two distinct ways. Firstly, at solar metallicity they lose well over half their initial mass via winds and sporadic outbursts as they pass through different phases of their lives. Secondly, they will eventually undergo a core-collapse SN event (either of Type II or Type Ibc) which can scatter much of their remaining mass into the ISM in one violent outburst. It is known that carbon is present in SN ejecta, but not in large quantities compared to oxygen. The carbon contribution from evolved massive stars before their SN events is not well known. However there are ideal candidates for such production in the form of carbon rich WR stars (WC stars) which have surface carbon abundances of 60%+ and strong mass loss rates (Crowther, 2007). Futhermore, WC stars are thought to form preferentially at high metallicities as it is thought that massive star mass loss rates are dependent on metallicity. Maeder (1992) presented a concise outline of theis idea, while Georgy et al. (2009) provide the most recent and thorough exploration of the initial mass and metallicity requirements for stars which become WC stars.

We will investigate this problem using chemical evolution models, as described in Chap-

[1] See Iben & Renzini (1983) and references therein.

ter 1. We can combine various sets of published yields – as described in Section 4.3 – into a simple, one-zone, GCE model and plot the resulting metallicity history against galactic abundance data (see Section 4.2) and search for agreement. This technique was used by each of the groups mentioned earlier with respect to their assumptions regarding the likely sites of carbon formation. Our model has been formulated to match that of Henry et al. (2000) in most respects, and we will test agreement with their models as part of our results (Section 4.5).

4.2 Model Constraints

In order to constrain our GCE models, we require data regarding the average chemical abundances of galaxies throughout their history. This can be measured for a variety of objects which we take to be representative of average Galactic abundances at the time of their formation. We will primarily be investigating the carbon abundance relative to oxygen, so our main requirement is accurate observational abundance determinations for these elements.

The objects whose abundances can be used as proxies for galactic abundances fall into three broad groups. Firstly, we can assume that the envelopes of certain types of stars represent material at the same metallicity as that from which the star formed. This assumption is valid for hot, massive, main sequence, stars, e.g. B stars, as they have had little time to evolve since their formation. Gummersbach et al. (1998) provide a catalog of the surface abundances of B stars. Given the short lives of massive stars, these might be expected to display current galactic abundances. This seems to be the case for oxygen, however there is a large spread in the carbon abundance. It is interesting to note that the B star carbon abundances were determined using the same [C I] lines in absorption which in Chapter 3 we were attempting to detect in emission from nebulae.

The assumption of unenriched stellar envelopes is also valid for some less massive main sequence stars. Gustafsson et al. (1999) measured abundances for a large sample of solar analogue F and G stars in the Galactic disk. However this assumption is usually applied to halo stars, as they represent a significantly different epoch of the abundance evolution of the Milky Way e.g. Tomkin et al. (1992). More recently, a study of Galactic halo stars concluded that there is a significant upturn in the log(C/O) ratio at very low metallicity ($12 + \log(\mathrm{O/H}) < 6.5$) which is evident in Figure 4.1 (Akerman et al., 2004; Fabbian et al., 2009).

The second major source of abundance data is extragalactic. Izotov & Thuan (1999) measured carbon abundances in blue compact dwarf (BCD) galaxies, or rather, in H II regions within BCG galaxies. Izotov & Thuan (1999) made use of the HST, and as such were able to observe UV carbon lines for their analysis.

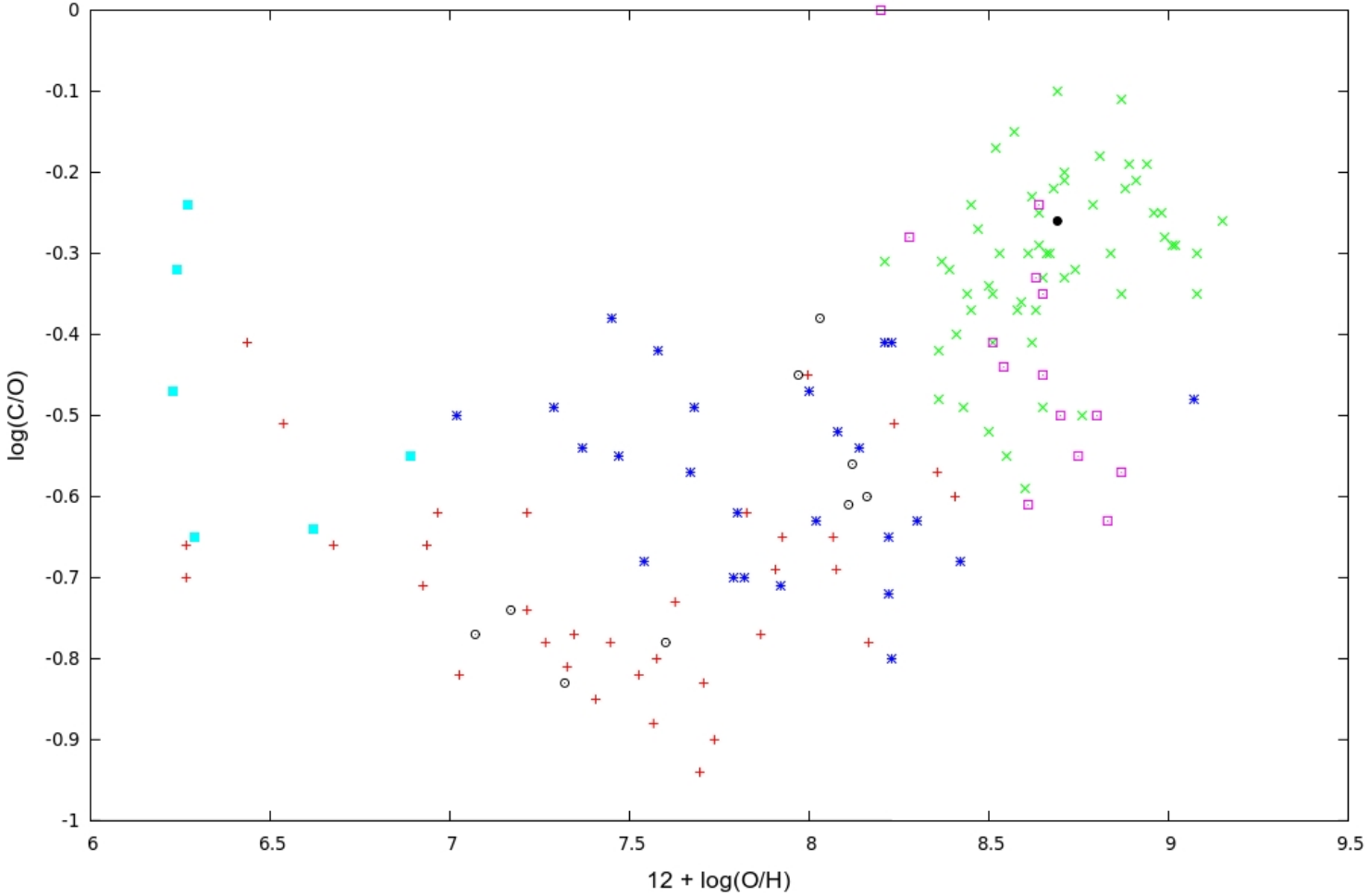

Figure 4.1: log(C/O) versus 12 + log(O/H) for astrophysical objects with abundances thought suitable for constraining GCE models. Shown are: halo star abundances of (Akerman et al., 2004) (red crosses) and (Tomkin et al., 1992) (blue stars), F&G star abundances (Gustafsson et al., 1999) (green crosses), B star abundances (Gummersbach et al., 1998) (pink boxes), extragalactic H II region abundances (Izotov & Thuan, 1999) (open black circles) and DLA abundances (Pettini et al., 2008) (turquoise filled squares) are shown along with the most recently published solar abundances (Asplund et al., 2009) (filled black circle).

The final constraint is closely related to the second, but distinct enough to form its own category. Damped Lyman-α systems, or DLAs, are thought to be proto-galactic objects (for a comprehensive review, see Wolfe et al. 2005). They are observable only as absorption systems on the sightlines to distant quasars. This makes abundance determinations very difficult and time consuming. Pettini et al. (2008) measured abundances in four of the highest redshift DLAs and found a continuation of the upturn in log(C/O) at low metallicities in agreement with the Akerman et al. (2004) halo star abundances.

Each of these data sources is shown in Figure 4.1 along with the latest published solar abundances (Asplund et al., 2009). There is a general trend evident in this data of high log(C/O) at early times (12+log(O/H) $\sim$ 6), followed by a minimum at 12+log(O/H) $\sim$ 7–8 and subsequently a rise towards and beyond solar metallicity (12+log(O/H) $\sim$ 8.5). These points roughly correspond to phases of the galaxy's history, as could be inferred from the types of objects listed previously in this section. The low metallicity objects represent the halo of our Galaxy which formed early in its history while the B,F and G stars represent the Galactic disk which is thought to have formed more recently and shows a trend of increasing carbon abundance above 12 + log(O/H) = 8.0.

4.3 Yield Data

It is important, before embarking on a discussion of yields, to be clear as to what the word "yield" implies. It is normally used to denote the newly created mass of a certain element which is expelled by the star, as a fraction of the star's mass (denoted q_i). This quantity can be negative for a specific element, implying that the star has further processed that element into other species. This is not always the manner in which yields are presented however, in some cases yields are stated as the total mass of that element which is expelled. In certain circumstances these two formulations can be very similar, e.g. in SNe ejecta where the material ejected is believed to be totally processed.

Stating yields as masses is very convenient from the point of view of GCE models as they allow for very simple inclusion via interpolation. The total expelled mass of a certain element is related to q_i in the following way:

$$E_{iM} = (M - M_F)X_i^0 + M_i q_i \tag{4.1}$$

where E_{iM} is the total expelled mass of a certain element over the lifetime of a star of initial mass M_i, final mass M_F and initial metallicity X_I^0.

From the perspective of attempting to ascribe a likely origin site for carbon, the quantity q_i

Table 4.1: Published massive star yields for CN and O which explicitly include pre-SN and SN mass loss

	Mass Range ($M_\odot$)	Metallicity Range (Z[1])
Maeder (1992)	9–120	0.001, 0.02
Henry et al. (2000)[2]	9–120	0.001, 0.02
Meynet & Maeder (2002)	2–60	10^{-5}
Hirschi et al. (2005)	12–60	0.02
Dray et al. (2003)	10.2–181.8	0.02
Dray & Tout (2003)	10.4 – $\sim$155	10^{-4} – 0.03

[1]: Where $Z_\odot \simeq 0.02$

[2]: The Henry et al. (2000) yields are a modified version of the Maeder (1992) yields.

is the most useful as it quantifies creation, rather than simple recyling of the initial abundance.

4.3.1 Pre-SN Massive Star Yields

Yields for massive stars come in two different flavours, based on the stages of massive star evolution that are being considered. In Table 4.1 we summarise the published yields massive stars that explicitly include mass loss via winds along with SNe.

As was discussed in the introduction, it is primarily the pre-SNe yields which we are interested in as a possible significant source of carbon. The SNe yields must also be included though as they allow us to be thorough in our treatment of oxygen.

We compare the carbon yields of massive stars from those works which include pre-SN mass loss in Figure 4.2. As would be expected, the onset of the WC phase ($M_i >\sim$ 30 $M_\odot$, Georgy et al. (2009)) brings a large increase in the carbon yield. While the data in Figure 4.2 includes the effects of SNe, a large fraction (90%+) of the carbon is being expelled via winds in pre-SN phases (see Dray et al. (2003) Figure 4, for example).

For solar metallicity then, the WC phase is the dominant phase of evolution during which massive stars eject carbon. We would expect this effect to vary with metallicity though, as the passage through the WC phase is thought to be metallicity dependent (Georgy et al., 2009). In Figure 4.3 we show the metallicity dependence of the carbon yields from different authors listed in Table 4.1 for a 40 $M_\odot$ star[2] as a function of overall metallicity. As expected, the carbon yields from close to solar metallicity are much higher than those at lower metallicities. An interesting point arises from Figure 4.3; because the metallicity regime is sparsely sampled by

[2]Dray et al. (2003); Dray & Tout (2003) did note use consistent masses in their grids, so for $Z \neq Z_\odot$ the q_c presented is for 41.6 $M_\odot$, while for $Z=Z_\odot$ the mass was 40.4 $M_\odot$.

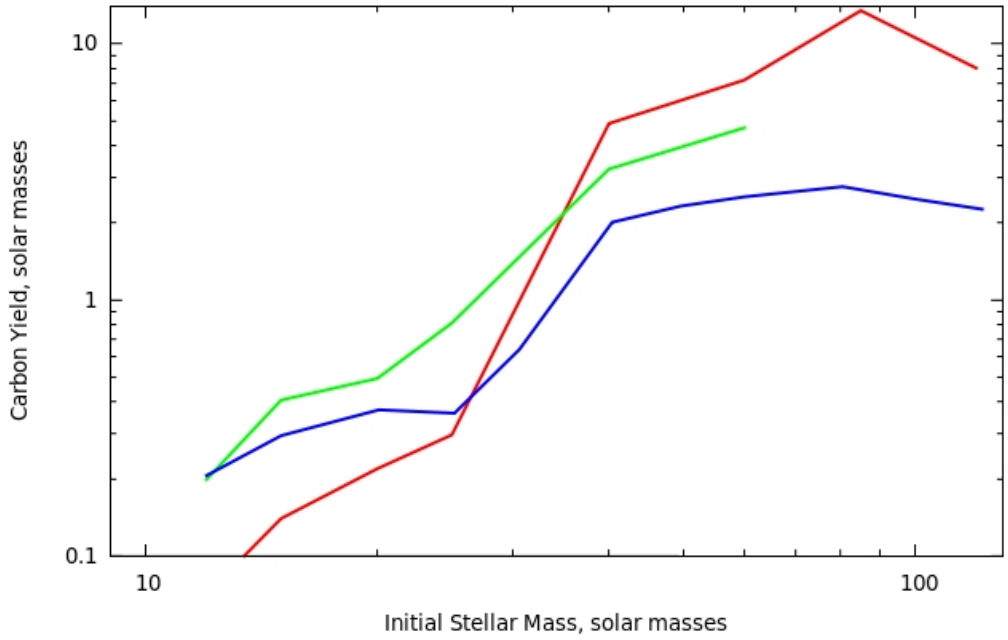

Figure 4.2: Total (winds + SNe) carbon yields for massive stars at solar metallicity (Z=0.02). Yields are from Maeder (1992) (red), Dray et al. (2003) (blue) and Hirschi et al. (2005) (green).

published stellar yields (with the exception of Dray et al. (2003)), linear interpolations between the metallicity datapoints are potentially problematic as they transform a very sharp transition into a shallow ascent.

It is important to note though that because Meynet & Maeder (2002) and Hirschi et al. (2005) included the effects of stellar rotation, their carbon yields are, in general, higher by a factor of roughly 1.5 (for lower mass stars) than those of Maeder (1992). This arises because stellar rotation increases the mixing within the outer layers and allows processed material to reach the surface earlier than for stationary models. This causes an increase in mass loss due to the increased surface abundances. This mechanism is frequently invoked to increase early universe yields since, for example, fast rotating stars with enhanced yields can be used to explain nitrogen and carbon abundances at early times (e.g. Chiappini et al. (2006)). However this idea has been questioned by Hunter et al. (2008), who found that there were significant discrepancies in the VLT/FLAMES Survey of Massive Stars dataset, specifically that there were relatively unenriched fast rotators and relatively enriched slow rotators.

It is worth noting that the yields listed in Table 4.1 are not necessarily the most common to appear in chemical evolution models. To constrain the chemical evolution of most elements, detailed prescriptions of pre-SN evolution are unnecessary, and as such several yield sets which focus solely on the SN yields are used e.g. Woosley & Weaver (1995), Nomoto et al. (1997),

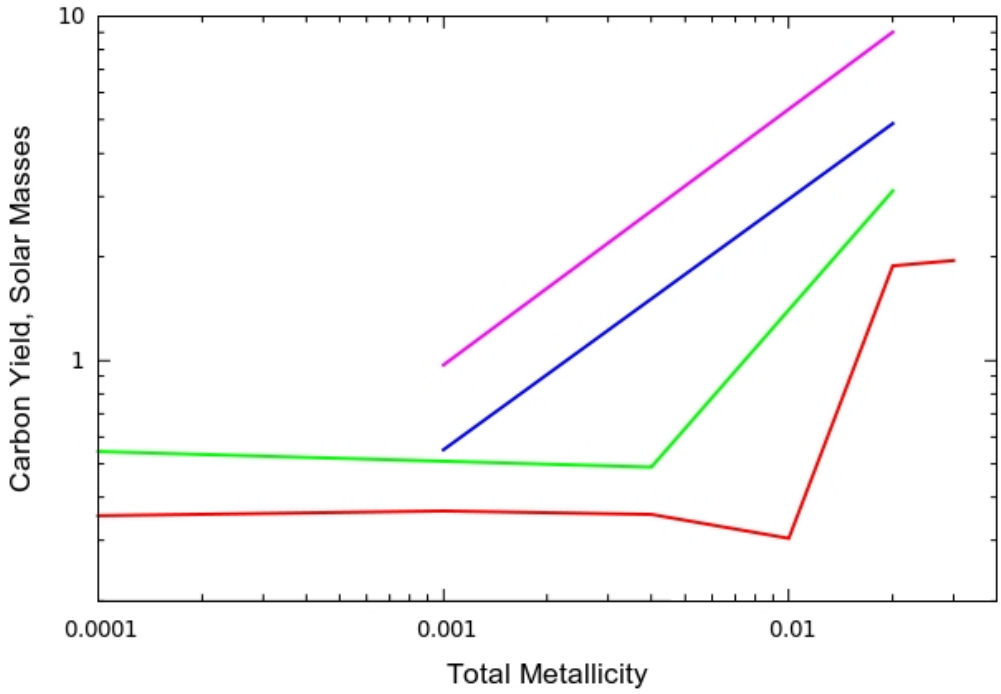

Figure 4.3: Total (winds + SNe) carbon yields for 40 $M_{\odot}$ star as a function of metallicity (Dray et al., 2003; Dray & Tout, 2003) (red), Meynet & Maeder (2002); Hirschi et al. (2005) (green), Maeder (1992) (blue) and Henry et al. (2000) (purple).

Kobayashi et al. (2006), Nomoto et al. (2006).

4.3.2 Low- And Intermediate-Mass stars (LIMS)

There are three major yield prescriptions in use for LIMs, firstly there are those of van den Hoek & Groenewegen (1997) (hereafter HG97), which are complete in the mass range 0.9–8 $M_{\odot}$ and metallicity range Z = 0.001–0.04. These were based on the pre-AGB stellar model tracks of the Geneva group (see Schaller et al. 1992 etc). The HG97 prescription accounted for all mass loss between the star leaving the main sequence and becoming a planetary nebula. Almost all successful GCE models have incorporated the HG97 yields as a baseline. Subseqently Marigo (2001) published a similar set of yields, although over a restricted mass/metallicity interval (0.8–5 $M_{\odot}$; Z=0.004,0.008,0.019), these were based on a different set of stellar models, those published by the Padova group (e.g. Bressan et al. (1993); Portinari et al. (1998)). More recently Karakas & Lattanzio (2007) published a set of yields which largely agree with those of HG97 but extend the grid of elemental yields by more than an order of magnitude in terms of the number of elements considered.

In Figure 4.4 we show the carbon yields, as a function of mass, at solar metallicity for stars in the LIMs mass range. The carbon yields shown in Figure 4.4 peak between 1.5 and $\sim$4 $M_{\odot}$.

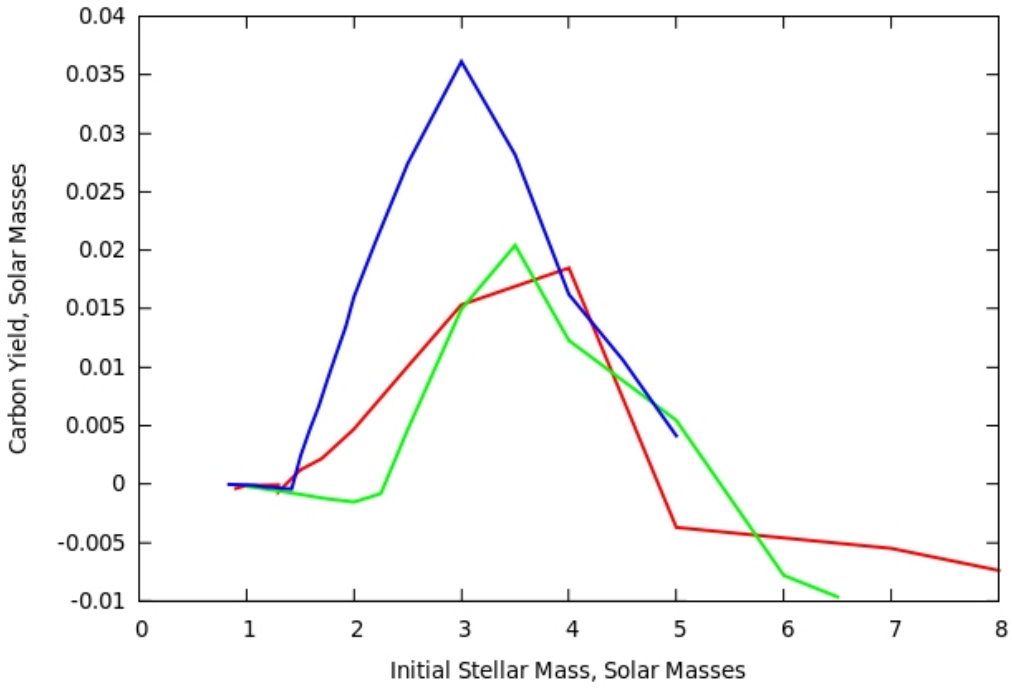

Figure 4.4: Carbon yields from LIMs in solar masses at solar metallicity (Z$\sim$0.02). Data from: van den Hoek & Groenewegen (1997) (red); Marigo (2001) (blue); and (Karakas & Lattanzio, 2007) (green)

The HG97 and Karakas & Lattanzio (2007) values are in rough agreement, whereas the Marigo (2001) yield is almost a factor of two higher in the 1 – 5 $M_{\odot}$ range.

These yields all attempt to model the same processes: the dredging up and expulsion of enriched material from He-burning zones within thermally pulsing AGB stars. Helium burning occurs via the triple-α process, as discussed in the introduction, the primary product of which is carbon. On inspection of the yields in Figure 4.4, we see that the carbon yield is only significant over a moderate mass range ($\sim$ 1.5 – $\sim$ 4 $M_{\odot}$). The reasons for this mass range are well established. The lower bound arises because a minimum mass, for both the core mass ($\sim$ 0.7 $M_{\odot}$) and the total stellar mass ($\sim$ 2 $M_{\odot}$) is required to produce a situation where the convective envelope of the star can descend into regions containing processed material. If the star is sufficiently massive (M $> \sim$ 5 $M_{\odot}$), the bottom of the convective envelope is sufficiently hot to further process the newly created C^{12} into first C^{13} and subsequently N^{14} via successive neutron captures (Iben & Renzini, 1983). In this way the range of stars recycling carbon is narrowed, however the nitrogen yields from such stars are thought to be the dominant contributors of nitrogen in the galaxy (e.g. Vila Costas & Edmunds 1993).

4.4 Models

4.4.1 Initial Conditions and Parameterisations

The initial mass function (IMF) can be of profound importance to chemical evolution studies. The aim of considering the relative contributions of low and high mass stars cannot be realised without having a reliable measure of the relative numbers of such stars. Measurements of the IMF began with studies of the relative numbers of different masses of stars in the solar neighbourhood (Salpeter, 1955). The result of that landmark paper was that the relationship between the relative number of stars and their masses is a power law with a slope of -2.35. This result has endured many subsequent follow-up studies with only minor corrections. Salpeter's initial description of the IMF was stated as:

$$\left[\frac{dN}{d(log_{10}M)}\right] = \phi(M) \propto M^{-\gamma} \tag{4.2}$$

where $\gamma = 2.35$, this is sometimes refered to as the "Salpeter Slope" (Bastian et al., 2010).

Currently there are several competing formulations of the IMF along with that of Salpeter, e.g. those of: Larson (1998), Kroupa (2002) and Chabrier (2003a). Kroupa adopts a similar functional form to Salpeter but replaces the single power law with four power laws to reduce the number of low and high mass stars to more closely match observations. This is usually expressed as follows:

$$\left[\frac{dN}{d(log_{10}M)}\right] = \phi(M) \propto \begin{cases} M^{-2.3} & M \geq 1M_{\odot} \\ M^{-2.7} & 0.5M_{\odot} < M \leq 1M_{\odot} \\ M^{-1.3} & 0.08M_{\odot} < M \leq 0.5M_{\odot} \\ M^{-0.3} & M < 0.08M_{\odot} \end{cases} \tag{4.3}$$

where the normalisation can be found by integrating over an appropriate mass range and the condition that the function is continuous at $0.5M_{\odot}$, $1M_{\odot}$ and $0.08M_{\odot}$. A comparison of Kroupa and Salpeter IMF's is shown in Figure 1.1, where we can clearly see the break at low values of M.

As we discussed in Section 4.3, the yields with which we are concerned are primarily for the mass ranges 1.5–4 $M_{\odot}$ and 20–100 $M_{\odot}$. In any particular IMF scheme, the proportions of stars in these two groups is fixed, for example using a Salpeter IMF there are a factor of 20 more stars in the low mass range than the high mass range. The factor controlling this ratio is the IMF exponent in the 1–120 $M_{\odot}$ range. As each of the competing IMF prescriptions feature very similar IMF exponents in this range (~ 2.3), using the Salpeter IMF should not adversely

affect the results. Later in this Chapter the result of switching between Salpeter and Kroupa IMFs will be shown.

We also require a prescription for the star formation rate (SFR). As discussed in the introduction, this is normally taken to be the Schmidt law (Schmidt, 1959), or some variant thereof. GCE models do not in general use the same units as the "vanilla" Schmidt law, however previous authors have derived appropriate relations using the same functional form. In this work we will follow the prescription of Timmes et al. (1995); Henry et al. (2000) and express the SFR as a Schmidt function with dependence on the total mass and a free parameter describing the star formation efficiency (SFE):

$$\psi(t) = \nu M \left(\frac{G}{M}\right)^2 M_{\odot} Gyr^{-1} pc^{-2} \tag{4.4}$$

Where M is the total mass of the system, G total gas mass and ν, the SFE, is defined by:

$$\nu = \nu_0 \left(1 + \frac{z}{0.001}\right) Gyr^{-1} pc^{-2} \tag{4.5}$$

The star formation efficiency normalisation factor ν_0 is a parameter multiplying the SFR that controls how efficient the star formation process is. Appropriate values of ν_0 are discussed by Henry et al. (2000) and cover a range from 0.03 to 0.20. This parameter is an attempt to describe how much of the material that is involved in the star formation process actually goes on to become stars. It is important to note that this is not the same SFE as is used by those working in the star formation field[3], it is merely a numerical parameterisation of the same idea.

Galactic inflows and outflows can be influential in GCE simulations. The first attempts to address the issue were made by Tinsley (1980). The obvious main conclusion arrived at was that inflows of unenriched material always leave the system less metal rich than it would have otherwise been. The exact masses and timescales involved with inflows are complex, the question is not solely about gas inflowing onto a galaxy but of how the galaxy formed at all. Common ideas of having the galaxy form in one infall episode have been explored thoroughly and this is the approach that will be taken here. Fundamentally though this is a very simplistic approach. More physical approaches have included the Chiappini et al. (1997) dual infall model which attempted to reconcile the different formation timescales of the halo and disk of our Galaxy by having two infall episodes which occur at different times and at different rates.

As with Henry et al. initially we shall adopt the Timmes et al. (1995) infall rate $\Lambda(t)$ to be:

[3]The star formation efficiency is sometimes quantified as the ratio of the luminosity generated by young, massive stars to the molecular mass of the galaxy e.g. Rownd & Young (1999).

$$\Lambda(t) = \Sigma_{t_0} \left\{ \tau_{scale} \left[1 - exp\left(-\frac{t_0}{\tau_{scale}} \right) \right] \right\}^{-1} exp\left(-\frac{t}{\tau_{scale}} \right) \quad M_{\odot} Gyr^{-1} pc^{-2} \qquad (4.6)$$

adopted from models of the effect of SNeII on galactic disks by Timmes et al. (1995). In the preceeding equation τ_{scale} and t_0 are free parameters describing the timescale of collapse of the disk and the age of the universe. Σ_{t_0} represents the surface density of the Milky Way at the current epoch in units of $M_{\odot} pc^{-2}$.

Outflows are a very different problem to describe within GCE simulations. Whereas inflows can be averaged over the whole disk and taken as part of formation scenarios, outflows tend to be the chaotic results of SNII events. When a SNII occurs it can throw off vast amounts of chemically enriched materials in all directions, including out of the disk. The upshot is that SNII can drive galactic winds and thus drive losses of chemically enriched materials. This is a very difficult problem to quantify and it is usually left as a free parameter or ignored entirely as in our model.

In addition to these simple parameterisations, some fundamental constants of the GCE model require definitions. Galaxies have had only the time since the big bang to evolve, hence it is needless to extrapolate beyond this point. The most recent estimate of the age of the universe is around 13.7 billion years (Jarosik et al., 2010).

The upper and lower IMF mass limits can be imposed with a combination of observational and common sense arguments. The higher end of the mass scale is determined observationally in that we do not generally see stars with masses greater than about $120 M_{\odot}$. This upper limit has been called into question recently by Crowther et al. (2010) who have detected multiple stars with masses greater than 150 $M_{\odot}$ in the R136 star cluster at the heart of the 30 Dor nebula in the LMC. The exact value of this limit is less rigorous than the lower mass boundary as it does not introduce a significant error into the results due to the nature of the IMF. There is also a pragmatic reason for adopting a 120 $M_{\odot}$ upper limit in that published stellar yields above this mass range are much less common than those in the more accepted region. The lower limit is also introduced for several pragmatic reasons, firstly, previous authors have adopted the value of 0.1 $M_{\odot}$ and we wish to compare our model results with theirs. Secondly, using this value sets the Salpeter IMF normalisation such that it closely matches the Kroupa IMF in the 1–120 $M_{\odot}$ range. It is important to note that stars under a certain mass (around 0.5 – 0.7 $M_{\odot}$) will never contribute to the model nucleosynthetically as their lifetimes are much longer than the age of the universe.

4.4.2 Numerical Model

The building blocks are now in place for us to lay out a numerical model of GCE. This section follows very closely the formulation laid out in Section 5.1 of Henry et al. (2000). Suppose at some time we have a box with some gas and some stars, the total mass would be:

$$M = G + S \tag{4.7}$$

Where G is the gas mass and S is the mass of stars. In general:

$$\left[\frac{dG}{dt}\right] = \Lambda(t) - \psi(t) + e(t) \tag{4.8}$$

Where $\Lambda(t)$ (see Equation 4.6) is the rate at which gas is infalling, $\psi(t)$ (see Equation 4.4) is the rate at which new stars are being formed and $e(t)$ is the rate of gas explusion from existing stars. Conversely:

$$\left[\frac{dS}{dt}\right] = \psi(t) - e(t) \tag{4.9}$$

These are the basic equations governing what takes place in the model. The balance of stars and gas is controlled by the SFR and the stellar gas expulsion rate.

In all of the following the quantity Z_x can be thought of as a vector representing the fractional abundances of each of the elements x that are taken into account in the model. Using this notation the non-stellar mass of each element in the model is represented by GZ_x. The quantity we need for modelling is the rate of change of Z_x w.r.t time. To find this we must differentiate GZ_x w.r.t time:

$$\left[\frac{d(GZ_x)}{dt}\right] = \left[\frac{dG}{dt}\right] Z_x + \left[\frac{dZ_x}{dt}\right] G = -Z_x(t)\psi(t) + Z_x^f \Lambda(t) + e_x(t) \tag{4.10}$$

Where $e_x(t)$ is the rate at which element x is ejected by stars (like Z_x, a vector over all x) and Z_x^f is the metallicity of the infalling gas. We can rearrange this equation and substitute $\frac{dG}{dt}$ for Equation 4.8 to give us an equation for the rate of change of Z_x w.r.t time:

$$\left[\frac{dZ_x}{dt}\right] = \left(\frac{\Lambda(t)[Z_x^f - Z_x(t)] + e_x(t) - e(t)Z_x(t)}{G}\right) \tag{4.11}$$

This is the main equation used in the modelling. It tells us how the proportion of different elements changes given the basic building blocks of the system. The last (and most important) quantities yet to be defined are $e(t)$ and $e_x(t)$. Expressions for these can be constructed logically. For example, $e(t)$ is all of the mass ejected by stars. Therefore $e(t)$ must be an integral

over all of the masses of stars that could be ejecting matter at time t, taking into account the number of such stars, the total amount of stars formed at the epoch which each stellar mass represents and the amount of matter that could be ejected (initial mass of the star, m - the remnant mass, $w(m)$). This assumes that individual stars lose all of their mass (minus the remnant mass) at the end of their lifetime; this is thought to be a reasonable assumption as all stars spend the bulk of their lives on the main sequence where their mass loss is relatively minor.

Thus the equation describing $e(t)$ is:

$$e(t) = \int_{M_{\tau_M}}^{M_{up}} [M - w(M)]\psi(t - \tau_M)\phi(M)dM \tag{4.12}$$

where the quantity τ_M is the main sequence lifetime of a star of mass M. Similarly, the equation describing $e_x(t)$ can be described as:

$$e_x(t) = \int_{M_{\tau_M}}^{M_{up}} \{[M - w(M)]Z_x(t - \tau_M) + Mp_{x,z_{t-\tau_M}}\}\psi(t - \tau_M)\phi(M)dM \tag{4.13}$$

where $p_{x,z_{t-\tau_M}}$, is the yield of element x of a star with initial metallicity $z_{t-\tau_M}$. The value of $p_{x,z_{t-\tau_M}}$ was found by linearly interpolating over the published yields discussed in Section 4.3.

The remnant mass function $w(M)$ was interpolated from Yoshii et al. (1996). The quantity M_{τ_M} which appears above is the turnoff mass, that is the stellar mass which at the current time is just leaving the main sequence having been born at the beginning of the system. It represents the lowest possible mass that can have had a nucleosynthetic effect on the system.

These equations describe a recipe for how the fractions of each element in our model, Z_x, change over each timestep:

1. calculate the current SFR $\psi(t)$
2. calculate the solution to Equation 4.11 at time $t = t + \delta t$ (where δt is the chosen timestep size) and multiply by δt to find the change in abundances over this timestep
3. add resulting increments to Z_x
4. solve Equations 4.8 and 4.9 and multiply the results by δt, add results to G and S

A program was written to implement this process over the time t=0,T_{end} (where T_{end} = 13.7 billion years) which also keeps track of other data of interest e.g. the fractions of different elements created by stars in specific mass ranges. In order to choose an appropriate value for the timestep size we run the code with many different values of timesteps (all of which are less

Table 4.2: Yield Combinations used in GCE models

Model No.	LIMs Yields	Massive Star Yields
1	van den Hoek & Groenewegen (1997)	Maeder (1992)
1a	van den Hoek & Groenewegen (1997)	Henry et al. (2000)
2	van den Hoek & Groenewegen (1997)	Dray et al. (2003); Dray & Tout (2003)
3	van den Hoek & Groenewegen (1997)	Meynet & Maeder (2002) + Hirschi et al. (2005)
A	Marigo (2001) + van den Hoek & Groenewegen (1997)	Maeder (1992)
B	Marigo (2001) + van den Hoek & Groenewegen (1997)	Dray et al. (2003); Dray & Tout (2003)
C	Marigo (2001) + van den Hoek & Groenewegen (1997)	Meynet & Maeder (2002) + Hirschi et al. (2005)

than the lifetime of the shortest lived, most massive stars) and choose the largest one that still produces convergence of the model. That is to say we choose the timestep that produces the shortest runtime while preserving the integrity of the results. This was found to be around δt = 1 Myr. Previous authors have adopted variable timesteps which increase with time, but this was never implemented as each model run was found to last less than $\sim$ 5 minutes.

4.5 Model Yields, Results & Discussion

4.5.1 Model Yield Combinations

The yield combinations adopted have been numbered and are presented in Table 4.2. In the low mass range we have restricted the yields utilised to either those of van den Hoek & Groenewegen (1997) for the entire $1 < M < 8$ $M_{\odot}$ range or those of Marigo (2001) for the $1 < M < 5$ $M_{\odot}$ range and van den Hoek & Groenewegen (1997) for $3 < M < 8$ $M_{\odot}$. This was done as van den Hoek & Groenewegen (1997) and Marigo (2001) show the greatest contrast in carbon production (see Figure 4.4).

In Figure 4.5 I show my model 1, 1a and the model presented by Henry et al. (2000). The Henry et al. (2000) model in Figure 4.5 differs from model 1 in that their model enhanced the massive star carbon yields at high metallicities; when their carbon enhanced yields were

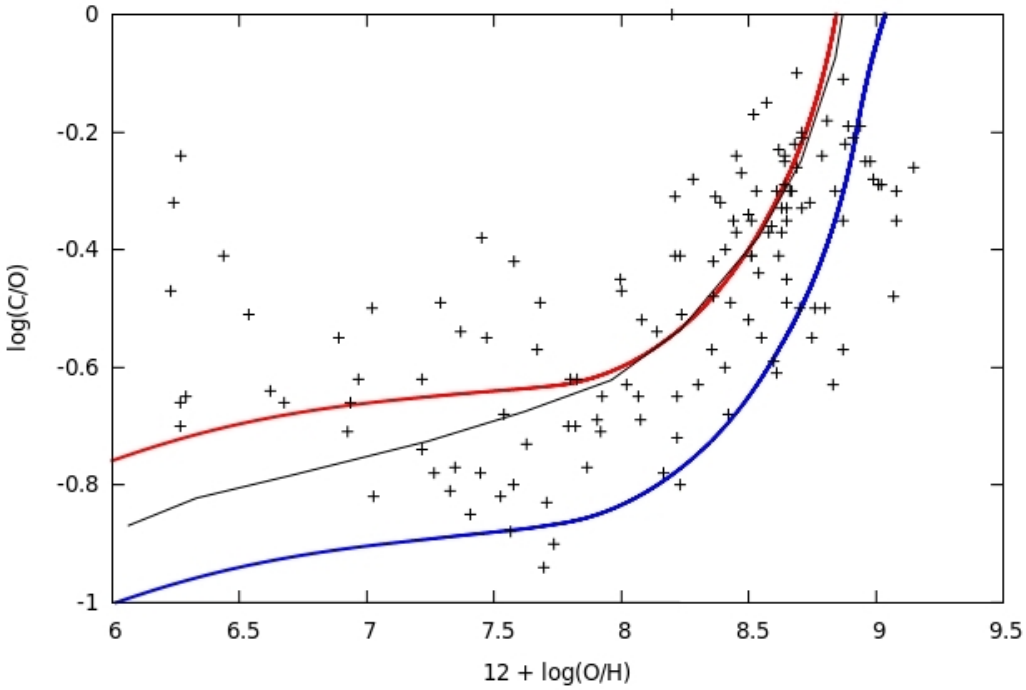

Figure 4.5: Model 1 (blue), and 1a(red) plotted with the same observational data points as presented in Figure 4.1 (although reduced to black points) compared to the model presented by Henry et al. (2000) (black). The model of Henry et al. used enhanced carbon yields to reach agreement with the observational data. Our model which also uses these yields (1a) agrees well at high O/H, with a slight disparity below this value.

included in our model 1a we find agreement at late times. The slight discrepancy (0.1 dex) in log(C/O) between our model 1a and that of Henry et al. (2000) at low metallicities (12 + log(O/H) $<$ 8 is puzzling. The parameters of our models were thoroughly checked to match those used by Henry et al. (2000) in every respect, yet the cause of this disagreement was never discovered.

4.5.2 Results

In Figure 4.6 we show the tracks of six models (1–3, A–C; see Table 4.2) in log(C/O) versus 12 + log(O/H) space along with model 1a. In general, the spread of observational data in the log(C/O) versus 12 + log(O/H) plane is quite wide, allowing most of the models to become plausible in some respect.

It is clear (see Figure 4.6, middle) that the models using the Dray et al. (2003) and Dray & Tout (2003) yields do not match the desired C/O ratios at late times, although they do provide a plausible match at early times. The late upturn observed in model 2 is too shallow to be said to match the data. This is likely a result of the Dray et al. (2003); Dray & Tout (2003) carbon yields not being a strong enough function of metallicity. Model B, which is the same as model 2 except that it uses the enhanced carbon yields from low mass stars predicted by Marigo (2001), overpredicts C/O at in the regime 7.5 $<$ 12 + log(O/H) $<$ 8.5 and reaches the galactic disk abundances at around solar metallicity. Both could plausibly be said to match the abundances within the galactic halo.

The yields of Meynet & Maeder (2002) and Hirschi et al. (2005) for rotating massive stars (Models 3 and C, Figure 4.6, bottom) also do not produce matches to the galactic trend at high metallicities. They also significantly under-predict the C/O ratio at low O/H. Model 3 replicates the general behaviour, and shows a steeper gradient than model 2, however this happens at a significantly higher 12+log(O/H) than the abundance data suggests. Model C exhibits the same behaviour as model B except that it deviates from the observed abundance data to an even greater degree.

Models 1, 1a and A (see Figure 4.6, top) display the best adherence to the late-time galactic abundance data. Models 1a and A in particular display the best matches to the abundance data for the galactic disk at 12+log(O/H) $\sim$ 8.5. This might have been expected of model 1a, which used yields tuned to match the observed data, as discussed in the previous section. However the combination of the Maeder (1992) massive star yields and the Marigo (2001) LIMs yields in model A produces a model which fits the disk abundance data as well as model 1a.

At low metallicity (12 + log(O/H) $<$ 7.5) we find that the models using Dray et al. (2003) and Dray & Tout (2003) yields (models 2 and B) provide the best matches to the observed

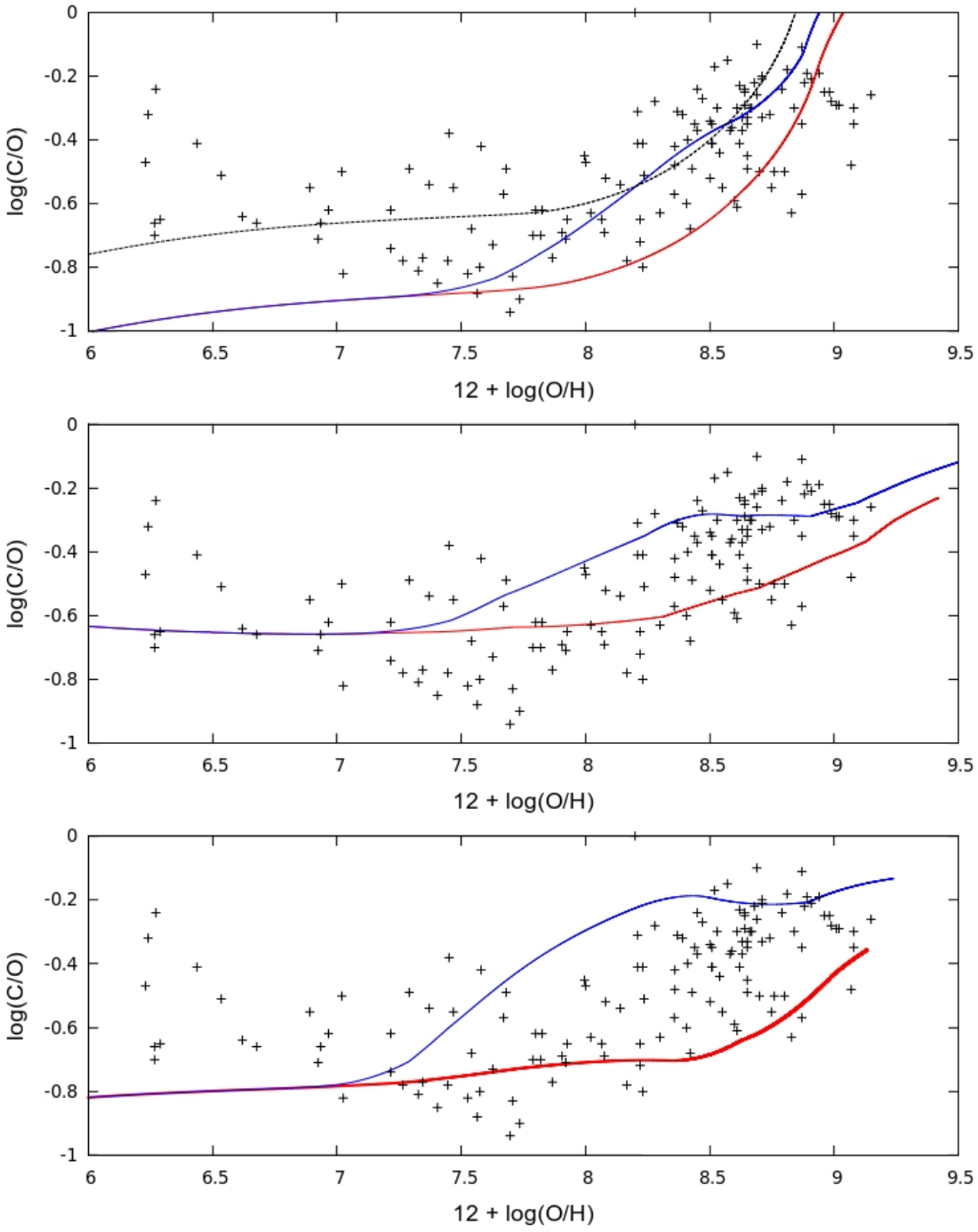

Figure 4.6: *Top*: Models 1 (red), 1a (black dotted) and A (blue). *Middle*: Models 2 (red) and B (blue). *Bottom*: Models 3 (red) and C (blue). *All*: Black crosses represent all of the observational data shown in Figure 4.1. See Table 4.2 for the yield combinations used in models 1-3, A-C.

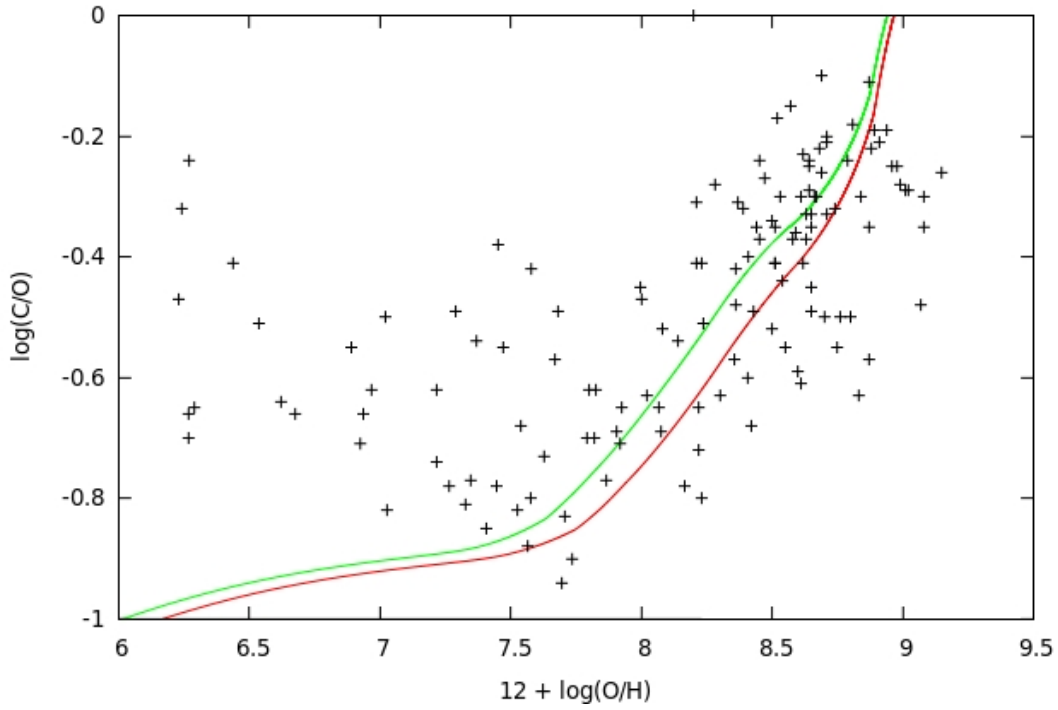

Figure 4.7: Model A, using the Salpeter (1955) IMF (green) and Kroupa (2002) IMF (red) along with the data points from Figure 4.1.

abundances. The other models all significantly underpredict the C/O ratio in this regime (with the exception of model 1a due to its very high carbon yields).

In Figure 4.7 we show the effects of adopting the Kroupa (2002) IMF, as discussed in Section 4.4. Use of the Kroupa IMF has a detectable effect, but ultimately this is small compared to the scatter in galactic abundances evident in Figure 4.1. The Kroupa IMF has the effect of increasing the O/H at every point in the model. This arises because more massive stars are made per unit star formation by a Kroupa IMF than by the Salpeter IMF, due to the difference in normalisation in the low mass range.

4.5.3 Discussion

Models 1a and A are interesting demonstrations of a rather general point, that is that we can reproduce the carbon abundance trend in the galactic disk and the later part of the chemical evolution of the halo by invoking high carbon yields from either massive or low mass stars. In the case of model A, the low mass star yields of Marigo (2001) are roughly a factor of 1.5–2 greater than those of van den Hoek & Groenewegen (1997) over the LIMs range. For model 1a, the agreement was forced by Henry et al. (2000) who boosted the Maeder (1992) massive star carbon yields by a factor of just under two.

As we saw in the previous two Chapters, there is very little observational evidence, in

the form of circumstellar carbon enhancements at least, that WC stars produce large amounts of carbon. This is especially strange in light of the fact that large nitrogen enhancements are routinely observed in nebulae around WN stars. It is possible that there is a simple explanation for this observation. When the observed nebulae around WR stars display abundance enhancements (usually nitrogen, as mentioned), the enhancements imply that the circumstellar nebula may have been generated by the expulsion of a red supergiant or LBV atmosphere e.g. Smith et al. (1988). If the transition from WN to WC star is not accompanied by a significant mass loss event, the nebulae which are observed may not have had time to show carbon enhancements.

For LIMs, we find very different circumstances in terms of carbon and nitrogen abundances, Stanghellini et al. (2005) find general agreement between the yields of van den Hoek & Groenewegen (1997), Marigo (2001) and an HST observed sample of LMC PNe. Stanghellini et al. (2005) found the greatest degree of agreement came in the lower mass range for both sets of yields ($M < 3.5\ M_{\odot}$) — the very LIMs mass range which both predict to be producing carbon preferentially.

4.6 Conclusions

In this Chapter we have shown that it is possible to match carbon abundance data over the majority of our Galaxy's history, using different combinations of published stellar yields for low- and high-mass stars. This broadly agrees with recent work (Carigi et al. (2005); Cescutti et al. (2009)) and not-so-recent work (Iben & Truran, 1978), suggesting that the contributions of carbon from low- and high-mass stars may be comparable, at least in the solar neighbourhood. We have found that the yield combinations which represent opposite extremes are the best fitting models. Other combinations could reproduce the Galactic halo abundances but most either significantly under- or over-predicted the C/O ratio at low O/H, with the exception of those using the yields provided by Dray et al. (2003) and Dray & Tout (2003).

The degeneracy in the results for massive stars having strongly metallicity dependent carbon yields and low mass stars having very long lifetimes, as was noted in the introduction, may render GCE modelling an inadequate approach to solving this problem. The large scatter in galactic abundances adds to this problem as it increases the number of models which could be said to "fit".

It should be noted that while some specific results of this chapter are available in the literature, an unbiased comparison of each of the available theoretical yield combinations as presented here is not. We have not attempted to alter the published yields in pursuit of a desired result - leading to models which do not fit the data as well as some which have been published.

However, altering the theoretical yields to fit the data is useful in the sense of asking the question ”what would the yields have to be in order to achieve the best fit to the data?”, e.g.Henry et al. (2000).

The Marigo (2001) low-mass yields suggest that massive stars may not have a major role in the chemical evolution of carbon. Likewise the Henry et al. (2000) suggest that low mass stars are irrelevant for carbon evolution. Clearly these are mutually contradictory extremes, the answer may lie somewhere in between as we have already mentioned. However if massive stars do play a significant role in carbon enrichment, as we are suggesting, then there ought to be some tangible circumstellar evidence of this phenomenon — which remains elusive.

Chapter 5

Dust Evolution in High Redshift Galaxies

"With four parameters I can fit an elephant, and with five I can make him wiggle his trunk."

– John von Neumann

5.1 Introduction

The recent detection of dusty ($M_D > 10^8$ $M_\odot$) high redshift ($z > 6$) galaxies over the last decade (Beelen et al. 2006, Bertoldi et al. 2003, Wang et al. 2008 etc) has sparked debate regarding the likely formation mechanisms for the dust in such galaxies. Two major dust sources have been proposed: formation by grain accretion within the ISM (Draine, 2009) and stellar dust production (e.g. stellar outflows and core collapse supernovae (CCSNe)). An additional complication arises because the actual *age* of the high redshift galaxies is unknown. Their redshift tells us the age of the universe at the time that the light we observed was emitted; it does not provide any information regarding when the galaxy actually formed.

The issue of time also dominates the main question regarding stellar dust sources: were massive stars largely responsible or do lower mass stars also play a role? Much work has been done on this subject, however in every case the stellar dust sources have been described by parameterised theoretical models e.g. Morgan & Edmunds (2003); Valiante et al. (2009). The aim of this Chapter is to determine whether observational constraints of local stellar dust sources are sufficient to explain high dust masses inferred for high redshift galaxies.

The two major sources of stellar dust in the universe arise from very different types of stars, intermediate- and high-mass stars. While it is known that high-mass stars do produce dust before their deaths as CCSNe, this dust may be destroyed by the SN (e.g., Zhukovska et al. (2008), Jones et al. (1996)). Although as we shall see in Section 5.2.3, this picture is becoming more murky with the detection of light-echos implying survival of previously created dust e.g. Mattila et al. (2008); Wesson et al. (2010). However if we accept the pre-SN dust total destruc-

tion model, the main source of dust production by massive stars becomes the CCSN itself, or rather, the post shocked ejecta of the SN. The general picture is that as the SN ejecta expands and cools, shock waves propagate through it and create overdensities where the conditions are such that dust grain formation ensues. The precise quantity of dust expected from such an event is dependent on the assumptions made regarding the SN ejecta material, its temperature structure etc. Bianchi & Schneider (2007) modelled the process of dust forming in SN ejecta, along with the associated shocks which create and destroy dust. They considered a range of stellar initial metallicities, (0,10^{-4},10^{-2},10^{-1},1)$Z_{\odot}$, and calculated the mass and composition of dust produced in each model (for stars in the initial mass range 10–40 $M_{\odot}$[1]). Bianchi & Schneider (2007) found very different dust compositions than alternative works (e.g., Nozawa et al. 2007) which used different SNII yields as a starting point.

A further source of interstellar dust, albeit one which is less significant in terms of the mass of dust produced, arises from novae. Despite being many orders of magnitude more frequent than SNe (van den Bergh & Tammann, 1991), they are thought to produce comparatively little dust (Gehrz, 1988; Dwek, 1998).

Dust yields from low- to intermediate-mass stars (LIMS) may also be important in high redshift, dusty galaxies. The asymptotic giant branch (AGB) phase of LIMS is accompanied by a cool, dense atmosphere (1000–1800K) and thermal pulsations — a suitable environment for dust formation (Salpeter, 1977). The stellar mass-loss rate at this stage is comparatively high (compared to the rest of the stars' lifetime) and these outflows are known to be sites of cosmic dust formation. The onset of the stellar wind which carries away the dust may actually be triggered by dust formation (Bowen & Willson, 1991). The most common theoretical sets of dust yields to describe this avenue of dust formation were provided by Ferrarotti & Gail (2006). Further work by the same group (Gail et al., 2009), compared these yields with data regarding the isotopes found in pre-solar grains. The models were found to match well, in the solar metallicity regime.

The relative contributions of the two sources of dust in high redshift galaxies have long been thought to be heavily weighted towards dust from CCSNe (Morgan & Edmunds, 2003; Dunne et al., 2003; Marchenko, 2006). This result seems sensible, on grounds of both stellar lifetimes, which we will discuss later, and the reddening law derived from the dust, which has been claimed to match the abundances expected of CCSNe dust (Maiolino et al., 2004). However, observations of dust formation in CCSNe ejecta do not totally support this picture.

[1]This range arises from the SNII stellar ejecta yields of Woosley & Weaver (1995) which were used as a starting point.

Observations quantifying dust formation by SNe are rare, owing more to the lack of suitably IR-bright SNe than lack of interest. Studies quantifying the dust created by CCSN exist for less than ten CCSN, e.g., SN1987A (Wooden et al., 1993), SN1999em (Elmhamdi et al., 2003), SN2003gd (Sugerman et al., 2006; Meikle et al., 2007), 2004et (Kotak et al., 2009), SN2006jc (Mattila et al., 2008) and Cas A (Rho et al., 2008; Barlow et al., 2010). The derived dust masses for these SN ejecta are generally below $\sim 10^{-3}$M$_{\odot}$, which has been interpreted as suggesting that they are not major producers of dust (Meikle et al., 2007), although the opposite view has also been proposed (e.g., Sugerman et al. (2006)).

AGB dust yields are normally measured in a slightly different way. Unlike SNe, AGB stars create dust over a long period of time and as such the dust production is normally measured in M$_{\odot}$ yr^{-1}. This creates a dependence upon the AGB lifetime (τ_{AGB}, by which we mean the length of time stars of different masses spend on the AGB, rather than the total lifetime of stars which will become AGB stars in their lives. Several attempts at constraining this parameter have been made, beginning with Vassiliadis & Wood (1993). Combining mass loss rates with τ_{AGB} allows direct access to the dust contributions in M$_{\odot}$ per star, allowing direct comparison with CCSNe. A further complexity for AGB stars is the split between carbon and oxygen rich subtypes, which are often found to have differing mass loss rates[2]. An inventory of dust producing AGB stars in the local solar neighbourhood was given by Jura & Kleinmann (1989) who found that the average gas mass loss rate per AGB star was around 10^{-5} M$_{\odot}$ yr^{-1} (at Z $\approx$ Z$_{\odot}$). At lower metallicity, Groenewegen (2006) provided AGB mass loss rates for the LMC as a function of AGB colours in different filters. These rates, along with Spitzer survey data, have subsequently been used to catalog the dust inventory of the LMC (Matsuura et al., 2009).

A third possible source of dust has been discovered recently. It is possible that some stars lying in the uncertain mass range between the AGB and CCSNe regimes (8M$_{\odot}$ $<$ M $<$ 12M$_{\odot}$) undergo a dust enshrouded phase before undergoing some SN-like transient event. A possible prototype for this kind of 'Super-AGB' object is discussed in Wesson et al. (2010), and we will further discuss the possible effects of this object, should it be typical of stars in this mass range.

Since the discovery of high redshift dusty galaxies, attempts have been ongoing to explain their inferred high dust masses using gas and dust phase GCE models. With one exception, all such GCE models have assumed theoretical models of dust formation for both CCSNe and AGB stars. This technique allows quantification of certain dust properties, primarily composition, that our approach will not. The first such model, presented by Morgan & Edmunds (2003),

[2]They will also of course produce dust of very different composition, but that is not a factor that we are considering.

showed that it was possible to make large amounts of dust in the early universe, under the assumptions that dust destruction was ineffectual and grain formation was efficient. Dwek et al. (2007) utilised the Woosley & Weaver (1995) SNII yield computations to derive maximal dust contributions for stars in the 10–40$M_{\odot}$ range. They used these with a combined gas & dust phase GCE model to model a range of galactic properties under the assumption that AGB stars played a negligible role, i.e., that the galaxy had formed recently. Dwek et al. (2007) found that unless the average CCSN produces around 1$M_{\odot}$ of dust, then it was impossible to reproduce the dust mass observed. Subsequently Valiante et al. (2009), challenged the assertion that the dust mass produced by AGB stars was negligible. They pointed out that an 8 $M_{\odot}$ star would have evolved off the main sequence at an age of 30 Myr. Subsequently their dust contribution could become *dominant* under certain conditions.

More recent models (e.g. Valiante et al. 2009) have utilised star formation rates derived from cosmological simulations of specific high-z galaxies e.g. SDSS J1148+5251 (Li et al., 2007) rather than assuming an average, constant, level of star formation. An interesting note regarding the Li et al. (2007) SFR result is that the most intense burst of star formation is offset from the time at which we are observing a high dust mass. This suggests that this model will favour high dust masses being produced by lower mass stars as they have lifetimes around the same order of magnitude as this difference. The work of Dwek & Cherchneff (2011) followed a similar path, although they concluded that the amount of star formation required to create the requisite dust mass was unphysical given the dynamical mass of the galaxy.

The aim of this work is to determine whether this complex approach is necessary to explain the high dust masses and contributions of AGB and CCSN dust respectively. To do this we will first review the observationally determined estimates of dust formation in SN ejecta and AGB stars and estimate an average value from these data (Section 5.2). Subsequently we will construct a simple model of the dust build up in high redshift galaxies, including only the most important effects to dust formation - the initial mass function, dust creation and dust destruction (Section 5.3). We will then compare our models to those previously published and show the results for models based on SDSS J1148+5251, the prototypical high redshift dusty galaxy (Section 5.4).

5.2 Observationally Derived Dust Yields

5.2.1 AGB Dust Yields

The simplest model of AGB dust formation runs as follows: if we assume that every star in the mass range $1M_{\odot} < M < \sim 8\ M_{\odot}$ ends its life as a $\sim 0.6\ M_{\odot}$ white dwarf[3], then the mass lost

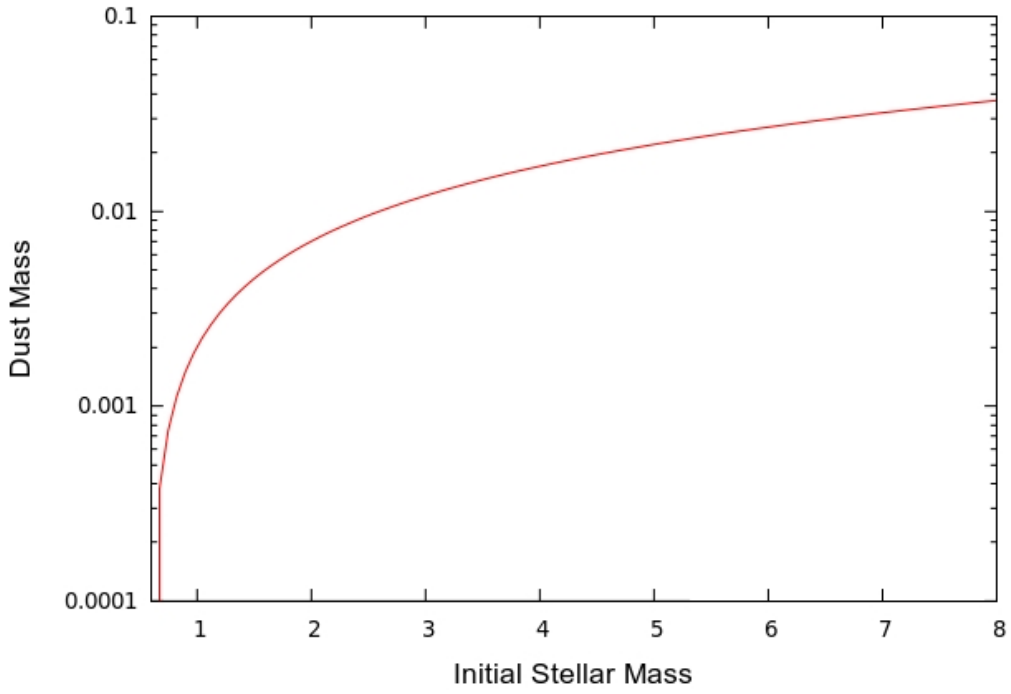

Figure 5.1: Equation 5.1 plotted for the initial masses of AGB stars. Both axes in units of solar masses ($M_\odot$).

over its lifetime is: M_{lost} = M_i - 0.6 $M_\odot$. If we apply the gas to dust mass ratio which we will discus later ($\sim$ 200) to this value then we attain a relation for the average dust produced per star of:

$$M_D = \frac{M_i - 0.6}{200} M_\odot \tag{5.1}$$

where M_i is the initial mass of the star. This relationship is plotted in Figure 5.1. This relationship is the upper limit to the dust mass we might expect as the gas-to-dust mass ratio which is relevant to AGB stars is extrapolated to all periods of mass loss.

Infrared (IR) observations of AGB stars can yield information regarding their mass loss rates via their IR colours (Jura, 1987; Jura & Kleinmann, 1989; Whitelock et al., 1994; Le Bertre, 1997; Groenewegen, 2006). If we assume a gas-to-dust mass ratio, along with an estimate of the time each star spends on the AGB, we can calculate an approximate dust contribution per star.

The gas-to-dust mass ratio is usually assumed to be in the region of 200 for carbon- and oxygen-rich stars in both the Galaxy and the LMC (Jura, 1986; Justtanont et al., 1994; Mat-

[3]In reality, the top end of the mass range quoted will produce slightly more massive white dwarfs, with the Chandrasekhar mass of 1.4 $M_\odot$ as a rigid upper limit.

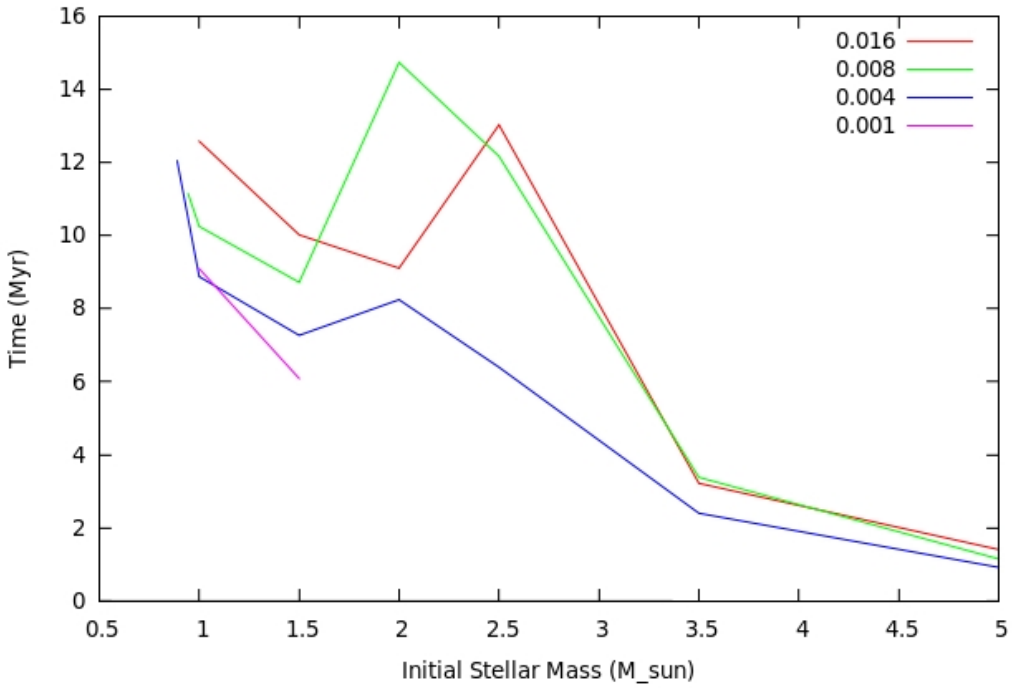

Figure 5.2: Vassiliadis & Wood (1993) prescription of AGB lifetimes as a function of initial mass and metallicity, the different lines correspond to different metallicities whose values are indicated by the figure key.

suura et al., 2005; Wachter et al., 2008). This value is largely repeated throughout the galaxy (Phillips, 2007), although it decreases at higher galactocentric radii (which correspond to lower metallicities).

The time each star spends on the AGB is a function of both age and initial metallicity. Vassiliadis & Wood (1993) provide such a scheme, for stars in the mass range of 1–5 $M_{\odot}$ (Figure 5.2). However it is clear that we cannot multiply the Vassiliadis & Wood (1993) lifetimes by the derived gas mass loss rates (which can be as high as 10^{-5} $M_{\odot}$/yr) as this would provide a rough M_D per star of around 2×10^{-5} $M_{\odot}$/yr $\times$ 10^7 yrs $\times$ $2{\times}10^{-2} \approx 1$ $M_{\odot}$, which is unphysical for all stars in the $1M_{\odot} < M < \sim 7M_{\odot}$ mass range, as it greatly exceeds their maximum total metal yield.

It is thought that the extremely high mass loss rates arise from a superwind phase of an AGB star rather than being the general case (e.g. Bowen & Willson 1991; Lagadec & Zijlstra 2008). In this picture the range of mass loss rates are interpreted as representing whether the star is currently in a superwind phase. Lower mass loss rates ($< 10^{-5}$ $M_{\odot}$ yr^{-1}), correspond to weak-winded, thermally pulsing, AGB stars, while the stars with mass loss rates higher than this are assumed to be in a dusty superwind phase. This superwind is thought to last around

10^4 yrs (Tanabé et al., 1997), as opposed to the $\sim 10^7$ yrs AGB lifetime mentioned earlier. This reduces the dust mass lost per star to roughly: $M_D \approx 1 \times 10^{-5}$ $M_\odot$ $yr^{-1} \times 10^4$ yrs $\times 2{\times}10^{-2}$ ≈ 0.0005 $M_\odot$.

A further check on these numbers exists in the form of Planetary Nebulae. Taking our gas-to-dust mass ratio of 200, we can apply it to calculated ionized masses of optically thin PN (e.g. Barlow 1987; Meatheringham et al. 1988). Studies of LMC PNe tend to arrive at a mass range of 0.2–0.4 $M_\odot$ for the ionized component, which translates to a dust contribution of 5×10^{-5} – 0.002 $M_\odot$ for the dust component. This approach should be valid for low mass, optically thin PN which are thought to arise from the lower end of the LIMs mass range ($1 < M_i <$ 3–4 $M_\odot$).

The adopted dust yields for AGB stars are shown in Table 5.2, along with those adopted for other mass ranges.

It should be noted that these recipes for AGB dust yields are only valid at non-zero metallicities. At zero metallicity, low and intermediate mass stars is suppressed as the only dust which can be produced is from freshly synthesized heavy elements (mainly carbon) as there is no initial abundance of heavy elements which can form dust without being processed by the star (Morgan & Edmunds, 2003).

5.2.2 Core Collapse SNe Dust Yields

Table 5.1 summarises the published yields of dust observed from SNe or SNRs. In general, these yields were computed indirectly by comparing models of SN ejecta spectral energy distributions (SEDs) with observed SEDs. The models are optimised by altering the dust mass and composition until the best fit to the observed SED is determined. This technique has been widely used to constrain masses of warm ($\sim$ 100K) dust which emits strongly in the spectral range accessible to the Spitzer Space Telescope. The same technique was also used to measure colder dust in SNRs, at correspondingly longer wavelengths, with the SCUBA instrument mounted on the JCMT (e.g. Dunne et al. (2003)). More recently longer wavelength studies have been performed using the Herschel Space Observatory (e.g. Barlow et al. 2010).

Generally, the (warm) dust masses yielded by these studies have been in the range of 10^{-4} – 0.02$M_\odot$. Some authors had suggested dust masses in SNRs of the order of several solar masses (e.g., Dunne et al. (2003) 2-4 $M_\odot$ of dust for Cas A). However their results were shown to be subject to significant contamination by foreground interstellar dust (Krause et al., 2004). Cas A was later re-examined at far-IR and sub-mm wavelengths by Sibthorpe et al. (2010) at balloon altitudes and by Barlow et al. (2010) using the Herschel Space Observatory. These more recent papers found much lower dust masses (see Table 5.1) and explicitly corrected for the contamination by cold foreground interstellar dust.

Table 5.1: Published observations of SNII Dust Yields

SN/SNR	τ_{obs} (years)	T (K)	Yield ($M_\odot$)	Ref
1987A	3.2	150	5×10^{-4}	Dwek et al. (1992)
1987A	2.1	307	$> 10^{-4}$	Wooden et al. (1993)
1987A	17-18	166	2.6×10^{-6}	Bouchet et al. (2006)
1987A	2.1		1.3×10^{-3}	Ercolano et al. (2007)
1999em	1.8		$\sim 10^{-4}$	Elmhamdi et al. (2003)
2003gd	1.4		1.7×10^{-3}	Sugerman et al. (2006)
2003gd	1.3-1.8	250	4×10^{-4}	Meikle et al. (2007)
2004dj	3.4	115	8×10^{-4}	Szalai et al. (2010)
2004et	2.2	400	$< 2 \times 10^{-4}$	Kotak et al. (2009)
2006jc	1.4		3×10^{-4}	Mattila et al. (2008)
2007od	1.3		4×10^{-4}	Andrews et al. (2010)
2007it	2.0		1.3×10^{-4}	Andrews et al., (2011) submitted
Cas A	324[a]		< 0.054	Rho et al. (2008)
Cas A	326[a]	35	0.06	Sibthorpe et al. (2010)
Cas A	328[a]	35	0.075	Barlow et al. (2010)

[a] Assuming SN date of 1681 (Fesen et al., 2006)

A further possible complication arises from the breakdown of one of the major assumptions mentioned in the introduction. It has previously been assumed that *all* dust created by pre-SN phases of massive star evolution was destroyed by the SN shock (Jones et al., 1996; Zhukovska et al., 2008). The discovery of IR echoes from dust around SNe (e.g. Mattila et al. 2008) suggests that significant quantities of dust can be ejected by SN progenitors. In the case of SN 2006jc, Mattila et al. (2008) attributed the echo to a dust shell produced by the star while it was a luminous blue variable (LBV). It is far from certain though that any of the pre-CCSN dust can survive the SN shock once it reaches is, so we may be observing the dust immediately prior to its destruction. However if the dust-survival fraction is significant, of the order of $\sim$ 1–2%, this could be a major effect, and one that is difficult to quantify at present due to lack of data.

The average of recent dust mass estimates (Sibthorpe et al. (2010); Barlow et al. (2010)) for Cas A, the youngest SNR observed at far-IR and submm wavelengths ($\sim$ 250 years old), is around 0.067 $M_\odot$. The SN which created the Cas A remnant was Type IIb (Krause et al., 2008), implying a larger progenitor mass (20-30 $M_\odot$) than other "normal" SNII (8-20 $M_\odot$). Observations of recent, extragalactic, SNe which are all thought to have been "normal" Type II

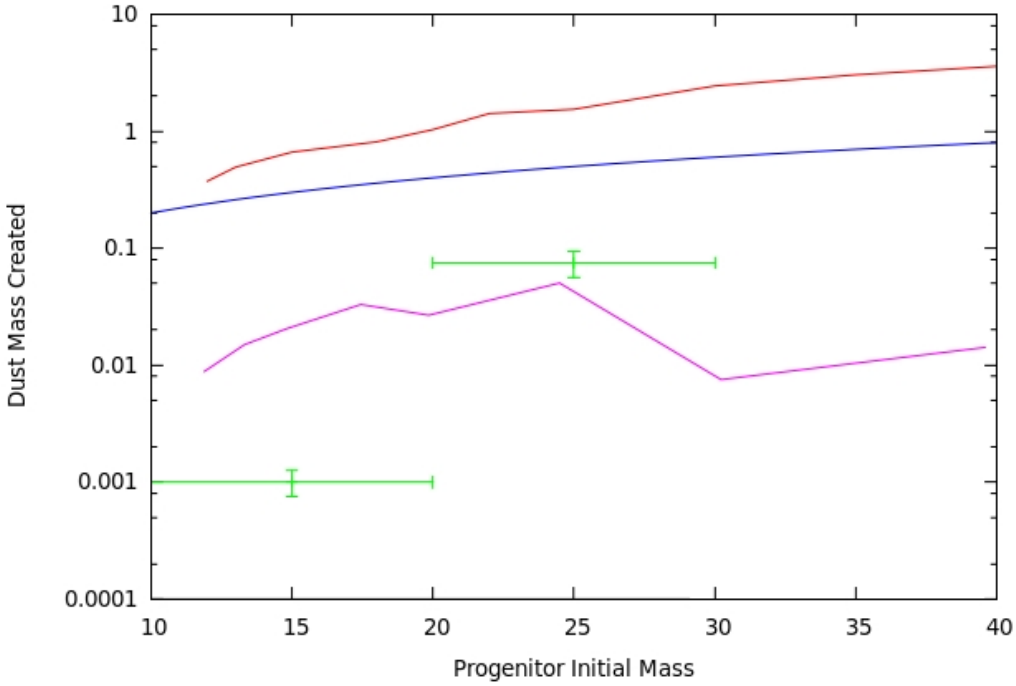

Figure 5.3: Adopted observational CCSN dust yields (green points); Red: Dwek et al. (2007) maximum model dust yields; Blue Nozawa et al. (2003) unmixed models dust yields; Purple: Valiante et al. (2009) model dust yields inferred from Bianchi & Schneider (2007) (purple). The units of each axis are solar masses ($M_{\odot}$).

SN, consistently indicate much lower dust masses, of around (3–17) $\times$ 10^{-4} $M_{\odot}$ (see Table 5.1).

We can draw from this some general conclusions, "normal" Type II SN can be shown to create, at most, $2\times$ 10^{-3} $M_{\odot}$ of dust. This figure is more likely to be in the range of a few $\times$ 10^{-4} $M_{\odot}$, due to differences in the initial mass of the SN listed in Table 5.1. SN II with more massive progenitors can potentially produce more dust due to the increased mass of their ejecta. If we take Cas A to be typical of the upper mass range of SNII's then the mass of dust produced per star could be in the 0.06-0.075 $M_{\odot}$ range. CCSNe of higher masses (Type Ib, Ic) are very difficult to constrain due to a lack of observational evidence. In Figure 5.3 we show our adopted dust mass yields along with theoretical predictions of dust yields from CCSNe. These adopted yields are summarised in Table 5.2.

5.2.3 Super-AGB (S-AGB) stars

The work of Thompson et al. (2009) suggests that a new category of dust-producing stars should be included. Stars with initial masses around 7-10 $M_{\odot}$ may experience a dust enshrouded phase which manifests itself via obscuration in the visible along with extremely red mid-infrared colours.

Table 5.2: Adopted Dust Yields

	Mass Range ($M_\odot$)	Average ($M_\odot$ per star)
SN II	9–20	5×10^{-4}
SN IIb	20–30	0.075
SN Ibc	30+	?
S-AGB[1]	6–9	0.01
AGB	1–8[2]	0.001

[1]: Where adopted

[2]: When S-AGB stars are included this range was 1–6

This is interpreted as representing an optically thick, short-lived, dust shell. In the case of SN2008S the dust was detected as a "light echo" when the dust was illuminated by the SN some months after the explosion, which allowed a lower limit to the mass of dust in the shell to be calculated (Wesson et al., 2010). Such relatively low luminosity events are rare in SN studies but it is not inconceivable that this is a phase through which many intermediate mass stars pass.

For S-AGB stars then, where we include them, we will take the Wesson et al. (2010) value of 0.01 $M_\odot$ for the mass of dust produced by all stars in the mass range 6-9 $M_\odot$ as their contribution to the overall dust budget of the galaxy. This value is ten times larger than that adopted for CCSNe with 9–20 $M_\odot$ progenitors. Standard IMFs predict many more stars in this S-AGB mass range than for CCSNe progenitors, indicating that these stars may have a greater effect than CCSNe.

Models not involving S-AGB stars will be included, since the inherent danger of extrapolating from one object is well understood, however their contribution could be vital in order to match the extremely large dust masses observed in the early universe.

5.3 Galactic Dust Evolution Model

5.3.1 Applicability of "local" dust yields to high redshift objects

For the purposes of our models of high redshift dusty galaxies and quasars we will assume that the dust production of individual objects varies negligibly with metallicity, i.e. we will use our solar metallicity dust yields at very low metallicity. This approximation is due to a lack of data, as the dust yields discussed in the previous section are neccessarily all from progenitors at near solar metallicity - i.e. those close enough that dust yields can be ascertained.

Massive, dusty high redshift quasars are presumed to be the progenitors of todays massive elliptical galaxies (Thomas et al., 2005). These galaxies are believed to have formed in a mas-

sive burst of star formation activity with star formation rates reaching 10^4 $M_\odot$ / year (Calura et al., 2009). Galactic Chemical Evolution models of these galaxies show that the oxygen abundance can reach within 0.2 dex of solar within the first gigayear (Calura et al., 2009).

This result has recently been strengthened by Matsuoka et al. (2009) who showed using VLT observations that high redshift radio galaxies at z $\sim$ 5 had largely completed their chemical evolution.

Our assumption that CCSNe dust yields are independent of redshift should hold as massive stars are known to produce the elements necessary for dust formation in the ejecta. For lower mass stars though the picture is less clear, stars with close to zero initial metallicity will have negligible secondary element production. This implies that they will only produce dust from elements they have directly synthesized – mainly carbon.

5.3.2 Stellar lifetimes

The relationship between stellar lifetimes τ_m and initial stellar masses m is relatively well constrained by theory. The stellar lifetime prescription has a large effect on the overall dust mass produced by the models as lower stellar lifetimes allow a given galactic dust mass to be reached faster.

In this work we will use the prescription of Raiteri et al. (1996) which paramaterised the models of the Padova group (Alongi et al. 1993, Bressan et al. 1993, Bertelli et al. 1994). This has the added advantage of being metallicity dependent, unlike other stellar lifetimes prescriptions (e.g. Maeder & Meynet 1989). The exact form of this parameterisation is:

$$\log(\tau_m) = a_0(Z) + a_1(Z)\log m + a_2(Z)(\log m)^2 \tag{5.2}$$

where

$$a_0(Z) = 10.13 + 0.07547\log_{10} Z - 0.008084(\log_{10} Z)^2, \tag{5.3}$$

$$a_1(Z) = -4.424 - 0.7939\log_{10} Z - 0.1187(\log_{10} Z)^2, \tag{5.4}$$

$$a_2(Z) = 1.262 + 0.3385\log_{10} Z + 0.05417(\log_{10} Z)^2. \tag{5.5}$$

and where τ_m is expressed in yr, m in solar units and Z is the metal mass fraction ($Z_\odot \simeq$ 0.02).

5.3.3 Initial Mass Function

Of the many Initial Mass Function (IMF) prescriptions available, most groups have used either a simple Salpeter IMF (Salpeter, 1955) or the multi-slope Kroupa IMF (e.g. Kroupa 2001a). Valiante et al. (2009) used the Larson (1998) prescription. Differing IMF prescriptions can have

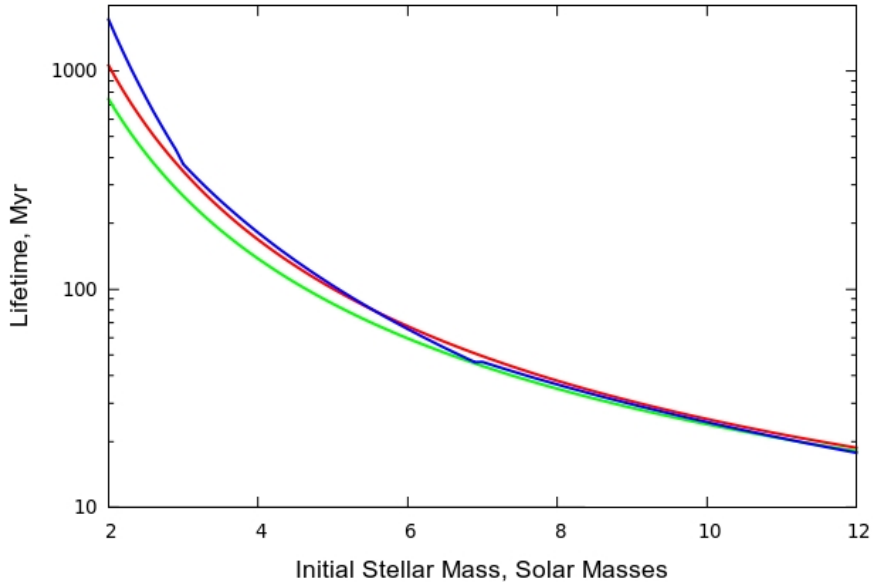

Figure 5.4: Plot of Lifetimes from Raiteri et al. (1996) at Z=0.02 (red), Raiteri et al. (1996) at Z=0.00002 (green), and the metallicity independent values of Maeder & Meynet (1989) (blue). The region shown is that of the AGB, S-AGB and low mass Type II SN progenitors - the differences in lifetimes at low metallicity can be important to acquire the high dust masses seen at high redshift.

a large influence on dust formation in the early universe as they define the relative numbers of high and low mass stars, which produce dust on different timescales. In this work we shall use a Salpeter type IMF with γ equal to 2.35, as we have previously seen in Chapter 4, Equation 4.2:

$$\left[\frac{dN}{d(\log_{10} M)}\right] = \phi(M) \propto M^{-\gamma} \tag{5.6}$$

In the context of our model we require a recipe for determining the number of stars N formed in given mass ranges corresponding to our input data for the stellar sources of dust discussed in Section 5.2. We can derive such an equation for the Salpeter IMF by re-arranging and integrating equation 5.6 to give:

$$N = \frac{N_0}{-1.35} \times (M_u^{-1.35} - M_l^{-1.35}) \tag{5.7}$$

where M_u and M_l are the upper and lower masses between which we would like to calculate the number of stars and in this formulation N_0 describes the total number of stars we would expect from 1 $M_\odot$ of star formation.

$$N_0 = \frac{-0.35}{M_{ul}^{-1.35} - M_{ll}^{-1.35}} \tag{5.8}$$

where M_{ul} and M_{ll} are the upper and lower limits over which we are calculating our IMF, in this case 0.1 – 120 $M_{\odot}$.

5.3.4 Dust Destruction Timescales

The timescales on which dust is destroyed in galaxies have been the subject of some debate. Simple parameterisations dependent on the rate of supernovae have been mooted which take the following form (Dwek, 1998; Dwek et al., 2007):

$$\tau_{dwek} = \frac{M_g(t)}{m_{ISM} R_{SNII}} yr \tag{5.9}$$

where $M_g(t)$ is the gas mass of the galaxy, m_{ISM} is the mass of gas in which a single SNe will destroy all the dust and R_{SN} is the rate of supernovae over the whole galaxy. With a Salpeter intial mass function R_{SN} takes the form:

$$R_{SNII} = \frac{\psi(t)}{147} yr^{-1} \tag{5.10}$$

where ψ is the star formation rate (SFR) in $M_{\odot}$ yr^{-1} and assuming that massive stars have effectively zero lifetime. Equation 5.9 presents a way of quantifying dust destruction by massive stars over correspondingly short timescales.

Type Ia SNe have been shown (Blinnikov & Sorokina, 2004) to have roughly equivalent energies to CCSNe, and as such we propose that at later times dust destruction by SNIa would have a similar effect upon the galactic dust mass. Following the Dwek (1998) parameterisation we arrive at the following:

$$\tau_{SNIa} = \frac{M_g(t)}{m_{ISM} R_{SNIa}} yr \tag{5.11}$$

where the quantities have the same meaning as in Equation 5.9, except R_{SNIa} which is the rate of SNIa.

Before proceeding it is useful to examine the meaning of these quantities. The form of τ is such that we are assuming that both types of SN are evenly spread throughout the entire galaxy. The long lifetimes of low mass stars suggest that this is a good approximation for τ_{SNIa}, however massive stars are known to exist mainly in clusters. If we consider the lifetime of a massive star cluster, we would guess that the most massive star would become the first supernova, its blast waves would destroy all of the dust in a certain mass of dust as quantified earlier. The subsequent SNe are unlikely to destroy the same amount of dust as they are co-located with the first SN. We might then formulate an equation such that:

$$\tau_{SNII} = \frac{M_g(t)}{m_{ISM}\left(\frac{R_{SNII}}{\omega}\right)} \tag{5.12}$$

Where the CCSN clumping factor, ω is the average number of stars which will explode as CCSNe in an average massive star cluster. Using a Salpeter IMF in the range 0.1–120 $M_\odot$, roughly 0.2% of stars will have masses greater than the ~ 10 $M_\odot$ required to become a CCSN. Portegies Zwart et al. (2010) suggests that young massive star clusters contain 10^3 – 10^6 stars implying that ω should range between 2 and 2000. This is at best a crude approximation, albeit one worthy of future study as the limit set on ω here allows τ values which will go from almost no dust destruction to dust destruction as quantified by Dwek (1998). It is also important to note that ω could, in principle, be very different in different types of galaxies in that starburst galaxies tend to have very massive star clusters[4]while more quiescent galaxies have smaller clusters.

In both equations m_{ISM}, the mass of gas in which all dust is destroyed, is taken to be around $500M_\odot$ following Dwek (1998). The main uncertainty with this value arises not from SN having different explosive energies, SN Ia and CCSNe both produce around 10^{51} ergs, but from differences in the density and composition of the surrounding ISM; CCSNe will usually reside in star formation regions while SN Ia should be evenly distributed in the disk and bulge.

5.3.5 Numerical Modelling

For a galaxy with a known Star Formation History (SFH) we can construct a simple model to estimate the maximum amount of dust formed over a given time frame. At each time step dt we can find the number of stars formed in different mass ranges by multiplying Equation 5.7 by the SFR $\psi(t)$:

$$N_{M_l}^{M_u} = \psi(t) \times \frac{N_0}{-1.35} \times (M_u^{-1.35} - M_l^{-1.35}) \tag{5.13}$$

By iterating through mass ranges from $0.7 - 120M_\odot$ with a granularity of around $dM = 0.01M_\odot$ we can apply the stellar lifetime prescriptions to find when the dust formed by stars in each mass range will be returned to the ISM. The quantity of dust created as a function of time can be thought of as a one dimensional array with bins of size dt, at each point in this array we store the cumulative mass of dust that would be released by each star which would return its dust to the ISM in this epoch.

In the simplest model of galactic dust formation - one with no destruction - the total dust mass at time $t_n = n \times dt$ is simply the sum of each of the n bins of our array which lie between

[4]M82 for example, posesses at least five "super" star clusters with masses up to 10^5 $M_\odot$ (Smith et al., 2006).

$t = 0$ and $t = t_n$. In our models though we complicate this slightly such that we can track the relative contributions of the three main sources of dust: SNII, AGB & S-AGB stars. The dust produced at each timestep can be stated as:

$$\frac{dM_d(t)}{dt} = \int_{M_{\tau_M}}^{120} \psi(t - \tau_M)\phi(M) \left(\frac{q_{dust}}{M}\right) dm - \psi(t)\frac{M_d}{M_g} - \frac{M_d(t)}{\tau(t)} \tag{5.14}$$

where τ_M is the age of a star of initial mass M, M_{τ_M} corresponds to the lowest mass where $\tau_M > t$ and q_{dust} is the dust yield as presented in Table 5.2 and M_d, M_g represent the galactic dust and gas masses respectively. The first factor in Equation 5.14 represents dust creation, the second dust destruction via SN and the third dust astration via star formation. This is a closed box model as we are not invoking infalls or outflows of matter. **Equation 5.14 is in essence a restatement of Dwek et al. (2007)[Equation 16].**

Our model tracks the masses of dust created by our three classes of dust producers as described above. The dust created by AGB and S-AGB stars is assumed to be instantly mixed into the disk (as this is where the majority of low mass stars will end their lives). The assumption of perfect mixing allows us to apply the dust destruction lifetime as a dust survival fraction per timestep based on the dust destruction rate (Dwek, 1998)):

$$\frac{dM_D(t)}{dt} \propto -\frac{M_D(t)}{\tau} \tag{5.15}$$

Where τ represents the appropriate dust destruction lifetime, M_D is the mass of dust in the model and ${}^{dM_D(t)}/_{dt}$ is the rate of change of the dust mass. Neglecting other factors and considering merely the rate of dust destruction, i.e.:

$$\left(\frac{dM_D(t)}{dt}\right)_{dd} = -\frac{M_D(t)}{\tau} \tag{5.16}$$

Where $({}^{dM_D(t)}/_{dt})_{dd}$ is the rate of dust destruction, we find an equation that is trivially integrable to the form:

$$M_D(t + dt) = M_D(t) \times e^{-\frac{dt}{\tau}} \tag{5.17}$$

This allows us to calculate the remaining dust mass after any timestep given the dust destruction lifetime.

SNII dust is assumed to be confined, at least during period of intense star formation, to the high mass star formation regions in which it is created. This implies that it should be susceptible to dust destruction driven by the coincident massive stars exploding as SNe and not strongly influenced by the evolution of lower mass stars until the star formation episode ceases and the

dust which has survived in the SF region merges with the rest of the dust in the disk. Thus SNII dust is created and destroyed on a different timescale to that created by AGB/S-AGB stars, until the galaxy enters a quiescent, phase whereupon the dust destruction rate is solely dependent on SNIa dust destruction.

It is important to note that this model is not self consistent in that we are not attempting to model the parameters which can control, for example, star formation. The star formation rate is typically treated as a function of the surface gas density and/or total galactic mass (Salpeter 1955; Kennicutt 1998. We have to define a Star Formation History (SFH) as an input to the model, however several specimen SFHs can be drawn from the literature and from successful Galactic Chemical Evolution (GCE) models.

5.3.6 Simple Galaxy models

The first test of this model is to compare it against previously published simple galaxy models. The first such example, was that presented by Morgan & Edmunds (2003) in their Figure 8. We show a comparison of the current model versus that of Morgan & Edmunds (2003) in Figure 5.5 using a constant SFR of 1 $M_{\odot}$ per year for a galaxy of mass 2×10^{10} $M_{\odot}$. The two models agree over the regime which was presented by Morgan & Edmunds; we have also shown the subsequent evolution of this galaxy. In the regime of a constant SFR, the dust from AGB stars will come to dominate (as shown in Figure 5.6) and dust destruction/creation processes start to find an equilibrium state. The dust destruction process is important at late times in this model as the Type Ia SNe begin to occur in significant numbers.

As mentioned in Section 5.3.1, the kinds of galaxies we ultimately wish to model have very different star formation histories than that presented in Figure 5.5. Massive elliptical galaxies have been inferred to complete almost all of their star formation at the start of their lives, usually in a very intermittent manner[5]. To sketch this process, I invoke a SFR which has bursts of star formation followed by periods of quiescence for the first 250 Myrs of its history. The behaviour of the dust mass is shown in Figure 5.7.

In Figure 5.7 the influence of dust destruction is obvious. The total dust mass reaches a equilibrium state where the dust destruction by Type Ia SNe is balanced by the dust created by AGB stars. The effect that dust destruction has on the total dust mass in this model is shown in Figure 5.8, where we compare the same model as shown in Figure 5.7 with a model which is identical except for dust destruction which has been disabled. In the first model dust destruction processes are destroying more than 50% of the dust created.

[5]This may be via intermittent starbursts quenching star formation via galactic mass ejection or multiple mergers.

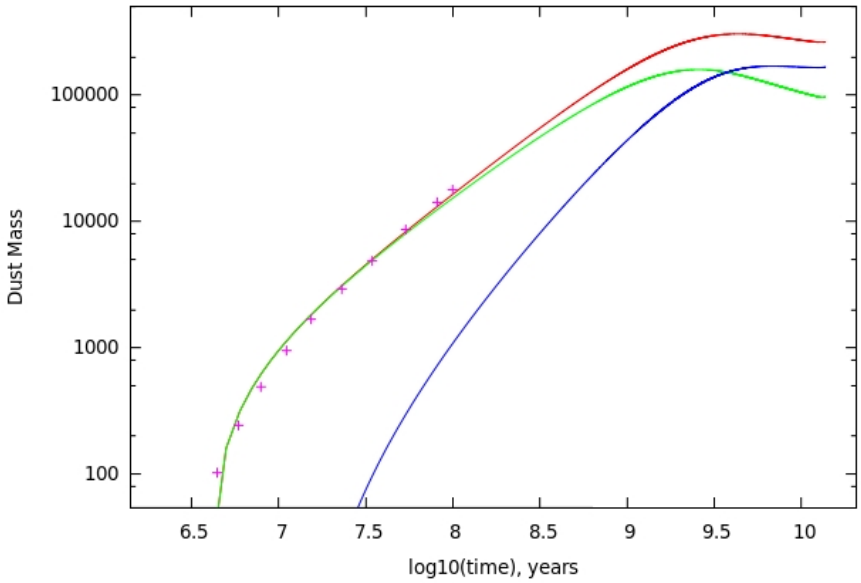

Figure 5.5: Comparison of the dust mass versus age model we have developed here (total dust mass in red, SN dust mass in green, AGB dust mass in blue) versus that presented by Morgan & Edmunds (2003) (mauve points).

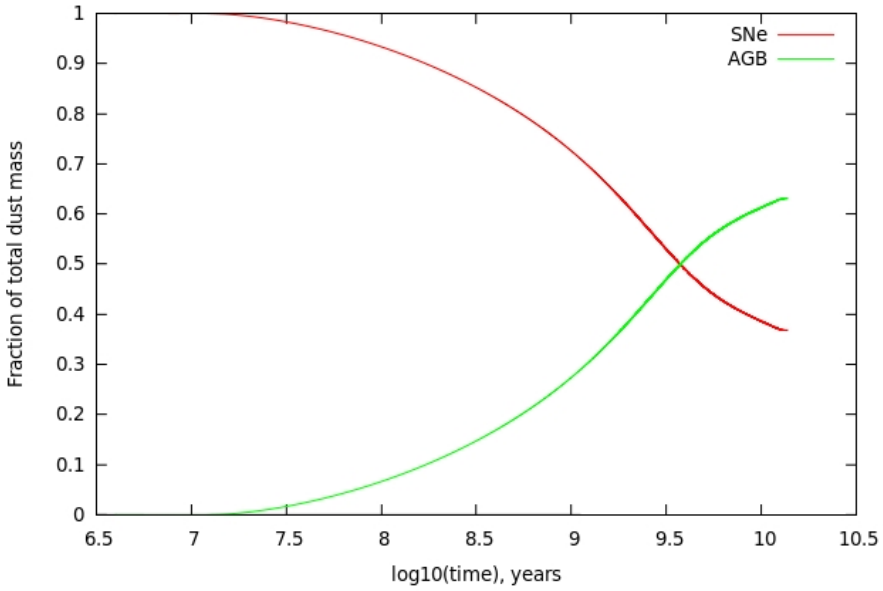

Figure 5.6: The fraction of total dust mass provided by SNe (red) and AGB stars (green), as a function of time.

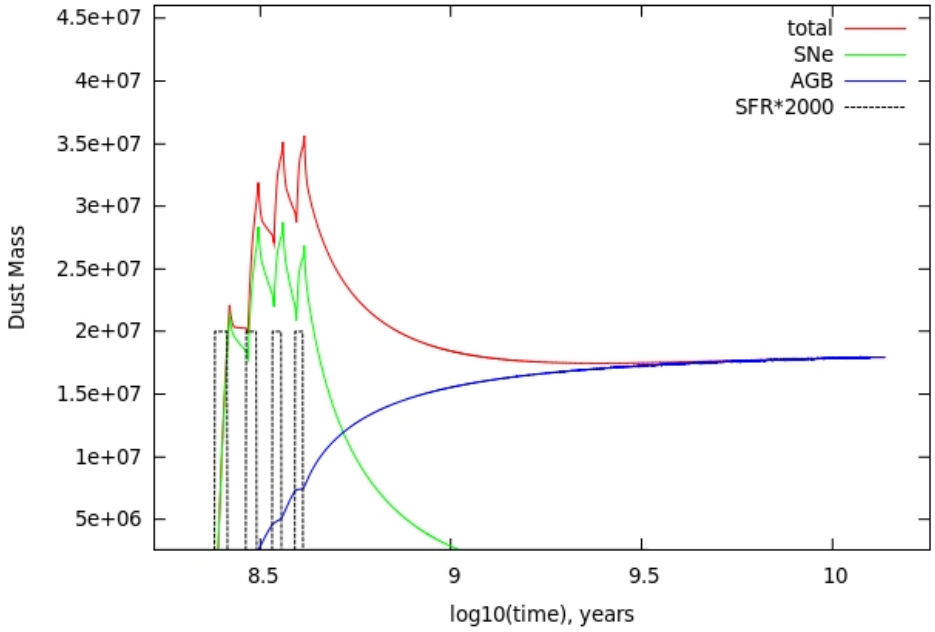

Figure 5.7: Simple dust mass versus age model for an elliptical galaxy with bursts of star formation. Shown are the total dust mass (red), SN II dust mass (green), AGB dust mass (blue), plus 2000 $\times$ SFR (multiplied for visibility, black dashed). See text for more details.

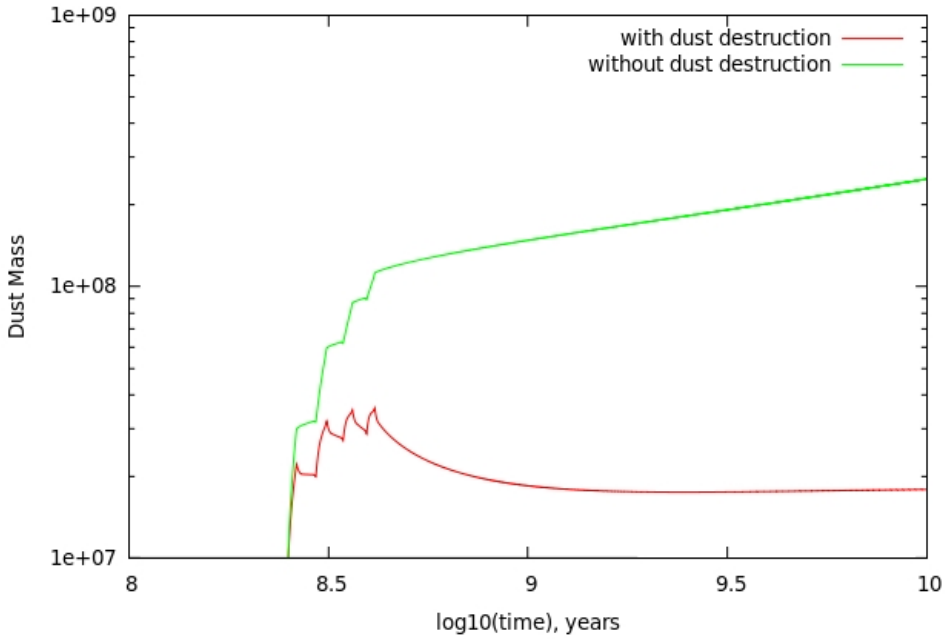

Figure 5.8: Simple model of an elliptical galaxy with bursts of star formation as in Figure 5.7. Shown are the total dust mass from the model with dust destruction (red) and the total dust mass for the same model where dust destruction has been disabled (green).

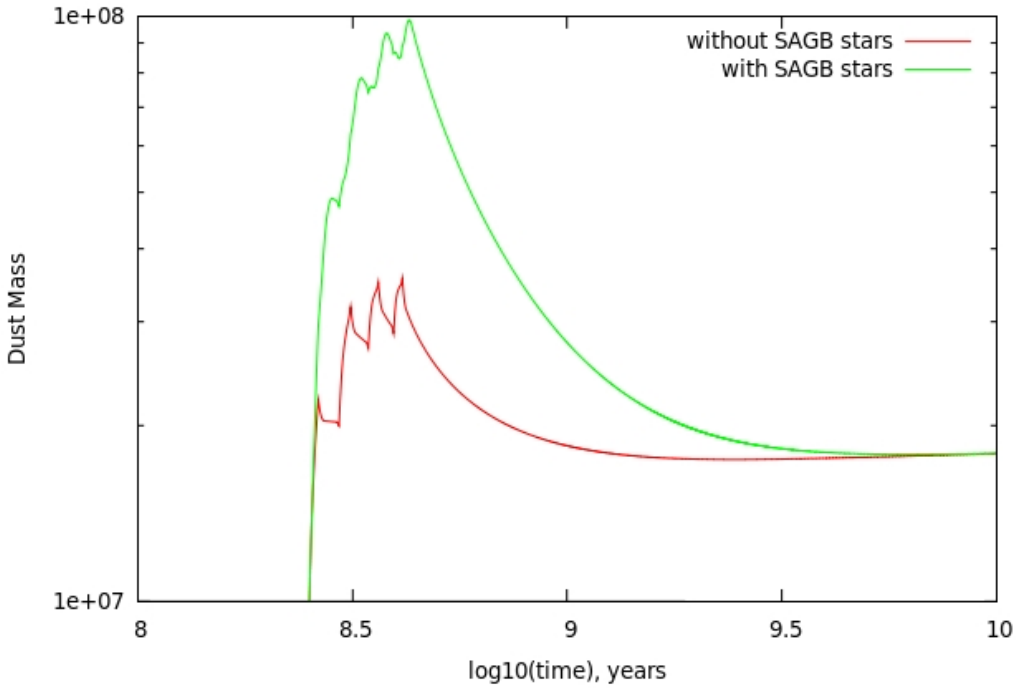

Figure 5.9: Simple model of an elliptical galaxy with bursts of star formation with the effects of S-AGB stars included. Shown are the total dust mass as a function of time from Figure 5.7 (red) along with the same model with S-AGB stars included (green).

5.3.6.1 Simple Models with S-AGB stars

In Figure 5.9 we show the effects of using a SFH with intermittent bursts of star formation identical to that used in Figure 5.7 but including the effects of S-AGB stars in the manner described in Table 5.2. The peak total dust mass is more than doubled by the inclusion of these objects, implying that if 6–9 $M_{\odot}$ stars do create as much dust as suggested by Wesson et al. (2010), they could be the dominant producers of dust in high redshift galaxies.

5.4 SDSS J1148+5251 Models

The classic example of a high redshift dusty galaxy, SDSS J1148+5251 (Bertoldi et al., 2003), has been studied in some detail by various groups. The intial observations, by Bertoldi et al. (2003), showed that SDSS J1148+5251 was at redshift z=6.42, had a far-IR luminosity of L_{FIR} = 1.2 $\times$ 10^{13} $L_{\odot}$ and an inferred dust mass of $\sim$ 7 $\times$ 10^{8} $M_{\odot}$. Subsequent observations by Beelen et al. (2006) largely agreed with these findings, finding L_{FIR} = 2.2 $\times$ 10^{13} $L_{\odot}$ and M_D = 4.2 $\times$ 10^{8} $M_{\odot}$. We will adopt a total galaxy mass in line with that adopted by previous studies — of the order $M_{J1148+5251} \sim 10^{12}$ $M_{\odot}$ (Valiante et al., 2009).

From the point of view of this study, the most important result was derived by Li et al. (2007). In that work the star formation history (SFH) of SDSS J1148+5251 was computation-

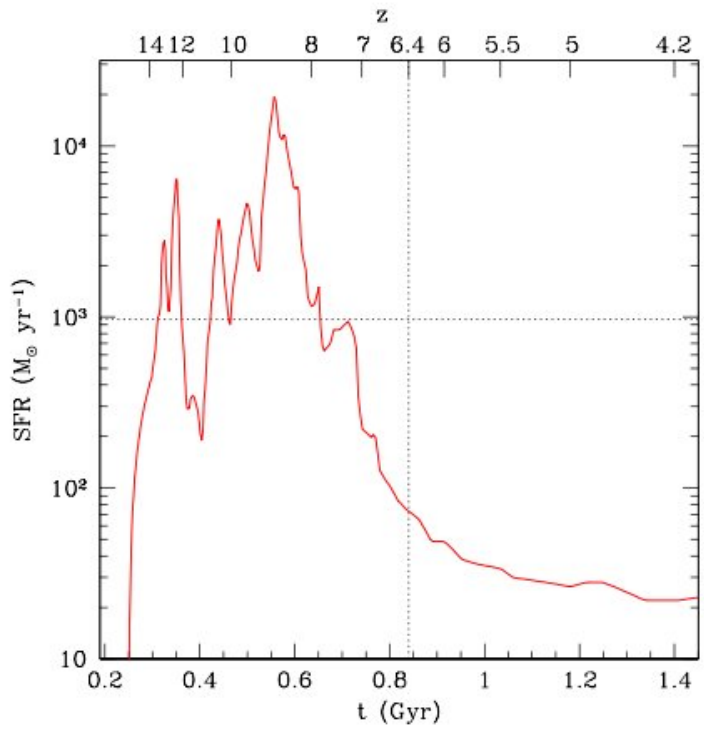

Figure 5.10: Star formation history (SFH) of J1148+5251 as modelled by Li et al. (2007) and adopted by Valiante et al. (2009). The horizontal line represents the average SFR before the time of observation, the vertical line represents the epoch at which the quasar was observed.

ally modelled to best match the observed properties of the galaxy. The star formation history, in the form which we will use, was presented by Valiante et al. (2009); (Figure 5) and is reproduced here as Figure 5.10.

According to Figure 5.10, SDSS J1148+5251 has undergone intermittent phases of intense star formation and relative quiescence. This arose in the models of Li et al. (2007) because they employed a multiple merger model. As was mentioned in the introduction, the peak SFR in the Li et al. (2007) model occurs significantly before ($\sim$ 270 Myrs before) the epoch at which the dust mass is being measured. This suggests an AGB origin for the dust should the Li et al. (2007) SFH be correct. However the SFH of this galaxy is assumed to start at t $\sim$ 250 Myr after the Big Bang and to finish at around 1.5 Gyr, so it is quite plausible that the strongest burst of star formation could be somewhat later, thus reducing the gap and increasing the likely CCSN dust contribution. For our models of SDSS J1148+5251, if the peak dust mass achieved is in the range that has been derived observationally for SDSS J1148+5251 we would consider that model to match the observations.

When the SFH from Figure 5.10, is incorporated into our model, as shown in Figure 5.11,

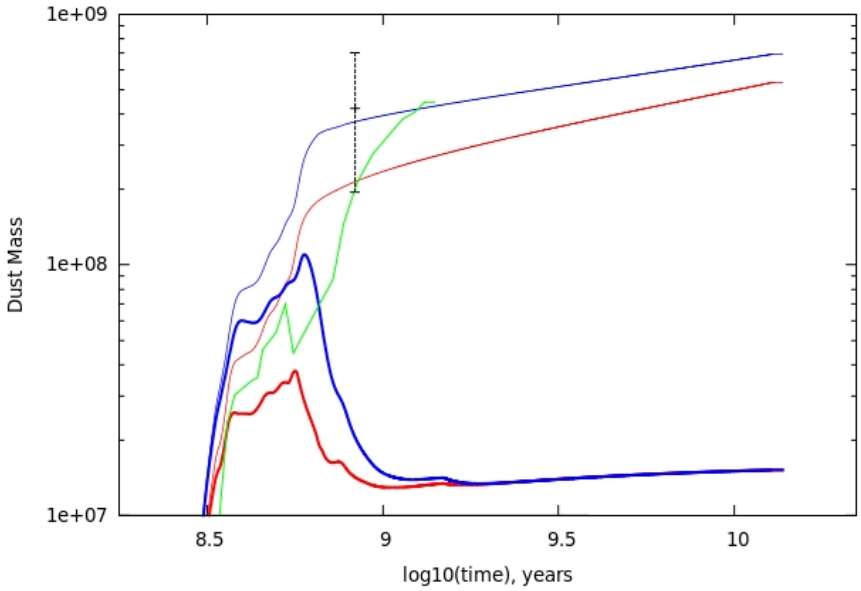

Figure 5.11: Total dust masses generated by models without S-AGB stars (red lines) and models with S-AGB stars (blue lines). The thin lines represent models where dust destruction was disabled. The model of Valiante et al. (2009) is shown in green while the black error bar represents the estimated dust mass in SDSS J1148+5251 (Bertoldi et al. 2003; Beelen et al. 2006).

it is clear that the dust mass observed in SDSS J1148+5251 cannot be reached by models which feature dust destuction. The Valiante et al. (2009) model is also shown in Figure 5.11. We attribute the larger dust masses that they found post-starburst to the fact that SNIa dust destruction was not included in their model. Their model includes only CCSN dust destruction, as discussed earlier, such that when the starburst has ceased, dust destruction ceases and the dust created by AGB stars is no longer destroyed.

In Figure 5.12 the effects are shown of disabling SNIa dust destruction and changing the dust yields to roughly match those used by Valiante et al. (2009). The general behaviour of the Valiante et al. (2009) model is reproduced in that we see an early peak in the dust mass which is largely generated by SNII, followed by a slight dip caused by astration during the most intense period of star formation activity. Subsequently AGB dust comes to dominate as it has no destruction mechanism in this model.

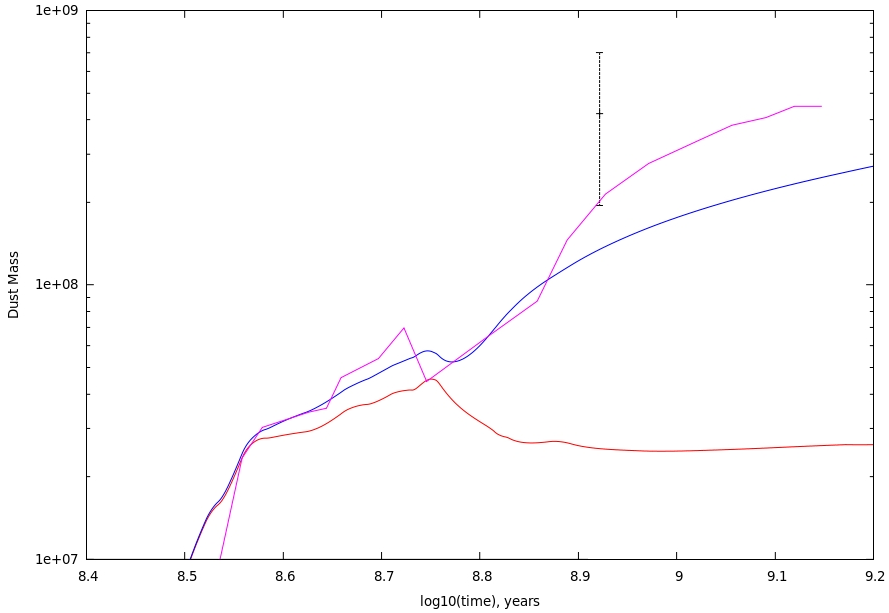

Figure 5.12: Modifying the model to match the parameters used by Valiante et al. (2009). Blue: our model with enhanced yield and disabled SNIa dust destruction; Pink: the Valiante et al. (2009) model; and Red: our model with enhanced yields but including the effects of SNIa dust destruction. The black error bar is the estimated SDSS J1148+5251 dust mass as shown in Figure 5.11, see text for more details.

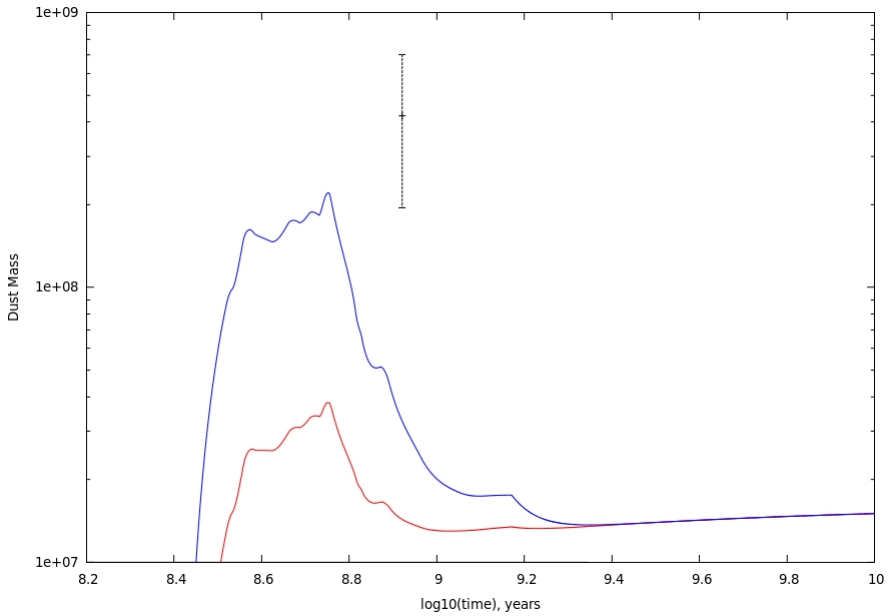

Figure 5.13: The effect of including an η Carinae-like dust production of 0.4 $M_{\odot}$ per star for stars with initial masses greater than 60 $M_{\odot}$. The red line is the total dust mass as in Figure 5.11 (without S-AGB contributions), the blue line is the total dust mass including the η Car-like enhanced dust production rate. The black error bar is the SDSS J1148+5251 dust mass estimate as shown in Figure 5.11 .

5.5 Discussion

5.5.1 Pre-SNe Dust Yields

In the introduction it was briefly mentioned that it was usually assumed that Type II SNe completely destroyed all pre-existing dust. Luminous Blue Variable stars (LBVs) and certain types of carbon rich WR stars (WC binaries) are known to produce dust. For example 0.4 $M_{\odot}$ of dust has been measured around the LBV η Carinae (Gomez et al., 2010) which is thought to have been formed during one of its "giant eruptions" in the 19^{th} century.

If we assume that the 0.4 $M_{\odot}$ produced by η Carinae is typical of stars with initial masses above 60 $M_{\odot}$, we get almost a factor of 2.6 increase in the peak dust mass produced by our model (see Figure 5.13).

5.5.2 The effects of varying τ_{SNII}

In Figure 5.14 we show the effects of varying the CCSN clumping factor ω discussed in Section 5.3.4. Models were computed using omega factors of 1 (as used in all previous models), 2, 20 and 2000. The ω = 2000 model is almost identical to the model in which SNII dust destruction was suppressed entirely and hence not shown in Figure 5.14.

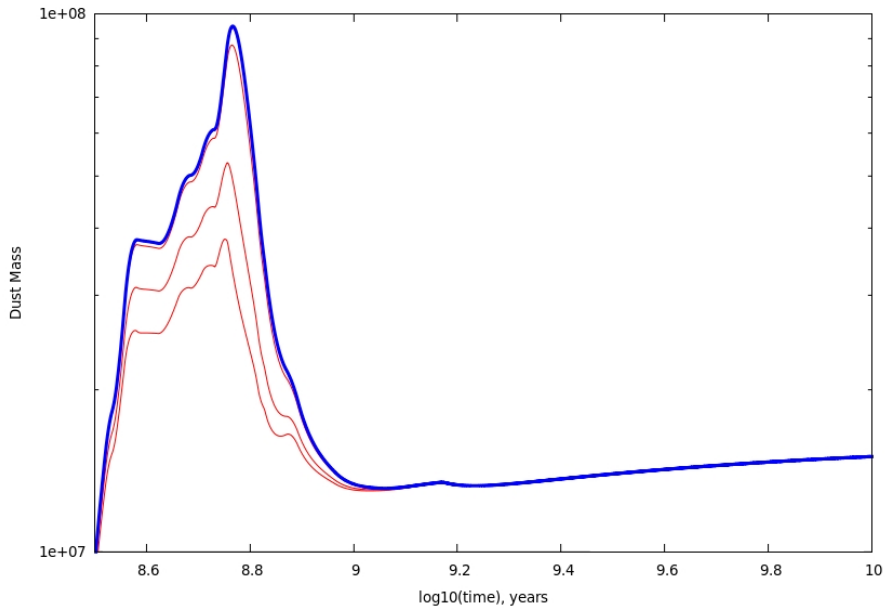

Figure 5.14: Exploring the effects of changing the dust destruction timescale for SNII dust. The red lines of increasing peak dust mass correspond to ω = 1, 2, 20 where ω is the CCSN clumping factor. The thick blue line corresponds to a model where SNII dust destruction was disabled.

When the ω value is increased, the peak dust mass, relative to the ω = 1 peak dust mass, also increases by the following factors: 1.4 ($\omega = 2$), 2.3 ($\omega = 20$) and 2.5 ($\omega = 200$ / CCSN dust destruction disabled). Most of the variation in this factor comes in the range ω = 2 – 20, which corresponds to average cluster masses in the range of 10^3 – 10^4 $M_\odot$; so if average cluster masses exceed 10^4 $M_\odot$, CCSN dust destruction effecrs will be negligible.

5.6 Conclusions

In order to reach the lower bound of the amount of dust in SDSS J1148+5251 ($\sim 2 \times 10^8$ $M_\odot$) with SN dust only, then in common with Dwek & Cherchneff (2011), we find that a SN dust yield of 0.1 $M_\odot$ is required for every star with an initial mass above 10 $M_\odot$. However, this is about two orders of magnitude above the current observational dust mass limits discussed earlier (Table 5.1) for "normal" Type II SNe in the mass range 10 – 20 $M_\odot$.

If all stars above 60 $M_\odot$ produce 0.4 $M_\odot$ of dust and the majority of this dust survives the eventual SN event, then the total dust mass produced can enter the J1148+5251 range.

Using the yields specified in Table 5.2 we cannot match the dust mass in SDSS J1148+5251 using the SFH presciption of Li et al. (2007). Under certain conditions[6]we can match the results of several previous dust evolution models such as those presented by Morgan

& Edmunds (2003) and Valiante et al. (2009).

The effects of S-AGB stars can be dominant if we follow the assumption that SN 2008S has produced a typical amount of dust for a star in the upper section of the AGB mass range $\sim 6 - \sim 9$ $M_{\odot}$.

We have introduced two new ideas in terms of dealing with dust destruction, firstly, that the CCSNe destruction is attenuated by a factor describing the co-location of CCSNe (the CCSN clumping factor) which is introduced as a modification to the Dwek (1998) prescription (see Equation 5.9) and secondly, that Type Ia SNe can have comparable effects to those of CCSNe. Dwek & Cherchneff (2011) noted in their conclusions that the Dwek (1998) dust destruction timescale (Equation 5.9) does not account for the spatial component of CCSNe dust destruction. However they did not quantify this as it has been in this Chapter.

The intoduction of the CCSN clumping factor implies that CCSNe driven dust destruction may be negligible under certain circumstances — where we would expect large clusters of massive stars. However, as we noted in Section 5.3.5, this factor is an initial approximate correction for the true dust destruction rate as in principle one would have to include the effects of "runaway" massive stars which have escaped the clusters in which they were born, and the physical dimensions of clusters. However, it does provide a plausible route to maximise the fraction of dust that can survive — which may go some way towards explaining the high dust masses observed.

Type Ia SN driven dust destruction may be of importance to high redshift, dusty galaxies — however the relative importance of this avenue increases dramatically at late times and it allows us to explain why massive galaxies have high dust masses at high redshifts and comparatively low dust masses, as massive elliptical galaxies, in the local universe.

[6]Primarily neglecting dust destruction, but also with slight tweaks to the stellar dust yields.

Chapter 6

Conclusions

> "I try not to think with my gut. If I'm serious about understanding the world, thinking with anything besides my brain, as tempting as that might be, is likely to get me into trouble. Really, it's okay to reserve judgment until the evidence is in."
> — Carl Sagan

In this thesis a search for evidence regarding the origins and evolution of elemental carbon and of dust has been presented. This work was prompted by the realisation that while massive stars are predicted to have large carbon yields, there is absolutely no observational evidence to corroborate this idea. The opening half of the thesis describes the search for nebulae around evolved, massive stars which may have exhibited evidence for high carbon yields and subsequent spectroscopic investigation in which it was shown that the nebulae which were deemed the most likely targets (those around carbon rich WR stars) did not display any traces of anomalous carbon abundances. Clearly, this does not rule out the idea that WC stars can produce copious amounts of carbon, it merely shows us that enhanced carbon is not present in those circumstellar nebulae which we observed.

However this does not render the search unfruitful, in Chapter 2 previous claims that ejecta type nebulae were present around many WR stars were shown to be false, and a new ejecta type nebulae was discovered around WR 8. A tentative anti-correlation between binarity and ejecta type nebulae was also established. The newly discovered ejecta type nebula around WR 8 was shown to display striking abundance enhancements in Chapter 3, a success for the concept of being able to categorise the origins of circumstellar nebulae via morphological categorisation. As mentioned, the carbon lines which were going to be used to derive carbon abundances were not detected in the sample of nebulae, with one puzzling exception: NGC 3199. The [C I] lines detected around NGC 3199 were found to most likely not be collisionally excited, but a product of C^+ recombination in PDRs — though with the mysterious and unexpected property of having the same FWHM as the collisionally excited lines from the ionized gas.

The question of "where is all the carbon that should be produced by massive stars?" remains unanswered though, and the position remains that where more observational evidence is needed to be certain that massive star carbon yields are of the same order of magnitude as have been predicted – possible avenues of investigation will be discussed below.

Chapters 5 and 4 investigated the evolution of gas-phase abundances in the Milky Way (MW) and dust masses in high redshift galaxies respectively. These topics may seem rather disparate, however they are linked by the tools used to investigate them. In Chapter 4 the evolution of carbon and oxygen in the MW was examined using chemical evolution models. It was found that, in line with other recent studies, low- and high-mass stars can both play a significant role in carbon production. In particular, using different combinations of published stellar yields, either mass range can be dominant in the production of carbon. Clearly, the true story may be somewhere between the two extremes, however in light of the previous discussion it is currently difficult to justify the position that massive stars produce a great deal more carbon than lower mass stars.

In Chapter 5 the GCE models of the previous chapter were re-purposed such that the yields involved now represented dust yields — allowing the same kind of model to be used for a very different context. The models were then computed with prameters aimed at closely matching those of high redshift, dusty galaxies and quasars discusssed. Several potentially important effects were included regarding dust destruction that have not been discussed by previous authors. Firstly, Type Ia SN have similar explosive energies as CCSNe, and therefore could also contribute to dust destruction. Secondly, a CCSN clumping factor was introduced as a way of allowing for the co-location of CCSN progenitors in clusters. The CCSN clumping factor suggests that CCSNe dust destruction may be negligible in some types of galaxy that preferentially form stars in high mass clusters ($> 10^4$ $M_\odot$).

6.1 Future Work

This work has suggested several new avenues of enquiry that may be fruitful. In the first chapter survey imagery from the SHS survey was used to search for nebulae around WR stars. The next large survey of the southern galactic plane, VPHAS+[1], will be digital rather than photographic and deeper than the SHS survey. This should enable a new search for fainter WR nebulae in the galactic plane. The resolution and sensitivity of the SHS survey also precluded an equivalent search for nebulae around LMC WR stars, a situation which could be rectified by using a suitably adaptive optics equipped instrument to improve the angular resolution.

[1] http://www.vphas.org/

A further proposal utilising the UVES instrument on the VLT is in preparation to observe the now bona-fide ejecta nebulae around WR 8 and possibly WR 16. The nebula around WR 8 in particular may yield the heavy element recombination lines which were not detected in NGC 3199 and allow quantification of the CEL versus recombination line abundance discrepancy. The WR 8 nebula also has the advantage of a stronger ionizing source (WR 8 is WC4/WN7 spectral type) which favours the detection of oxygen lines which will allow the determination of an accurate N/O ratio. In the new proposal UVES will be set up in such a way that we can access the temperature sensitive [N II] 5755Å line, which will allow the first accurate determination of the nebular temperature in a WR ejecta nebula. Any progress in finding evidence of carbon around massive stars would help constrain their carbon yields, which in turn would increase our faith in using massive star yields with significant carbon components in GCE models.

Further work regarding the models presented here would focus on a more formal treatment of massive star dust destruction and creation. The CCSN clumping factor discussed earlier is an interesting starting point, however it may be too simple to be an accurate representation of the true role CCSNe play in galactic dust evolution. The next stage of investigating this idea would be to model individual star formation regions using the current estimates of their size and mass to see how much overlap we would expect between the ejecta from each SN. Using Monte-Carlo techniques we could then generalise this process across various physically plausible cluster mass ranges which would allow quantification of the effects of CCSNe on the dust content of galaxies.

Should the search for carbon in nebulae around WR stars prove fruitless, there are other ways to begin to quantify the carbon yields of WR stars. The carbon mass loss rate can be derived via spectroscopy of the WR winds, however this ties the total carbon yield to the lifetime of the WR star in its carbon rich phase – which is very uncertain.

Bibliography

Abell, G. O. 1966, ApJ, 144, 259

Akerman, C. J., Carigi, L., Nissen, P. E., Pettini, M., & Asplund, M. 2004, A&A, 414, 931

Alongi, M., Bertelli, G., Bressan, A., Chiosi, C., Fagotto, F., Greggio, L., & Nasi, E. 1993, A&AS, 97, 851

Alpher, R. A., Bethe, H., & Gamow, G. 1948, Phys. Rev., 73, 803

Alpher, R. A., & Herman, R. C. 1948, Phys. Rev., 74, 1737

Andrews, J. E., et al. 2010, ApJ, 715, 541

Arimoto, N., Sofue, Y., & Tsujimoto, T. 1996, PASJ, 48, 275

Arnett, W. D., & Schramm, D. N. 1973, ApJ, 184, L47+

Asplund, M., Grevesse, N., Sauval, A. J., & Scott, P. 2009, ARA&A, 47, 481

Baluja, K. L., & Zeippen, C. J. 1988, Journal of Physics B Atomic Molecular Physics, 21, 1455

Barlow, M. J. 1987, MNRAS, 227, 161

Barlow, M. J., et al. 2010, A&A, 518, L138+

Bastian, N., Covey, K. R., & Meyer, M. R. 2010, ARA&A, 48, 339

Beals, C. S. 1929, MNRAS, 90, 202

Beelen, A., Cox, P., Benford, D. J., Dowell, C. D., Kovács, A., Bertoldi, F., Omont, A., & Carilli, C. L. 2006, ApJ, 642, 694

Berrington, K. A. 1988, Journal of Physics B Atomic Molecular Physics, 21, 1083

Berrington, K. A., & Burke, P. G. 1981, Planet. Space Sci., 29, 377

Bertelli, G., Bressan, A., Chiosi, C., Fagotto, F., & Nasi, E. 1994, A&AS, 106, 275

Bertoldi, F., Carilli, C. L., Cox, P., Fan, X., Strauss, M. A., Beelen, A., Omont, A., & Zylka, R. 2003, A&A, 406, L55

Bethe, H. A. 1939, Phys. Rev., 55, 434

Bianchi, S., & Schneider, R. 2007, MNRAS, 378, 973

Blinnikov, S., & Sorokina, E. 2004, Ap&SS, 290, 13

Boothroyd, A. I., Sackmann, I., & Wasserburg, G. J. 1995, ApJ, 442, L21

Bouchet, P., et al. 2006, ApJ, 650, 212

Bowen, G. H., & Willson, L. A. 1991, ApJ, 375, L53

Bressan, A., Fagotto, F., Bertelli, G., & Chiosi, C. 1993, A&AS, 100, 647

Breysacher, J., Azzopardi, M., & Testor, G. 1999, A&AS, 137, 117

Burbidge, E. M., Burbidge, G. R., Fowler, W. A., & Hoyle, F. 1957, Reviews of Modern Physics, 29, 547

Burstein, D., & Heiles, C. 1982, AJ, 87, 1165

Burton, M. G., Bulmer, M., Moorhouse, A., Geballe, T. R., & Brand, P. W. J. L. 1992, MNRAS, 257, 1P

Butler, K., & Zeippen, C. J. 1989, A&A, 208, 337

Buzzoni, B., et al. 1984, The Messenger, 38, 9

Calura, F., Pipino, A., Chiappini, C., Matteucci, F., & Maiolino, R. 2009, A&A, 504, 373

Cappa, C. E., Goss, W. M., Niemela, V. S., & Ostrov, P. G. 1999, AJ, 118, 948

Cappa, C. E., Goss, W. M., & Pineault, S. 2002, AJ, 123, 3348

Carigi, L., Peimbert, M., Esteban, C., & García-Rojas, J. 2005, ApJ, 623, 213

Cescutti, G., Matteucci, F., McWilliam, A., & Chiappini, C. 2009, A&A, 505, 605

Chabrier, G. 2003a, PASP, 115, 763

—. 2003b, ApJ, 586, L133

Chandrasekhar, S. 1934, MNRAS, 94, 522

Chiappini, C., Hirschi, R., Meynet, G., Ekström, S., Maeder, A., & Matteucci, F. 2006, A&A, 449, L27

Chiappini, C., Matteucci, F., & Gratton, R. 1997, ApJ, 477, 765

Chiappini, C., Romano, D., & Matteucci, F. 2003, MNRAS, 339, 63

Chu, Y. 1982, ApJ, 254, 578

Chu, Y. 2003, in IAU Symposium, Vol. 212, A Massive Star Odyssey: From Main Sequence to Supernova, ed. K. van der Hucht, A. Herrero, & C. Esteban, 585–+

Chu, Y.-H. 1981, ApJ, 249, 195

—. 1983, ApJ, 269, 202

Chu, Y. H. 1991, in IAU Symposium, Vol. 143, Wolf-Rayet Stars and Interrelations with Other Massive Stars in Galaxies, ed. K. A. van der Hucht & B. Hidayat, 349–+

Chu, Y.-H., Troland, T. H., Gull, T. R., Treffers, R. R., & Kwitter, K. B. 1982, ApJ, 254, 562

Clegg, R. E. S., Miller, S., Storey, P. J., & Kisielius, R. 1999, A&AS, 135, 359

Crowther, P. A. 2007, ARA&A, 45, 177

Crowther, P. A., Schnurr, O., Hirschi, R., Yusof, N., Parker, R. J., Goodwin, S. P., & Kassim, H. A. 2010, MNRAS, 408, 731

Crowther, P. A., Smith, L. J., & Willis, A. J. 1995, A&A, 304, 269

Dabringhausen, J., Fellhauer, M., & Kroupa, P. 2010, MNRAS, 403, 1054

Danziger, I. J., & Goad, L. E. 1973, Astrophys. Lett., 14, 115

Dearborn, D., Schramm, D. N., & Tinsley, B. M. 1978, ApJ, 223, 557

Dekker, H., D'Odorico, S., Kaufer, A., Delabre, B., & Kotzlowski, H. 2000, in Society of Photo-Optical Instrumentation Engineers (SPIE) Conference Series, Vol. 4008, Society of Photo-Optical Instrumentation Engineers (SPIE) Conference Series, ed. M. Iye & A. F. Moorwood, 534–545

Dopita, M. A. 1972, A&A, 17, 165

Dopita, M. A., Bell, J. F., Chu, Y.-H., & Lozinskaya, T. A. 1994, ApJS, 93, 455

Dopita, M. A., McGregor, P. J., Rawlings, S. J., & Lozinskaia, T. A. 1990, ApJ, 351, 563

Draine, B. T. 2009, in Astronomical Society of the Pacific Conference Series, Vol. 414, Astronomical Society of the Pacific Conference Series, ed. T. Henning, E. Grün, & J. Steinacker, 453–+

Dray, L. M., & Tout, C. A. 2003, MNRAS, 341, 299

Dray, L. M., Tout, C. A., Karakas, A. I., & Lattanzio, J. C. 2003, MNRAS, 338, 973

Drew, J. E., et al. 2005, MNRAS, 362, 753

Dunbar, D. N., Pixley, R. E., Wenzel, W. A., & Whaling, W. 1953, Physical Review, 92, 649

Dunne, L., Eales, S., Ivison, R., Morgan, H., & Edmunds, M. 2003, Nature, 424, 285

Dwek, E. 1998, ApJ, 501, 643

Dwek, E., & Cherchneff, I. 2011, ApJ, 727, 63

Dwek, E., Galliano, F., & Jones, A. P. 2007, ApJ, 662, 927

Dwek, E., Moseley, S. H., Glaccum, W., Graham, J. R., Loewenstein, R. F., Silverberg, R. F., & Smith, R. K. 1992, ApJ, 389, L21

Dyson, J. E., & Meaburn, J. 1971, A&A, 12, 219

Elmegreen, B. G. 2009, in The Evolving ISM in the Milky Way and Nearby Galaxies

Elmhamdi, A., et al. 2003, MNRAS, 338, 939

Ercolano, B., Barlow, M. J., & Sugerman, B. E. K. 2007, MNRAS, 375, 753

Escalante, V., Sternberg, A., & Dalgarno, A. 1991, ApJ, 375, 630

Escalante, V., & Victor, G. A. 1990, ApJS, 73, 513

Esteban, C., Smith, L. J., Vilchez, J. M., & Clegg, R. E. S. 1993, A&A, 272, 299

Esteban, C., & Vilchez, J. M. 1992, ApJ, 390, 536

Esteban, C., Vilchez, J. M., Manchado, A., & Edmunds, M. G. 1990, A&A, 227, 515

Esteban, C., Vilchez, J. M., Manchado, A., & Smith, L. J. 1991, A&A, 244, 205

Esteban, C., Vilchez, J. M., Smith, L. J., & Clegg, R. E. S. 1992, A&A, 259, 629

Fabbian, D., Nissen, P. E., Asplund, M., Pettini, M., & Akerman, C. 2009, A&A, 500, 1143

Ferrarotti, A. S., & Gail, H. 2006, A&A, 447, 553

Fesen, R. A., et al. 2006, ApJ, 645, 283

Foellmi, C., Moffat, A. F. J., & Guerrero, M. A. 2003, MNRAS, 338, 1025

Gail, H., Zhukovska, S. V., Hoppe, P., & Trieloff, M. 2009, ApJ, 698, 1136

Garnett, D. R., & Chu, Y. 1994, PASP, 106, 626

Garnett, D. R., Chu, Y.-H., & Dopita, M. A. 1993, Revista Mexicana de Astronomia y Astrofisica, 27, 141

Gehrz, R. D. 1988, ARA&A, 26, 377

Georgy, C., Meynet, G., Walder, R., Folini, D., & Maeder, A. 2009, A&A, 502, 611

Getman, K. V., Feigelson, E. D., Garmire, G., Broos, P., & Wang, J. 2007, ApJ, 654, 316

Gibson, B. K. 1997, MNRAS, 290, 471

Girardi, L., Bressan, A., Bertelli, G., & Chiosi, C. 2000, A&AS, 141, 371

Gomez, H. L., Vlahakis, C., Stretch, C. M., Dunne, L., Eales, S. A., Beelen, A., Gomez, E. L., & Edmunds, M. G. 2010, MNRAS, 401, L48

Gosachinskij, I. V., & Lozinskaya, T. A. 2002, Astronomy Letters, 28, 701

Groenewegen, M. A. T. 2006, A&A, 448, 181

Guillermo Gimenez de Castro, C., & Niemela, V. S. 1998, MNRAS, 297, 1060

Gummersbach, C. A., Kaufer, A., Schaefer, D. R., Szeifert, T., & Wolf, B. 1998, A&A, 338, 881

Gustafsson, B., Karlsson, T., Olsson, E., Edvardsson, B., & Ryde, N. 1999, A&A, 342, 426

Hayashi, C. 1950, Progress of Theoretical Physics, 5, 224

Hayashi, C., & Nishida, M. 1956, Progress of Theoretical Physics, 16, 613

Henry, R. B. C., Edmunds, M. G., & Köppen, J. 2000, ApJ, 541, 660

Hirschi, R., Meynet, G., & Maeder, A. 2005, A&A, 433, 1013

Howarth, I. D. 1983, MNRAS, 203, 301

Hoyle, F. 1954, ApJS, 1, 121

Hummer, D. G., & Storey, P. J. 1987, MNRAS, 224, 801

Humphreys, R. M. 1991, in IAU Symposium, Vol. 143, Wolf-Rayet Stars and Interrelations with Other Massive Stars in Galaxies, ed. K. A. van der Hucht & B. Hidayat, 485–+

Hunter, I., et al. 2008, ApJ, 676, L29

Iben, Jr., I., & Renzini, A. 1983, ARA&A, 21, 271

Iben, Jr., I., & Truran, J. W. 1978, ApJ, 220, 980

Isserstedt, J., Moffat, A. F. J., & Niemela, V. S. 1983, A&A, 126, 183

Izotov, Y. I., & Thuan, T. X. 1999, ApJ, 511, 639

Jarosik, N., et al. 2010, ArXiv e-prints

Jewitt, D. C., Danielson, G. E., Kupferman, P. N., & Maran, S. P. 1983, ApJ, 268, 683

Johnson, C. T., Burke, P. G., & Kingston, A. E. 1987, Journal of Physics B Atomic Molecular Physics, 20, 2553

Johnson, H. M., & Hogg, D. E. 1965, ApJ, 142, 1033

Jones, A. P., Tielens, A. G. G. M., & Hollenbach, D. J. 1996, ApJ, 469, 740

Jungwiert, B., Carraro, G., & dalla Vecchia, C. 2004, Ap&SS, 289, 441

Jura, M. 1986, ApJ, 303, 327

—. 1987, ApJ, 313, 743

Jura, M., & Kleinmann, S. G. 1989, ApJ, 341, 359

Justtanont, K., Skinner, C. J., & Tielens, A. G. G. M. 1994, ApJ, 435, 852

Karakas, A., & Lattanzio, J. C. 2007, Publications of the Astronomical Society of Australia, 24, 103

Kennicutt, Jr., R. C. 1998, ApJ, 498, 541

Kingsburgh, R. L., & Barlow, M. J. 1994, MNRAS, 271, 257

Kobayashi, C., Umeda, H., Nomoto, K., Tominaga, N., & Ohkubo, T. 2006, ApJ, 653, 1145

Kodama, T. 1997, PhD thesis, PhD thesis, Institute of Astronomy, Univ. Tokyo , (1997)

Komiya, Y., Suda, T., Habe, A., & Fujimoto, M. Y. 2008, in American Institute of Physics Conference Series, Vol. 990, First Stars III, ed. B. W. O'Shea & A. Heger, 462–466

Kotak, R., et al. 2009, ApJ, 704, 306

Krause, O., Birkmann, S. M., Rieke, G. H., Lemke, D., Klaas, U., Hines, D. C., & Gordon, K. D. 2004, Nature, 432, 596

Krause, O., Birkmann, S. M., Usuda, T., Hattori, T., Goto, M., Rieke, G. H., & Misselt, K. A. 2008, Science, 320, 1195

Kroupa, P. 2001a, MNRAS, 322, 231

Kroupa, P. 2001b, in Astronomical Society of the Pacific Conference Series, Vol. 228, Dynamics of Star Clusters and the Milky Way, ed. S. Deiters, B. Fuchs, A. Just, R. Spurzem, & R. Wielen, 187–+

—. 2002, Science, 295, 82

Kwitter, K. B. 1984, ApJ, 287, 840

Lagadec, E., & Zijlstra, A. A. 2008, MNRAS, 390, L59

Lamers, H. J. G. L. M., & Cassinelli, J. P. 1999, Introduction to Stellar Winds, ed. Lamers, H. J. G. L. M. & Cassinelli, J. P.

Landi, E., Del Zanna, G., Young, P. R., Dere, K. P., Mason, H. E., & Landini, M. 2006, ApJS, 162, 261

Larson, R. B. 1976, MNRAS, 176, 31

—. 1998, MNRAS, 301, 569

Le Bertre, T. 1997, A&A, 324, 1059

Li, Y., et al. 2007, ApJ, 665, 187

Liu, X., Barlow, M. J., Danziger, I. J., & Clegg, R. E. S. 1995, MNRAS, 273, 47

Liu, X., Storey, P. J., Barlow, M. J., Danziger, I. J., Cohen, M., & Bryce, M. 2000, MNRAS, 312, 585

Löckmann, U., Baumgardt, H., & Kroupa, P. 2010, MNRAS, 402, 519

Macri, L. M., Stanek, K. Z., Bersier, D., Greenhill, L. J., & Reid, M. J. 2006, ApJ, 652, 1133

Maeder, A. 1992, A&A, 264, 105

Maeder, A., & Meynet, G. 1989, A&A, 210, 155

Maiolino, R., Schneider, R., Oliva, E., Bianchi, S., Ferrara, A., Mannucci, F., Pedani, M., & Roca Sogorb, M. 2004, Nature, 431, 533

Maller, A. H., Katz, N., Kereš, D., Davé, R., & Weinberg, D. H. 2006, ApJ, 647, 763

Maness, H., et al. 2007, ApJ, 669, 1024

Marchenko, S. V. 2006, in Astronomical Society of the Pacific Conference Series, Vol. 353, Stellar Evolution at Low Metallicity: Mass Loss, Explosions, Cosmology, ed. H. J. G. L. M. Lamers, N. Langer, T. Nugis, & K. Annuk, 299–+

Marigo, P. 2001, A&A, 370, 194

Marston, A. P. 1995, AJ, 109, 1839

—. 1997, ApJ, 475, 188

—. 2001, ApJ, 563, 875

Marston, A. P., Chu, Y., & Garcia-Segura, G. 1994a, ApJS, 93, 229

Marston, A. P., Welzmiller, J., Bransford, M. A., Black, J. H., & Bergman, P. 1999, ApJ, 518, 769

Marston, A. P., Yocum, D. R., Garcia-Segura, G., & Chu, Y.-H. 1994b, ApJS, 95, 151

Matsuoka, K., Nagao, T., Maiolino, R., Marconi, A., & Taniguchi, Y. 2009, A&A, 503, 721

Matsuura, M., et al. 2009, MNRAS, 396, 918

—. 2005, A&A, 434, 691

Matteucci, F. 2003, The Chemical Evolution of the Galaxy, ed. Matteucci, F.

Mattila, S., et al. 2008, MNRAS, 389, 141

Meatheringham, S. J., Dopita, M. A., & Morgan, D. H. 1988, ApJ, 329, 166

Meikle, W. P. S., et al. 2007, ApJ, 665, 608

Melioli, C., Brighenti, F., D'Ercole, A., & de Gouveia Dal Pino, E. M. 2009, MNRAS, 399, 1089

Mendoza, C. 1983, in IAU Symposium, Vol. 103, Planetary Nebulae, ed. D. R. Flower, 143–172

Mendoza, C., & Zeippen, C. J. 1982a, MNRAS, 199, 1025

—. 1982b, MNRAS, 198, 127

Metzler, C. A., & Evrard, A. E. 1994, ApJ, 437, 564

Meynet, G., & Maeder, A. 2002, A&A, 390, 561

Michaud, G., Richer, J., & Richard, O. 2007, ApJ, 670, 1178

Miller, G. J., & Chu, Y.-H. 1993, ApJS, 85, 137

Milne, E. A. 1926, MNRAS, 86, 459

Moore, B. D., Hester, J. J., & Scowen, P. A. 2000, AJ, 119, 2991

Morgan, H. L., & Edmunds, M. G. 2003, MNRAS, 343, 427

Munch, G., & Hippelein, H. 1982, Annals of the New York Academy of Sciences, 395, 170

Murali, C., Katz, N., Hernquist, L., Weinberg, D. H., & Davé, R. 2002, ApJ, 571, 1

Nazé, Y., Rauw, G., Manfroid, J., Chu, Y., & Vreux, J. 2003, A&A, 401, L13

Nichols, J. S., & Fesen, R. A. 1994, A&A, 291, 283

Nomoto, K., Hashimoto, M., Tsujimoto, T., Thielemann, F., Kishimoto, N., Kubo, Y., & Nakasato, N. 1997, Nuclear Physics A, 616, 79

Nomoto, K., Tominaga, N., Umeda, H., Kobayashi, C., & Maeda, K. 2006, Nuclear Physics A, 777, 424

Nozawa, T., Kozasa, T., Habe, A., Dwek, E., Umeda, H., Tominaga, N., Maeda, K., & Nomoto, K. 2007, ApJ, 666, 955

Nozawa, T., Kozasa, T., Umeda, H., Maeda, K., & Nomoto, K. 2003, ApJ, 598, 785

Nussbaumer, H., & Rusca, C. 1979, A&A, 72, 129

Osterbrock, D. E., & Ferland, G. J. 2006, Astrophysics of gaseous nebulae and active galactic nuclei, ed. Osterbrock, D. E. & Ferland, G. J.

Padovani, P., & Matteucci, F. 1993, ApJ, 416, 26

Pagel, B. E. J. 1997, Nucleosynthesis and Chemical Evolution of Galaxies, ed. Pagel, B. E. J.

Pagel, B. E. J., & Tautvaisiene, G. 1995, MNRAS, 276, 505

Parker, Q. A., et al. 2005, MNRAS, 362, 689

Peebles, P. J. 1966a, Physical Review Letters, 16, 410

Peebles, P. J. E. 1966b, ApJ, 146, 542

Penzias, A. A., & Wilson, R. W. 1965, ApJ, 142, 419

Pequignot, D., & Aldrovandi, S. M. V. 1976, A&A, 50, 141

Pettini, M., Zych, B. J., Steidel, C. C., & Chaffee, F. H. 2008, MNRAS, 385, 2011

Phillips, J. P. 2007, MNRAS, 381, 117

Portegies Zwart, S. F., McMillan, S. L. W., & Gieles, M. 2010, ARA&A, 48, 431

Portinari, L., Chiosi, C., & Bressan, A. 1998, A&A, 334, 505

Pradhan, A. K. 1976, MNRAS, 177, 31

Prialnik, D. 2000, An Introduction to the Theory of Stellar Structure and Evolution, ed. Prialnik, D.

Puls, J., Sundqvist, J. O., Najarro, F., & Hanson, M. M. 2009, in American Institute of Physics Conference Series, Vol. 1171, American Institute of Physics Conference Series, ed. I. Hubeny, J. M. Stone, K. MacGregor, & K. Werner, 123–135

Raiteri, C. M., Villata, M., & Navarro, J. F. 1996, A&A, 315, 105

Renzini, A., & Voli, M. 1981, A&A, 94, 175

Rho, J., et al. 2008, ApJ, 673, 271

Romano, D., Chiappini, C., Matteucci, F., & Tosi, M. 2004, ArXiv Astrophysics e-prints

Rosa, M. R., & Mathis, J. S. 1990, in Astronomical Society of the Pacific Conference Series, Vol. 7, Properties of Hot Luminous Stars, ed. C. D. Garmany, 135–138

Rownd, B. K., & Young, J. S. 1999, AJ, 118, 670

Salpeter, E. E. 1955, ApJ, 121, 161

—. 1977, ARA&A, 15, 267

Scalo, J. M. 1986, Fund. Cosmic Phys., 11, 1

Schaller, G., Schaerer, D., Meynet, G., & Maeder, A. 1992, A&AS, 96, 269

Schlegel, D. J., Finkbeiner, D. P., & Davis, M. 1998, ApJ, 500, 525

Schmidt, M. 1959, ApJ, 129, 243

Sibthorpe, B., et al. 2010, ApJ, 719, 1553

Smith, L. F., & Payne-Gaposhkin, C. 1968, in Wolf-Rayet Stars, ed. K. B. Gebbie & R. N. Thomas, 21–+

Smith, L. J., & Gallagher, J. S. 2001, MNRAS, 326, 1027

Smith, L. J., Pettini, M., Dyson, J. E., & Hartquist, T. W. 1988, MNRAS, 234, 625

Smith, L. J., Westmoquette, M. S., Gallagher, J. S., O'Connell, R. W., Rosario, D. J., & de Grijs, R. 2006, MNRAS, 370, 513

Snodgrass, C., Saviane, I., Monaco, L., & Sinclaire, P. 2008, The Messenger, 132, 18

Stanghellini, L., Shaw, R. A., & Gilmore, D. 2005, ApJ, 622, 294

Storey, P. J., & Zeippen, C. J. 2000, MNRAS, 312, 813

Stupar, M., Parker, Q. A., & Filipovic, M. D. 2010a, MNRAS, 401, 1760

—. 2010b, ArXiv e-prints

Sugerman, B. E. K., et al. 2006, Science, 313, 196

Szalai, T., Vinkó, J., Balog, Z., Gáspár, A., Block, M., & Kiss, L. L. 2010, ArXiv e-prints

Talbot, J., J. R., & Arnett, D. W. 1974, ApJ, 190, 605

Talbot, Jr., R. J., & Arnett, W. D. 1971, ApJ, 170, 409

Tanabé, T., et al. 1997, Nature, 385, 509

Thomas, D., Maraston, C., Bender, R., & Mendes de Oliveira, C. 2005, ApJ, 621, 673

Thompson, T. A., Prieto, J. L., Stanek, K. Z., Kistler, M. D., Beacom, J. F., & Kochanek, C. S. 2009, ApJ, 705, 1364

Tielens, A. G. G. M. 2005, The Physics and Chemistry of the Interstellar Medium, ed. Tielens, A. G. G. M.

Timmes, F. X., Woosley, S. E., & Weaver, T. A. 1995, ApJS, 98, 617

Tinsley, B. M. 1978, in IAU Symposium, Vol. 76, Planetary Nebulae, ed. Y. Terzian, 341–351

Tinsley, B. M. 1980, Fund. Cosmic Phys., 5, 287

Tomkin, J., Lemke, M., Lambert, D. L., & Sneden, C. 1992, AJ, 104, 1568

Tosi, M. 1982, ApJ, 254, 699

Tsamis, Y. G., Barlow, M. J., Liu, X., Danziger, I. J., & Storey, P. J. 2003, MNRAS, 338, 687

Valiante, R., Schneider, R., Bianchi, S., & Andersen, A. C. 2009, MNRAS, 397, 1661

van den Bergh, S. 1962, AJ, 67, 486

van den Bergh, S., & Tammann, G. A. 1991, ARA&A, 29, 363

van den Hoek, L. B., & Groenewegen, M. A. T. 1997, A&AS, 123, 305

van der Hucht, K. A. 2001, New Astronomy Reviews, 45, 135

—. 2006, A&A, 458, 453

Vassiliadis, E., & Wood, P. R. 1993, ApJ, 413, 641

Vila Costas, M. B., & Edmunds, M. G. 1993, MNRAS, 265, 199

Wachter, A., Winters, J. M., Schröder, K., & Sedlmayr, E. 2008, A&A, 486, 497

Wachter, S., Mauerhan, J. C., Van Dyk, S. D., Hoard, D. W., Kafka, S., & Morris, P. W. 2010, AJ, 139, 2330

Wagoner, R. V., Fowler, W. A., & Hoyle, F. 1967, ApJ, 148, 3

Wang, R., et al. 2008, ApJ, 687, 848

Wesson, R., et al. 2010, MNRAS, 403, 474

Whitelock, P., Menzies, J., Feast, M., Marang, F., Carter, B., Roberts, G., Catchpole, R., & Chapman, J. 1994, MNRAS, 267, 711

Wolfe, A. M., Gawiser, E., & Prochaska, J. X. 2005, ARA&A, 43, 861

Wooden, D. H., Rank, D. M., Bregman, J. D., Witteborn, F. C., Tielens, A. G. G. M., Cohen, M., Pinto, P. A., & Axelrod, T. S. 1993, ApJS, 88, 477

Woosley, S. E., & Weaver, T. A. 1995, ApJS, 101, 181

Yoshii, Y., Tsujimoto, T., & Nomoto, K. 1996, ApJ, 462, 266

Zeippen, C. J. 1982, MNRAS, 198, 111

Zhukovska, S., Gail, H., & Trieloff, M. 2008, A&A, 479, 453